UNIVERSITY COLLEGE LONDON

Gradient-based methods for quantitative photoacoustic tomography

Teedah Soonthornsaratoon

A thesis submitted in partial fulfillment for the
degree of Doctor of Philosophy

in the

Photoacoustic Imaging Group
Department of Medical Physics and Bioengineering

October 2014

Declaration of Authorship

I, Teedah Soonthornsaratoon, confirm that the work presented in this thesis is my own. Where information has been derived from other sources, I confirm that this has been indicated in the thesis.

Signed: _____

Date: _____

“If you would not be forgotten, as soon as you are dead and rotten, either write things worth reading, or do things worth the writing.”

Benjamin Franklin

Abstract

Photoacoustic tomography (PAT) is showing its potential as a non-invasive biomedical imaging modality, and interest in the field is growing rapidly. The images possess excellent contrast, high spatial resolution and good specificity, however, they are largely qualitative and not directly representative of the optically absorbing structures of interest. Quantitative PAT (QPAT) aims to determine quantitatively accurate spatial maps of the underlying tissue chromophores, in order to obtain highly-resolved images of functional information such as blood oxygen saturation and haemoglobin concentration. PAT images are inherently three-dimensional (3D), and their high resolution means that the data sets are of an extremely large scale; a typical problem can easily possess 10^7 unknowns. Existing methods for QPAT have failed to address their applicability to real, 3D PAT images, either by making restrictive approximations to the light model or by using computational intensive techniques which are impractical for large-scale data sets. This thesis develops a practical inversion method for the full and general QPAT problem, in which the tissue geometry is arbitrary, the optical coefficients are unknown and the data is large-scale. The accuracy of the inversion method is ensured by use of the radiative transfer equation (RTE), which provides a highly accurate description of the propagation of light within biological tissue. Using the RTE, a thorough investigation into the effects of errors in the scattering coefficient on the reconstructed absorption coefficient is performed. Computational efficiency in the inversion is provided through an adjoint-assisted, gradient-based minimisation scheme, which iteratively adjusts the parameters of interest until the model prediction matches the measured data. Since the RTE proves too computationally intensive for large data sets, an extension to 3D simulated data is facilitated by the incorporation of the δ-Eddington approximation, thereby providing an accurate, efficient inversion method for QPAT that may be readily applied to experimental data.

Acknowledgements

Firstly and foremostly, I would like to express my sincerest gratitude to my principal supervisor, Ben Cox, for the opportunity to work with him on this research project, and for his guidance, support and endless enthusiasm that has been essential in my completing this thesis.

Special thanks go to my second supervisor, Simon Arridge, for his invaluable advice and encouragement. I would also like to offer my deepest thanks to Tanja Tarvainen, who has been a tremendous ambassador of this work, and has provided useful advice and insight into the research problem.

In addition to my academic advisors, I am grateful to all members of the Department of Medical Physics and Bioengineering at UCL for providing me with such a fantastic working environment. I am not sure I could have completed the journey without the support of my close friends and colleagues. In particular, I am grateful to Thomas Allen, James Avery, Paul Beard, Sophie Brand, Jo Brunker, Robert Cooper, Teresa Correia, Adrien Desjardins, Louise Enfield, Alejandro Giacometti, Adam Gibson, Jenny Griffiths, Jack Honeysett, Jem Hebden, Roman Hochuli, Jan Laufer, Tom Millard, Eoin O'Finnerty, Dan O'Flynn, George Randall and Brad Treeby for their friendship, advice and support throughout the course of my PhD. A special thank you goes to my closest friends, Gemma Bale, Luke Dunne, Nick Everdell, Emma Malone and Sam Powell.

This experience, like so many others, would not have been possible without the constant support and encouragement of my parents, Fran and Richard, my brother, Chad, and my grandparents, Jack and Margaret. I am grateful every day for everything that you have given to me, and I dedicate this thesis to all of you.

Contents

Declaration of Authorship iii

Abstract vii

Acknowledgements ix

List of Figures xv

Abbreviations xxi

List of Symbols xxiii

1 Introduction and background 1
- 1.1 Biomedical photoacoustic imaging . . . 2
  - 1.1.1 Formation of a photoacoustic image . . . 3
    - 1.1.1.1 Photoacoustic imaging . . . 4
- 1.2 Quantitative photoacoustic imaging . . . 7
- 1.3 Challenges . . . 10
  - 1.3.1 Inherent challenges . . . 12
    - 1.3.1.1 Nonlinearity . . . 13
    - 1.3.1.2 Spectral colouring and structural distortion . . . 13
    - 1.3.1.3 Nonuniqueness . . . 15
  - 1.3.2 Practical challenges . . . 15
    - 1.3.2.1 Acoustic reconstruction . . . 15
    - 1.3.2.2 Accuracy of the light model . . . 16
    - 1.3.2.3 Large-scale . . . 16
    - 1.3.2.4 Grüneisen coefficient . . . 16
- 1.4 Structure of the thesis . . . 17

2 Light transport in turbid media 19
- 2.1 Absorption . . . 21
- 2.2 Scattering . . . 23
- 2.3 Optical properties of biological tissue . . . 26
- 2.4 Models of light transport . . . 28
  - 2.4.1 The Monte Carlo method . . . 29

2.4.2 The radiative transfer equation . . . 30
2.4.3 P_n approximations . . . 33
2.4.4 Diffusion approximation . . . 34
2.4.5 Delta-Eddington approximation . . . 36

3 QPAT inversion schemes 39
3.1 Non-scattering media . . . 40
3.2 Homogeneous scattering media . . . 42
3.2.1 Estimating blood oxygen saturation from PA measurements in blood 43
3.3 Arbitrary (known) scattering . . . 46
3.3.1 Complementary DOT measurements . . . 46
3.3.2 Linearisation . . . 47
3.3.2.1 Unchanging fluence . . . 48
3.3.2.2 Born approximation . . . 52
3.3.3 Nonlinear methods . . . 54
3.3.3.1 Fixed point iteration . . . 55
3.3.3.2 Noniterative reconstruction . . . 61
3.3.4 Minimisation-based approach . . . 62
3.4 Unknown scattering . . . 64
3.4.1 Uniqueness and ill-posedness . . . 65
3.4.1.1 Overcoming nonuniqueness using multiple illuminations 66
3.4.1.2 Overcoming nonuniqueness using multiple wavelengths 70
3.4.1.3 Reconstructing the photoacoustic efficiency parameter . 72
3.4.1.4 Diffusivity of the light field . . . 72
3.4.1.5 Sensitivity of error functional to absorption and scattering 73
3.5 Minimisation-based approaches to QPAT . . . 75
3.5.1 Jacobian-based methods . . . 78
3.5.2 Gradient-based vs Jacobian-based methods . . . 80
3.6 Summary . . . 82

4 Gradient-based QPAT using the RTE 1: recovering absorption 83
4.1 Minimisation-based methods in QPAT . . . 84
4.1.1 The radiative transfer equation . . . 84
4.1.2 Gradient-based approach . . . 85
4.1.3 Calculating the gradient of the error functional . . . 86
4.1.4 Implementation . . . 90
4.1.5 Comparison with a finite difference calculation . . . 94
4.2 Numerical examples to recover absorption . . . 97
4.2.1 Simulation of measurement data . . . 98
4.2.2 Inversions with known scattering . . . 100
4.2.2.1 Single point source . . . 100
4.2.2.2 Single line source . . . 102
4.2.3 Extension to multiple illumination directions . . . 104
4.2.3.1 Two point sources . . . 105

4.2.3.2 Four point sources . . . 106
4.2.3.3 Two line sources . . . 107
4.2.3.4 Four line sources . . . 109
4.2.4 Sensitivity to initial guess at absorption . . . 110
4.2.5 Sensitivity to errors in the scattering . . . 112
4.2.6 Inversions with estimated scattering . . . 118
4.2.6.1 Single line source . . . 118
4.2.6.2 Two line sources . . . 120
4.2.6.3 Four line sources . . . 122
4.3 Conclusions . . . 125

5 Gradient-based QPAT using the RTE 2: recovering absorption and scattering 131
5.0.1 Functional gradient with respect to the scattering coefficient . . . 132
5.0.2 Implementation . . . 135
5.0.2.1 Extension to multiple illumination positions . . . 137
5.0.3 Comparison with finite difference calculation . . . 138
5.0.4 Regularisation . . . 140
5.1 Numerical examples recovering absorption and scattering . . . 143
5.1.1 Simulation of measurement data . . . 143
5.1.2 Inversion results: recovering absorption and scattering . . . 145
5.1.2.1 Two point sources . . . 145
5.1.2.2 Two line sources . . . 147
5.1.2.3 Four point sources . . . 149
5.1.2.4 Four line sources . . . 151
5.2 Conclusions . . . 152

6 Gradient-based QPAT using the δ-Eddington approximation 157
6.1 The δ-Eddington approximation . . . 159
6.1.1 Model verification . . . 167
6.2 Incorporation into a gradient-based minimisation scheme . . . 171
6.2.1 Functional gradient for the absorption coefficient . . . 172
6.2.2 Functional gradient for the scattering coefficient . . . 175
6.2.3 Verification of functional gradient calculations . . . 176
6.3 Numerical examples using 2D simulated data . . . 180
6.3.1 Simulation of 2D PAT images . . . 180
6.3.2 Inversion for absorption coefficient . . . 183
6.3.3 Inversion for scattering coefficient . . . 185
6.3.4 Inversion for absorption and scattering . . . 187
6.3.4.1 Example using two line sources . . . 187
6.3.4.2 Example using four top hat sources . . . 189
6.3.4.3 Example using four line sources . . . 190
6.4 Simulating PAT images using the Monte Carlo method . . . 193
6.4.1 Inversion for absorption coefficient . . . 194
6.4.2 Inversion for absorption and scattering . . . 195

6.5 Numerical examples using 3D simulated data . . . 195
6.5.1 Simulation of 3D PAT images . . . 197
6.5.2 Inversion for absorption and scattering . . . 199
6.6 Conclusions . . . 202

7 Conclusions **207**
7.1 Known scattering . . . 209
7.2 Homogeneous scattering . . . 211
7.3 Unknown scattering . . . 211
7.4 The δ-Eddington approximation . . . 213
7.5 Future work . . . 216
7.5.0.1 Determining absolute blood oxygen saturation . . . 217
7.5.0.2 Recovery of chromophore concentrations . . . 218
7.5.0.3 Limited-view data . . . 218

A Scaling the measured data **221**
A.0.1 Functional gradients using logarithmic data . . . 222
A.1 Numerical example using two line sources . . . 226

B Using quotient data to remove the PA efficiency **229**
B.1 Quotient data type using multiple illumination positions . . . 230
B.1.1 Functional gradient for the absorption coefficient . . . 231
B.1.2 Functional gradient for the scattering coefficient . . . 233
B.2 Implementation . . . 234
B.2.1 Functional gradient for absorption . . . 235

C Including the acoustic propagation and reconstruction **237**

D Newton and quasi-Newton methods **271**
D.1 Newton's method in optimisation . . . 271
D.1.1 Line search methods . . . 273
D.2 Quasi-Newton methods . . . 274

Bibliography **277**

List of Figures

1.1 Early photoacoustic image of an absorption phantom . . . 3
1.2 Photoacoustic signal generation and detection. . . . 4
1.3 Photoacoustic image of a subcutaneous tumour in a mouse . . . 5
1.4 Depth-dependent spatial resolution of photoacoustic imaging . . . 6
1.5 Spectroscopic capabilities of PAT . . . 8
1.6 Structural distortion of a PAT image due to the light fluence . . . 14

2.1 Phase function symmetry . . . 25
2.2 Specific absorption spectra of common tissue chromophores . . . 26
2.3 Contributing terms in the radiative transfer equation . . . 31

3.1 Absorption and scattering coefficients used to demonstrate the change in the fluence due to perturbations in the optical coefficients . . . 48
3.2 Optical fluence modelled due to background and heterogeneous optical coefficients . . . 50
3.3 Fluence perturbation $\Phi^{\delta} = \Phi - \Phi^{0}$ due to three different cases of scattering coefficients . . . 52
3.4 Heterogeneous optical absorption and scattering coefficients used to simulate the measurement data . . . 57
3.5 Fixed point iteration: recovery of absorption coefficient when the scattering is known *a priori* . . . 58
3.6 Fixed point iteration: recovery of absorption coefficient when the scattering contains a 10% error . . . 59
3.7 Fixed point iteration: recovery of absorption coefficient when the scattering coefficient is fixed at its background value . . . 60
3.8 Sensitivity of the absorption reconstruction to errors in the scattering coefficient when using the fixed-point iteration . . . 61
3.9 Example of absorption-scatter nonuniqueness . . . 65
3.10 Overcoming the absorption-scatter nonuniqueness using multiple illumination positions . . . 66
3.11 Mesh geometry, source location and perturbation location used to show the sensitivity of the error functional to changes in the absorption and scattering coefficients . . . 73
3.12 Contour and surface plot showing the sensitivity of the error functional to changes in the absorption and scattering coefficients . . . 74

3.13 Memory required to store the Hessian approximation using gradient- and Jacobian-based minimisation methods 81

4.1 Comparison of the error functional gradient with respect to absorption calculated using the gradient-based method with a finite difference method 96
4.2 Point sources used to simulate the measurement data 98
4.3 Line source arrays used to simulate the measurement data 99
4.4 Reconstructed absorption coefficient when the scattering is known *a priori* (single point source) 101
4.5 Reconstructed absorption coefficient when the scattering is known *a priori* (single line source) 103
4.6 Reconstructed absorption coefficient when the scattering is known *a priori* (two point sources) 105
4.7 Reconstructed absorption coefficient when the scattering is known *a priori* (four point sources) 107
4.8 Reconstructed absorption coefficient when the scattering is known *a priori* (two line sources) 108
4.9 Reconstructed absorption coefficient when the scattering is known *a priori* (four line sources) 109
4.10 Sensitivity of the absorption reconstruction to changes in the initial guess at absorption 111
4.11 Sensitivity of the absorption reconstruction to errors in the scattering coefficient using a single point source. 113
4.12 Sensitivity of the absorption reconstruction to errors in the scattering coefficient using four line sources 114
4.13 Improvement of errors in the absorption reconstruction when multiple illumination positions are used 115
4.14 Sensitivity of the absorption reconstruction to errors in the scattering coefficient using the fixed point iteration and the gradient-based minimisation when using a single line source 116
4.15 Sensitivity of the absorption reconstruction to errors in the scattering coefficient using the fixed point iteration (single line source) and the gradient-based minimisation (four line sources) 117
4.16 Reconstructed absorption coefficient when the scattering is fixed at its mean value (single line source) 119
4.17 Comparison of the reconstructed absorption coefficients when the scattering is known *a priori* and when it is fixed at its mean value (single line source) 119
4.18 Reconstructed absorption coefficient when the scattering is fixed at its mean value (two line sources) 120
4.19 Comparison of the reconstructed absorption coefficients when the scattering is known *a priori* and when it is fixed at its mean value (two line sources) 121
4.20 Reconstructed absorption coefficient when the scattering is fixed at its mean value (four line sources) 122

4.21 Comparison of the reconstructed absorption coefficients when the scattering is known *a priori* and when it is fixed at its mean value (four line sources) . . . 123
4.22 Reconstructed absorption coefficient when the scattering is fixed at twice its mean value ($\mu_s = 11.1$ mm^{-1}) . . . 125

5.1 Error functional gradient with respect to scattering calculated using the adjoint-assisted method and compared with a finite difference method . 139
5.2 The effect of varying the regularisation parameter β on the reconstructed optical coefficients. . . . 141
5.3 Profile comparison showing the effect of varying the regularisation parameter β on the reconstructed optical coefficients. . . . 143
5.4 Simultaneous recovery of absorption and scattering coefficients using two point sources . . . 145
5.5 Simultaneous recovery of absorption and scattering coefficients using two point sources (profiles) . . . 146
5.6 Simultaneous recovery of absorption and scattering coefficients using two line sources . . . 147
5.7 Simultaneous recovery of absorption and scattering coefficients using two line sources (profiles) . . . 148
5.8 Simultaneous recovery of absorption and scattering coefficients using four point sources . . . 149
5.9 Simultaneous recovery of absorption and scattering coefficients using four point sources (profiles) . . . 150
5.10 Simultaneous recovery of absorption and scattering coefficients using four line sources . . . 151
5.11 Simultaneous recovery of absorption and scattering coefficients using four line sources (profiles) . . . 152

6.1 Absorbed optical energy calculated using the Monte Carlo method, δ-Eddington approximation and the diffusion approximation . . . 168
6.2 Profile comparison of the absorbed optical energy calculated using the Monte Carlo method, δ-Eddington approximation and the diffusion approximation . . . 170
6.3 Absorption and scattering coefficients used to compare the error functional gradients . . . 177
6.4 Comparison of the absorption functional gradient calculated using the adjoint-assisted method and a finite difference calculation . . . 178
6.5 Comparison of the scattering functional gradient calculated using the adjoint-assisted method and a finite difference calculation . . . 179
6.6 Mesh structure and source geometry used to simulate PAT images (line sources) . . . 181
6.7 Mesh structure and source geometry used to simulate PAT images (top hat sources) . . . 182
6.8 Forward data calculated using the δ-Eddington approximation to the RTE 183

6.9 Reconstructed absorption coefficient using the gradient-based method based on the δ-Eddington approximation (known scattering) 184
6.10 Profile comparison of the true and reconstructed absorption coefficient (known scattering) 184
6.11 Reconstructed scattering coefficient using the gradient-based method based on the δ-Eddington approximation (known absorption) 186
6.12 Profile comparison of the true and reconstructed scattering coefficient (known absorption) 186
6.13 Reconstructed absorption and scattering coefficients from 2D simulated data using the δ-Eddington approximation (two line sources) 188
6.14 Profile comparison of the true and reconstructed absorption and scattering coefficients from 2D simulated data using the δ-Eddington approximation (two line sources) 188
6.15 Reconstructed absorption and scattering coefficients from 2D simulated data using the δ-Eddington approximation (four point sources) 189
6.16 Profile comparison of the true and reconstructed absorption and scattering coefficients from 2D simulated data using the δ-Eddington approximation (four point sources) 190
6.17 Reconstructed absorption and scattering coefficients from 2D simulated data using the δ-Eddington approximation (four line sources) 191
6.18 Profile comparison of the true and reconstructed absorption and scattering coefficients from 2D simulated data using the δ-Eddington approximation (four line sources) 192
6.19 Reconstructed absorption coefficient using the gradient-based δ-Eddington minimisation where the forward data is simulated using the MC method. 194
6.20 Reconstructed absorption and scattering coefficients using the gradient-based δ-Eddington minimisation where the forward data is simulated using the MC method. 196
6.21 Reconstructed absorption and scattering coefficients using the gradient-based δ-Eddington minimisation where the forward data is simulated using the MC method. 196
6.22 Optical absorption and scattering coefficients used to simulate 3D PAT images 197
6.23 Forward data calculated using the 3D δ-Eddington approximation to the RTE 198
6.24 Profiles of the forward data calculated using the 3D δ-Eddington approximation to the RTE 199
6.25 Slices of the true and reconstructed absorption coefficient from 3D simulated data (four sources) 200
6.26 Slices of the true and reconstructed scattering coefficient from 3D simulated data (four sources) 201
6.27 Profiles of the true and reconstructed absorption and scattering coefficients from 3D simulated data (four sources) 202

A.1 Contour and surface plot showing the sensitivity of the error functional to changes in the absorption and scattering coefficients 222

A.2 Contour and surface plot showing the improved sensitivity of the error functional to changes in the absorption and scattering coefficients when using logarithmic data 222
A.3 Simultaneous recovery of absorption and scattering coefficients from logarithmic data using two line sources 227
A.4 Simultaneous recovery of absorption and scattering coefficients from logarithmic using two line sources (profiles) 228

Abbreviations

2D	Two-dimensional
3D	Three-dimensional
DA	Diffusion approximation
DOT	Diffuse optical tomography
FE	Finite element
FEM	Finite element method
MC	Monte Carlo
NIR	Near-infrared
PA	Photoacoustic
PAT	Photoacoustic tomography
QPAT	Quantitative photoacoustic tomography
RTE	Radiative transfer equation
sO_2	Oxygen saturation

List of Symbols

Quantity	Meaning	Units
n	Dimension	
$\mathbb{R}^n$	n-dimensional real space	
Ω	Domain	
$\partial\Omega$	Domain boundary	
S^{n-1}	Angular space	
$\|\cdot\|$	Euclidean norm	
$\mathbf{r}$	Position vector	mm
$\hat{\mathbf{n}}$	Outward normal to boundary	
$\hat{\mathbf{s}}$	Unit vector in S^{n-1}	
t	Time	s
λ	Optical wavelength	nm
c	Speed of light	mm s^{-1}
c_0	Speed of sound	mm s^{-1}
ν	Frequency	s^{-1}
h	Planck's constant	J s
c_k	Concentration of k^{th} chromophore	mmol/L
α_k	Specific absorption coefficient	$(\mathrm{mmol/L})^{-1}$ mm^{-1}
σ_{a}	Absorption cross-section	mm^{-2}
σ_{s}	Scattering cross-section	mm^{-2}
μ_{a}	Optical absorption coefficient	mm^{-1}
μ_{s}	Optical scattering coefficient	mm^{-1}
μ'_{s}	Reduced optical scattering coefficient	mm^{-1}

μ_{t}	Total attenuation coefficient	mm^{-1}
μ_{eff}	Effective attenuation coefficient	mm^{-1}
κ	Diffusion coefficient	
$\hat{\mu}_{\mathrm{s}}$	Modified optical scattering coefficient	mm^{-1}
$\hat{\mu}_{\mathrm{t}}$	Modified total attenuation coefficient	mm^{-1}
$\hat{\kappa}$	Modified diffusion coefficient	
g	Anisotropy factor	
Θ	Scattering phase function	
Φ	Optical fluence	$\mathrm{J\ mm}^{-2}$
ϕ	Optical (time-integrated) radiance	$\mathrm{J\ mm}^{-2}\ \mathrm{sr}^{-1}$
Φ^*	Adjoint optical fluence	$\mathrm{J\ mm}^{-2}$
ϕ^*	Adjoint optical radiance	$\mathrm{J\ mm}^{-2}\ \mathrm{sr}^{-1}$
h	Absorbed optical energy density	$\mathrm{J\ mm}^{-3}$
p_0	Initial pressure distribution	$\mathrm{J\ mm}^{-3}$
$\hat{\Gamma}$	Photoacoustic efficiency	
Γ	Grüneisen parameter	

Chapter 1

Introduction and background

Photoacoustic tomography (PAT) is a hybrid imaging modality possessing both the superior contrast of optical techniques and the high spatial resolution of ultrasound. The spectroscopic capabilities of optical imaging techniques can be exploited to obtain useful information about the molecular composition of the underlying biological tissue. Quantitative photoacoustic tomography (QPAT) offers the possibility of high-resolution molecular imaging by exploiting the spectral capabilities of PAT to quantify molecular concentrations in biological tissue. QPAT comprises two inverse problems: (1) the construction of a photoacoustic image from surface measurements of photoacoustic wave pulses over time, and (2) the determination of the optical properties of the imaged region. The first is a well-studied area for which a number of solution methods are available, while the second is, in general, a nonlinear, ill-posed inverse problem. Many inversion methods for QPAT have failed to consider whether the method will be applicable to real PAT images, where the data is 3D and of a large scale. The aim of this thesis is to provide an inversion method for the full and general QPAT problem which models the propagation of light within the tissue rigorously and enables the practical extension to real, 3D data sets.

1.1 Biomedical photoacoustic imaging

The potential for photoacoustic imaging to be routinely used in a broad range of biomedical imaging applications is beginning to be realised, as evidenced by the emergence of a wide variety of *in vivo* images, including breast imaging [1], small animal imaging for preclinical studies [2, 3], and molecular imaging [4]. Although photoacoustic (PA) imaging is a relatively new biomedical imaging modality, research into the underlying physics of PA techniques has a much longer history. PA imaging is based on the photoacoustic effect, that is, the conversion of energy between light and acoustic waves due to absorption and localised thermal excitation. The generation of sound by light was first described by Alexander Graham Bell in 1880 [5], where it was discovered that an intense, pulsed light source incident on a sample of matter can produce audible sound. Bell observed the generation of sound owing to the absorption of modulated sunlight with an invention called the 'photophone'. Realising the potential application to spectroscopy, Bell also developed the 'spectrophone', enabling the measurement of spectra outside of the visible range. Bell's findings were initially concerned with solid samples and, in 1881, Tyndall in Britain and Roentgen in Germany performed subsequent experiments to demonstrate that the effect was also encountered in liquids and gases [6, 7]. Despite these achievements and the enthusiasm that followed the discovery, an application of the effect did not come until 1938, when the technique was utilised in gas concentration analysis by Viengerov to measure CO_2 concentrations by detecting the light-induced propagated acoustic waves travelling through the gas with a microphone [8]. Few other implementations arose in the years to follow, and even after the development of the laser in the 1960s, it was the gas detection technique which dominated PA applications. It was not until the mid-1990s that the PA effect was investigated for biomedical imaging techniques and the first PA images were produced [9–12], and not until the mid-2000s that the first *in vivo* images began to appear. Figure 1.1 shows an early (1995) example of PA imaging.

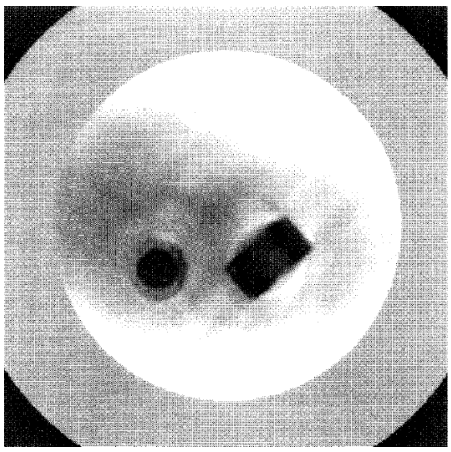

FIGURE 1.1: Early photoacoustic image of an absorption phantom. Figure 5 in [9].

1.1.1 Formation of a photoacoustic image

When tissue is irradiated with modulated electromagnetic radiation, such as short laser or radio frequency pulses, ultrasound waves are excited. In PA imaging, optical wavelengths in the visible and near-infrared (NIR) part of the spectrum are used. If the wavelengths of the stimulating radiation lie in the microwave band (300 MHz - 3 GHz), the technique is referred to as thermoacoustic imaging. In the case of optical excitation, the energy is absorbed by tissue chromophores (light-absorbing molecules) such as water, haemoglobin, melanin or lipids. This is followed by a rapid conversion to heat, which produces a small, local increase in temperature (typically less than 0.1 K - well below that required to cause physical changes or damage to tissue [13]). This leads to an increase in pressure, which subsequently relaxes and propagates broadband acoustic waves which may be detected at the tissue surface, either by a single ultrasound receiver or an array of receivers. By measuring the times-of-arrival of these waves and knowing the speed of sound in biological tissue, an image of the distribution of initial pressure can be formed. A schematic of the generation of a PA wave and its subsequent detection at the measurement surface can be seen in Figure 1.2.

The principal source of contrast in PA imaging is based on the optical absorption in the photoacoustic excitation phase [14]. In biological tissue, a 'spectral window' exists in

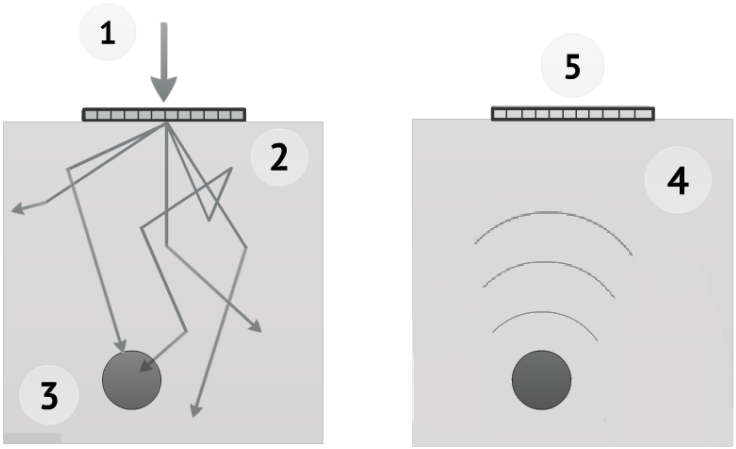

FIGURE 1.2: Photoacoustic signal generation and detection. 1. A short laser pulse is delivered through a transparent ultrasound detector and illuminates the tissue region. 2. Photons are scattered throughout the tissue and illuminate the region. 3. Some photons are absorbed by chromophores (light-absorbing molecules) within the tissue, resulting in a distribution of absorbed optical energy. 4. The absorbed optical energy causes an increase in pressure, which propagates as an acoustic wave. 5. An ultrasound detector at the tissue surface records the times-of-arrival of the acoustic waves.

the near-infrared (NIR) optical wavelength range of approximately 600-900 nm. Tissue is predominantly water, which is relatively weakly absorbing in this range. These wavelengths therefore offer the greatest penetration depths in biological tissue (up to several cm), enabling the detection of deeper structures. Within this window, oxyhaemoglobin and deoxyhaemoglobin absorb the light relatively strongly, making PAT particularly suited to imaging the microvasculature. Figure 1.3 demonstrates a typical preclinical application of PAT: the PAT imaging system was used to image a subcutaneous tumour in a mouse, in order to study the response of the tumour vasculature following the administration of a therapeutic vascular disrupting agent [2].

1.1.1.1 Photoacoustic imaging

PA imaging is a hybrid imaging technique based on laser-generated ultrasound which benefits from both the high contrast associated with optical imaging techniques and the high spatial resolution of ultrasound imaging. In PA imaging, the image contrast is

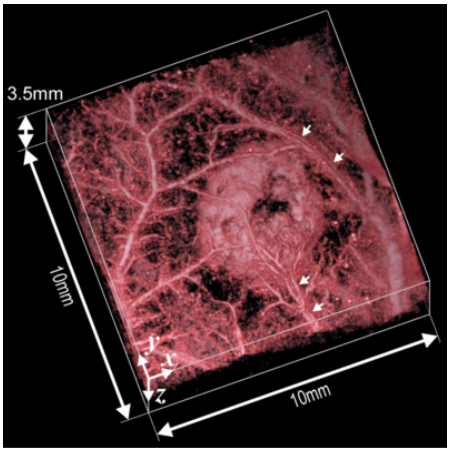

FIGURE 1.3: Photoacoustic image of a subcutaneous tumour in a mouse. This volume-rendered 3D PAT image was obtained used an optical wavelength of 600 nm and a scan step size of 70 μm. Figure 2(a) in [2].

largely dominated by the optical absorption, which can provide greater tissue differentiation and specificity than ultrasonic imaging, since differences in optical absorption between tissue types can be much larger than differences in acoustic impedance [13]. Various endogenous and exogenous absorbers, such as haemoglobin, melanin, water, lipid, organic dyes, nanoparticles, and reporter genes, can serve as contrast agents. This enables the visualisation of the vasculature, blood oxygenation levels, biomarkers and gene expression [15], and can also extend the applications of photoacoustics to molecular imaging [16].

Optical imaging techniques are severely restricted by the ability of the light to penetrate biological tissue. Consequently, applications in adult humans are limited mainly to the breast and skin, a limitation which has so far prevented optical imaging techniques from reaching routine clinical use. Whilst the imaging depth in PA imaging is also limited by optical attenuation, it does significantly exceed that of purely optical imaging techniques, which typically rely on unscattered or ballistic photons. The signal-to-noise ratio will be determined by the maximum permissible exposure of the light on the tissue surface and the noise equivalent pressure of the acoustic detector. Another advantage that PA imaging has over purely optical imaging techniques is that the improved spatial resolution can provide incredibly detailed structural images at depths of up several centimetres. In PA imaging, it is the frequency-dependent acoustic attenuation exhibited by most

soft tissue which limits the spatial resolution. Under these circumstances, the spatial resolution scales with depth [13]. Other limiting factors can be the detector bandwidth, element size and the area over which the PA signals are recorded. At imaging depths typically used in PA imaging the spatial resolution is excellent (typically tens of micrometres, though sub-micrometre is possible for shallower imaging depths). This offers a number of clinical and preclinical applications, including breast imaging, whole-body small animal imaging and drug development and enhancement. Figure 1.4 illustrates the depth-dependent spatial resolution and potential applications of PA imaging.

FIGURE 1.4: Depth-dependent spatial resolution of photoacoustic imaging. (A) Maximum intensity projection of a 3D photoacoustic image of a human breast. The penetration depth is around 4 cm, with spatial resolution of around 250 μm. Figure 5(a) in [1]. (B) Photoacoustic imaging of the skin vasculature. The penetration depth is less than 1 cm, with spatial resolution of less than 100 μm. Image courtesy of Paul Beard. (C) Photoacoustic microscopy imaging of capillaries in the mouse ear. The penetration depth is less than 1 mm, with spatial resolution of less than 10 μm. Figure 4 in [17].

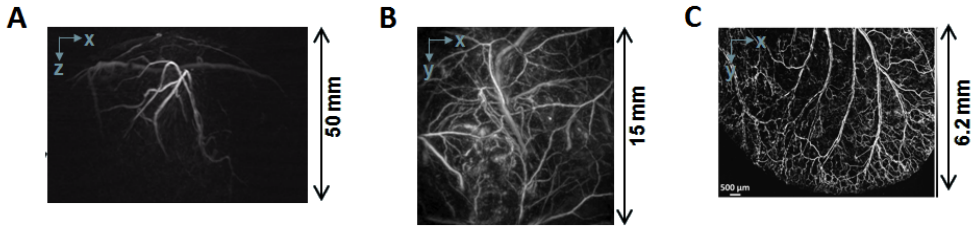

The ability to take spectroscopic measurements can be exploited to obtain useful information about the molecular composition of the underlying biological tissue. For example, blood oxygen saturation (sO_2) is an extremely important prognostic factor for determining tissue health, and can also be used to characterise cancerous tissue, which typically exhibits abnormal levels of blood sO_2. Blood sO_2 is calculated through knowledge of the concentrations of oxyhaemoglobin and deoxyhaemoglobin. Tuning the laser to wavelengths where oxyhaemoglobin and deoxyhaemoglobin absorb the light relatively strongly could therefore provide a measurement of the blood oxygen saturation of a tissue region. Figure 1.5 shows how the choice of wavelength can highlight different or additional information regarding the underlying tissue chromophores. Blood sO_2 is a major prognostic factor for the progression of tumours and their resistance to anticancer treatment. The most widely used technique to measure blood sO_2 is pulse

oximetry, based on near-infrared spectroscopy. This technique measures the light passing through a region of tissue at two or more optical wavelengths to determine the absorbance due to the oxygenated blood alone. Pulse oximetry, however, is only informative about the average tissue oxygenation of an entire region, and is unable to produce the spatially-resolved images required for cancer detection and tumour assessment. Existing techniques which are able to produce spatially-resolved images of blood sO_2 require a harmful radiation dose (x-ray computed tomography, positron emission tomography), are extremely expensive (magnetic resonance imaging), or possess poor spatial resolution (diffuse optical tomography, bioluminsence imaging). PAT is a non-ionising, non-invasive, fast and affordable biomedical imaging modality which retains excellent spatial resolution. The absorption-based contrast and dependence on optical wavelength means that there is a potential for PAT to be used to provide quantitatively accurate images of blood sO_2 with spatial resolution far superior to other optical imaging modalities. This would have direct physiological relevance, finding application in many clinical and research applications, such as the blood oxygenation distribution of tumours, the assessment of vascular lesions, soft tissue damage such as burns and wounds, and any other tissue abnormalities characterised by changes in tissue oxygenation. The determination of absolute values of specific chromophore concentrations is not straightforward, since a PA image is not a quantitative representation of the optical absorption within the tissue, and so is not directly representative of the absolute values of the concentrations of specific chromophores. However, since PA images are certainly dependent on these properties, it is possible that this information may be extracted from the image.

1.2 Quantitative photoacoustic imaging

A photoacoustic (PA) image is dependent on the optical properties of the tissue, namely the optical absorption and optical scattering coefficients, which reflect the tissue structure and physiology. A conventional PAT image is an image of the initial pressure distribution arising from the absorbance of optical energy by chromophores within the tissue. Whilst PAT images can be qualitatively informative, they are not quantitatively representative

FIGURE 1.5: Spectroscopic capabilities of PAT. The differences in the absorption spectra of different chromophores (in this case, oxyhaemoglobin (HbO_2) and deoxyhaemoglobin (Hb)) mean that imaging at different optical wavelengths can highlight a particular chromophore of interest. In this figure, two PAT images are taken at 600 nm and 640 nm. The image at 640 nm highlights vein-artery pairs that are not present in the image obtained at 600 nm. Images courtesy of Paul Beard.

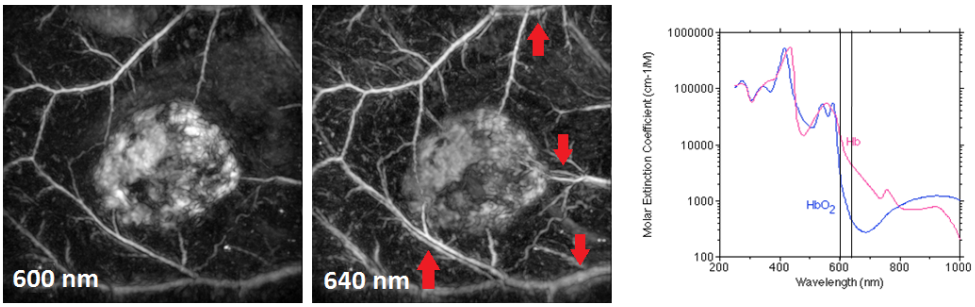

of the concentrations of the chromophores present in the imaged region. QPAT aims to exploit the spectroscopic capabilities of PAT by converting multi-wavelength sets of PAT images into quantitative spatial maps of the underlying tissue chromophores. The ability to recover absolute values of specific chromophore concentration distributions could then provide a wealth of absolute, spatially-resolved estimates of physiological parameters such as haemoglobin, oxygen saturation and lipid content [13, 18, 19]. Quantities such as these could be used to study a range of processes which are characterised by functional or structural changes in the blood vasculature, including blood flow, tumour biology and angiogenesis, brain function, and cardiovascular disease. This technique could also be applied to exogenous chromophores such as contrast agents in order to offer the possibility of use in functional or structural imaging at a cellular or molecular level, for example, in high-resolution molecular imaging of small animals. QPAT would therefore provide a non-ionising, non-invasive, fast and affordable method of obtaining highly-resolved functional and molecular information. Such a range of applications to structural and functional imaging in a single imaging modality would give PAT the potential to become a truly powerful technique in biomedical applications.

The optical absorption coefficient is linearly related to the concentrations of the chromophores present within the imaged tissue region. If a technique to recover a quantitatively accurate, spatially-resolved estimate of the absorption coefficient were available,

images of the absolute concentrations of individual chromophores could be determined straightforwardly. Images of the absorption coefficient would also provide for a truer image contrast distribution, since a PA image is actually representative of the initial pressure distribution following the light pulse. Furthermore, recovery of the absorption coefficient would remove the depth-dependent fall-off due to optical attenuation, aiding the visual interpretation of an image.

The reconstruction of images of chromophore concentration distributions (or the optical absorption coefficient) from the measured PA time series is an inverse problem. The forward problem in PAT consists of the propagation of light through the tissue and the absorption of optical energy, which leads to the propagation of acoustic waves that are detected at the tissue surface. The acoustic propagation occurs on a microsecond time scale, about three orders of magnitude slower than the optical propagation. This allows the optical and acoustic parts of the forward problem, and hence their corresponding inverse problems, to be decoupled and treated separately. The first inverse problem of QPAT, typically referred to as the acoustic inverse problem, involves the reconstruction of the initial acoustic pressure distribution from time-dependent acoustic measurements at the domain's boundary. This problem is considered largely solved; there are several exact solutions for the case of complete data and acoustically homogeneous tissue [20, 21]. The case in which the sound speed or acoustic absorption varies within the tissue is significantly more challenging, but will not be the subject of discussion in this thesis.

The solution to the acoustic inverse problem provides the measurement data for a second inverse problem, often referred to as the optical inverse problem. Since a number of solution techniques for the acoustic inverse problem exist, the optical inverse problem is typically considered the remaining problem of QPAT, and methods for its solution will be the main concern of this thesis. The optical inverse problem begins by assuming that the initial acoustic pressure distribution has been reconstructed accurately. The initial pressure distribution is the product of the absorbed optical energy h and the photoacoustic efficiency parameter, $\hat{\Gamma}$. $\hat{\Gamma}$ is typically assumed to be known and constant, so that PAT images are proportional to the distribution of absorbed optical energy. The absorbed

optical energy density is also the product of two quantities; the optical fluence Φ and the absorption coefficient μ_{a}. Since the fluence itself is absorption-dependent, determining the absorption coefficient (and hence the concentrations of tissue chromophore) from a measured PAT image is not straightforward. Some of the associated challenges are inherent to the problem, while others are practical considerations related to a specific experimental setup or solution method. The next section will discuss some of these challenges.

1.3 Challenges

When considering how we can extract information about tissue chromophores from a PAT image, we must first consider what the image represents, and the physical properties upon which it depends. We have briefly discussed how a PA signal is generated and how an image is formed; firstly, light is delivered into a region of biological tissue $\Omega \subset \mathbb{R}^n$, $n = 2, 3$, where it is multiply scattered and absorbed. Given that the temporal length of the optical excitation and absorption is several orders of magnitude shorter than the acoustic propagation (nanoseconds compared to microseconds), the former is considered to happen instantaneously. The result of the tissue illumination is therefore described by the optical fluence, Φ, which represents the total optical energy at a given point $\mathbf{r} \in \Omega$. The fluence is dependent on certain optical properties within the tissue, that is,

$$\Phi = \Phi(\mathbf{r}; \mu_{\mathrm{a}}, \mu_{\mathrm{s}}), \tag{1.1}$$

where $\mu_{\mathrm{a}} = \mu_{\mathrm{a}}(\mathbf{r})$ is the optical absorption coefficient and $\mu_{\mathrm{s}} = \mu_{\mathrm{s}}(\mathbf{r})$ is the optical scattering coefficient. These properties represent the rate at which optical energy will be absorbed or scattered, respectively, per unit length at a position $\mathbf{r}$ within the tissue. The distribution of absorbed optical energy is therefore given by

$$h = \mu_{\mathrm{a}}\Phi. \tag{1.2}$$

This absorption of optical energy results in a small increase in local temperature, which leads to a corresponding increase in local pressure

$$p_0 = \hat{\Gamma} h \quad \Rightarrow \quad p_0 = \hat{\Gamma} \mu_{\mathrm{a}} \Phi, \tag{1.3}$$

where $\hat{\Gamma}$ is the PA efficiency. (In an absorbing fluid, $\hat{\Gamma}$ is typically equated to the Grüneisen parameter, Γ, a dimensionless, thermodynamic property of a material which provides a measure of the efficiency of the conversion from heat to pressure.) Due to the elastic nature of tissue, the increase in local pressure subsequently becomes a propagating acoustic wave. We therefore refer to p_0 as the initial pressure distribution, since it becomes an initial condition for modelling the acoustic wave propagation.

In PAT, the propagated acoustic waves are measured at the tissue surface by an ultrasound detector or array of detectors, resulting in a measured time series, $p(\mathbf{r}, t)$, which represents the acoustic pressure at time $t \in \mathbb{R}^+$ and at position $\mathbf{r} \in \Omega$. Assuming the sound speed c_0 and density are uniform, the acoustic propagation obeys the photoacoustic wave equation

$$\left(\frac{\partial^2}{\partial t^2} - c_0^2 \nabla^2 \right) p(\mathbf{r}, t) = 0, \tag{1.4}$$

with initial conditions

$$p(\mathbf{r}, t)|_{t=0} = p_0, \quad \frac{\partial p}{\partial t}|_{t=0} = 0. \tag{1.5}$$

This can be used as a forward model to simulate the propagation of the acoustic waves, or can be solved as an inverse initial value problem to reconstruct the initial pressure distribution from the recorded pressure time signals. In the latter case, we denote the reconstructed initial pressure distribution by p_0^{obs}, and it is this which constitutes the PAT image. There are several methods available for reconstructing the initial pressure distribution, including time-reversal and filtered back-projection [20]. In QPAT, it is typically assumed that the initial pressure distribution has been reconstructed sufficiently accurately. The remaining problem is then to determine quantitatively accurate spatial

maps of the chromophore concentrations.

The chromophore concentrations are related to the absorption coefficient via the linear sum

$$\mu_{\mathrm{a}}(\mathbf{r},\lambda) = \sum_{k=1}^{K} \alpha_k(\lambda) c_k(\mathbf{r}), \tag{1.6}$$

where α_k is the specific absorption coefficient of the $k\mathrm{th}$ chromophore, and c_k is its concentration. The specific absorption coefficients are typically known for chromophores present in biological tissue (see Section 2.3). This means that the K chromophore concentrations can be recovered straightforwardly provided that a quantitative estimate of the absorption coefficient μ_{a} is found for at least K different wavelengths. Furthermore, it is possible that the system may be calibrated to find $\hat{\Gamma}$; in this case, we can determine the measured absorbed energy map h^{obs} straightforwardly using

$$h^{\mathrm{obs}} = \frac{p_0^{\mathrm{obs}}}{\hat{\Gamma}}. \tag{1.7}$$

Because of this, many inversion methods for QPAT aim to determine μ_{a} from the measured absorbed energy map h^{obs}, under the assumptions that $\hat{\Gamma}$ is known *a priori* or can be measured, the absorption spectra for the constituent tissue chromophores are known, and that multi-wavelength measurements and a linear inversion for the chromophore concentrations will follow.

1.3.1 Inherent challenges

Let us assume that $\hat{\Gamma}$ is known *a priori*, or can be accurately measured, as discussed above. Let us also assume that the specific absorption coefficients are known for the chromophores of interest. We are now concerned with whether we can determine μ_{a} from the measured absorbed energy map h^{obs}. The following properties are inherent

to the inverse problem, and arise regardless of the inversion approach or experimental setup.

1.3.1.1 Nonlinearity

The absorbed energy is given by

$$h^{\mathrm{obs}} = \mu_{\mathrm{a}}\Phi(\mu_{\mathrm{a}}, \mu_{\mathrm{s}}), \tag{1.8}$$

so that the h^{obs} depends nonlinearly on μ_{a}. Were it possible to somehow measure the light fluence, finding μ_{a} given h^{obs} would be straightforward. While methods for measuring the fluence exist, e.g. DOT, they are limited by their poor spatial resolution, and hence do not provide a sufficiently accurate estimate of μ_{a}. The light fluence therefore remains unknown, and depends nontrivially on both the unknown optical absorption μ_{a} and the unknown optical scattering coefficient μ_{s}.

1.3.1.2 Spectral colouring and structural distortion

In an arbitrary region of tissue, the optical coefficients and fluence will vary both with wavelength λ and position $\mathbf{r}$, so that equation 1.8 can be written as

$$h^{\mathrm{obs}}(\mathbf{r}, \lambda) = \mu_{\mathrm{a}}(\mathbf{r}, \lambda)\Phi(\mathbf{r}, \lambda; \mu_{\mathrm{a}}(\mathbf{r}, \lambda), \mu_{\mathrm{s}}(\mathbf{r}, \lambda)). \tag{1.9}$$

The fluence at a given point will depend on the distribution of the optical coefficients over the entire illuminated volume. The spectra of all of the chromophores and the scatterers in this volume will therefore be encoded onto the absorbed energy spectrum at this point. To see this, consider two spectrally distinct absorbers located such that one lies directly beneath the other. In this case, the light must pass through the one absorber to reach the absorber beneath, so that the absorbed energy spectrum of the latter will consist of the spectral characteristics of both. As tissue is a highly scattering medium, this kind of spectral cross-talk can occur even if two absorbers are located side by side

at the same depth, or, if there is enough backscattering, from a deeper absorber to one above.

As well as being a function of wavelength, the fluence is also a function of position and therefore affects the absorbed energy map spatially as well as spectrally. It is therefore not appropriate to assume that the PAT image is directly proportional to μ_{a}, and performing a simple linear inversion to recover the chromophore concentrations directly from h^{obs} is unlikely to be successful. The structural distortion of a PAT image by the fluence distribution can be seen in Figure 1.6. This shows a PAT image of a homogeneously absorbing tube of ink which has been positioned so that there is some overlapping of the tube. This results in distortion and a shadowing effect in some parts of the image, two of which are highlighted by arrows. There are some exceptions, for example, if the target is optically homogeneous (though this rarely occurs in biological tissues *in vivo*), or in the case of optical resolution photoacoustic microscopy (OR-PAM), which images highly superficial features within a few hundred micrometres of the surface.

FIGURE 1.6: Structural distortion of a PAT image due to the light fluence. In this image, a homogeneously absorbing tube of ink (left-hand image) is used as the target to obtain a 3D PAT image (central and right-hand images). The image is proportional to the product of the absorption coefficient and the optical fluence. Since the fluence is a function of position as well as wavelength, the measured PAT image can distort the image structurally as well as spatially. A PAT image cannot therefore be considered to be directly proportional to the absorption coefficient.

1.3.1.3 Nonuniqueness

In Chapter 3, we will look at methods for determining the absorption coefficient from a PAT image given that scattering is known *a priori*. In practice, the scattering coefficient may not be known, and it may be difficult to measure or estimate the optical scattering within a given region of tissue. In this case, the absorption and scattering coefficients will need to be recovered simultaneously from the measured images. However, determining both optical coefficients from a single PAT image obtained using a single wavelength may not have a unique solution. The incorporation of additional information from multiple PAT images, obtained using either multiple illumination positions or multiple optical wavelengths, can be used to ensure a unique solution [22–33]. The use of multiple illuminations has also been shown to improve the stability of the reconstruction [34]. The nonuniqueness problem is discussed in more detail in Section 3.4.1.

1.3.2 Practical challenges

These challenges arise due to practical requirements of the inversion method or possible limitations of the experimental setup.

1.3.2.1 Acoustic reconstruction

In most of the literature for QPAT, it is typically assumed that the initial pressure distribution has been recovered accurately. In practice, the acoustic inverse problem will need to be solved first, and the reconstructed initial pressure distribution will provide the measurement data from which the absorption coefficient should be recovered. Although the acoustic inverse problem is considered largely solved, there are still difficulties in recovering a quantitatively accurate estimate of the initial pressure distribution for particular measurement surfaces and unknown and/or heterogeneous acoustic properties [21]. In this work, we will assume that an accurate solution for the acoustic inverse problem has been found. Appendix C discusses the inclusion of the acoustic propagation and reconstruction in the simulation of the measurement data used for the QPAT problem.

1.3.2.2 Accuracy of the light model

For model-based inversion methods, the accuracy of the computational light model used to simulate the transportation of light through the tissue will be an important factor in determining the practicality and success of the method. The radiative transfer equation provides a rigorous, mathematical description of the transportation of particles of energy throughout a scattering medium, however, its complexity means that an analytical solution is unavailable for anything but the simplest of tissue geometries. A numerical implementation of the RTE can be used to produce a highly accurate model of light transport in biological tissue, although the computational effort required to solve it can become impractical for large problems. Approximations to the RTE can provide a much more tractable model, however, quantitative accuracy in all regions of interest must be ensured for the model to be sufficient for QPAT. In Section 2.4, we will discuss various models of light transport in biological tissue and their applicability to QPAT.

1.3.2.3 Large-scale

For 3D photoacoustic data sets, model-based minimisation schemes can quickly become impractical; the chosen minimisation scheme may require so much computational memory for a 3D inversion that its implementation is not feasible, or the complexity of the numerical model may mean that such an inversion is extremely time-consuming. Since PAT images are inherently 3D, these limitations must be overcome before a model-based inversion scheme can be successfully and routinely applied to experimental data. Section 3.5.2 discusses the importance of computational efficiency in proposed methods for QPAT.

1.3.2.4 Grüneisen coefficient

In QPAT, the PA efficiency parameter, $\hat{\Gamma}$, is typically assumed to be known *a priori*. In practice, it is not likely that this will be the case, nor is it likely that $\hat{\Gamma}$ will be easy to

estimate or to measure. In this thesis, we will assume that the PA efficiency parameter is known and constant such that $\hat{\Gamma}(\mathbf{r}) = 1 \; \forall \mathbf{r} \in \Omega$, and hence

$$p_0 = h = \mu_a \Phi. \tag{1.10}$$

Appendix B discusses the validity of this assumption, and proposes a method for dealing with an unknown $\hat{\Gamma}$.

1.4 Structure of the thesis

The thesis is structured as follows.

In Chapter 2, a brief overview of the processes involved in the propagation of light through biological tissue is provided. Here, we discuss the optical properties of tissue and review common mathematical methods used for modelling light transport. In particular, the radiative transfer equation (RTE), an analytical expression to describe the propagation of light in biological tissue, is introduced. Chapter 3 provides a detailed review of existing inversion methods for QPAT. Chapter 3 also outlines the challenges involved in the simultaneous reconstruction of the optical absorption and scattering coefficients, and discusses the application of these methods to 3D data. Chapter 4 proposes, derives and demonstrates the use of a gradient-based minimisation scheme for QPAT, which utilises the full RTE to determine quantitative estimates of the optical absorption coefficient from 2D simulated PAT images given that the scattering is known *a priori*. Chapter 4 also looks at how well the absorption coefficient can be reconstructed when the scattering is incorrectly assumed to be a homogeneous distribution. In Chapter 5, the gradient-based method is extended to the case where both optical coefficients are unknown and heterogeneous.

The RTE explicitly considers the light as a function of angle at every position, and so 3D inversions using the RTE will be computationally intensive and time-consuming. To tackle this, Chapter 6 proposes the use of the δ-Eddington approximation to the RTE in a gradient-based minimisation scheme for QPAT. The δ-Eddington approximation first models the collimated light, found straightforwardly using the Beer-Lambert law, and uses this as the source term to determine the scattered light, which is the solution to a diffusion equation. The sum of the collimated and scattered fields then provides the total field, which more accurately models the light in those regions where the DA breaks down. The delta-Eddington approximation is therefore a more suitable model for QPAT, since it is simultaneously accurate and tractable enough to use in a 3D gradient-based minimisation scheme. Numerical examples in Chapter 6 demonstrate the ability of the gradient-based method which uses the delta-Eddington approximation to successfully recover quantitative estimates of optical absorption and scattering from noisy, simulated 3D PAT images.

Finally, the overall conclusions of the thesis can be found in Chapter 7.

Chapter 2

Light transport in turbid media

The transportation of light through a turbid medium such as biological tissue can be described through electromagnetic theory and transport theory [35]. Electromagnetic theory starts with Maxwell's equations, which can provide exact expressions in the case of a uniform, non-scattering medium. However, because of the inhomogeneity of biological tissue, analytic approaches using Maxwell's equations do not lead to solvable equations for any case of practical interest in tissue. An approach that has proven effective is the photon transport equation that describes the transfer of energy through a turbid medium [36]. In transport theory, phase and polarisation are typically ignored, and the light is considered as packets of energy rather than photons in a quantum sense.

As light travels throughout a turbid medium, its propagation is characterised mainly by two phenomena: the absorption of light by chromophores in the tissue and the scattering of light within the tissue. The overall effect of the absorption process is the loss of intensity of light throughout the medium. In a non-scattering medium, this can be described by an exponential decay. Scattering occurs when light traversing the medium is forced to change its direction of propagation. If the scattering event does not result in a change of energy in the photon, the process is known as elastic scattering.

The propagation of light in a scattering medium is sometimes described in terms of discrete particles and sometimes in terms of a continuous flow of energy. A photon with frequency ν s^{-1} has energy $h\nu$ J, where $h \approx 6.626 \times 10^{-34}$ J s is Planck's constant. When describing the light in terms of photons, a key quantity is the number of photons per unit volume travelling in a direction $\hat{\mathbf{s}}$ at a particular time t. This is the *directional photon density* (units mm^{-3}), which we will denote by $\mathbf{P}(\mathbf{r}, \hat{\mathbf{s}}, t)$, where $\mathbf{r} \in \Omega \subset \mathbb{R}^n$, $n = 2, 3$ is a point in the tissue region Ω, $\hat{\mathbf{s}} \in S^{n-1}$ is the direction of travel and t denotes continuous time. The equivalent expression in terms of energy flow is the *radiance* ϕ (units W sr^{-1} mm^{-2}), which is the rate of energy flow per unit area in a particular direction $\hat{\mathbf{s}}$ at position $\mathbf{r}$ and time t, and is given by

$$\phi(\mathbf{r}, \hat{\mathbf{s}}, t) = h\nu c\mathbf{P}(\mathbf{r}, \hat{\mathbf{s}}, t), \tag{2.1}$$

where $c \approx 3 \times 10^8$ m s^{-1} is the speed of each photon. Another useful quantity is the number of photons per unit volume travelling in any direction at a particular time, denoted $\mathbf{F}(\mathbf{r}, t)$ and with units of mm^{-3}, which is the integral of $\mathbf{P}$ over all directions, i.e.

$$\mathbf{F}(\mathbf{r}, t) = \int_{S^{n-1}} \mathbf{P}(\mathbf{r}, \hat{\mathbf{s}}, t)\, \mathrm{d}\hat{\mathbf{s}}, \tag{2.2}$$

and is referred to as the *photon density*. The equivalent energy term is the *fluence rate*, given by

$$\varphi(\mathbf{r}, t) = \int_{S^{n-1}} \phi(\mathbf{r}, \hat{\mathbf{s}}, t)\, \mathrm{d}\hat{\mathbf{s}} = h\nu c\mathbf{F}(\mathbf{r}, t), \tag{2.3}$$

which has units of W mm^{-2}. This should not be confused with the *fluence*, denoted Φ, which is the time-integrated fluence rate, that is,

$$\Phi(\mathbf{r}) = \int \varphi(\mathbf{r}, t)\, \mathrm{d}t, \tag{2.4}$$

and has units of J mm^{-2}. In this thesis, we will typically use the quantities ϕ and Φ to describe the light propagation.

2.1 Absorption

The overall effect of the absorption of light in a particular medium is the loss of intensity as it travels further through the medium. A relationship between the intensity of light in a purely absorbing medium was first determined by Bouguer before 1729, and was formulated again mathematically by Lambert in 1760. The expression, sometimes known as the Lambert-Bougeur law, describes how each layer $\mathrm{d}l$ of the medium absorbs the same fraction $\mathrm{d}I/I$ of collimated radiation for a constant absorption coefficient μ_{a}, which has units of reciprocal length (say, mm^{-1}). The absorption coefficient of a material hence describes the rate at which a photon is absorbed per unit length, so that a larger absorption coefficient means that the light is weakened more quickly as it passes through the medium. The absorption coefficient will be dependent on the density of the light-absorbing molecules present within a particular medium, for example, in blood it will be the density of haem molecules that determine μ_{a}. Let us denote the density of chromophores, which is the particle count per unit volume (units mm^{-3}), by ρ, and the absorption cross-section of the chromophore by σ_{a}, (units mm^{-2}). If the medium contains only one type of chromophore, the absorption coefficient can be expressed as

$$\mu_{\mathrm{a}} = \rho\sigma_{\mathrm{a}}. \tag{2.5}$$

For media containing a number of different absorbing compounds, say, K, the absorption coefficient can be written as the sum of the individual coefficients:

$$\mu_{\mathrm{a}} = \sum_{k=1}^{K} \rho\sigma_{\mathrm{a}}^{k}, \tag{2.6}$$

where σ_{a}^{k} is the absorption cross-section of the k^{th} chromophore. To derive the Lambert-Bouguer law, consider a collimated beam incident in the z-direction on an infinitesimally thin slice of tissue. The amount of radiation absorbed by the tissue as it travels through the slice is related to the radiation incident on the slice I, the absorption coefficient throughout the slice μ_{a} and the depth of the slice $\mathrm{d}z$ by

$$\mathrm{d}I = -I\mu_{\mathrm{a}}\mathrm{d}z, \tag{2.7}$$

or, equivalently,

$$\frac{\mathrm{d}I}{I} = -\mu_{\mathrm{a}}\mathrm{d}z. \tag{2.8}$$

Integrating this equation gives

$$\ln(I) = -\mu_{\mathrm{a}}z + C, \tag{2.9}$$

where C is an arbitrary constant of integration. The Lambert-Bouguer law is derived by considering the difference between Equation (2.9) evaluated at $z = 0$ and $z = L$, which is

$$\begin{aligned} \ln(I_L) - \ln(I_0) &= -\mu_{\mathrm{a}}L + C + \mu_{\mathrm{a}} \cdot 0 - C \\ \Rightarrow \ln\left(\frac{I_L}{I_0}\right) &= -\mu_{\mathrm{a}}L \\ \Rightarrow I_L &= I_0 \exp(-\mu_{\mathrm{a}}L), \end{aligned} \tag{2.10}$$

where I_L and I_0 are the values of the light intensity at position $z = L$ and $z = 0$, respectively. This can be extended to the case where μ_{a} is heterogeneous, in which case the relationship becomes

$$I(z) = I_0 \exp\left(-\int_0^z \mu_{\mathrm{a}}(z')\ \mathrm{d}z'\right). \tag{2.11}$$

In 1852, Beer extended the Lambert-Bouguer law by determining that the absorption coefficient of a substance can be related to its concentration c diluted in a non-absorbing medium:

$$\mu_{\mathrm{a}}(z, \lambda) = \alpha(\lambda)c(z) \tag{2.12}$$

where α is the specific absorption coefficient of the substance at the incident wavelength λ. Substituting Equation 2.12 into Equation 2.10 gives the Beer-Lambert-Bouguer law

$$I(z) = I_0 \exp(-\alpha c z), \tag{2.13}$$

Similarly to Equation 2.6, in a medium which contains K absorbing compounds, the absorption coefficient can be written as the linear sum

$$\mu_{\mathrm{a}}(z,\lambda) = \sum_{k=1}^{K} \alpha_k(\lambda) c_k(z), \tag{2.14}$$

where the α_k are the specific absorption spectra and the c_k are the concentrations of the chromophores. It should be noted that the Beer-Lambert-Bougeur law is sometimes described in terms of the specific *absorption* spectra α and sometimes the specific *extinction* spectra ϵ. Both represent the level of absorption per micromole (or millimole) of compound per mm (or cm), but the specific extinction spectra are described using base 10 logarithm units, while absorption is described using natural logarithm units. The difference between them is therefore a scaling factor of $\ln(10)$, so that

$$\alpha = \ln(10)\epsilon \approx 2.3\epsilon. \tag{2.15}$$

2.2 Scattering

The scattering coefficient μ_{s} is the probability per unit length that light will be scattered. In a purely scattering medium, a proportion of the light is scattered out of the light beam and the radiance will decay. Similar arguments to those that describe the absorption of light can be applied to the scattering coefficient to find that

$$I(z) = I_0 \exp\left(-\mu_{\mathrm{s}} z\right), \tag{2.16}$$

or

$$I(z) = I_0 \exp(-\int_0^z \mu_{\mathrm{s}}(z')\,\mathrm{d}z'), \tag{2.17}$$

in the case of heterogeneous scattering.

When light strikes a particle with an index of refraction different from its environment, the light is refracted. The angle at which the light is bent will be a function of the size and shape of the particle as well as the wavelength of the incident light and the incidence angle of the light [37]. In general, each particle will have a different scattering profile, called the scattering phase function. The scattering phase function, often referred to as simply the phase function, has no connection with the phase of the incident light waves, and would be more appropriately called the scattering function. The scattering phase function will differ in general from particle to particle, and so for simplicity it is common to approximate the average behaviour of a group of photons by using an average scattering phase function for the entire domain. The average scattering phase function $\Theta(\hat{\mathbf{s}}, \hat{\mathbf{s}}')$ is used to describe the probability that a photon travelling in a direction $\hat{\mathbf{s}}$ will be scattered into a different direction $\hat{\mathbf{s}}'$. There are a number of ways to normalise this phase function, and one common method is to force the requirement that the integral of Θ over all possible angles is equal to unity, so that

$$\int_{S^{n-1}} \Theta(\hat{\mathbf{s}}, \hat{\mathbf{s}}') \, \mathrm{d}\hat{\mathbf{s}}' = 1, \tag{2.18}$$

where S^{n-1} is the set of all possible directions for dimension n. This condition does not permit the phase function to describe absorption of light by the particle, and hence the phase function is a description of only the distribution of scattering by the particle. The scattering phase function is further constrained by assuming that scattering is axially symmetric relative to the original propagation direction, so that $\Theta(\hat{\mathbf{s}}, \hat{\mathbf{s}}') = \Theta(\hat{\mathbf{s}}', \hat{\mathbf{s}})$ (see Figure 2.1). This means that the $\Theta(\hat{\mathbf{s}}, \hat{\mathbf{s}}') = \Theta(\hat{\mathbf{s}} \cdot \hat{\mathbf{s}}')$, so that the scattering phase function depends only on the angle θ between the forward (unscattered) direction and the scattered beam direction, since

$$\hat{\mathbf{s}} \cdot \hat{\mathbf{s}}' = \cos\theta. \tag{2.19}$$

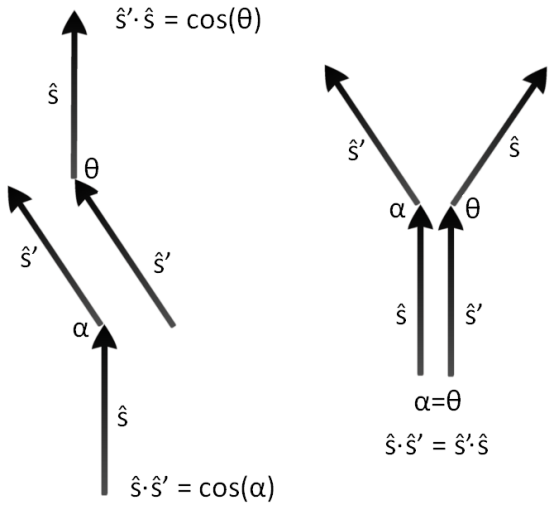

FIGURE 2.1: The symmetry of the phase function means that the probability of a photon travelling in a direction $\hat{\mathbf{s}}$ has the same probability of being scattering at an angle α as it does of being scattering at an angle θ, so that scattering is axially symmetric relative to the unscattered direction.

A common phase function when considering biological tissue is the Henyey-Greenstein phase function [38], given by

$$\Theta_{\mathrm{HG}}(\hat{\mathbf{s}}, \hat{\mathbf{s}}') = \frac{1}{4\pi} \frac{1 - g^2}{(1 + g^2 - 2g(\hat{\mathbf{s}} \cdot \hat{\mathbf{s}}'))^{3/2}}, \tag{2.20}$$

which has the 2D analogue

$$\Theta_{\mathrm{HG}}(\hat{\mathbf{s}}, \hat{\mathbf{s}}') = \frac{1}{2\pi} \frac{1 - g^2}{(1 + g^2 - 2g(\hat{\mathbf{s}} \cdot \hat{\mathbf{s}}'))}. \tag{2.21}$$

The scattering is characterised by the anisotropy factor g, which is described by the mean cosine of the scattering angle

$$g = \int_{-1}^{1} (\hat{\mathbf{s}} \cdot \hat{\mathbf{s}}') \Theta(\hat{\mathbf{s}} \cdot \hat{\mathbf{s}}') \, \mathrm{d}(\hat{\mathbf{s}} \cdot \hat{\mathbf{s}}'). \tag{2.22}$$

Anisotropy is the property of being directionally dependent, and so g is a measure of the direction of the single scattering pattern and has values of $-1 < g < 1$; a value of $g = 0$ implies that the scattered light is distributed equally over all angles (isotropy), while $g > 0$ and $g < 0$ correspond to forward- and backward-dominated scattering of the light, respectively. In biological tissue, light has been shown to be scattered predominantly in

the forward direction [39].

2.3 Optical properties of biological tissue

Although the absorption of light in tissue at near-infrared (NIR) wavelengths is relatively low, the difference in the absorption spectra of the main chromophores is significantly different (see Figure 2.2). The main constituents of tissue are water, haemoglobin (to include oxyhaemoglobin and deoxyhaemoglobin) and lipids, and the change in their absorption levels depending on what excitation wavelength is used to obtain a photoacoustic image can be exploited. For example, one may wish to obtain an image of the lipid content of a blood vessel in order to monitor the progression of atherosclerosis. In this case, the blood vessel could first be identified by obtaining a photoacoustic image at a wavelength where haemoglobin is highly absorbing, and the lipid content of the vessel could then be seen by obtaining another image using a wavelength where the lipid absorbs more strongly.

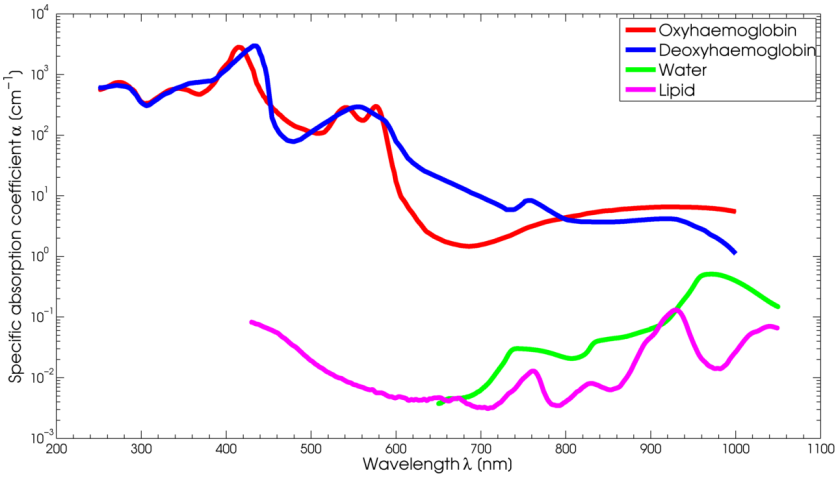

FIGURE 2.2: Specific absorption spectra of common tissue chromophores, namely oxyhaemoglobin, deoxyhaemoglobin, water and lipid (fat), in the near-infrared wavelength range. These spectra were obtained from [40] (water), [41] (oxy- and deoxyhaemoglobin) and [42] (lipid).

The attenuation of light in soft tissue is the main factor limiting the depth of a PAT image. At NIR wavelengths the absorption of light by the main constituents of tissue, namely water and haemoglobin, is low. Tissue is thus at its most 'transparent', meaning the light is attenuated the least, when the light source is in the NIR range. The attenuation of light within biological tissue is characterised by the effective attenuation coefficient μ_{eff}, which is dependent on the absorption coefficient μ_{a} and the scattering coefficient μ_{s}. The absorption and scattering coefficients of a material describe the probability that a photon will be absorbed or scattered per unit length, respectively. The effective attenuation coefficient is defined as

$$\mu_{\text{eff}} = \sqrt{3\mu_{\text{a}}(\mu_{\text{a}} + \mu_{\text{s}}')}, \tag{2.23}$$

where μ_{s}' is the reduced scattering coefficient, given by

$$\mu_{\text{s}}' = \mu_{\text{s}}(1 - g). \tag{2.24}$$

At depths greater than several transport mean free paths, where a transport mean free path l is defined as the reciprocal of the total attenuation coefficient μ_{t}, with

$$l = \frac{1}{\mu_{\text{t}}} = \frac{1}{(\mu_{\text{a}} + \mu_{\text{s}})}, \tag{2.25}$$

which is the mean distance between photon interactions, the light becomes diffuse and the fluence rate φ will decrease exponentially with distance from the source with decay constant μ_{eff}, so that the fluence, Φ, is given by

$$\Phi(\mathbf{r}) = \Phi_0 \exp(-\mu_{\text{eff}}\mathbf{r}), \tag{2.26}$$

where Φ_0 is the fluence at the tissue surface. The optical penetration depth, which is the depth at which the fluence has decreased to $1/e$, is found by taking the natural logarithm of Equation 2.26 and setting $\Phi(\mathbf{r}) = 1/e$:

$$\ln(\Phi(\mathbf{r})) = -\mu_{\text{eff}}\mathbf{r} \Rightarrow \ln(1) - \ln(e) = -\mu_{\text{eff}}\mathbf{r} \Rightarrow \mathbf{r} = \frac{1}{\mu_{\text{eff}}}. \tag{2.27}$$

To estimate this depth we assume that the tissue has a physiologically realistic tissue composition of $Hb0_2$ and HHb (1% by volume with 95% sO_2), water (74% by volume) and lipid (25% by volume) [13]. The absorption coefficient is then given by the weighted sum of the contribution from each constituent's absorption coefficient, *i.e.*

$$\mu_{\mathrm{a}} = 0.74\mu_{\mathrm{water}} + 0.24\mu_{\mathrm{lipid}} + 0.095\mu_{\mathrm{HbO_2}} + 0.005\mu_{\mathrm{HHb}}. \tag{2.28}$$

These parameters can be found using the data displayed in Figure 2.2, which at a wavelength of 1000 nm provides a value of $\mu_{\mathrm{a}} = 0.035$ mm^{-1}. Using additional physiological estimates $\mu_{\mathrm{s}} = 1.6$ mm^{-1} and $g = 0.9$, the effective attenuation coefficient $\mu_{\mathrm{eff}} \approx 0.14$. The $1/e$ optical penetration depth is then calculated from $\mathbf{r} = 1/\mu_{\mathrm{eff}} \approx 7$mm. This limitation is one of the major challenges of PA imaging, as it means that the light has been reduced by around 37% of its value at the surface after travelling approximately 7 mm. After another 7 mm, the light will have decreased by a factor of $1/e^2$, about 74% of its surface value. Despite this limitation, an informed choice of wavelength and optimisation of the light delivery, as well as the consideration of illuminating from more than one position, has lead to the attainment of PA images at several centimetres below the tissue surface.

2.4 Models of light transport

Transport theory describes mathematically the movement of particles, where the random nature of particles is described by a field of probability density functions or distribution functions. Transport theory can be modelled through stochastic methods, which model individual particle interactions, or deterministic methods, which describe the transportation of particles using partial differential equations. One of the most important equations in transport theory is Boltzmann's transport equation, and when describing low-energy photon transport this equation is often referred to as the radiative transfer equation (RTE), or linear transport equation. Though analytic solutions to the RTE exist for the most simple geometries, numerical methods are typically required to solve the RTE for

more general domains.

2.4.1 The Monte Carlo method

The Monte Carlo (MC) method is a popular stochastic method for modelling light propagation in biological tissue [43], and is often chosen as the reference method to which other solutions are compared. The MC method is based on the random walks that photons make as they travel through a turbid medium. In MC modelling, 'photon packets' which have an initial 'weight' are launched into a medium and may be absorbed, scattered, propagate undisturbed, internally reflected or transmitted out of the tissue [44]. Once launched, the photon is moved a distance where it may be scattered, lose energy through absorption, propagated undisturbed, internally reflected, or transmitted out of the tissue. The photon is repeatedly moved until it either escapes from or is absorbed by the tissue, i.e. its weight drops below some user-defined tolerance. If the photon escapes from the tissue, the reflection or transmission of the photon is recorded. If the photon is absorbed, the position of the absorption is recorded and its weight reduced. This process is repeated until the desired number of photons have been propagated. If N is the total number of photon packets which has been propagated, the absorbed energy distribution obtained using MC approaches the analytical solution to the RTE as $N \to \infty$. The MC model is considered the 'gold standard' in describing photon transport in biological tissue, though Monte Carlo simulations are often computationally inefficient, since a large number of samples may be required to obtain a desirable degree of precision. This is because the probabilistic error bound decreases as the reciprocal square root of the number of photon packets ($1/\sqrt{n}$, where n is the number of photon packets), so that achieving one more decimal digit of precision requires $10^2 = 100$ more iterations [45]. Variance reduction methods attempt to combat this, but often do not overcome the slow reduction of the error bound [44]. The problem can be overcome by parallelising the method, whereby multiple threading allows different parts of the problem to be executed at the same time to improve efficiency, and indeed the independence of each sample means that the MC method is well suited to parallelisation. The availability of large

computing clusters and clusters of graphical processing units is increasing quickly, and so Monte Carlo methods are become increasingly faster [46]. In the case of QPAT, a further problem arises, since MC models require that each new absorption distribution must be coded for, making the model particularly unsuitable for iterative methods, which are shown in Chapter 3 to be a useful technique in solving the inverse problem. Furthermore, the fact that stochastic methods such as Monte Carlo are not governed by a set of partial differential equations means that they are not suitable for inversion methods which require manipulation of the governing equations. Whilst not particularly suited to the type of inversion technique proposed in this thesis, Monte Carlo methods provide a simple, accurate model of light transport that can be used to validate other numerical light models.

2.4.2 The radiative transfer equation

The propagation of light through a turbid medium is affected by absorption, emission and scattering, and the RTE is an integro-differential equation which accurately describes these processes. The RTE can be derived via the principle of energy conservation, by equating the rate of change of the number of photons within some small control volume ΔV in a time Δt and travelling in a direction $\hat{\mathbf{s}}$ with the amount of photons entering or leaving at a given time. Recall from Section 2.4 that the directional photon density $\mathbf{P}(\mathbf{r}, \hat{\mathbf{s}}, t)$ is the number of photons at a point $\mathbf{r}$ travelling in a direction $\hat{\mathbf{s}}$ at a time t. The terms of the RTE are calculated by noting that a photon travelling at a speed c can travel a distance $c\Delta t$ in a time Δt, so that the change in the number of photons within ΔV travelling in a direction $\hat{\mathbf{s}}$ in a time Δt is given by $(\Delta t \Delta V)\partial \mathbf{P}(\mathbf{r}, \hat{\mathbf{s}}, t)/\partial t$. This is then equated to

- the number of photons travelling in a direction $\hat{\mathbf{s}}$ that are injected into ΔV in a time Δt by means of a source of photons Q, which is given by $(c\Delta t \Delta V)Q(\mathbf{r}, \hat{\mathbf{s}}, t)$;
- minus the net outflow of photons travelling in a direction $\hat{\mathbf{s}}$ in ΔV in time Δt due to the gradient $\nabla \mathbf{P}(\mathbf{r}, \hat{\mathbf{s}}, t)$, given by $(c\Delta t \Delta V)\hat{\mathbf{s}} \cdot \nabla \phi(\mathbf{r}, \hat{\mathbf{s}}, t)$;

- minus the number of photons travelling in a direction $\hat{\mathbf{s}}$ that are absorbed into ΔV in a time Δt, given by $(c\Delta t\Delta V)\mu_{\mathrm{a}}(\mathbf{r})\mathbf{P}(\mathbf{r},\hat{\mathbf{s}},t)$, where μ_{a} is the absorption coefficient;

- minus the number of photons travelling within ΔV in a direction $\hat{\mathbf{s}}$ that are scattered into another direction in a time Δt, given by $(c\Delta t\Delta V)\mu_{\mathrm{s}}(\mathbf{r})\mathbf{P}(\mathbf{r},\hat{\mathbf{s}},t)$, where μ_{s} is the scattering coefficient;

- plus the number of photons travelling within ΔV in a direction $\hat{\mathbf{s}}'$ that are scattered into the direction $\hat{\mathbf{s}}$ in a time Δt, given by $(c\Delta t\Delta V)\mu_{\mathrm{s}}\int_{S^{n-1}}\Theta(\hat{\mathbf{s}},\hat{\mathbf{s}}')\mathbf{P}(\mathbf{r},\hat{\mathbf{s}}',t)\,\mathrm{d}\hat{\mathbf{s}}'$, where S^{n-1} is the set of all possible directions in dimension n and Θ is the scattering phase function.

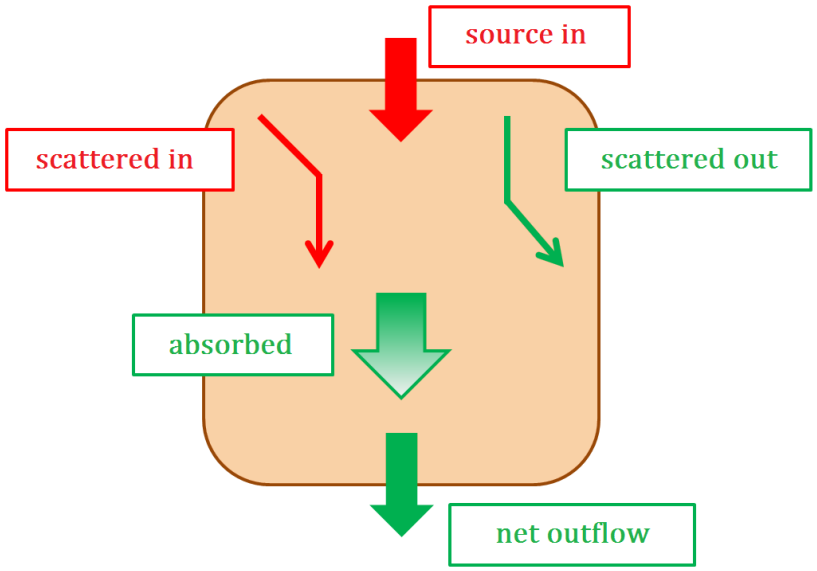

FIGURE 2.3: Contributing terms in the radiative transfer equation (RTE). The RTE is derived by considering the conservation of energy at a particular point within a small control volume, at a particular time, and travelling in a particular direction. Energy can be gained from a source or from the scattering of photons into the direction of interest, or can be lost due to absorption, the scattering of photons out of the direction of interest, or through the net outflow due to the gradient.

Figure 2.3 illustrates the processes which contribute to derivation of the RTE. Recall from Section 2.4 that the directional photon density is equal to $\mathbf{P} = h\nu\phi$, where $h\nu$ is the energy of the photon and $\phi = \phi(\mathbf{r},\hat{\mathbf{s}},t)$ is the radiance. Substituting this expression

into the above terms and rearranging a little gives us the radiative transfer equation:

$$\frac{1}{c}\frac{\partial\phi}{\partial t}(\mathbf{r},\hat{\mathbf{s}},t) = q(\mathbf{r},\hat{\mathbf{s}},t) - (\hat{\mathbf{s}}\cdot\nabla + \mu_{\mathrm{a}}(\mathbf{r}) + \mu_{\mathrm{s}}(\mathbf{r}))\phi(\mathbf{r},\hat{\mathbf{s}},t) + \mu_{\mathrm{s}}(\mathbf{r})\int_{S^{n-1}}\Theta(\hat{\mathbf{s}},\hat{\mathbf{s}}')\phi(\mathbf{r},\hat{\mathbf{s}}',t)\,\mathrm{d}\hat{\mathbf{s}}', \tag{2.29}$$

where q is a source of energy with $q = h\nu Q$. In photoacoustic imaging, the time-scale of the optical problem is so short in comparison with the acoustic part of the problem that it can be considered to be instantaneous [13]. This means that in PAT we are interested in the total energy deposited during this very small amount of time, and so the RTE is integrated with respect to time t to obtain the time-independent RTE:

$$(\hat{\mathbf{s}}\cdot\nabla + \mu_{\mathrm{a}}(\mathbf{r}) + \mu_{\mathrm{s}}(\mathbf{r}))\phi(\mathbf{r},\hat{\mathbf{s}}) = \mu_{\mathrm{s}}(\mathbf{r})\int_{S^{n-1}}\Theta(\hat{\mathbf{s}},\hat{\mathbf{s}}')\phi(\mathbf{r},\hat{\mathbf{s}}')\,\mathrm{d}\hat{\mathbf{s}}' + q(\mathbf{r},\hat{\mathbf{s}}). \tag{2.30}$$

Assuming that no photons travel in an inward direction at the boundary $\partial\Omega$ except at the source position $\mathbf{r}_s \subset \partial\Omega$ gives the boundary condition

$$\phi(\mathbf{r},\hat{\mathbf{s}}) = \begin{cases} \phi_0(\mathbf{r},\hat{\mathbf{s}}), & \mathbf{r}\in\cup\mathbf{r}_s, \quad \hat{\mathbf{s}}\cdot\hat{\mathbf{n}} < 0 \\ 0, & \mathbf{r}\in\partial\Omega\setminus\cup\mathbf{r}_s, \quad \hat{\mathbf{s}}\cdot\hat{\mathbf{n}} < 0, \end{cases} \tag{2.31}$$

where ϕ_0 is the boundary source and $\hat{\mathbf{n}}$ is a unit vector normal to $\partial\Omega$.

The general solution to the RTE is not known, and analytic solutions are limited to simple conditions and geometries. Numerical solutions can be made to solve the RTE for more versatile conditions and arbitrary geometries, though since in PAT we are generally interested in three-dimensional images, a numerical solution to the RTE will still require significant computational memory and time due to the angular dependence of the phase function. This is due to the fact that the solution $\phi(\mathbf{r},\hat{\mathbf{s}})$ is a function of angle at each point within the domain, so that a three-dimensional problem essentially becomes a five-dimensional problem (in this case the radiance is a function of five variables: the radiance is a function of five variables: three in the $\mathbf{r}$ vector and two in the $\hat{\mathbf{s}}$ unit vector).

2.4.3 P_n approximations

One way to simplify the RTE is to express the directional dependence as a sum of spherical harmonics [47], the angular portion of the solution to Laplace's equation in spherical coordinates. In this case, the quantities in Equation 2.29 are substituted with

$$\phi(\mathbf{r},\hat{\mathbf{s}},t) = \sum_{l}^{\infty}\sum_{m=-l}^{l}\left(\frac{2l+1}{4\pi}\right)^{\frac{1}{2}}\Psi_{l,m}(\mathbf{r},t)Y_{l,m}(\hat{\mathbf{s}}), \tag{2.32}$$

$$q(\mathbf{r},\hat{\mathbf{s}},t) = \sum_{l}^{\infty}\sum_{m=-l}^{l}\left(\frac{2l+1}{4\pi}\right)^{\frac{1}{2}}q_{l,m}(\mathbf{r},t)Y_{l,m}(\hat{\mathbf{s}}), \tag{2.33}$$

where $Y_{l,m}$ is the spherical harmonic of order l and degree m, given by

$$Y_{l,m}(\hat{\mathbf{s}}) = \left(\left(\frac{2l+1}{4\pi}\right)\frac{(l-|m|)!}{(l+|m|)!}\right)^{1/2}(-1)^{\frac{1}{2}(m+|m|)}P_l^{|m|}((\hat{\mathbf{s}}\cdot\hat{\mathbf{s}}'))e^{im\vartheta}, \tag{2.34}$$

where P_l is the associated Legendre polynomial and the normalisation factor $((2l+1)/(4\pi))^{\frac{1}{2}}$ has been introduced for convenience in all cases [47]. Usually the form of the scattering phase function Θ is not known, and since biological tissues have a complex structure, determining its form is nontrivial. The Henyey-Greenstein phase function (2.20) can also be written as an infinite sum of Legendre polynomials

$$\Theta_{\mathrm{HG}} = \sum_{l=1}^{\infty}\frac{2l+1}{4\pi}g^l P_l(\hat{\mathbf{s}}\cdot\hat{\mathbf{s}}'). \tag{2.35}$$

These approximations can be substituted back into Equation 2.29 and, after some algebra, the resulting expression can be written as an infinite set of coupled partial differential equations. The P_N approximation is then obtained by assuming that $\Psi_{l,m} = 0$ for $l > N$, allowing us to reduce the number of equations to as many as are needed (or can be dealt with) for the desired accuracy.

2.4.4 Diffusion approximation

By using the spherical harmonics approximations to the radiance, source and the scattering phase function, the angular dependence can be removed entirely, resulting in a more tractable, albeit less accurate, model of light transport. The diffusion approximation (DA) to the RTE can be derived by truncating the infinite set of P_N approximations at $N = 1$, by assuming that $\Psi_{l,m} = 0$ for $l > 1$ [47]. This results in a new phase function, sometimes called the Eddington phase function, given by

$$\Theta_{\mathrm{E}} = \frac{1}{|S^{n-1}|}(1 + 3g(\hat{\mathbf{s}} \cdot \hat{\mathbf{s}}')). \tag{2.36}$$

The truncation of the radiance at $N = 1$ means that the radiance can be expressed as

$$\phi(\mathbf{r}, \hat{\mathbf{s}}) = \frac{1}{|S^{n-1}|}\Phi(\mathbf{r}) + \frac{n}{|S^{n-1}|}\hat{\mathbf{s}} \cdot \mathbf{J}(\mathbf{r}), \tag{2.37}$$

where n is the dimension of the domain ($n = 2, 3$), Φ is the fluence and $\mathbf{J}$ is the radiant flux vector, defined by

$$\Phi(\mathbf{r}) = \int_{S^{n-1}} \phi(\mathbf{r}, \hat{\mathbf{s}})\, \mathrm{d}\hat{\mathbf{s}}, \qquad \mathbf{J}(\mathbf{r}) = \int_{S^{n-1}} \phi(\mathbf{r}, \hat{\mathbf{s}})\hat{\mathbf{s}}\, \mathrm{d}\hat{\mathbf{s}}. \tag{2.38}$$

A similar approximation of the source term leads to

$$q(\mathbf{r}, \hat{\mathbf{s}}) \approx \frac{1}{|S^{n-1}|}q_0(\mathbf{r}) + \frac{n}{|S^{n-1}|}\hat{\mathbf{s}} \cdot \mathbf{q}_1(\mathbf{r}) \tag{2.39}$$

where q_0 and $\mathbf{q}_1$ are the isotropic and dipole components of the source, respectively, with

$$q_0(\mathbf{r}) = \int_{S^{n-1}} q(\mathbf{r}, \hat{\mathbf{s}})\, \mathrm{d}\hat{\mathbf{s}} \tag{2.40}$$

$$\mathbf{q}_1 = \int_{S^{n-1}} \hat{\mathbf{s}} q(\mathbf{r}, \hat{\mathbf{s}})\, \mathrm{d}\hat{\mathbf{s}}. \tag{2.41}$$

In the time-independent case, this leads to a pair of coupled equations

$$\mu_{\mathrm{a}}(\mathbf{r})\Phi(\mathbf{r}) + \nabla \cdot \mathbf{J}(\mathbf{r}) = q_0(\mathbf{r}) \tag{2.42}$$

$$\mathbf{J}(\mathbf{r}) = -\kappa(\mathbf{r})\nabla\Phi(\mathbf{r}) + 3\kappa(\mathbf{r})\mathbf{q}_1, \tag{2.43}$$

where κ is the diffusion coefficient, defined by

$$\kappa = \frac{1}{3(\mu_\mathrm{a} + \mu_\mathrm{s}(1-g))}. \tag{2.44}$$

Assuming the source is isotropic means that $\mathbf{q}_1 = 0$, which enables the derivation of the DA

$$(\mu_\mathrm{a} - \nabla \cdot \kappa(\mathbf{r})\nabla)\Phi(\mathbf{r}) = q_0(\mathbf{r}). \tag{2.45}$$

The DA cannot satisfy the boundary condition Equation 2.31. Instead, it is often replaced by the approximation that the total inward current is equal to zero [48], i.e.

$$\int_{\hat{\mathbf{s}}\cdot\hat{\mathbf{n}}<0} \phi(\mathbf{r},\hat{\mathbf{s}})(\hat{\mathbf{s}}\cdot\hat{\mathbf{n}})\,\mathrm{d}\hat{\mathbf{s}} = 0. \tag{2.46}$$

Substituting the approximation Equation 2.37 leads to a Robin boundary condition for the DA [48, 49]

$$\Phi(\mathbf{r}) + \frac{1}{2\gamma_n}\kappa(\mathbf{r})\hat{\mathbf{n}}\cdot\nabla\Phi(\mathbf{r}) = 0, \quad \mathbf{r}\in\partial\Omega, \tag{2.47}$$

where $\gamma_2 = 1/\pi$ and $\gamma_3 = 1/4$. The expansion of the radiance and phase function into spherical harmonics is one of a number of ways to derive the DA [36, 47, 50], and although the details have been omitted, the derivation of the diffusion equation above closely follows that of [36].

For a homogeneously absorbing and scattering medium, an analytical solution to the DA can be found using the free-space Green's function, G_0 [51–53]. G_0 is the solution to $(\mu_\mathrm{a} - \kappa\nabla^2)G_0(\mathbf{r},\mathbf{r}') = \delta(\mathbf{r})$, and (in the 3D case) is given by

$$G_0(\mathbf{r},\mathbf{r}') = \frac{\exp(-\mu_\mathrm{eff}\,\|\mathbf{r}-\mathbf{r}'\|)}{4\pi\,\|\mathbf{r}-\mathbf{r}'\|}, \tag{2.48}$$

where μ_eff is called the effective attenuation coefficient, and is defined by

$$\mu_\mathrm{eff} = \sqrt{3\mu_\mathrm{a}(\mu_\mathrm{a}+\mu_\mathrm{s}')}. \tag{2.49}$$

The solution to the DA can then be found from

$$\Phi(\mathbf{r}) = \int_{\Omega} G_0(\mathbf{r} - \mathbf{r}')q_0(\mathbf{r}') \, \mathrm{d}\mathbf{r}'. \tag{2.50}$$

For heterogeneous media, numerical implementations of the DA must be used to obtain a solution.

The removal of angular dependence and reduction to a diffusion equation means that solving the DA numerically requires much less computational effort to solve than a numerical implementation of the RTE. However, the effect of using this approximation to the scattering phase function is that the scattering of light is assumed to be near-isotropic throughout the entire domain, though, as discussed in Section 2.4.2, the scattering of light in biological tissue is highly forward-peaked and will not behave diffusely until at least a few scattering events have occurred. This move into the diffusive regime occurs around a few transport mean free paths away from the source, where a transport mean free path is given by $l = (\mu_\mathrm{a} + \mu_\mathrm{s}(1-g))^{-1}$. For this reason, the DA breaks down at regions within a few transport mean free paths from any light sources, where the scattering of light in tissue cannot be considered diffuse. For PAT these regions may be significantly large and contain information of great interest. The DA is therefore not likely to be accurate enough to provide sufficiently accurate quantification of the optical properties of the tissue region required for QPAT.

2.4.5 Delta-Eddington approximation

Another phase function that may be suitable for modelling the transportation of light in biological tissue is the δ-Eddington phase function [54]. The δ-Eddington phase function incorporates a modification to the Eddington phase function 2.36 to account for the forward-scattering of the light. The δ-Eddington phase function is given by

$$\Theta_{\delta-\mathrm{E}} = \frac{1}{4\pi}\left[2f\delta(1-(\hat{\mathbf{s}}\cdot\hat{\mathbf{s}}')) + (1-f)(1+3\hat{g}(\hat{\mathbf{s}}\cdot\hat{\mathbf{s}}'))\right], \tag{2.51}$$

where f is the fraction of light scattered into the forward peak and $\hat{g}$ is the modified anisotropy factor. As $f \to 1$, the δ-Eddington phase function approaches a delta function, and as $f \to 0$ it reduces to the Eddington phase function [55]. The substitution of the δ-Eddington phase function into the RTE also allows the reduction of the transport equation to a diffusion equation. A full derivation of this approximation can be found in Chapter 6, where we will consider the applicability of the δ-Eddington approximation to QPAT in greater detail.

Chapter 3

QPAT inversion schemes

Various approaches to tackling QPAT have been proposed. Early suggestions have involved invasive or clinically inapplicable methods such as tissue excision [56] or the embedding of absorbers beneath the skin [57]. Others have required additional information, such as the incorporation of contrast agents [58] or the use of measurements obtained using another imaging modality, e.g. optical tomography [59]. The most recent inversion methods have taken a model-based approach in order to incorporate an accurate description of the light propagation and reduce the number of approximations and produce higher accuracy in the reconstructions. This chapter provides a detailed review of the existing inversion methods for QPAT. We begin by looking at methods which assume that the medium is non-scattering (Section 3.1). Following this, we will review those methods which assume a known, homogeneous scattering coefficient (Section 3.2), followed by those which have the ability to incorporate a known, heterogeneous scattering coefficient (Section 3.3). Finally, we review those methods which attempt to deal with an unknown, heterogeneous scattering (Section 3.4), and their associated challenges.

3.1 Non-scattering media

The simplest tissue geometry to consider is a homogeneously absorbing, non-scattering half-space that is illuminated by an infinitely wide, collimated beam of light. Under these conditions, the light field may be considered to be one-dimensional (1D), and the fluence will decay according to the Beer-Lambert-Bouguer law (Equation 2.13). The absorbed optical energy density can therefore be written as

$$h(z) = \mu_{\mathrm{a}} \Phi_0 \exp(-\mu_{\mathrm{a}} z), \tag{3.1}$$

where Φ_0 is the incident fluence at the surface of the tissue ($z = 0$). The resulting detected acoustic pressure signal will retain this exponential shape, and can be expressed by

$$p(t) = \left(\frac{\hat{\Gamma} \mu_{\mathrm{a}} \Phi_0}{2} \right) \exp(-\mu_{\mathrm{a}} c_0 t), \tag{3.2}$$

where $\hat{\Gamma}$ is the PA efficiency, c_0 is the sound speed and t is time. Acoustic reflections at the surface are ignored here, but they can be straightforwardly included. In this case, the fluence will attain its maximum value at the surface of the tissue, and so, if $\hat{\Gamma}$ and Φ_0 are known, the absorption coefficient μ_{a} (a scalar, since the tissue is homogeneously absorbing) can be found. If either $\hat{\Gamma}$ or Φ_0 is unknown, the absorption coefficient can be estimated by fitting a curve to the exponentially decaying slope of the PA signal.

Guo *et al.* attempt to deal with the fact that $\hat{\Gamma}$ and Φ_0 are unknown by proposing a frequency-domain method which uses the ratio of PA acoustic spectra measured at two optical wavelengths λ_1 and λ_2 [60]. The magnitude of the Fourier transform of Equation 3.2, from time t to frequency ω, is

$$|P(\omega)| = \left(\frac{\hat{\Gamma} \mu_{\mathrm{a}} \Phi_0}{2} \right) \frac{1}{\sqrt{\omega^2 + (\mu_{\mathrm{a}} c_0)^2}}. \tag{3.3}$$

By taking the ratio of two measurements made at two different optical wavelengths, λ_1 and λ_2, the wavelength-independent PA efficiency parameter cancels, leaving

$$\frac{|P(\omega,\lambda_1)|}{|P(\omega,\lambda_2)|} = \frac{\Phi_0(\lambda_1)}{\Phi_0(\lambda_2)} \frac{\sqrt{(\omega/\mu_{\mathrm{a}}(\lambda_2))^2 + c_0^2}}{\sqrt{(\omega/\mu_{\mathrm{a}}(\lambda_1))^2 + c_0^2}}. \tag{3.4}$$

By fitting this ratio to the measured acoustic spectra, Guo *et al*. derived absolute values of μ_{a} at the two different wavelengths and also the ratio $\Phi_0(\lambda_1)/\Phi_0(\lambda_2)$.

In order for Equation 3.4 to hold, and indeed for any 1D approximation to be applicable, the medium properties and fluence distribution should be planar on the scale of interest. Though this will not generally be the case, in some applications these assumptions may be justified. For example, in [60], the quantification of μ_{a} was made using a photoacoustic microscopy (PAM) measurements, where the light beam is focused to a spot much smaller than a typical blood vessel diameter. In this case, the domain of interest may be considered to be homogeneously absorbing and non-scattering. Furthermore, since PAM is only concerned with regions very close to the tissue surface, the fluence distribution is dominated by ballistic photons and hence does not scatter significantly. However, the restriction of the illumination zone to a small focal spot will not generate purely planar acoustic waves. To be considered one-dimensional, the generated PA waves must be planar from initiation up to detection. When the phase change across the acoustic sensor array is significantly less than the acoustic wavelength, it may be reasonable to assume the PA waves appear planar to the acoustic detector.

Techniques for QPAT which ignore the effects of light scattering will always be limited, since in biological tissue the light is scattered significantly at depths beyond a few hundred microns. In order to make accurate quantitative measurements at these depths, the effects of scattering must be taken into account.

3.2 Homogeneous scattering media

The introduction of optical scattering means that the fluence will no longer attain its maximum at the tissue surface, but some distance below it due to backscattering. The maximum amplitude of the signal may therefore no longer be used to estimate μ_{a}. Furthermore, fitting an exponential to the decaying part of the curve will no longer recover μ_{a}, since the decay rate of the fluence will now also depend on the optical scattering coefficient μ_{s}. After a few transport mean free paths, where a transport mean free path is defined as $l = 1/\mu_{\mathrm{t}}$, where μ_{t} is the total attenuation coefficient, given by

$$\mu_{\mathrm{t}} = \mu_{\mathrm{a}} + \mu_{\mathrm{s}}, \tag{3.5}$$

the light has undergone several scattering events and become diffuse. Beyond this point it will decay approximately as $\exp(-\mu_{\mathrm{eff}} z)$, where μ_{eff} is the effective attenuation coefficient, given by

$$\mu_{\mathrm{eff}} = \sqrt{3\mu_{\mathrm{a}}(\mu_{\mathrm{a}} + \mu_{\mathrm{s}}')}. \tag{3.6}$$

In this case, a scaling factor can be introduced to modify the 1D solution to the DA to account for the fact that the exponential decay model does not include the loss of light back out of the tissue. Oraevsky *et al.* [61] used

$$\Phi(z) \approx (1 + 7.1R_{\mathrm{d}\infty})\Phi_0 \exp(-\mu_{\mathrm{eff}} z), \quad z >> \frac{1}{\mu_{\mathrm{t}}}, \tag{3.7}$$

where $R_{\mathrm{d}\infty}$ is the total diffuse reflectance from the surface. This means that the absorbed energy is approximated by

$$h(z) \approx \mu_{\mathrm{a}}(1 + 7.1R_{\mathrm{d}\infty})\Phi_0 \exp(-\mu_{\mathrm{eff}} z). \tag{3.8}$$

The diffuse reflectance was measured, and the exponentially decaying part of the PA signal was fitted to this curve. The absorption coefficient μ_{a} was then found by extrapolating to $z = 0$. Fainchtein *et al.* [62] used a similar method, but instead modelled the

diffuse reflectance as $R_{\mathrm{d}\infty} \approx \exp(-7\mu_{\mathrm{a}}/\mu_{\mathrm{eff}})$.

In [63], Xia *et al.* used a similar approach to [60] (discussed in Section 3.1) by taking the ratio of two PA images to remove the unknown, wavelength-independent PA efficiency parameter. The ratio of two PA images at two different optical wavelengths is given by

$$\frac{p_0(\lambda_1)}{p_0(\lambda_2)} \approx \frac{\mu_{\mathrm{a}}(\lambda_1)\Phi(\lambda_1)}{\mu_{\mathrm{a}}(\lambda_2)\Phi(\lambda_2)}. \tag{3.9}$$

The ratio of the fluence at the two wavelengths, in a one-dimensional setting, can be written as

$$\frac{\Phi(\lambda_1)}{\Phi(\lambda_2)} = \frac{\Phi_0(\lambda_1)}{\Phi_0(\lambda_2)} \frac{\exp(-\mu_{\mathrm{eff}}(\lambda_1)z)}{\exp(-\mu_{\mathrm{eff}}(\lambda_2)z)}. \tag{3.10}$$

In [63], this ratio was approximated by the ratio of the fluences at the surface, that is,

$$\frac{\Phi(\lambda_1)}{\Phi(\lambda_2)} \approx \frac{\Phi_0(\lambda_1)}{\Phi_0(\lambda_2)}. \tag{3.11}$$

This assumption therefore relies on the fact that the optical attenuation coefficient μ_{eff} is the same at the two different wavelengths, which will rarely be satisfied in deep tissue due to the differences in optical absorption and scattering at different wavelengths. This work also looked at the ratio of PA images resulting from two blood oxygen saturation values, $\mathrm{sO}_2(a)$ and $\mathrm{sO}_2(b)$. This second ratio relies on the assumption that the local fluence does not change during the transition, i.e. $\Phi(\lambda_1, \mathrm{sO}_2(a)) = \Phi(\lambda_1, \mathrm{sO}_2(b))$. While this may be true for very small changes in sO_2, it will not hold in general.

3.2.1 Estimating blood oxygen saturation from PA measurements in blood

As the dominant chromophore in the near-infrared (NIR) window, haemoglobin is a natural source of contrast for PA imaging. The ability to determine properties of blood such as total haemoglobin and blood oxygen saturation (sO_2) using PA methods are

therefore of particular interest. Savateeva *et al*. [64] and Esenaliev *et al*. [65] determined the optical attenuation coefficient by fitting a curve to the exponential part of a PA time series, and observed that the optical attenuations varied linearly with blood oxygen saturation for the wavelengths investigated. This enabled relative changes in sO_2 to be inferred from the PA signal, though absolute values were not obtained in either study.

Laufer *et al*. [66–69] developed a series of papers which looked at determining absolute values of chromophore concentrations. The work looked to gradually reduce the amount of *a priori* knowledge in the problem and move closer to a more realistic tissue geometry, beginning with 1D measurements of blood and later using 2D measurements of tissue-mimicking phantoms. In [66], absolute blood oxygen saturation was determined from 1D *in vitro* measurements of a saline suspension of red blood cells, and validated with measurements made using a CO-oximeter. Two methods to determine sO_2 were investigated: one employed a linear forward model which assumed the PA signal amplitude is proportional to the absorption coefficient, and therefore that the fluence is independent of optical wavelength. The other modelled the PA signal using the 1D δ-Eddington approximation (see Section 2.4.5 and Chapter 6 for more information on the δ-Eddington approximation), and iteratively adjusted for the concentrations of oxy- and deoxyhaemoglobin. Both methods produced results that were comparable in accuracy to the CO-oximeter, though the authors note that the success of the linear model is likely to be due to the very simple geometrical conditions and limited range of optical coefficients used in the study. It was also found that, despite these favourable conditions, the effects of light scattering were significant enough to reduce the accuracy of the sO_2 measurements made using the linear technique. The iterative application of the δ-Eddington approximation provided more accurate estimations of sO_2. The incorporation of an accurate light model such as the δ-Eddington approximation is a significant and perhaps necessary step in the development of a general method for QPAT; a nonlinear model will not only improve the accuracy of the recovered concentrations, but can also account for an arbitrary tissue geometry and has the potential to be translated to three dimensions.

This method was extended to determine spatially-resolved measurements of the absolute concentrations of absorbers in a tissue phantom by using a 2D delta-Eddington light model [67]. The optical parameters were recovered from a medium which consisted of a purely scattering background and three blood-filled capillaries. The technique was further extended to account for a background which was both absorbing and scattering [68], and later to determining the concentrations of absorbers from 2D multiwavelength PA images [69]. The main limitation of this technique is that it relies on prior knowledge of the target geometry, which is either known or inferred from the PA image.

The methodology developed in this series of papers has so far failed to tackle many aspects of the full problem of QPAT, in which the data is three-dimensional, the medium is highly optically heterogeneous and a limited amount of information is known about the target geometry. However, its ability to account for the effects of optical scattering and the wavelength-dependence of the fluence, the fact that the technique has been demonstrated with experimental data from tissue phantoms, and its potential to be applied to a full 3D QPAT inversion, make it arguably the best attempt at a practical and general method for quantitative PA imaging to date. The work of Laufer *et al*. urges us to conclude that a nonlinear model should necessarily be incorporated into the optical inversion if quantitative results are desired, and has offered insight into how this may be achieved in a more general experimental setting. This work has therefore been an encouraging and important intermediate step to achieving the eventual goal of recovering 3D maps of chromophore concentrations. To move further towards this goal, however, some nontrivial extensions to the method must be made, such as the incorporation of a 3D light model, the use of more efficient minimisation routines, and the application of the method to 3D absorbed optical energy images reconstructed from PA signals recorded over a line or surface.

3.3 Arbitrary (known) scattering

When the 1D assumptions break down, e.g. if 2D or 3D images of chromophore concentration distributions are desired, more complex light models are required. In highly scattering media, transport-based models such as the RTE can be used in 2D or 3D to model the fluence distribution. Increasing the complexity of the model means that an analytical solution is no longer likely to be available, and so numerical implementations will be necessary. This has the advantage that it reduced the number of assumptions in the problem and can be expected to provide higher accuracy in the reconstructions. This section will consider previous attempts to estimate the absorption coefficient in heterogeneous scattering media when the scattering coefficient is known *a priori*. Many of the methods discussed in this section have assumed homogeneous scattering; the reason they have been placed in this section is that they do not break down when this assumption fails, and can be easily extended to the heterogeneous case.

3.3.1 Complementary DOT measurements

The recovery of chromophore concentration distributions would be almost trivial if it were possible to accurately measure the optical fluence within the tissue, since the absorption coefficient could be calculated directly from $\mu_{\mathrm{a}} = h^{\mathrm{obs}}/\Phi$. Yin *et al.* [70] combined conventional PAT with diffusing light measurements coupled with an optimisation procedure based on the diffusion approximation (DA). The method first recovered the absorbed energy density from a measured PA image. This was done by finding the distribution which minimised the difference between the measured and modelled time series, where the modelled data was based on a finite element solution to the PA wave equation in the frequency domain. The second part of the method sought to estimate the distribution of the light fluence within the domain using a least-squares minimisation scheme, whereby the optimal absorption coefficient is found by minimising the difference between the measured and modelled fluence on the boundary. The light model was based on the diffusion approximation (DA) to the radiative transfer equation (RTE), and

the measurement of the fluence was obtained using diffuse optical tomography (DOT), where diffusing light measurements are collected along the surface of the imaged region. Yuan and Jiang [71] applied the method to recover images of the concentration distributions of several chromophores by incorporating multispectral data. The use of the DA to model the fluence limits the accuracy of the method, since the DA breaks down at regions close to sources and boundaries, significantly affecting its applicability to QPAT. Furthermore, in estimating the fluence distribution the authors assume the optical coefficients are homogeneous when in fact the simulated phantoms contain heterogeneities in both absorption and scattering. This assumption will lead to further errors in the fluence estimation, and is discussed later in Section 3.3.2.1. Estimating the fluence by using DOT measurements might be useful where quantitative estimates of absorption are required but spatial resolution is not of high importance, though specialist hardware would be required to collect DOT measurements. However, the main advantage of coupled physics modalities such as PAT over purely optical imaging techniques is the significant improvement in spatial resolution. Since DOT images typically exhibit poor spatial resolution due to the diffuse nature of photon transport and the ill-posedness of the inverse problem, incorporating diffusing light measurements will always produce reconstructions of limited accuracy. Any reconstructions performed using these measurements will therefore also carry these limitations.

3.3.2 Linearisation

Nonlinear behaviour is minimal when changes in the model parameters are small, and so the problem may be linearised if we consider only a small perturbation to the absorption, denoted $\mu_{\mathrm{a}}^{\delta}$, over a known homogeneous background. If the background absorption is denoted by μ_{a}^{0} then the perturbation to the absorption at a point $\mathbf{r}$ is given by

$$\mu_{\mathrm{a}}(\mathbf{r}) = \mu_{\mathrm{a}}^{0} + \mu_{\mathrm{a}}^{\delta}(\mathbf{r}). \tag{3.12}$$

The fluence experiences a corresponding change, so that the fluence is the sum of the background fluence Φ^{0}, arising from the background absorption, and the perturbed

fluence $\Phi^{\delta}(\mathbf{r})$ arising from the absorption perturbation, *i.e.*

$$\Phi(\mathbf{r}) = \Phi^{0}(\mathbf{r}) + \Phi^{\delta}(\mathbf{r}). \tag{3.13}$$

Using a Taylor series expansion and neglecting second order terms, the change in the absorbed energy is given by

$$h^{\delta}(\mathbf{r}) = \mu_{\mathrm{a}}^{\delta}(\mathbf{r})\Phi^{0}(\mathbf{r}) + \mu_{\mathrm{a}}^{0}\Phi^{\delta}(\mathbf{r}). \tag{3.14}$$

Under the assumption that the background optical properties are known, the background fluence Φ^{0} can be calculated using a numerical light model. The task then is to deal with the fluence perturbation, Φ^{δ}.

3.3.2.1 Unchanging fluence

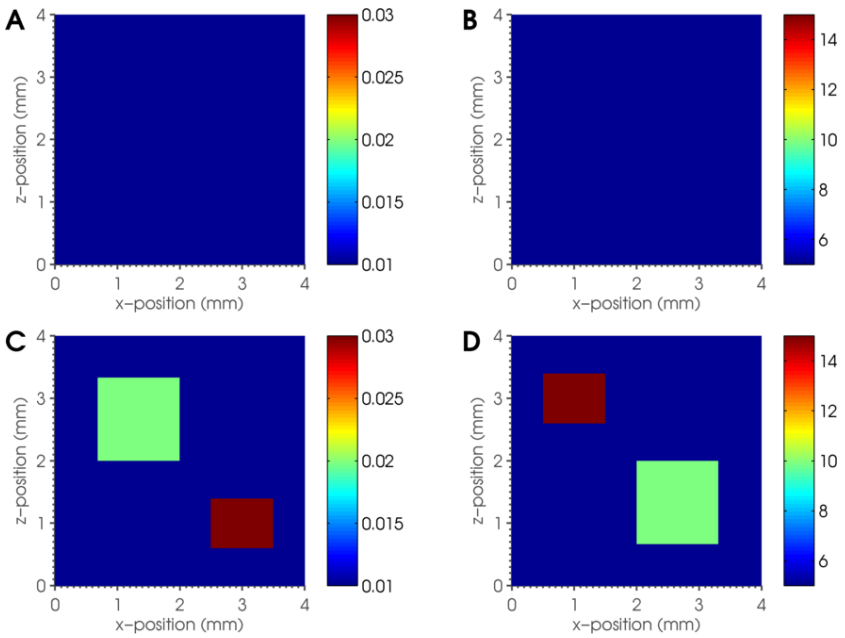

FIGURE 3.1: Absorption and scattering coefficients used to demonstrate the change in the fluence due to perturbations in the optical coefficients. (A) Background absorption coefficient μ_{a}^{0}, (B) background scattering μ_{s}^{0}, (C) heterogeneous absorption μ_{a}, and (D) heterogeneous scattering μ_{s}. The fluence resulting from these optical coefficients will be used to investigate whether the assumption that the fluence distribution is unaffected by heterogeneities in the absorption and scattering distributions is valid.

Ripoll and Ntziachristos [72] recovered small perturbations in the absorption coefficient by assuming that the scattering coefficient is known and homogeneous, the background absorption is known and homogeneous, and there is little or no effect on the fluence by perturbations in the absorption. This means that $\Phi^{\delta}(\mathbf{r}) \approx 0$, so that the second term in Equation 3.14 is negligible and

$$h^{\delta}(\mathbf{r}) \approx \mu_{\mathrm{a}}^{\delta}(\mathbf{r})\Phi^{0}(\mathbf{r}). \tag{3.15}$$

The absorption perturbation can therefore be found from

$$\mu_{\mathrm{a}}^{\delta}(\mathbf{r}) = \frac{h^{\delta}(\mathbf{r})}{\Phi^{0}(\mathbf{r})}. \tag{3.16}$$

The negligible effect of the change in absorption on the fluence may be a reasonable assumption to make for a relatively weakly absorbing domain, but it does not hold in general, and its application is therefore limited. Furthermore, the method relies on knowledge of the background absorption coefficient and the scattering coefficient, and assumes either that the optical scattering is homogeneous or that scattering heterogeneities will have little or no effect on the fluence perturbation. In many applications, the scattering coefficient of biological tissue will be highly heterogeneous, as well as being difficult to measure or estimate; in reality one will be fortunate to make an accurate guess at its background or mean properties. In this case, even if the target is so weakly absorbing that changes in the absorption coefficient have little effect on the fluence, it is not be reasonable to assume that the effects of unknown heterogeneities in the optical scattering will also be negligible.

We can demonstrate the effect of perturbations in the optical coefficients by using a numerical light model. Consider the optical coefficients shown in Figure 3.1. The top row (A and B) shows some background absorption and background scattering, both homogeneous, with values of $\mu_{\mathrm{a}}^{0} = 0.01$ mm^{-1} and $\mu_{\mathrm{s}}^{0} = 5$ mm^{-1}. The bottom row (C and D) shows heterogeneous absorption and scattering coefficients, which are equal to the background properties with added rectangular heterogeneities with values of 0.2 mm^{-1} and 0.3 mm^{-1} for the absorption coefficient, and 10 mm^{-1} and 15 mm^{-1} for the

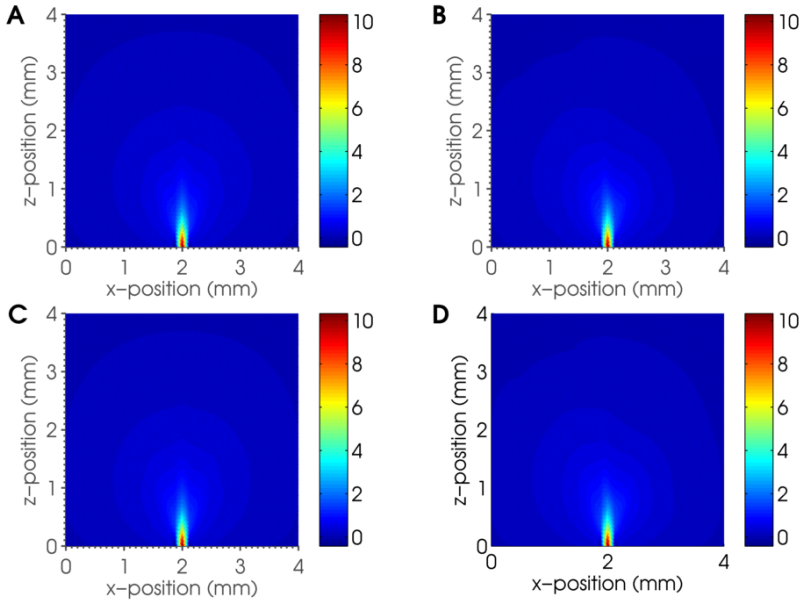

FIGURE 3.2: Optical fluence modelled due to background and heterogeneous optical coefficients shown in Figure 3.1. The optical fluence is modelled using a finite-element model based on the RTE. The domain is illuminated with a single, collimated point source. Four different fluence distributions, relating to different combinations of the optical coefficients, have been calculated using the RTE to demonstrate the change in the fluence distribution due to absorbing and scattering heterogeneities. (A) shows the resulting fluence due to the background absorption and scattering coefficients. (B) shows the fluence due to homogeneous background absorption and heterogeneous scattering. (C) shows the fluence due to heterogeneous absorption and homogeneous background scattering. (D) shows the fluence due to the heterogeneous absorption and heterogeneous scattering.

scattering. Note that we will only investigate the case where the absorption perturbations are not relatively strong compared to the background; in the case where $\mu_{\mathrm{a}}^{0} << \mu_{\mathrm{a}}^{\delta}$, the fluence perturbation will clearly be affected by the heterogeneity and the assumption of an unchanging fluence will certainly not hold. Using these optical coefficients, we have used a numerical light model based on the RTE [73] to determine the resulting optical fluences and assess the results of these heterogeneities on the background light field. A single, collimated point source was used to illuminate the domain. The anisotropy factor g was considered to be known and constant, with $g = 0.8$, and the scattering phase function is considered to be the two-dimensional Henyey-Greenstein phase function (see Section 2.4.4 for more details). We investigated three different cases: (1) the case where the scattering is homogeneous and known, (2) the case where the scattering is heterogeneous and known, and (3) the case where the scattering is heterogeneous and

only the background scattering is known. The resulting fluence for each of these cases, and also the fluence resulting from the background optical properties, were calculated with the RTE model and can be seen in Figure 3.2. In all cases we assume the background properties are known. In case (1), we are only interested in the effects of the absorption perturbation on the optical fluence, and so we look at the difference between the fluence due to the heterogeneous optical absorption and the fluence due to the background absorption when the scattering is homogeneous, that is,

$$\Phi_1^\delta = \Phi(\mu_\mathrm{a}, \mu_\mathrm{s}^0) - \Phi(\mu_\mathrm{a}^0, \mu_\mathrm{s}^0). \tag{3.17}$$

In case (2), the scattering is known and heterogeneous, and so the background fluence is calculated using the background absorption and heterogeneous scattering:

$$\Phi_2^\delta = \Phi(\mu_\mathrm{a}, \mu_\mathrm{s}) - \Phi(\mu_\mathrm{a}^0, \mu_\mathrm{s}). \tag{3.18}$$

In practice, we are more likely to be in the position of case (3), that is, the scattering will be unknown and heterogeneous. In this case, the fluence perturbation is given by

$$\Phi_3^\delta = \Phi(\mu_\mathrm{a}, \mu_\mathrm{s}) - \Phi(\mu_\mathrm{a}^0, \mu_\mathrm{s}^0). \tag{3.19}$$

These three perturbations to the fluence can be seen in Figure 3.3. In cases (1) and (2) (corresponding to Figure 3.3(A) and Figure 3.3(B), respectively), the effect of the perturbations to the optical coefficients on the fluence is indeed small, and it may be reasonable in this low-absorption case to consider Φ^δ to be negligible. However, in case (3) (Figure 3.3(C)), where the scattering is heterogeneous and only the background is known, the fluence perturbation is certainly non-zero, and Equation 3.15 is not likely to be a useful approximation. In this case, this assumption of an unchanged fluence fails and cannot be straightforwardly extended to account for unknown, heterogeneous scattering. Figure 3.3(C) also demonstrates that, in optically heterogeneous media such as biological tissue, it is insufficient to assume that the total fluence can be approximated using only the known background optical coefficients, an approximation which has been used to recover quantitative absorption estimates in e.g. [71, 74].

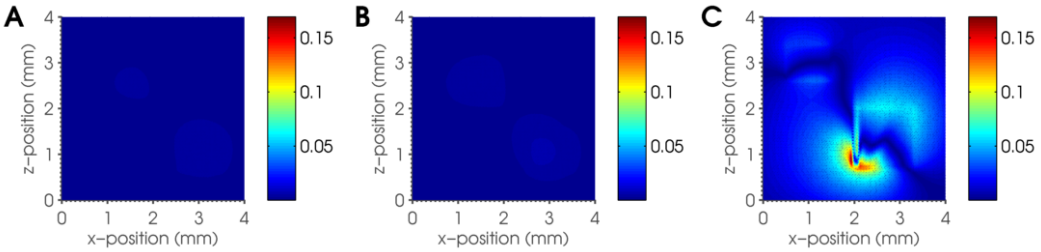

FIGURE 3.3: Fluence perturbation $\Phi^\delta = \Phi - \Phi^0$ due to three different cases of scattering coefficients. In all three cases, the absorption coefficient is a known, homogeneous background with two unknown absorbing heterogeneities. In case (A), the scattering coefficient is homogeneous and known. In case (B), the scattering coefficient is heterogeneous and known. In case (C) scattering coefficient is heterogeneous and unknown. These results suggest that it may not be reasonable to assume that the fluence perturbation is negligible if the scattering distribution is not known, even in the case where the absorbing heterogeneities are not relatively strong compared with the background.

3.3.2.2 Born approximation

Another method which approached the problem through linearisation was made by Zemp [25], where the Green's function solution to the DA was used to calculate the fluence perturbation Φ^δ. Recall from Section 2.4.4 that the DA (Equation 2.45) is given by

$$(\mu_\mathrm{a} - \nabla \cdot \kappa(\mathbf{r})\nabla)\Phi(\mathbf{r}) = q_0(\mathbf{r}), \tag{3.20}$$

and that, for homogeneous absorbing media, an analytical solution to the DA can be found using

$$\Phi(\mathbf{r}) = \int_\Omega G_0(\mathbf{r} - \mathbf{r}')q_0(\mathbf{r}')\ \mathrm{d}\mathbf{r}', \tag{3.21}$$

where G_0 is the free space Green's function (Equation 2.48). It was noted in [25] that, when the fluence obeys the DA, the resulting change in the fluence also obeys a diffusion equation:

$$(\mu_\mathrm{a}^0 - \kappa^0\nabla^2)\Phi^\delta(\mathbf{r}) = -\mu_\mathrm{a}^\delta(\mathbf{r})\Phi(\mathbf{r}), \tag{3.22}$$

where κ^0 is the optical diffusion coefficient due to the background absorption

$$\kappa^0 = \frac{1}{3(\mu_\mathrm{a}^0 + \mu_\mathrm{s}')}. \tag{3.23}$$

The Green's function solution to Equation 3.22 is therefore given by

$$\Phi^{\delta}(\mathbf{r}) = -\int_{\Omega} G_0(\mathbf{r}-\mathbf{r}')\mu_{\mathrm{a}}^{\delta}(\mathbf{r}')\Phi(\mathbf{r}')\,\mathrm{d}\mathbf{r}'. \tag{3.24}$$

To deal with the unknown fluence Φ in this expression, the first-order Born approximation is applied. This assumes that the fluence due to a perturbation to the absorption is much smaller than the unperturbed field $\Phi^{\delta} \ll \Phi^{0}$, so that the total field can be approximated by the unperturbed field, and so

$$\Phi^{\delta}(\mathbf{r}) = -\int_{\Omega} G_0(\mathbf{r}-\mathbf{r}')\mu_{\mathrm{a}}^{\delta}(\mathbf{r}')\Phi^{0}(\mathbf{r}')\,\mathrm{d}\mathbf{r}'. \tag{3.25}$$

The total fluence is then calculated using

$$\Phi(\mathbf{r}) = \Phi^{0}(\mathbf{r}) - \int_{\Omega} G_0(\mathbf{r}-\mathbf{r}')\mu_{\mathrm{a}}^{\delta}(\mathbf{r}')\Phi^{0}(\mathbf{r}')\,\mathrm{d}\mathbf{r}. \tag{3.26}$$

To recover the absorption perturbation, two PAT images, p_0^1 and p_0^2, obtained using two different illumination positions, e.g. one using a point source placed at the top boundary and another using a point source placed at the bottom boundary. These are used to form the measurement data through the quotient

$$\frac{p_0^1}{p_0^2} = \frac{\hat{\Gamma}\mu_{\mathrm{a}}\Phi^1}{\hat{\Gamma}\mu_{\mathrm{a}}\Phi^2} = \frac{\Phi^1}{\Phi^2}. \tag{3.27}$$

This has the advantage that $\hat{\Gamma}$ and μ_{a}, which are independent of the source location, cancel out and leave just the ratio of two fluences. For each source, the unknown fluences Φ^1 and Φ^2 can then be substituted by Equation 3.26, and Equation 3.27 can be rearranged into a matrix form and solved for $\mu_{\mathrm{a}}^{\delta}$.

The main drawbacks here are the assumptions that the background optical properties are known and homogeneous, and that the light is diffusive throughout the tissue, which is not the case at regions close to sources or boundaries, as discussed in Section 2.4.4. Furthermore, linearised inversions such as these are also only useful when the perturbations to the absorption coefficient are small. An interesting feature of this method is the

fact that it uses the ratio of two PA images obtained using multiple illumination positions. This is similar to the method used by [60], which was discussed in Section 3.1, which used a ratio of PA data at two different optical wavelengths to remove the wavelength-independent PA efficiency. In [25], Zemp uses the ratio of two PA images taken at the same optical wavelength, but with different illumination positions. This means that the strong dependence of the image on the absorption coefficient and the PA efficiency parameter $\hat{\Gamma}$, are removed from the problem, leaving the ratio of the two fluences resulting from the two different illuminations. This idea is interesting, since the majority of methods to solve the optical inverse problem in the mathematical literature rely on the fact that the PA efficiency parameter is known, and therefore start with the assumption that the data is the absorbed optical energy density h^{obs}. This method starts by assuming the data is the measured initial pressure distribution and attempts to deal with the fact that the PA efficiency is unknown. This work has been extended to recovering perturbations to the absorption and scattering coefficients, which is discussed later in Section 3.4.1.1, along with other methods which have used images obtained using multiple illumination positions. The idea of using a quotient of PAT images to remove the unknown PA efficiency parameter is discussed further in Appendix B.

3.3.3 Nonlinear methods

So far we have seen attempts to simplify the inverse problem through simplification of the tissue geometry and linearisation of the forward model. These simplifications, though applicable for some particular situations, do not provide enough accuracy to be considered a solution to the full and general QPAT problem where the tissue geometry is unknown and the absorption and scattering coefficients are both unknown and heterogeneous. In this section, we discuss methods which have tackled the nonlinearity of the problem by including a nonlinear model of light transport in the inversion scheme.

3.3.3.1 Fixed point iteration

To obtain an accurate estimate of the fluence using a computational light model, the underlying optical properties should be known. Since these are exactly the properties to be recovered, it is often the case that an iterative scheme is used, whereby an initial guess at the absorption and scattering coefficients provide an initial approximation to the fluence and hence the photoacoustic data. Using this initial guess, an appropriate calculation is then iterated until the difference between the modelled photoacoustic data and the measured photoacoustic data is minimised. One such iterative process was proposed in [75, 76], where a simple fixed point iteration was used to recover the absorption coefficient from a simulated, two-dimensional measurement of the absorbed energy map. The method assumes the scattering coefficient is known *a priori*, and uses a numerical light model based on the DA, which is applied iteratively until a quantitative estimate of the absorption coefficient is found. The absorbed energy map is simulated using the light transport model and some known optical coefficients, and the 'measured' image h^{obs} is then the simulated absorbed energy map plus additive Gaussian noise. The algorithm works as follows:

(1) Make an initial estimate for the distribution of the absorption coefficient μ_{a} by setting it to zero, *i.e.* set

$$\mu_{\text{a}}^{(0)} = 0. \tag{3.28}$$

(2) Calculate the initial fluence from the initial absorption coefficient and known scattering μ_{s} using a numerical light model, *i.e.* calculate

$$\Phi^{(0)} = \Phi(\mu_{\text{a}}^{(0)}, \mu_{\text{s}}). \tag{3.29}$$

(3) Using the measured absorbed optical energy h^{obs}, calculate a new estimate of the absorption based on the previous estimate of the fluence:

$$\mu_{\text{a}}^{(i+1)} = \frac{h^{\text{obs}}}{\Phi^{(i)} + \sigma}, \tag{3.30}$$

where σ is some small constant, included as a form of regularisation in case $\Phi^{(i)}(\mathbf{r}) = 0$ for some $\mathbf{r} \in \Omega$.

(4) Calculate a new estimate for the fluence:

$$\Phi^{(i+1)} = \Phi(\mu_{\mathrm{a}}^{(i+1)}, \mu_{\mathrm{s}}). \tag{3.31}$$

(5) Iterate until the difference between the measured absorbed energy and the modelled absorbed energy is less than some chosen tolerance ϵ, *i.e.* until

$$|h^{\mathrm{obs}} - \mu_{\mathrm{a}}^{(k)}\Phi^{(k)}| < \epsilon, \tag{3.32}$$

for some k.

An iterative process such as this will be aided by a computational light model that is both accurate and fast. In this case the light model is based on the DA. Whilst a very efficient model, the DA is not sufficiently accurate; the shortcomings of using the DA for QPAT are noted in [75] and also in Section 2.4.4. Many methods for QPAT are disadvantaged by the fact that they are reliant on using the DA to model the forward problem. The fixed point iteration presented here has the advantage that any computational light model could be used to calculate the optical fluence, and so the use of the DA in this case is not a problem. The problem is remedied in [77] via the inclusion of a more accurate light model, namely the δ-Eddington approximation. The diffusion model with the δ-Eddington adjustment has been shown to agree with a Monte Carlo model for homogeneous absorbing medium [66], and the accuracy of the model when absorbing heterogeneities are present was verified in [77].

The fixed point iteration described above has been shown to provide a good estimate of the absorption coefficient in both the case of noise-free and noisy simulated data, where the scattering coefficient and anisotropy factor are known *a priori*. Yuan and Jiang [78] also applied the method to experimental data to validate that the optical absorption coefficient can be recovered using this fixed point iteration, and Yao *et al.* [79] extended

FIGURE 3.4: Heterogeneous optical absorption (A) and scattering (B) coefficients, consisting of a homogeneous background with two square inclusions, are used to simulate PAT images for the forward problem. The fluence (C) is calculated using the 2D FE RTE light model, and the absorbed optical energy density (D) is found from $h^{\text{obs}} = \mu_{\text{a}}\Phi + \eta$, where η is some additive Gaussian noise. In this case, additive noise scaled to 5% of the mean absorbed energy has been included.

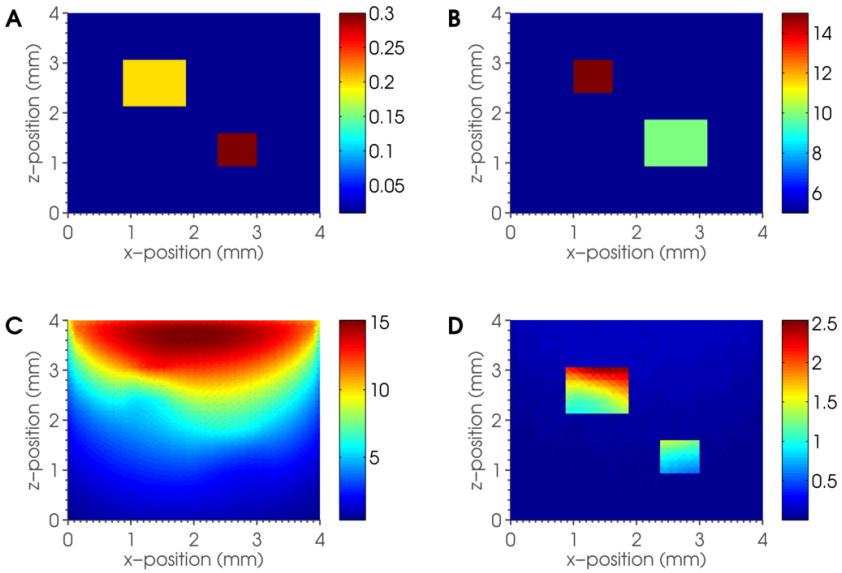

the method to incorporate a more accurate light model based on the RTE and compared the inversion results to those found using the DA for simulated and experimental data [80]. Jetzfellner *et al.* [81] also tested a diffusion-based method on experimental data, and claimed that the method is sensitive both to errors in the reduced scattering estimate and to noise and artefacts in the PAT image.

To verify the sensitivity of this method to errors in the scattering coefficient, we implemented the fixed point iteration using simulated 2D data. Heterogeneous optical absorption and scattering coefficients, consisting of a homogeneous background with two square inclusions, have been used to simulate PAT images for the forward problem. A numerical light model based on the RTE [73] was used to simulate the optical fluence resulting from a single, collimated point source. The simulated PAT image is then a product of the absorption coefficient and the optical fluence. The optical coefficients, fluence and absorbed energy with added noise are shown in Figure 3.4. The computational mesh was the 4 mm $\times$ 4 mm square $[0,4] \times [0,4]$ mm^2, consisting of $N_e = 3840$ triangular elements, $N_n = 1983$ nodes and an angular discretisation of $N_a = 16$ equal angles. The

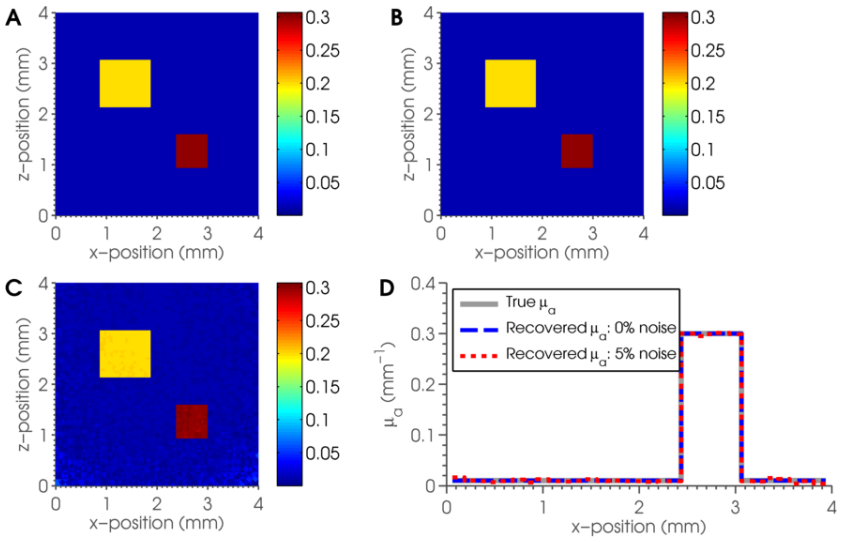

FIGURE 3.5: Fixed point iteration: recovery of absorption coefficient when the scattering is known *a priori*. (A) True absorption; (B) Noise-free reconstruction: 0.004% relative error; (C) Noisy reconstruction: 10.8% relative error;(D) Profile comparison.

anisotropy factor was considered to be known and constant at $g = 0.8$, and the scattering coefficient μ_{s} was chosen such that $\mu_{\mathrm{s}}' = \mu_{\mathrm{s}}(1-g)$ varies between 1 mm^{-1} and 3 mm^{-1}, giving a background value of $\mu_{\mathrm{s}}^{\mathrm{bg}} = 5$ mm^{-1} and two non-smooth scattering inclusions of $\mu_{\mathrm{s}}^{1} = 10$ mm^{-1} and $\mu_{\mathrm{s}}^{2} = 15$ mm^{-1}. The absorption coefficient had a background value of $\mu_{\mathrm{a}}^{\mathrm{bg}} = 0.01$ mm^{-1} and two non-smooth absorbing inclusions of $\mu_{\mathrm{a}}^{1} = 0.2$ mm^{-1} and $\mu_{\mathrm{a}}^{2} = 0.3$ mm^{-1}.

Two different cases are investigated; in the first, the absorbed energy distribution does not contain any added noise, while the second includes additive Gaussian noise scaled to 5% of the mean absorbed optical energy. Figure 3.5 shows the results of the inversion when the scattering coefficient is known *a priori*. In this example, the absorption coefficient can be recovered almost exactly in the noise-free case, with a relative error of 0.004% when compared with the true μ_{a}. The addition of additive Gaussian noise does not seem to affect the inversion too adversely, but the error is larger at 10.8%. The absorption estimate is worse at deeper regions far from the source, where the signal to noise ratio is relatively low, but the profile comparison shows that ultimately the method is able to provide a good quantitative estimate of μ_{a} despite the addition of noise. If we introduce a 10 % error into the estimate of the scattering coefficient by scaling μ_{s}, that is,

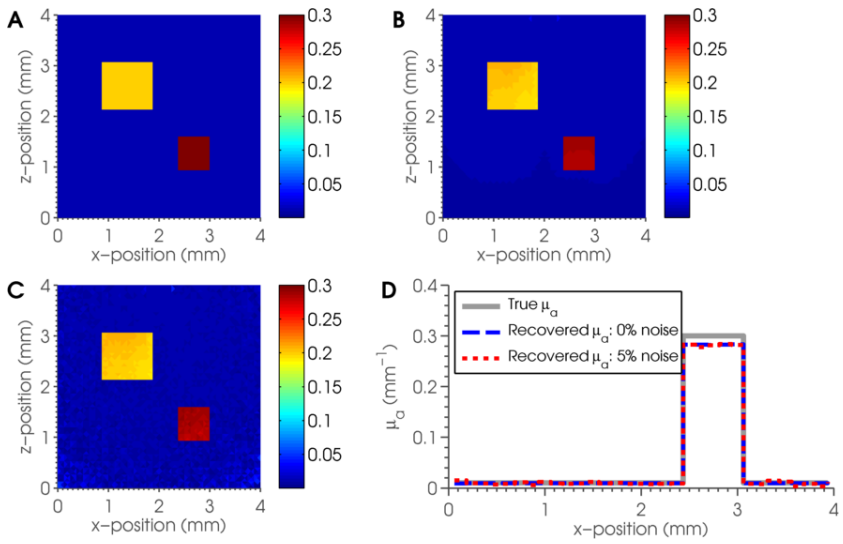

FIGURE 3.6: Fixed point iteration: recovery of absorption coefficient when the scattering contains a 10% error. (A) True absorption; (B) Noise-free reconstruction: 5.75% relative error; (C) Noisy reconstruction: 10.9% relative error; (D) Profile comparison.

$\tilde{\mu}_s = 0.9\mu_s$, the absorption reconstruction is similarly underestimated (see Figure 3.6). In this case the errors are 5.75% and 10.9% for the noise-free and noisy cases, respectively. Though the error in the noisy case hasn't changed significantly, as it is mostly dominated by errors due to noise, the profile in Figure 3.6 shows that the underestimation of the scattering coefficient has produced a corresponding underestimation of the absorption coefficient. The absorption reconstruction becomes worse again if we introduce more error into the scattering estimate. Figure 3.7 shows the resulting reconstruction using the fixed point iteration when the scattering coefficient is considered to be constant and fixed at its background value, $\mu_s = 1$ mm^{-1}. In this case, there was an error of 16.7% in the noise-free case and 18.0% in the noisy case.

The fixed point iteration is a fast and simple method for recovering a quantitative estimate of absorption. Jetzfellner *et al.* found in [81] that the method failed to converge to a solution, and was overly sensitive to noise and artifacts in the data. However, in the simulated inversions presented here, it was found that the method converged quickly to an absorption estimate and was not overly sensitive to the additive Gaussian noise included in our simulated data. While the increase in noise level does, naturally, produce larger errors in the reconstruction than the noise-free case, the reconstructions are not

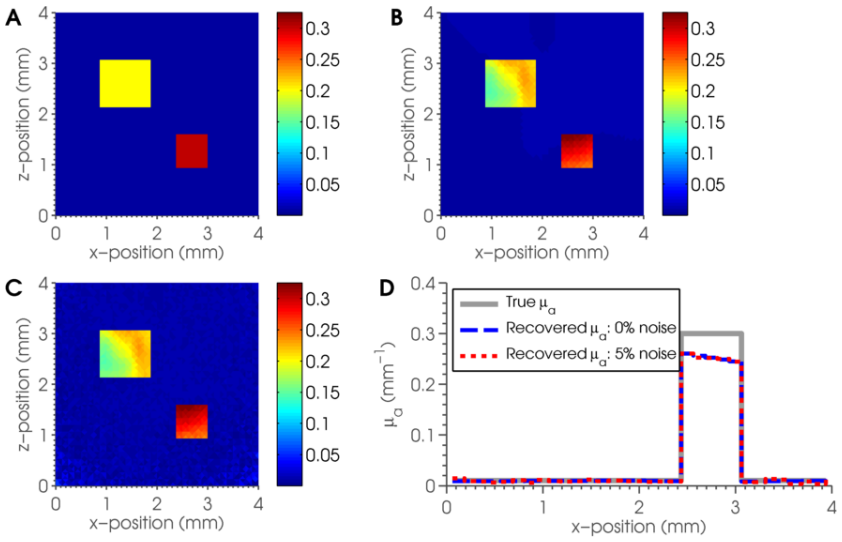

FIGURE 3.7: Fixed point iteration: recovery of absorption coefficient when the scattering coefficient is fixed at its background value. (A) True absorption; (B) Noise-free reconstruction: 16.7% relative error; (C) Noisy reconstruction: 18.0% relative error; (D) Profile comparison.

overly sensitive and a reasonable reconstruction is still obtained. The incorporation of appropriate regularisation could improve the reconstructions from noisy data further. The main drawback of this method is its reliance on knowledge of the scattering coefficient. The results from this method indicate that errors in the scattering estimate when using the fixed point iteration will produce corresponding errors in the reconstructed absorption coefficient. We investigated this further by looking at the change in percent relative error in the recovered absorption coefficient as errors are introduced into the scattering coefficient. Three different levels of additive Gaussian noise are considered: 0%, 5% and 10%. Figure 3.8 shows the resulting error in the reconstructed absorption coefficient as the scattering is under- and overestimated. The method appears to be reasonably robust to errors in the scattering coefficient, in that the error produced in the reconstructed absorption coefficient appears to increase fairly linearly with the error in the scattering. The fixed point iteration is a very straightforward method, which may be a very useful tool in any case where the scattering is known or can be estimated with some confidence. However, the errors in the reconstructed μ_a are significant enough that the fixed point iteration is not likely to be accurate enough to be a suitable method for QPAT when the scattering is not known *a priori*.

FIGURE 3.8: Sensitivity of the absorption reconstruction to errors in the scattering coefficient when using the fixed-point iteration proposed in [75].

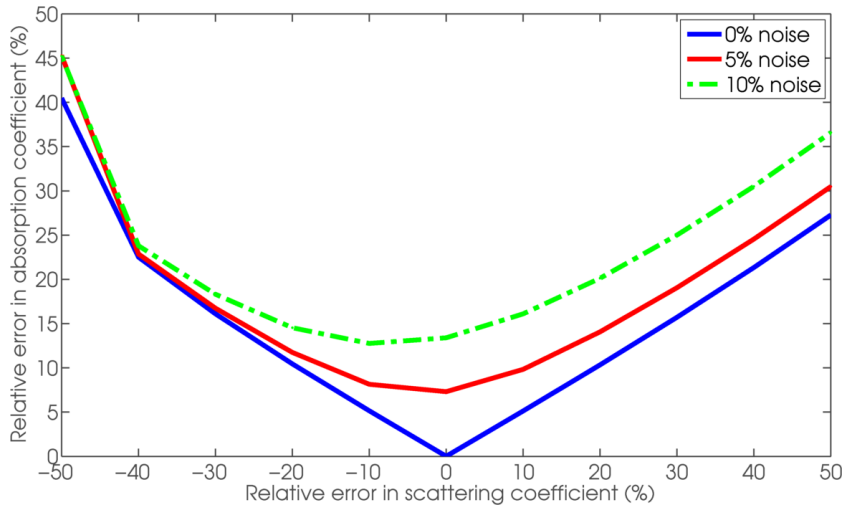

3.3.3.2 Noniterative reconstruction

Banerjee et al. [82] used a noniterative method, which uses a model of light propagation to recover the absorption coefficient from a (simulated) measurement of the absorbed optical energy distribution. The method relies on the fact that the reduced scattering coefficient is known *a priori*, and uses the diffusion approximation (DA) to the radiative transfer equation (RTE) (discussed in Section 2.4.4 and defined by Equation 2.45) to model the light propagation within the tissue. The diffusion coefficient κ depends on both the absorption coefficient and the reduced scattering coefficient $\mu_s' = \mu_s(1-g)$, and is defined by

$$\kappa := \frac{1}{3(\mu_a + \mu_s')}. \tag{3.33}$$

However, the DA also assumes that the target is weakly absorbing relative to the scattering coefficient, with $\mu_a \ll \mu_s'$. Banerjee et al. therefore assume that κ may be considered to be independent of the absorption coefficient, and use

$$\kappa = \frac{1}{3\mu_s'}. \tag{3.34}$$

With this assumption, and by noting that the absorbed energy map appears in the light model since $h^{\mathrm{obs}} = \mu_{\mathrm{a}}\Phi$, the DA (Equation 2.45) can be recast as

$$-\nabla \cdot \kappa \nabla \Phi = q - h^{\mathrm{obs}}. \tag{3.35}$$

This can now be solved for the fluence Φ, which can then be used to find the absorption coefficient μ_{a} using

$$\mu_{\mathrm{a}} = \frac{h^{\mathrm{obs}}}{\Phi}. \tag{3.36}$$

The simulations in [82] assume that the reduced scattering coefficient is homogeneous, though the method does not rely on this assumption providing that it is known *a priori*. The fact that the method is noniterative is an advantage, since iterative schemes can take a number of iterations and therefore can become time-consuming, especially for large sets of data. Unfortunately, the main drawback of the method is its reliance on the DA; the DA is not sufficiently accurate for QPAT in significantly large regions close to boundaries and sources, and it is therefore unlikely that this method will hold up to the use of experimental data. Indeed, the results in [82] indicate that the reconstruction of μ_{a} suffers where a more accurate model of light transport (namely a Monte Carlo light model) has been used to simulate the measurement data. As the method directly manipulates the DA, it is not obvious how one might go about extending this method to include a more accurate light model such as the RTE. It is possible, however, that one might extend Banerjee's method to deal with an absorption-dependent diffusion coefficient by iterating the method.

3.3.4 Minimisation-based approach

Several attempts to recover the absorption coefficient given that the scattering coefficient is known *a priori* have been discussed, but these methods have been shown to be either sensitive to errors in the scattering estimate or an initial guess, or to be dependent on a model of light transport which may be inaccurate in the case of photoacoustics.

To combat this, an alternative approach has been developed, whereby the absorption coefficient can be recovered, given prior knowledge of the scattering coefficient, by using a numerical model based on the DA in an iterative optimisation scheme [83]. The method solves the problem by finding the optical absorption coefficient which minimises an objective function ε, a least-squares error functional which quantifies the difference between the measured absorbed energy distribution h^{obs} and a modelled prediction h. The minimiser is found by iteratively adjusting the estimate of the absorption coefficient μ_a, running the model with this new set of parameters and evaluating the objective function until its value falls under a given tolerance. The least-squares error functional to be minimised is given by

$$\varepsilon = \frac{1}{2}\int_{\Omega}(h(\mu_{\mathrm{a}}) - h^{\mathrm{obs}})^2\, dV, \tag{3.37}$$

and the update to the estimate of μ_{a} at each iteration can be found by calculating its gradient with respect to μ_{a}. The functional gradient can be used in a nonlinear optimisation scheme, such as a quasi-Newton method (see Section 3.5 and Appendix D for more discussion on minimisation schemes). In [83], the functional gradients are calculated by solving the adjoint equation

$$(\mu_{\mathrm{a}} - \nabla\cdot\kappa\nabla)\Phi^* = \mu_{\mathrm{a}}(h - h^{\mathrm{obs}}) \tag{3.38}$$

for the adjoint fluence Φ^*. The adjoint equation arises to assist the gradient calculation, as it enables the functional gradient with respect to the absorption coefficient to be calculated extremely efficiently; only one run each of the forward and adjoint light models is needed to evaluate the gradient at each iteration. The main drawback of this method, as has been the case with many of the methods discussed so far, is that it is based on the DA, the validity of which has been discussed in Section 2.4.4. The development of this method resulted in a series of papers [22, 26, 84], in which a number of improvements have been made. These include the incorporation of the RTE and a method for accounting for unknown scattering. The latter is particularly useful, given that heretofore proposed methods for QPAT have typically assumed that the scattering is known *a priori*, when in practice this is unlikely to be the case. The next section will

discuss methods for QPAT which have accounted for the fact that both optical coefficients are likely to be unknown and heterogeneous.

Yao *et al*. [79] also approached the QPAT inversion using a Jacobian-based minimisation method, this time based on the full RTE. Here, the method used measured data from absorbing phantoms. The reconstructions of the absorption coefficient from the phantom data are reasonable, though no numerical demonstrations are included to show that the method works properly or has been implemented correctly. The scattering coefficient was not so much known, but estimated using knowledge of the homogeneous reduced scattering coefficient and an estimation of the anisotropy factor. It is possible that these reconstructions could have been improved if the method had aimed to recover both absorption and scattering coefficients simultaneously.

3.4 Unknown scattering

We have discussed how quantitative estimates of the optical absorption coefficient can be recovered when the scattering is assumed to be known throughout the entire domain. In practice, however, it is likely that both the absorption and scattering coefficients will be unknown and heterogeneous. A typical region of tissue will be highly optically scattering, and we will at best be able to make a rough guess at the average scattering coefficient over the region. Even this will be a challenge, and will require that previous measurements have been made on that particular tissue type, and that they are available in the literature. This will clearly result in a very crude estimate of the true scattering distribution, and for most applications requiring quantitative estimate of absorption, a more accurate reconstruction will be required. To obtain a more accurate quantitative estimate of absorption coefficient, we therefore need to account for the effects of scattering in the inversion method, and it may be necessary to recover both absorption and scattering simultaneously. The recovery of two optical coefficients, however, raises

questions regarding the uniqueness of a solution and the well-posedness of the problem.

3.4.1 Uniqueness and ill-posedness

It has been shown that determining both optical coefficients from a PAT image is non-unique if the image has been obtained by illuminating the domain from a single side using one optical wavelength [23, 85]. This is due to the fact that changes in the optical absorption and scattering at one point will affect the nearby fluence, and so a situation may arise in which the change due to the scattering counteracts exactly the change due to the absorption coefficient. In this case, two different sets of optical coefficients would give rise to the same absorbed optical energy image, and so a unique solution to the inverse problem would not exist. Figure 3.9 shows an illustrative example of this type of absorption-scatter nonuniqueness [27].

FIGURE 3.9: Example of absorption-scatter nonuniqueness. When using a single illumination position and one optical wavelength, it is possible that two different sets of optical absorption and scattering coefficients can produce the same absorbed optical energy image. It is therefore not guaranteed that a unique solution to the corresponding inverse problem exists when recovering for both optical absorption simultaneously. Figure 1 in [27].

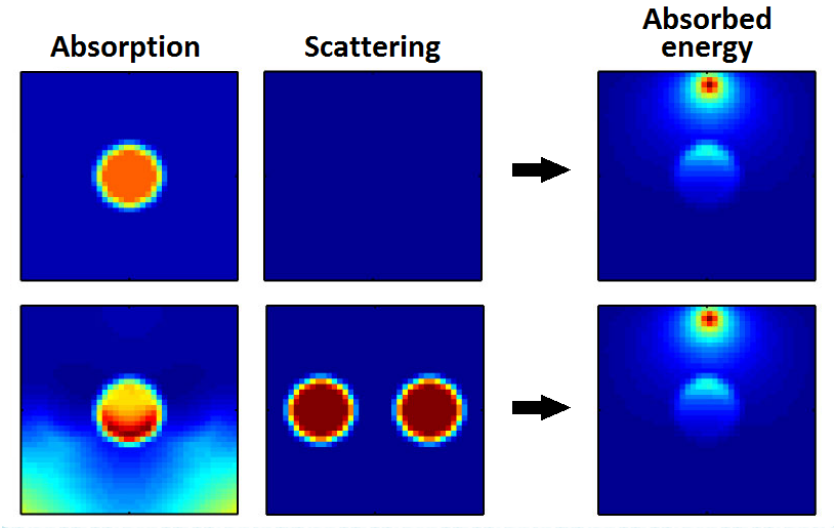

3.4.1.1 Overcoming nonuniqueness using multiple illuminations

Bal *et al*. have provided mathematical proof that additional information must be incorporated if a unique solution is to be guaranteed [23, 34, 85]. This work also demonstrated that the use of a set of PAT images obtained using multiple illumination positions may be used to guarantee a unique solution. In [34], it has been shown that using two 'well-chosen' illumination positions will guarantee uniqueness, though the combination of illuminations is based on the construction of complex geometric optics solutions, and are not particularly explicit. The use of multiple illumination positions to ensure a unique solution is illustrated in [27] (see Figure 3.10), where the example of absorption-scatter nonuniqueness in Figure 3.9 is remedied by the inclusion of additional information obtained using a source located on a different boundary.

FIGURE 3.10: Overcoming the absorption-scatter nonuniqueness using multiple illumination positions. The optical coefficients shown in Figure 3.9 are used to generate absorbed energy images using a point source placed at the centre of the top boundary. A second point source placed at the centre of the left-hand boundary is used to produce another set of images. The incorporation of an additional illumination positions now ensured that there is a difference between the two sets of absorbed energy densities, so that a unique solution is guaranteed. Figure 1 in [27].

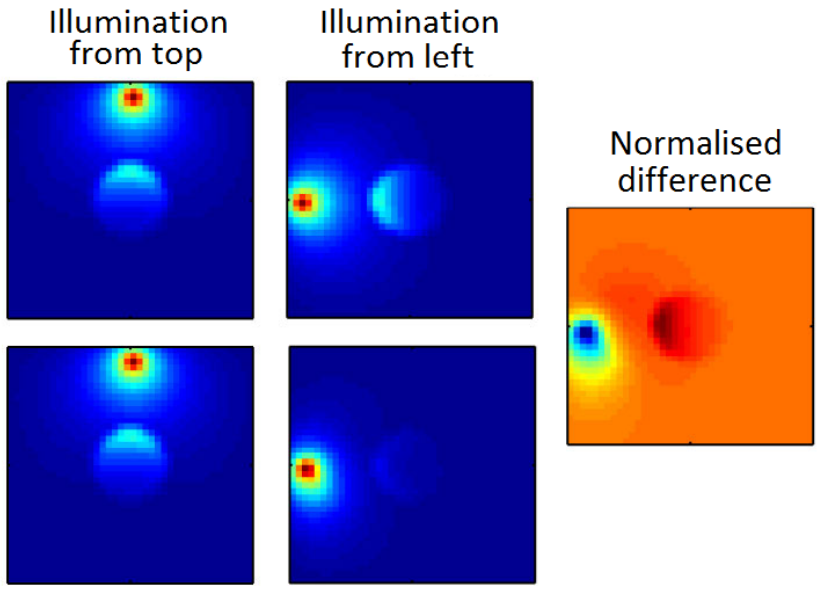

Bal *et al*. applied their results on the use of multiple illumination positions for QPAT to a non-iterative method for the simultaneous reconstruction of the absorption coefficient

μ_s and the diffusion coefficient κ from simulated PAT images [23, 34]. The method reconstructs κ rather than μ_s as it uses the DA to model light transport. The method assumes that two (or more) PAT images (denoted h_1 and h_2) have been obtained using two (or more) illumination positions. The fluence resulting from the first illumination is denoted Φ_1, and the fluence resulting from the second illumination is denoted by Φ_2. The diffusion equation for the first illumination is then multiplied by Φ_2, and vice versa. One of these equations can then be subtracted from the another and rearranged to obtain

$$\nabla \cdot \left(\mu^2 \beta\right) = 0, \tag{3.39}$$

where

$$\mu := \frac{\sqrt{\kappa}}{\mu_a} \tag{3.40}$$

and β is the vector field

$$\beta := h_1 \nabla h_2 - h_2 \nabla h_1 = \mu_a^2 \Phi_1^2 \nabla \left(\frac{\Phi_2}{\Phi_1}\right). \tag{3.41}$$

To ensure uniqueness, the illumination patterns must be chosen so that Equation 3.41 is satisfied. While there are no guidelines for choosing the illumination positions, [34] shows that a large class of illuminations will ensure uniqueness and provide stable and robust reconstructions in the two-dimensional setting. Furthermore, this series of work has established that the use of multiple illuminations can also improve the stability of the reconstructions [34]. The fact that the method neither requires linearisation nor the iterative updating of the fluence is a distinct advantage, although solving the transport equation 3.41 is nontrivial (two distinct methods are provided in [23, 34]). Two major disadvantages of the method are its reliance on the DA to model the light propagation and its sensitivity to noise. Since it is not obvious how this method may be extended to include a more accurate light model, it is likely that the method will not provide sufficient quantitative accuracy when reconstructing the optical coefficients from real PAT images. The sensitivity of the noise arises from the last term in Equation 3.41. Since the method is non-iterative, it will not be possible to apply the iterative regularisation usually

employed to reduce the amplification of noise in the inversion. Despite these drawbacks, the results of this work on ensuring uniqueness and stability in QPAT reconstructions have proved to be incredibly useful and insightful.

The linearisation approach proposed by Zemp [25] (discussed in Section 3.3.2.2) has been extended to recover perturbations to the absorption and scattering coefficients simultaneously [27]. In this case, Equation 3.22 contains an additional term related to the scattering perturbation:

$$(\mu_{\mathrm{a}}^{0} - \nabla \cdot \kappa^{0} \nabla \Phi^{\delta}(\mathbf{r}) = -\left(\nabla \cdot \kappa^{\delta}(\mathbf{r}) \nabla - \mu_{\mathrm{a}}^{\delta}(\mathbf{r})\right) \Phi(\mathbf{r}), \tag{3.42}$$

where κ^{δ} is the perturbation to the optical diffusion coefficient. By obtaining the Green's function solution to Equation 3.42 and applying the first-order Born approximation, the perturbation to the fluence is now given by

$$\begin{aligned} \Phi^{\delta}(\mathbf{r}) \quad = \quad & -\int_{\Omega} G_0(\mathbf{r}-\mathbf{r}') \mu_{\mathrm{a}}^{\delta}(\mathbf{r}') \Phi^{0}(\mathbf{r}') \, \mathrm{d}\mathbf{r}' \\ & -\int_{\Omega} G_0(\mathbf{r}-\mathbf{r}') \nabla \Phi^{0}(\mathbf{r}') \, \mathrm{d}\mathbf{r}', \end{aligned} \tag{3.43}$$

so that the total fluence can be written as

$$\begin{aligned} \Phi(\mathbf{r}) \quad = \quad & \Phi^{0}(\mathbf{r}) - \int_{\Omega} G_0(\mathbf{r}-\mathbf{r}') \mu_{\mathrm{a}}^{\delta}(\mathbf{r}') \Phi^{0}(\mathbf{r}') \, \mathrm{d}\mathbf{r} \\ & -\int_{\Omega} \kappa^{\delta}(\mathbf{r}') \nabla G_0(\mathbf{r}-\mathbf{r}') \cdot \nabla \Phi^{0}(\mathbf{r}') \, \mathrm{d}\mathbf{r}. \end{aligned} \tag{3.44}$$

As in [25], a quotient of PAT images is formed using data from two illumination positions, giving

$$\frac{p_0^1}{p_0^2} = \frac{\Phi^1}{\Phi^2}. \tag{3.45}$$

The unknown fluences Φ^1 and Φ^2 can then be substituted by Equation 3.44, and Equation 3.45 can be rearranged into a matrix form and solved for $(\mu_a^\delta, \kappa^\delta)$. The limitations of this method remain the same as those in [25]; the light propagation is modelled using the DA, the background optical properties must be known and homogeneous, and the Born approximation is only accurate for small perturbations in the optical coefficients.

Multiple illumination positions have been used to extend the minimisation-based approach described in Section 3.3.4 to the case where both optical coefficients are unknown [24, 26, 29, 30, 32, 33]. In this case, the error function is minimised with respect to both optical coefficients in order to approximate a solution to both absorption and scattering. These approaches typically either use the DA to model the light field, or use computationally intensive Jacobian-based minimisation methods to perform the inversion. Both of these approaches will struggle in the application to real data: the DA will not provide the quantitative accuracy required from the light model, and the Jacobian-based minimisations will require an impractical amount of computer memory to perform a large-scale 3D inversion. Minimisation-based methods for QPAT are discussed further in Section 3.5.

Tarvainen *et al.* used multiple illumination positions to ensure uniqueness when using a Bayesian approach to QPAT [86]. The measurement noise is typically modelled as a Gaussian distribution, however, since in the optical inverse problem the data is the solution to the acoustic inverse problem, the noise is affected by the inversion method applied to perform the first inversion. In [86], a Bayesian approach was used to model the noise statistics of the optical data in order to improve the reconstructions of the optical coefficients. The results of this approach were shown to improve the reconstructions, though the method is computationally very intensive even for a small 2D problem. Extension to real data will therefore be challenging.

3.4.1.2 Overcoming nonuniqueness using multiple wavelengths

The absorption-scatter nonuniqueness can also be overcome by incorporating additional information from images obtained using multiple wavelengths, instead of using multiple illuminations [22, 28]. In [22], the minimisation-based method described in Section 3.3.4 was extended to the multiple wavelength case in order to obtain estimates of both optical absorption and scattering coefficients simultaneously. The recovery of the concentration of two chromophores was demonstrated using simulated photoacoustic images obtained using four different wavelengths. The light propagation was modelled using the DA. Recall that if there are K chromophores present in the tissue region of interest, the absorption coefficient can be written as the linear sum

$$\mu_{\mathrm{a}}(\mathbf{r}, \lambda) = \sum_{k=1}^{K} c_k(\mathbf{r}) \alpha_k(\lambda), \tag{3.46}$$

where λ is the wavelength, c_k are the chromophore concentrations and α_k are the specific absorption spectra. The use of multiple wavelengths requires prior knowledge of the absorption spectra $\alpha_k(\lambda)$ for the wavelengths of interest, and also the wavelength-dependence of the scattering coefficient. In this case, the wavelength-dependence of the reduced scattering coefficient μ_{s}' is assumed to be proportional to some experimentally determined constant $b > 0$, so that

$$\mu_{\mathrm{s}}'(\mathbf{r}, \lambda) \approx a(x) \lambda^{-b}. \tag{3.47}$$

The quantities to be recovered are now the chromophore concentration distributions c_k and the spatial dependence of the scattering $a(x)$. The error functional is minimised using a Gauss-Newton method, which calculates the functional gradients via the construction of the Jacobian matrix $\mathbf{J}$ and subsequent approximation to the Hessian matrix $H \approx \mathbf{J}^{\mathrm{T}}\mathbf{J}$ (details of the construction of Jacobian and Hessian matrices can be found in Section 3.5). The method was subsequently used to recover multiple chromophore distributions from real, 2D multiwavelength photoacoustic images from known phantoms, where the scattering coefficient was homogeneous and unknown and prior knowledge

of the target geometry was available [69].

Bal *et al*. extended the vector-field approach to the multiple wavelength case [28]. This approach also uses the DA to model the light field, and so carries with it the same limitations as the method described in Section 3.4.1.1. Furthermore, the uniqueness proofs are only valid for diffusion coefficients which are C^2 in space. Since the distribution of the absorption and scattering coefficient, and hence the diffusion coefficient, will be unknown, a method which required smoothness in these parameters will not be suitable as a general solution for QPAT, where non-smooth absorbers such as blood vessels appear often. For non-smooth diffusion coefficients, Bal *et al.* moved to the minimisation-based approach described above [28].

The Bayesian approach to QPAT has also been extended to the multiple wavelength case [87], however, the method remains extremely computationally intensive even for small 2D simulations.

Determining the absolute values of chromophore concentrations from quantitative estimates of the absorption coefficient will require the use of inversions at multiple wavelengths. Since multiple wavelengths can also be used to overcome absorption-scatter nonuniqueness, this method therefore has the advantage that fewer measured images will need to be obtained than in the multiple illumination case. This reduces the amount of unknowns in the problem, however, this may not affect the speed of the inversion in the multiple illumination case, since single-wavelength inversions for μ_{a} can be performed straightforwardly in parallel. Another disadvantage of using multiple wavelength images to perform the inversion is that the spectral dependence of the scattering coefficient must be known. Furthermore, it is possible that the use of multiple illuminations can improve the stability of the reconstructions [34], and so it may desirable to obtain measurement data from different illuminations where possible. Where this is not possible, the use of multiple wavelengths to perform the inversion may provide a suitable

alternative.

3.4.1.3 Reconstructing the photoacoustic efficiency parameter

Another uniqueness problem arises when we consider that a PAT image also depends on the PA efficiency parameter, $\hat{\Gamma}$. It has been shown that if we assume that the data has the form $\hat{\Gamma}\mu_{\mathrm{a}}\Phi$ and attempt to reconstruct $\hat{\Gamma}$, μ_{a} and μ_{s} simultaneously, then only two out of the three of these coefficients can be reconstructed uniquely, even for an arbitrary number of illuminations [34]. Since $\hat{\Gamma}$ is independent of wavelength, it is possible that this may be remedied by incorporating measurement data obtained using multiple illumination positions *and* multiple wavelengths. In Appendix B, we discuss a method which uses a quotient data type to eliminate the PA efficiency parameter from the inverse problem.

3.4.1.4 Diffusivity of the light field

Another form of ill-posedness in the inverse problem is caused by the diffuse nature of the optical propagation. The high spatial frequencies in the distributions of the optical properties have limited influence on the fluence distribution, so that sharp features in the fluence tend to be smoothed out [88]. In PAT, the measurement data is the absorbed energy density, which is strongly dependent on the absorption coefficient μ_{a}, not only through the fluence $\Phi(\mu_{\mathrm{a}}, \mu_{\mathrm{s}})$, but through the product $\mu_{\mathrm{a}}\Phi(\mu_{\mathrm{s}}, \mu_{\mathrm{s}})$. High frequencies in the absorption coefficient therefore have a significant influence on the measured data. On the other hand, the scattering has a second-order effect on the measurement data, since it only affects the absorbed energy through its effect on the fluence. The forward operator therefore acts as a low pass filter to reduce the amplitudes of the high frequency components of the scattering distribution, and consequently inverting for the scattering coefficient will grow the high frequency components. This will also have the effect of amplifying noise in the measured data. For iterative techniques, such as the

minimisation-based method discussed in Section 3.3.4, a penalty term can be included to reduce the unwanted amplification of noise. These methods are called regularisation methods, and since this effect is common to many inverse problems, a large number of techniques for their implementation are available in the literature, e.g. [89–94].

3.4.1.5 Sensitivity of error functional to absorption and scattering

The strong dependency of the data on the absorption compared with the scattering coefficient can be seen by looking at the sensitivity of the error functional

$$\varepsilon = \frac{1}{2}\int_{\Omega}(h^{\mathrm{obs}} - h(\mu_{\mathrm{a}}, \mu_{\mathrm{s}}))^2 \,\mathrm{d}V \tag{3.48}$$

to changes in the optical coefficients. A similar investigation was performed by Tarvainen *et al.* in [30], where it was shown that the RTE is better posed than the DA for small domain sizes relevant to QPAT.

FIGURE 3.11: Mesh geometry, source location and perturbation location used to demonstrate the sensitivity of the error functional to changes in the absorption and scattering coefficients. The source is placed at the centre of the top boundary of the structured triangular mesh, and is indicated with a red circle. The perturbation is a 1 mm square located at (2 mm,3 mm), and has been highlighted in dark red.

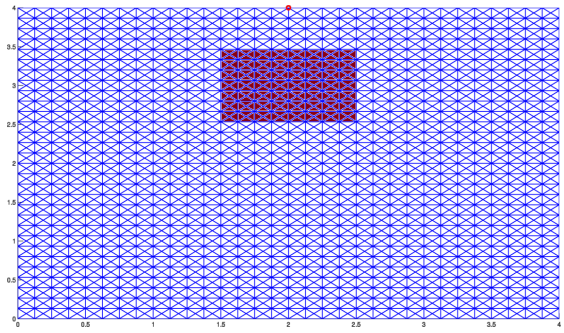

Consider the domain $\Omega = [0,4] \times [0,4]$ mm^2. The optical parameters are a single square perturbation at $\mathbf{r} = (2,3)$ to a homogeneous, known background, with background values $\mu_{\mathrm{a}}^{\mathrm{bg}} = 0.01$ mm^{-1} and $\mu_{\mathrm{s}}^{\mathrm{bg}} = 5$ mm^{-1}. The error functional ε can be plotted as a

function of $\mu_{\mathrm{a}}^{\mathrm{pert}}$ and $\mu_{\mathrm{s}}^{\mathrm{pert}}$:

$$\varepsilon(\mu_{\mathrm{a}}^{\mathrm{pert}}, \mu_{\mathrm{s}}^{\mathrm{pert}}) = \frac{1}{2}\int_{\Omega} (h(\mu_{\mathrm{a,ref}}^{\mathrm{pert}}, \mu_{\mathrm{s,ref}}^{\mathrm{pert}}) - h(\mu_{\mathrm{a}}^{\mathrm{pert}}, \mu_{\mathrm{s}}^{\mathrm{pert}}))^2 \, \mathrm{d}V \tag{3.49}$$

where $h(\mu_{\mathrm{a,ref}}^{\mathrm{pert}}, \mu_{\mathrm{s,ref}}^{\mathrm{pert}})$ is the reference data, obtained with the correct perturbation values $\mu_{\mathrm{a,ref}}^{\mathrm{pert}} = 0.3\ \mathrm{mm}^{-1}$ and $\mu_{\mathrm{s,ref}}^{\mathrm{pert}} 15\ \mathrm{mm}^{-1}$. The background parameters are kept fixed at their correct values. The anisotropy factor was constant, with g = 0.8. The test data were generated for 20 absorption perturbation values in the range of 0.03 to 0.6 mm^{-1} and 20 scattering perturbation values in the range from 1.5 to 30 mm^{-1} (up to twice the correct perturbation values). The RTE was used to simulate the forward data, which was generated using a single point source placed at the centre of the top boundary. The compuational mesh used for the finite element (FE) implementation of the RTE consisted of 3840 triangular elements and 1983 nodes, and an angular discretisation of 16 equal angles. The mesh geometry, source location and the location of the perturbation are shown in Figure 3.11.

FIGURE 3.12: (A) Contour and (B) surface plot showing the sensitivity of the error functional to changes in the absorption and scattering coefficients. The error map reaches its absolute minimum of zero at the correct perturbation data set, when $\mu_{\mathrm{a}}^{\mathrm{pert}} = 0.3\ \mathrm{mm}^{-1}$ and $\mu_{\mathrm{s}}^{\mathrm{pert}} = 15\ \mathrm{mm}^{-1}$, which is indicated by a blue cross. The error functional ε is much less sensitive to changes in the scattering coefficient than changes in the absorption coefficient.

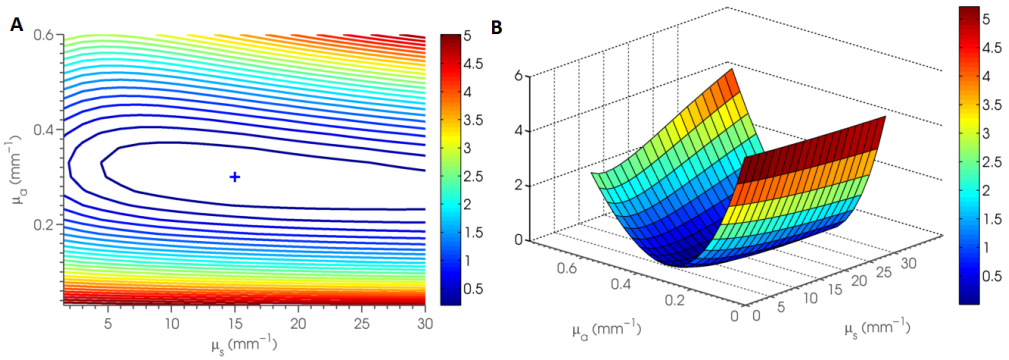

Figure 3.12 show a contour and surface plots of $\varepsilon(\mu_{\mathrm{a}}^{\mathrm{pert}}, \mu_{\mathrm{s}}^{\mathrm{pert}})$. The error map reaches its absolute minimum of zero at the correct perturbation data set, indicated by a blue cross. These plots show that the error functional ε is much less sensitive to changes in the scattering coefficient than changes in the absorption coefficient. This indicates

that recovering the scattering coefficient is likely to be much more difficult than the absorption coefficient. Recovering both optical coefficients simultaneously will therefore be challenging. However, we should bear in mind that it is a quantitative estimate of the absorption coefficient that is required to provide us with chromophore concentration distributions, and the recovery of the scattering coefficient is performed only to deal with the fact that it is an unknown parameter. Reconstructing for both coefficients may provide a more accurate estimate of μ_{a} than attempting to estimate μ_{s}, but a detailed reconstruction of μ_{s} is not required to achieve the ultimate aim of QPAT.

3.5 Minimisation-based approaches to QPAT

We have discussed how minimisation-based techniques, which seek to iteratively adjust the parameters in a numerical model until the difference between the measured and modelled data is minimised, have previously been shown to successfully recover the optical coefficients from 2D simulated PAT images. However, we are yet to discuss exactly how these methods work, the available techniques and their applicability to the QPAT problem.

The general minimisation problem is to take some function $f : \mathbb{R}^n \to \mathbb{R}$, usually called the objective function, and find the vector of variables $\mathbf{x} \in \mathbb{R}^n$ which minimises f, i.e.

$$\underset{\mathbf{x}}{\operatorname{argmin}} f(\mathbf{x}). \tag{3.50}$$

Minimisation algorithms are iterative, beginning with an initial guess at the variable $\mathbf{x}$ and generating a sequence of improved estimates, called iterates, until they terminate, hopefully at a solution. There are a number of methods which can be used to move from one iterate to the next, and many will determine the next iterate using the objective function f, its first derivative and possibly its second derivative. Nocedal and Wright [95] consider the ideal minimisation algorithm to be

- Robust, meaning the algorithm will perform well for a variety of problems of its class, and for a reasonable range of starting values.
- Efficient, both in terms of computer time or storage.
- Accurate, in that it should be able to identify a solution with precision, without being overly sensitive to errors in the data or to arithmetic rounding errors that may occur from its numerical implementation.

Given that QPAT is a large-scale, ill-posed and nonlinear problem, it is perhaps not surprising that it is not straightforward to find a single minimisation scheme for which all of these goals will obviously be fulfilled. The choice of algorithm is likely to lead to trade-offs between convergence rate and storage requirements, speed and robustness, and so on. Nearly all methods require the calculation of a direction in which to move in (ideally towards the global minimum) and a step length to define how far in that direction we should move. The algorithms available can be separated into two strategies: line-search method and trust-region methods. These really only differ in the order they choose the direction in which to travel and the step-length. Line-search methods first search for an appropriate direction $\mathbf{p}_k$ and then decide on a step-length α_k, calculating the next iterate using

$$\mathbf{x}_{k+1} = \mathbf{x}_k + \alpha_k \mathbf{p}_k. \tag{3.51}$$

Trust-region methods first define a region around the current iterate in which to search for a suitable direction, i.e. they search for a $\mathbf{p}_k$ such that $\mathbf{x}_k + \alpha_k \mathbf{p}_k$ lies inside the pre-defined trust-region. The algorithm used to search for the direction $\mathbf{p}_k$ typically defines which method is being used, as it is also defining of the method's rate of convergence, storage requirements, etc. The step-length α_k can be chosen in a number of ways, but typically looks to travel in the direction $\mathbf{p}_k$ until no further progress can be made (e.g. we are no longer travelling 'downhill'). The most intuitive choice for a search direction would be to travel along the direction in which f decreases most rapidly, i.e. $-\nabla f$,

where ∇f is the gradient of f, defined by

$$\nabla f = \left[\frac{\partial f}{\partial \mathbf{x}(1)} \frac{\partial f}{\partial \mathbf{x}(2)} \cdots \frac{\partial f}{\partial \mathbf{x}(n)} \right]^{\mathrm{T}}. \tag{3.52}$$

This search direction is used by the gradient-descent method, also known as the steepest-descent method. This method is robust and will provide accurate results, however, for many problems it is likely to be very slow. A better search direction can be found using the second-order Taylor series approximation to $f(\mathbf{x}_k + \mathbf{p}_k)$, given by

$$f(\mathbf{x}_k + \mathbf{p}_k) \approx f_k + \mathbf{p}_k^{\mathrm{T}} \nabla f_k + \frac{1}{2} \nabla^2 f_k \mathbf{p}_k, \tag{3.53}$$

where $\nabla^2 f_k$ is the Hessian matrix of second-order partial derivatives, defined by

$$\nabla^2 f_k = \begin{bmatrix} \frac{\partial^2 f}{\partial \mathbf{x}(1)^2} & \frac{\partial^2 f}{\partial \mathbf{x}(1) \partial \mathbf{x}(2)} & \cdots & \frac{\partial^2 f}{\partial \mathbf{x}(1) \partial \mathbf{x}(n)} \\ \frac{\partial^2 f}{\partial \mathbf{x}(2) \mathbf{x}(1)} & \frac{\partial^2 f}{\partial \mathbf{x}(2)^2} & \cdots & \frac{\partial^2 f}{\partial \mathbf{x}(2) \partial \mathbf{x}(n)} \\ \vdots & \vdots & \ddots & \vdots \\ \frac{\partial^2 f}{\partial \mathbf{x}(n) \partial \mathbf{x}(1)} & \frac{\partial^2 f}{\partial \mathbf{x}(n) \partial \mathbf{x}(2)} & \cdots & \frac{\partial^2 f}{\partial \mathbf{x}(n)^2} \end{bmatrix}. \tag{3.54}$$

The vector $\mathbf{p}_k$ which minimises Equation 3.53 is found by setting its derivative to zero, from which we obtain

$$\mathbf{p}_k = -(\nabla^2 f_k)^{-1} \nabla f_k, \tag{3.55}$$

which is called the Newton direction. Use of the Newton direction requires that the Hessian matrix $\nabla^2 f_k$ is positive definite, which guarantees that the Hessian is invertible and that the Newton direction is a descent direction. In the case that the Hessian is not positive definite modifications to the Newton method can be made (see e.g. [95]). Newton's method is simple, robust and has a fast rate of local convergence. It also benefits from the fact that it has a natural step-length of $\alpha_k = 1 \; \forall k$. However, the calculation of the Hessian matrix can be expensive, its storage will require a significant amount of memory, and its use in Equation 3.55 will also require its inversion. A number of methods have therefore been developed to approximate the inverse Hessian; the choice of which method is appropriate for a particular problem will typically involve a trade-off

between greater accuracy in the inverse Hessian approximation and greater computational efficiency in regards to its calculation and storage.

3.5.1 Jacobian-based methods

A useful approximation to the Hessian matrix can be formed when the objective function takes the special form of

$$f(\mathbf{x}) = \frac{1}{2} \|r(\mathbf{x})\|_2^2 , \tag{3.56}$$

where $r : \mathbb{R}^n \to \mathbb{R}^m$ is a vector of residuals. Finding the vector which minimises f in this case is called a least-squares minimisation problem, and its form allows a useful approximation to the Hessian matrix to be made. In QPAT, r is the difference between the measured absorbed energy h^{obs} and the modelled absorbed energy $h = \mu_{\text{a}}\Phi$, $\mathbf{x}$ is the absorption coefficient μ_{a} (or chromophore concentrations c). If the scattering is known *a priori*, the number of measured data points will be equal to the number of unknowns, so that $m = n$. The error functional $\varepsilon : \mathbb{R}^n \to \mathbb{R}$ which we wish to minimise is given by

$$\begin{aligned} \varepsilon(\mu_{\text{a}}) &= \frac{1}{2} \left\| h^{\text{obs}} - h(\mu_{\text{a}}) \right\|^2 \\ &= \frac{1}{2} \|r(\mu_{\text{a}})\|^2 \\ &= \frac{1}{2} \sum_{i=1}^{n} r_i^2, \end{aligned} \tag{3.57}$$

where $r_i = r(\mu_{\text{a}}(\mathbf{r}_i))$ is the residual at the spatial point $\mathbf{r}_i$. The Jacobian $\mathbf{J}(\mu_{\text{a}})$ of $r(\mu_{\text{a}})$, which is generally a $m \times n$ matrix of first-order partial derivatives (though in this case it

is $n \times n$), can then be defined by

$$\mathbf{J}(\mu_{\mathrm{a}}) = \nabla r(\mu_{\mathrm{a}})^{\mathrm{T}} = \begin{bmatrix} \nabla r_1^{\mathrm{T}} \\ \nabla r_2^{\mathrm{T}} \\ \vdots \\ \nabla r_n^{\mathrm{T}} \end{bmatrix}, \tag{3.58}$$

where each ∇r_i, $i = 1, \ldots, n$ is the gradient of r_i. Using the chain rule, the gradient vector and Hessian matrix of the objective function can then be expressed as

$$\begin{aligned} \nabla \varepsilon(\mu_{\mathrm{a}}) &= \sum_{i=1}^{n} \nabla r_i r_i \\ &= \mathbf{J}(\mu_{\mathrm{a}})^{\mathrm{T}} r(\mu_{\mathrm{a}}), \end{aligned} \tag{3.59}$$

and

$$\begin{aligned} \nabla^2 \varepsilon(\mu_{\mathrm{a}}) &= \sum_{i=1}^{n} \nabla r_i \nabla r_i^{\mathrm{T}} + \sum_{i=1}^{n} r_i \nabla^2 r_i(\mu_{\mathrm{a}}) \\ &= \mathbf{J}(\mu_{\mathrm{a}})^{\mathrm{T}} \mathbf{J}(\mu_{\mathrm{a}}) + \sum_{i=1}^{n} r_i \nabla^2 r_i. \end{aligned} \tag{3.60}$$

The Jacobian of residuals is typically straightforward to calculate, and so we can use Equation 3.59 to form the gradient vector. Furthermore, since the $\nabla^2 r_i$ are relatively small, the Hessian can be approximated by $\nabla^2 \varepsilon(\mu_{\mathrm{a}}) \approx \mathbf{J}^{\mathrm{T}}\mathbf{J}$. The Gauss-Newton method uses this Hessian approximation to find the search direction, so that Equation 3.55 becomes

$$\mathbf{p}_k = -(\mathbf{J}_k(\mu_{\mathrm{a}})^{\mathrm{T}} \mathbf{J}_k(\mu_{\mathrm{a}}))^{-1} \mathbf{J}_k(\mu_{\mathrm{a}})^{\mathrm{T}} r_k(\mu_{\mathrm{a}}). \tag{3.61}$$

Since the first term in Equation 3.60 typically dominates the second, this approximation provides a robust minimisation scheme for least-squares problems, with a convergence rate similar to that of Newton's method.

Hessian- and Jacobian-based methods are reliable and converge quickly, however, for large-scale problems the calculation and storage of the Hessian or Jacobian matrix may require a significant amount of memory. For two-dimensional examples the storage of these large, dense matrices may be computationally feasible, but real PAT images are inherently three-dimensional, and as the data sets become larger this Jacobian-based technique becomes much less practical. An alternative is to approximate the Hessian matrix using only the gradient. Jacobian-based methods typically require much fewer iterations to obtain a solution than a gradient-based method (approximately 5-10 iterations compared to 1000 or more), but for a large-scale problem such as QPAT, Jacobian-based inversion methods may not be tractable due to memory requirements.

3.5.2 Gradient-based vs Jacobian-based methods

Consider a PAT image with typical dimensions 10 mm $\times$ 10 mm $\times$ 3.5 mm and spatial resolution 70 μm, which are the dimensions of the images obtained in [2]. The spatial resolution of the image will dictate the required discretisation of the computational mesh and hence the number of elements required. For this image size, varying the spatial resolution between 1 mm and 50 μm results in a range of 484 to $>$2.8 million elements. Supposing that we require single precision data, the total memory required to store the Hessian approximation for the gradient- and Jacobian-based methods is shown in Figure 3.13. The memory requirement for a Jacobian-based method becomes significantly large as the resolution improves. For example, the PAT images obtained in [2] possessed a spatial resolution of 70 μm. In this case, a gradient-based method would require 2.1 MB of memory to store the Hessian approximation, while a Jacobian-based method would require over 2.1 TB. Gradient-based methods have been proposed and used successfully to reduce the computational requirements of a quantitative inversion for DOT [96].

Furthermore, we can use an adjoint model to assist the gradient calculation and significantly reduce the number of model evaluations required to calculate the gradient

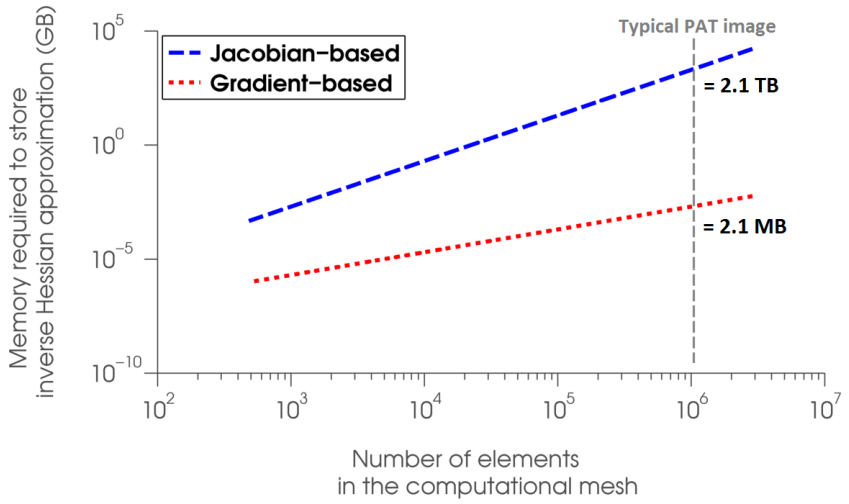

FIGURE 3.13: Memory required to store the Hessian approximation using Jacobian-based (blue dashed) and gradient-based (red dotted) minimisation methods. The number of elements in the computational domain were calculated using a typical domain size of 10 mm $\times$ 10 mm $\times$ 3.5 mm (based on the images obtained in [2]) and varying spatial resolution of 1 mm - 50 μm. The number of elements when using a resolution of 70 μm (as in [2]) have been marked by a grey dashed line. In this case, the gradient-based method required 2.1 MB to store the inverse Hessian approximation, while the Jacobian-based method would require over 2.1 TB.

[84, 97]. Jacobian-based minimisations can also use an adjoint model to calculate the Jacobian [26], though this will require significantly more evaluations of the forward model than an adjoint-assisted gradient-based method: if the number of unknowns equals the number of measurements n, then a Gauss-Newton iteration will require n runs of each of the forward and adjoint models (equivalent to $2n$ evaluations of the forward model), compared to one run each for a gradient-based method (equivalent to 2 evaluations). The number of evaluations to calculate the Jacobian therefore scales with the domain size ($2n$ evaluations of the forward model), while a gradient-based method requires 2 evaluations regardless of the number of elements in the computational mesh. This means that, although Jacobian-based methods such as Gauss-Newton require significantly fewer iterations, the amount of time taken to obtain a solution to a large-scale 3D problem is likely to be less when using a gradient-based method. Matrix-free methods, which evaluate only matrix-vector products when calculating the Hessian approximation [98], may also be used to avoid the memory problem, however, the operation count will remain high.

3.6 Summary

The literature on inversion methods for QPAT have shown that the solution to this challenging inverse problem is possible, and a number of methods for solving the problem have been suggested. These are typically sensitive to noise, require *a priori* knowledge of the scattering coefficient, are computationally too intensive to be applied to real PAT data, or are only accurate under restrictive conditions (e.g. where the approximate light model is accurate). In order for QPAT to be successfully applied to real PAT dat, new methods for QPAT which are simultaneously accurate and extendable to large-scale 3D data sets are required.

Chapter 4

Gradient-based QPAT using the RTE 1: recovering absorption

Quantitative photoacoustic imaging aims to solve a nonlinear, ill-posed, large-scale inverse problem. Solution of the problem will provide quantitatively accurate estimates of chromophore concentrations, which may prove useful in preclinical applications including, but not limited to, small animal molecular imaging and functional parameter estimation. One approach to solving the problem is to instead obtain a quantitatively accurate estimate of the absorption coefficient, from which the spatial maps of the chromophore concentrations can be recovered via a linear inversion. While this is both a valid and popular approach, the challenges of the inverse problem remain unchanged.

In this chapter, we propose the use of a gradient-based method which incorporates the full radiative transfer equation (RTE) for determining quantitatively accurate estimates of the optical absorption coefficient from simulated PAT images. Incorporating the full RTE into a minimisation-based inversion scheme ensures accuracy in the computational model and maintains flexibility in the inversion approach. The use of a gradient-based minimisation method reduces the memory requirements of the inversion, enabling the extension of the method to large-scale three-dimensional (3D) data. Section 4.1.3 presents an adjoint-assisted method for the efficient calculation of the gradient of the objective

function to be minimised. This is incorporated into a quasi-Newton minimisation scheme to determine the optical absorption coefficient. Section 4.2.2 demonstrates the ability of the method to provide quantitative estimates of the absorption coefficient where the scattering coefficient is known *a priori*. Given that the scattering coefficient will not typically be known in practice, Section 4.2.6 investigates how well the absorption coefficient can be reconstructed if the heterogeneous scattering coefficient is (incorrectly) assumed to be homogeneous throughout the domain.

4.1 Minimisation-based methods in QPAT

Minimisation-based techniques aim to iteratively adjust the parameters in a numerical model (in this case the optical absorption coefficient) until the difference between the measured and modelled data is minimised. In quantitative photoacoustic tomography (QPAT), these types of inversion scheme have the potential to produce quantitative results with few approximations and little *a priori* knowledge; it is possible to account for arbitrary tissue geometries, heterogeneous optical coefficients and an unknown scattering coefficient (the case of unknown scattering will be discussed later in Chapter 5). This class of methods could therefore be considered to be the most promising candidate for a general solution to the full QPAT problem to date.

4.1.1 The radiative transfer equation

Chapter 3 showed that many methods for QPAT rely on the diffusion approximation (DA) to the RTE. The DA relies on the assumption that the light is only weakly anisotropic throughout the entire domain. In biological tissue, however, the scattering of light is highly anisotropic, and light entering the region will be highly forward-directed until at least a few scattering events have occurred. This means that the DA breaks down close to sources or boundaries, and is not valid until a distance of approximately a few transport mean free paths from any source. In a typical region of biological tissue, a

transport mean free path may be on the order of 1 mm, which means that using the DA as a light model for PAT may provide inaccurate results in a significantly large portion of the image. This means that the DA will not provide sufficient quantitative accuracy for the quantitative inversion of QPAT in practice. In this chapter we propose an inversion technique for QPAT which utilises a two-dimensional (2D) model of light transport which solves a finite element (FE) implementation of the RTE [73]. By using the full RTE, accuracy in all regions of importance is ensured, although the computational effort required to solve a comparable problem is increased. To assess the inversion method, the RTE is used to simulate 2D PAT images, which provide the measured data from which the optical absorption coefficient is to be recovered.

4.1.2 Gradient-based approach

In the existing literature for QPAT, a further difficulty regarding the large-scale nature of the problem is not often addressed. This is likely due to the fact that most methods have been developed using two-dimensional simulated data, or have assumed prior knowledge of the tissue geometry to reduce the number of unknowns in the problem. In practice, any method to perform the QPAT inversion will have to translate to three dimensions and also account for a potentially huge number of unknowns.

The RTE has been used in a Gauss-Newton minimisation scheme for QPAT [26, 30], whereby the inverse Hessian is approximated using the Jacobian matrix of first partial derivatives. Since this is a large, dense matrix, terabytes of computer memory may be required to store the Jacobian for a typical 3D QPAT inversion. We therefore propose the use of a gradient-based minimisation scheme, which uses information regarding the gradient of the objective function to approximate the inverse Hessian. These are often called quasi-Newton methods, since they are based on Newton's method for finding the stationary point of a function (see Appendix D for more details on Newton's method and quasi-Newton methods). The use of gradient information rather than the Jacobian reduces the computational memory required significantly (a reduction of terabytes to

megabytes for a typical problem), since the inverse Hessian can be approximated by a vector the size of one column of the Jacobian matrix (see Section 3.5.2 for a comparison of Jacobian- and gradient-based methods for QPAT). This reduction in memory requirements enables the application of an iterative minimisation method to the types of large-scale data sets that are likely to be encountered in practice when dealing with real PAT images. Although gradient-based methods are memory-efficient, the process does typically require a large number of iterations than a full Newton method or Jacobian-based method. It is therefore important that the functional gradient calculation is relatively fast, since the functional gradients will need to be evaluated at each iteration of the method.

4.1.3 Calculating the gradient of the error functional

To perform a gradient-based method, we require the calculation of the gradient of the error functional with respect to the absorption coefficient. This could be calculated using a finite difference method, whereby the sensitivity of the error functional to a change in the absorption at each point in the domain is calculated element by element. If N_e denotes the number of elements in the computational mesh, this calculation would require N_e+1 evaluations of the forward model for each iteration of the method, and will therefore be a very expensive procedure. Instead, an adjoint RTE operator can be used to assist the gradient calculation; in this section we will derive the functional gradient with respect to the absorption coefficient and show how the adjoint RTE model can greatly reduce the operation count compared with a finite difference method. Recall that the idea of the minimisation-based approach for QPAT is to minimise the error functional

$$\begin{aligned} \varepsilon(\mu_{\mathrm{a}}) &= \frac{1}{2}\left\| h^{\mathrm{obs}} - h(\mu_{\mathrm{a}}) \right\|^2 \\ &= \frac{1}{2}\int_{\Omega} (h^{\mathrm{obs}} - h(\mu_{\mathrm{a}}))^2 \, \mathrm{d}\Omega. \end{aligned} \tag{4.1}$$

The functional gradient calculation in the case of a single PAT image is considered first, and an extension to multiple images using different illumination positions will be included later in Section 4.2.3.

To calculate the absorption gradient of the objective function, first differentiate Equation 4.1 with respect to μ_{a} at a single point $\mathbf{r}_i$ (and for notational convenience define $\mu_{\mathrm{a}}^i := \mu_{\mathrm{a}}(\mathbf{r}_i)$) to obtain

$$\frac{\partial \varepsilon}{\partial \mu_{\mathrm{a}}^i} = -\int_\Omega \frac{\partial h}{\partial \mu_{\mathrm{a}}^i}(h^{\mathrm{obs}} - h)\,\mathrm{d}\Omega. \tag{4.2}$$

The derivative of the modelled data h can be found via the product rule:

$$\begin{aligned}\frac{\partial h}{\partial \mu_{\mathrm{a}}^i} &= \frac{\partial \mu_{\mathrm{a}}}{\partial \mu_{\mathrm{a}}^i}\Phi + \frac{\partial \Phi}{\partial \mu_{\mathrm{a}}^i}\mu_{\mathrm{a}} \\ &= \Phi\delta(\mathbf{r}-\mathbf{r}_i) + \frac{\partial \Phi}{\partial \mu_{\mathrm{a}}^i}\mu_{\mathrm{a}},\end{aligned} \tag{4.3}$$

where $\delta(\mathbf{r}-\mathbf{r}_i)$ is the Dirac delta function, a generalised function with the properties

$$\int_{-\infty}^{\infty} \delta(\mathbf{r}-\mathbf{r}_i) f(\mathbf{r})\,\mathrm{d}x = f(\mathbf{r}_i), \tag{4.4}$$

$$\int_{-\infty}^{\infty} \delta(\mathbf{r}) = 1, \tag{4.5}$$

for a given function f. Substituting this into Equation 4.2 provides an expression for the gradient of the error functional with respect to μ_{a}^i:

$$\frac{\partial \varepsilon}{\partial \mu_{\mathrm{a}}^i} = -\Phi(\mathbf{r}_i)(h^{\mathrm{obs}}(\mathbf{r}_i) - h(\mathbf{r}_i)) - \int_\Omega \frac{\partial \Phi}{\partial \mu_{\mathrm{a}}^i}\mu_{\mathrm{a}}(h^{\mathrm{obs}} - h)\,\mathrm{d}\Omega. \tag{4.6}$$

Recall that the time-independent RTE is given by

$$(\hat{\mathbf{s}}\cdot\nabla + \mu_{\mathrm{a}}(\mathbf{r}) + \mu_{\mathrm{s}}(\mathbf{r}))\phi(\mathbf{r},\hat{\mathbf{s}}) = \mu_{\mathrm{s}}(\mathbf{r})\int_{S^{n-1}} \Theta(\hat{\mathbf{s}},\hat{\mathbf{s}}')\phi(\mathbf{r},\hat{\mathbf{s}}')\,\mathrm{d}\hat{\mathbf{s}}' + q(\mathbf{r},\hat{\mathbf{s}}). \tag{4.7}$$

The sensitivity of the fluence Φ to changes in the absorption coefficient can be found by differentiating the Equation 4.7 with respect to μ_{a}^i, which yields

$$(\hat{\mathbf{s}}\cdot\nabla+\mu_{\mathrm{a}}+\mu_{\mathrm{s}})\frac{\partial\phi}{\partial\mu_{\mathrm{a}}^i}-\mu_{\mathrm{s}}\int_{S^{n-1}}\Theta(\hat{\mathbf{s}},\hat{\mathbf{s}}')\frac{\partial\phi(\hat{\mathbf{s}}')}{\partial\mu_{\mathrm{a}}^i}\,\mathrm{d}\hat{\mathbf{s}}'=-\phi(\hat{\mathbf{s}})\delta(\mathbf{r}-\mathbf{r}_i). \tag{4.8}$$

An adjoint model may now be introduced to assist the gradient calculation. The adjoint model is defined by

$$(-\hat{\mathbf{s}}\cdot\nabla+\mu_{\mathrm{a}}+\mu_{\mathrm{s}})\phi^*(\hat{\mathbf{s}})-\mu_{\mathrm{s}}\int_{S^{n-1}}\Theta(\hat{\mathbf{s}},\hat{\mathbf{s}}')\phi^*(\hat{\mathbf{s}}')\mathrm{d}\hat{\mathbf{s}}'=\mu_{\mathrm{a}}(h^{\mathrm{obs}}-h), \tag{4.9}$$

and has solution ϕ^*, the adjoint radiance. Evaluating $\phi^*\times$(4.8) $-(\partial\phi/\partial\mu_{\mathrm{a}}^i)\times$(4.9) yields

$$\begin{aligned}
&\phi^*(\hat{\mathbf{s}})(\hat{\mathbf{s}}\cdot\nabla)\frac{\partial\phi(\hat{\mathbf{s}})}{\partial\mu_{\mathrm{a}}^i}+\frac{\partial\phi(\hat{\mathbf{s}})}{\partial\mu_{\mathrm{a}}^i}(\hat{\mathbf{s}}\cdot\nabla)\phi^*(\hat{\mathbf{s}})\\
&\quad-\phi^*(\hat{\mathbf{s}})\mu_{\mathrm{s}}\int_{S^{n-1}}\Theta(\hat{\mathbf{s}},\hat{\mathbf{s}}')\frac{\partial\phi(\hat{\mathbf{s}}')}{\partial\mu_{\mathrm{a}}^i}\,\mathrm{d}\hat{\mathbf{s}}'+\frac{\partial\phi(\hat{\mathbf{s}})}{\partial\mu_{\mathrm{a}}^i}\mu_{\mathrm{s}}\int_{S^{n-1}}\Theta(\hat{\mathbf{s}},\hat{\mathbf{s}}')\phi^*(\hat{\mathbf{s}}')\,\mathrm{d}\hat{\mathbf{s}}'\\
&\quad=-\phi^*(\hat{\mathbf{s}})\phi(\hat{\mathbf{s}})\delta(\mathbf{r}-\mathbf{r}_i)-\frac{\partial\phi(\hat{\mathbf{s}})}{\partial\mu_{\mathrm{a}}^i}\mu_{\mathrm{a}}(h^{\mathrm{obs}}-h).
\end{aligned} \tag{4.10}$$

This equation is reduced significantly when it is noted that the left-hand side equates to zero. To see this, first integrate over all angles $\hat{\mathbf{s}}\in S^{n-1}$ and also over the volume Ω with surface $\partial\Omega$ to obtain

$$\begin{aligned}
&\int_\Omega\int_{S^{n-1}}\phi^*(\hat{\mathbf{s}})(\hat{\mathbf{s}}\cdot\nabla)\frac{\partial\phi(\hat{\mathbf{s}})}{\partial\mu_{\mathrm{a}}^i}\,\mathrm{d}\hat{\mathbf{s}}\,\mathrm{d}\Omega+\int_\Omega\int_{S^{n-1}}\frac{\partial\phi(\hat{\mathbf{s}})}{\partial\mu_{\mathrm{a}}^i}(\hat{\mathbf{s}}\cdot\nabla)\phi^*(\hat{\mathbf{s}})\,\mathrm{d}\hat{\mathbf{s}}\,\mathrm{d}\Omega\\
&\quad-\int_\Omega\mu_{\mathrm{s}}\int_{S^{n-1}}\phi^*(\hat{\mathbf{s}})\int_{S^{n-1}}\Theta(\hat{\mathbf{s}},\hat{\mathbf{s}}')\frac{\partial\phi(\hat{\mathbf{s}}')}{\partial\mu_{\mathrm{a}}^i}\,\mathrm{d}\hat{\mathbf{s}}'\,\mathrm{d}\hat{\mathbf{s}}\,\mathrm{d}\Omega\\
&\quad+\int_\Omega\mu_{\mathrm{s}}\int_{S^{n-1}}\frac{\partial\phi(\hat{\mathbf{s}})}{\partial\mu_{\mathrm{a}}^i}\int_{S^{n-1}}\Theta(\hat{\mathbf{s}},\hat{\mathbf{s}}')\phi^*(\hat{\mathbf{s}}')\,\mathrm{d}\hat{\mathbf{s}}'\,\mathrm{d}\hat{\mathbf{s}}\,\mathrm{d}\Omega\\
&\quad=-\int_\Omega\delta(\mathbf{r}-\mathbf{r}_i)\int_{S^{n-1}}\phi^*(\hat{\mathbf{s}})\phi(\hat{\mathbf{s}})\,\mathrm{d}\hat{\mathbf{s}}\,\mathrm{d}\Omega\\
&\qquad-\int_\Omega\mu_{\mathrm{a}}(h^{\mathrm{obs}}-h)\int_{S^{n-1}}\frac{\partial\phi(\hat{\mathbf{s}})}{\partial\mu_{\mathrm{a}}^i}\,\mathrm{d}\hat{\mathbf{s}}\,\mathrm{d}\Omega.
\end{aligned} \tag{4.11}$$

By using a form of the divergence theorem, given by

$$\int_\Omega ab\cdot\nabla c\,\mathrm{d}\Omega+\int_\Omega cb\cdot\nabla a\,\mathrm{d}\Omega=\int_{\partial\Omega}b\cdot\hat{n}ac\,\mathrm{d}\Omega, \tag{4.12}$$

along with the substitutions

$$a = \phi^*(\hat{\mathbf{s}}), \quad b = \hat{\mathbf{s}} \quad \text{and} \quad c = \frac{\partial \phi(\hat{\mathbf{s}})}{\partial \mu_{\mathrm{a}}^i},$$

the first two terms of (4.11) can be replaced with a single term, since

$$\begin{aligned}
&\int_\Omega \int_{S^{n-1}} \phi^*(\hat{\mathbf{s}})(\hat{\mathbf{s}}\cdot\nabla)\frac{\partial \phi(\hat{\mathbf{s}})}{\partial \mu_{\mathrm{a}}^i}\,\mathrm{d}\hat{\mathbf{s}}\,\mathrm{d}\Omega + \int_\Omega \int_{S^{n-1}} \frac{\partial \phi(\hat{\mathbf{s}})}{\partial \mu_{\mathrm{a}}^i}(\hat{\mathbf{s}}\cdot\nabla)\phi^*(\hat{\mathbf{s}})\,\mathrm{d}\hat{\mathbf{s}}\,\mathrm{d}\Omega \\
&\quad = \int_{\partial\Omega} \int_{S^{n-1}} (\hat{\mathbf{s}}\cdot\hat{\mathbf{n}})\phi^*(\hat{\mathbf{s}})\frac{\partial \phi(\hat{\mathbf{s}})}{\partial \mu_{\mathrm{a}}^i}\,\mathrm{d}\hat{\mathbf{s}}\,\mathrm{d}\Omega. \qquad (4.13)
\end{aligned}$$

Since both $\phi^* \to 0$ and $\partial\phi/\partial\mu_{\mathrm{a}}^i \to 0$ on the boundary $\partial\Omega$, the integrand of this term, and hence the integral, equates to zero. This means that Equation 4.11 reduces to

$$\begin{aligned}
&\int_\Omega \mu_{\mathrm{s}} \int_{S^{n-1}} \phi^*(\hat{\mathbf{s}}) \int_{S^{n-1}} \Theta(\hat{\mathbf{s}},\hat{\mathbf{s}}')\frac{\partial \phi(\hat{\mathbf{s}}')}{\partial \mu_{\mathrm{a}}^i}\,\mathrm{d}\hat{\mathbf{s}}'\,\mathrm{d}\hat{\mathbf{s}}\,\mathrm{d}\Omega \\
&\quad - \int_\Omega \mu_{\mathrm{s}} \int_{S^{n-1}} \frac{\partial \phi(\hat{\mathbf{s}})}{\partial \mu_{\mathrm{a}}^i} \int_{S^{n-1}} \Theta(\hat{\mathbf{s}},\hat{\mathbf{s}}')\phi^*(\hat{\mathbf{s}}')\,\mathrm{d}\hat{\mathbf{s}}'\,\mathrm{d}\hat{\mathbf{s}}\,\mathrm{d}\Omega \\
&\quad = \int_\Omega \delta(\mathbf{r}-\mathbf{r}_i) \int_{S^{n-1}} \phi^*(\hat{\mathbf{s}})\phi(\hat{\mathbf{s}})\,\mathrm{d}\hat{\mathbf{s}}\,\mathrm{d}\Omega \\
&\qquad + \int_\Omega \mu_{\mathrm{a}}(h^{\mathrm{obs}} - h) \int_{S^{n-1}} \frac{\partial \phi(\hat{\mathbf{s}})}{\partial \mu_{\mathrm{a}}^i}\,\mathrm{d}\hat{\mathbf{s}}\,\mathrm{d}\Omega. \qquad (4.14)
\end{aligned}$$

The left-hand side of this equation can be rearranged as

$$\begin{aligned}
&\int_\Omega \mu_{\mathrm{s}} \int_{S^{n-1}} \int_{S^{n-1}} \Theta(\hat{\mathbf{s}},\hat{\mathbf{s}}')\phi^*(\hat{\mathbf{s}})\frac{\partial \phi(\hat{\mathbf{s}}')}{\partial \mu_{\mathrm{a}}^i}\,\mathrm{d}\hat{\mathbf{s}}'\,\mathrm{d}\hat{\mathbf{s}}\,\mathrm{d}\Omega \\
&\quad - \int_\Omega \mu_{\mathrm{s}} \int_{S^{n-1}} \int_{S^{n-1}} \Theta(\hat{\mathbf{s}},\hat{\mathbf{s}}')\phi^*(\hat{\mathbf{s}}')\frac{\partial \phi(\hat{\mathbf{s}})}{\partial \mu_{\mathrm{a}}^i}\,\mathrm{d}\hat{\mathbf{s}}'\,\mathrm{d}\hat{\mathbf{s}}\,\mathrm{d}\Omega. \qquad (4.15)
\end{aligned}$$

Since Θ is a symmetric function, that is, $\Theta(\hat{\mathbf{s}},\hat{\mathbf{s}}') = \Theta(\hat{\mathbf{s}}',\hat{\mathbf{s}})$, these two terms equate to zero. Equation 4.14 therefore reduces to

$$\int_\Omega \mu_{\mathrm{a}}(h^{\mathrm{obs}} - h) \int_{S^{n-1}} \frac{\partial \phi(\hat{\mathbf{s}})}{\partial \mu_{\mathrm{a}}^i}\,\mathrm{d}\hat{\mathbf{s}}\,\mathrm{d}\Omega = -\int_\Omega \delta(\mathbf{r}-\mathbf{r}_i) \int_{S^{n-1}} \phi^*(\hat{\mathbf{s}})\phi(\hat{\mathbf{s}})\,\mathrm{d}\hat{\mathbf{s}}\,\mathrm{d}\Omega. \quad (4.16)$$

The fluence Φ is equal to the integral over all directions $\hat{\mathbf{s}}$ of the time-integrated radiance ϕ, that is,

$$\Phi(\mathbf{r}) = \int_{S^{n-1}} \phi(\mathbf{r},\hat{\mathbf{s}})\mathrm{d}\hat{\mathbf{s}}. \qquad (4.17)$$

It therefore follows that

$$\frac{\partial \Phi}{\partial \mu_{\mathrm{a}}^i} = \int_{S^{n-1}} \frac{\partial \phi(\hat{\mathbf{s}})}{\partial \mu_{\mathrm{a}}^i} \mathrm{d}\hat{\mathbf{s}}, \tag{4.18}$$

and hence Equation 4.16 can be written as

$$\int_\Omega \frac{\partial \Phi}{\partial \mu_{\mathrm{a}}^i} \mu_{\mathrm{a}} (h^{\mathrm{obs}} - h) \, \mathrm{d}\Omega = -\left[\int_{S^{n-1}} \phi^*(\hat{\mathbf{s}}) \phi(\hat{\mathbf{s}}) \, \mathrm{d}\hat{\mathbf{s}} \right]_{\mathbf{r}=\mathbf{r}_i}. \tag{4.19}$$

The left-hand side of this equation is exactly the last term in Equation 4.6. If Equation 4.19 is substituted here, the expression for the absorption gradient becomes

$$\frac{\partial \varepsilon}{\partial \mu_{\mathrm{a}}^i} = -\Phi(\mathbf{r}_i)(h^{\mathrm{obs}}(\mathbf{r}_i) - h(\mathbf{r}_i)) + \left[\int_{S^{n-1}} \phi^*(\hat{\mathbf{s}}) \phi(\hat{\mathbf{s}}) \, \mathrm{d}\hat{\mathbf{s}} \right]_{\mathbf{r}=\mathbf{r}_i}. \tag{4.20}$$

It then follows that, in general, the functional gradient is given by

$$\frac{\partial \varepsilon}{\partial \mu_{\mathrm{a}}} = -\Phi(h^{\mathrm{obs}} - h) + \int_{S^{n-1}} \phi^*(\hat{\mathbf{s}}) \phi(\hat{\mathbf{s}}) \, \mathrm{d}\hat{\mathbf{s}}. \tag{4.21}$$

4.1.4 Implementation

When implementing the minimisation, the formulation of the numerical light model must be accounted for, and the continuous gradient calculations should be transferred to their discrete counterparts. The implementation of the RTE follows the FE implementation found in [73]. The domain is triangulated to form a mesh consisting of structured triangular elements, the vertices of which are called the mesh nodes. Some quantities, such as the absorption and scattering coeffients, are best described as being piecewise continuous over the mesh elements. The superscript $(\cdot)^e$ will be used to denote definition of a quantity on the mesh elements, while $(\cdot)^h$ will denote definition on the mesh nodes. The absorption and scattering coefficients will be considered to be piecewise constant on

the elements of the computational mesh, and can hence be written as

$$\mu_{\mathrm{a}}(\mathbf{r}) \approx \mu_{\mathrm{a}}^{e}(\mathbf{r}) = \sum_{k=1}^{N_e} \mu_{\mathrm{a}}^{k} \chi_k(\mathbf{r}), \quad \mu_{\mathrm{s}}(\mathbf{r}) \approx \mu_{\mathrm{s}}^{e}(\mathbf{r}) = \sum_{k=1}^{N_e} \mu_{\mathrm{s}}^{k} \chi_k(\mathbf{r}), \tag{4.22}$$

where N_e is the number of elements in the computational mesh and χ_k is the characteristic function of element k, which is equal to 1 in the support of element k and 0 elsewhere. In the FE formulation of the time-integrated RTE, its solution ϕ is approximated by

$$\phi(\mathbf{r}, \hat{\mathbf{s}}) \approx \phi^{h}(\mathbf{r}, \hat{\mathbf{s}}) = \sum_{j=1}^{N_n} \sum_{l=1}^{N_a} \phi_{jl} \psi_j(\mathbf{r}) \psi_l(\hat{\mathbf{s}}), \tag{4.23}$$

where N_n is the number of spatial nodes in the computational mesh and N_a is the number of angular directions. ϕ_{jl} represents the radiance and $\psi_j(\mathbf{r})$ and $\psi_l(\hat{\mathbf{s}})$ the nodal basis functions of the spatial and angular FE meshes, respectively, in the nodal point j and direction l. The FE RTE model calculates the radiance ϕ by solving

$$A\phi^{h} = b, \tag{4.24}$$

where A is the FE system matrix representing the terms in the RTE and b is the source term. The matrix A can be written as

$$A = A_1 + A_2 + A_3 + A_4, \tag{4.25}$$

where $A_{1,\ldots,4}$ have been obtained by determining a variational formulation of the RTE and making a finite dimensional approximation to this variational formulation, constructed using piecewise linear bases for both the spatial and angular discretisations.

The components of A are given by

$$A_1 = -\int_\Omega \int_{S^{n-1}} \hat{\mathbf{s}} \cdot \nabla \psi_{j'}(\mathbf{r}) \psi_{l'}(\hat{\mathbf{s}}) \psi_l(\hat{\mathbf{s}}) \, \mathrm{d}\hat{\mathbf{s}} \; \psi_j(\mathbf{r}) \, \mathrm{d}\mathbf{r}, \tag{4.26}$$

$$A_2 = \int_{\partial\Omega} \psi_j(\mathbf{r}) \psi_{j'}(\mathbf{r}) \, \mathrm{d}S \int_{S^{n-1}} (\hat{\mathbf{s}} \cdot \hat{\mathbf{n}})_+ \psi_l(\hat{\mathbf{s}}) \psi_{l'}(\hat{\mathbf{s}}) \, \mathrm{d}\hat{\mathbf{s}}, \tag{4.27}$$

$$A_3 = \int_\Omega (\mu_\mathrm{a}^e(\mathbf{r}) + \mu_\mathrm{s}^e(\mathbf{r})) \psi_j(\mathbf{r}) \psi_{j'}(\mathbf{r}) \, \mathrm{d}\mathbf{r} \int_{S^{n-1}} \psi_l(\hat{\mathbf{s}}) \psi_{l'}(\hat{\mathbf{s}}) \, \mathrm{d}\hat{\mathbf{s}}, \tag{4.28}$$

$$A_4 = -\int_\Omega \mu_\mathrm{s}^e(\mathbf{r}) \psi_j(\mathbf{r}) \psi_{j'}(\mathbf{r}) \, \mathrm{d}\mathbf{r} \int_{S^{n-1}} \int_{S^{n-1}} \Theta(\hat{\mathbf{s}}, \hat{\mathbf{s}}') \psi_l(\hat{\mathbf{s}}') \, \mathrm{d}\hat{\mathbf{s}}' \; \psi_{l'}(\hat{\mathbf{s}}) \, \mathrm{d}\hat{\mathbf{s}}. \tag{4.29}$$

The fluence Φ^e is equal to the integral of the radiance over all directions, and can therefore be calculated from

$$\Phi^e = M\phi^h, \tag{4.30}$$

where M is a measurement matrix which performs the summation over the angular directions. The measurement matrix also has the effect of expressing the fluence as piecewise constant over the mesh elements; its value over a single element is the average of its value at each node attached to that element. This average is taken because the absorbed energy is the product of the absorption coefficient and the fluence, with

$$h^e = \mu_\mathrm{a}^e \Phi^e, \tag{4.31}$$

and since the absorption coefficient is piecewise constant over the mesh elements it is not defined at element boundaries, and hence not at the mesh nodes. Another way to overcome this problem would be to express the absorption coefficient using nodal basis functions. While this is not explored here, we will look at defining all quantities this way later in Chapter 6. For notational convenience we will now drop the superscripts and write $\mu_\mathrm{a} = \mu_\mathrm{a}^e$, $\mu_\mathrm{s} = \mu_\mathrm{s}^e$, $\phi = \phi^e$, $\Phi = \Phi^e$ and $h = h^e$.

Using this implementation, the least-squares error functional (Equation 4.1) can be written in vector notation as

$$\varepsilon(\mu_{\mathrm{a}}) = \frac{1}{2}(h^{\mathrm{obs}} - h)^{\mathrm{T}}(h^{\mathrm{obs}} - h), \tag{4.32}$$

and its derivative with respect to μ_{a}^k, the absorption over the k^{th} element, as

$$\begin{aligned}
\frac{\partial \varepsilon}{\partial \mu_{\mathrm{a}}^k} &= -\left(\frac{\partial h}{\partial \mu_{\mathrm{a}}^k}\right)^{\mathrm{T}} (h^{\mathrm{obs}} - h) \\
&= -\left(\mu_{\mathrm{a}} \frac{\partial \Phi}{\partial \mu_{\mathrm{a}}^k} + \frac{\partial \mu_{\mathrm{a}}}{\partial \mu_{\mathrm{a}}^k}\Phi\right)^{\mathrm{T}} (h^{\mathrm{obs}} - h) \\
&= -\left(\mu_{\mathrm{a}} M \frac{\partial \phi}{\partial \mu_{\mathrm{a}}^k} + \frac{\partial \mu_{\mathrm{a}}}{\partial \mu_{\mathrm{a}}^k}\Phi\right)^{\mathrm{T}} (h^{\mathrm{obs}} - h) \\
&= \left(\frac{\partial \mu_{\mathrm{a}}}{\partial \mu_{\mathrm{a}}^k}\Phi\right)^{\mathrm{T}} (h^{\mathrm{obs}} - h) - \left(\mu_{\mathrm{a}} M \frac{\partial \phi}{\partial \mu_{\mathrm{a}}^k}\right)^{\mathrm{T}} (h^{\mathrm{obs}} - h).
\end{aligned} \tag{4.33}$$

The sensitivity of the radiance to changes in the absorption coefficient is found by differentiating Equation 4.24 with respect to μ_{a}^k. Applying the product rule, we obtain

$$\begin{aligned}
\frac{\partial A}{\partial \mu_{\mathrm{a}}^k}\phi + A\frac{\partial \phi}{\partial \mu_{\mathrm{a}}^k} &= 0 \\
\Rightarrow \frac{\partial \phi}{\partial \mu_{\mathrm{a}}^k} &= -A^{-1}\left(\frac{\partial A}{\partial \mu_{\mathrm{a}}^k}\right)\phi.
\end{aligned} \tag{4.34}$$

Substituting this into Equation 4.33 then gives

$$\frac{\partial \varepsilon}{\partial \mu_{\mathrm{a}}^k} = \left(\mu_{\mathrm{a}} M A^{-1}\left(\frac{\partial A}{\partial \mu_{\mathrm{a}}^k}\right)\phi\right)^{\mathrm{T}} (h^{\mathrm{obs}} - h) - \left(\frac{\partial \mu_{\mathrm{a}}}{\partial \mu_{\mathrm{a}}^k}\Phi\right)^{\mathrm{T}} (h^{\mathrm{obs}} - h), \tag{4.35}$$

where $\partial A/\partial \mu_{\mathrm{a}}^k$ is the gradient of the FE system matrix, given by Equation 4.25, with respect to the absorption coefficient. For each element $k = 1, \ldots, N_e$, this is the single term

$$\frac{\partial A}{\partial \mu_{\mathrm{a}}^k} = \int_{\Omega} \chi_k(\mathbf{r})\psi_j(\mathbf{r})\psi_{j'}(\mathbf{r})\,\mathrm{d}\mathbf{r} \int_{S^{n-1}} \psi_l(\hat{\mathbf{s}})\psi_{l'}(\hat{\mathbf{s}})\,\mathrm{d}\hat{\mathbf{s}}. \tag{4.36}$$

Applying the following property for the transpose of the product of i arbitrary matrices

$$(A_1 A_2 \dots A_i)^{\mathrm{T}} = A_i^{\mathrm{T}} \dots A_2^{\mathrm{T}} A_1^{\mathrm{T}} \tag{4.37}$$

to Equation 4.35 gives

$$\frac{\partial \varepsilon}{\partial \mu_{\mathrm{a}}^k} = \phi^{\mathrm{T}} \left(\frac{\partial A}{\partial \mu_{\mathrm{a}}^k} \right)^{\mathrm{T}} (A^{-1})^{\mathrm{T}} (\mu_{\mathrm{a}} M)^{\mathrm{T}} (h^{\mathrm{obs}} - h) - \Phi^{\mathrm{T}} \left(\frac{\partial \mu_{\mathrm{a}}}{\partial \mu_{\mathrm{a}}^k} \right)^{\mathrm{T}} (h^{\mathrm{obs}} - h), \tag{4.38}$$

and since A^{-1} is a symmetric matrix, $(A^{-1})^{\mathrm{T}} = (A^{\mathrm{T}})^{-1}$, and so

$$\frac{\partial \varepsilon}{\partial \mu_{\mathrm{a}}^k} = \phi^{\mathrm{T}} \left(\frac{\partial A}{\partial \mu_{\mathrm{a}}^k} \right)^{\mathrm{T}} (A^{\mathrm{T}})^{-1} (\mu_{\mathrm{a}} M)^{\mathrm{T}} (h^{\mathrm{obs}} - h) - \Phi^{\mathrm{T}} \left(\frac{\partial \mu_{\mathrm{a}}}{\partial \mu_{\mathrm{a}}^k} \right)^{\mathrm{T}} (h^{\mathrm{obs}} - h). \tag{4.39}$$

The FE RTE adjoint model corresponding to Equation 4.9 is given by

$$A^{\mathrm{T}} \phi^* := (\mu_{\mathrm{a}} M)^{\mathrm{T}} (h^{\mathrm{obs}} - h), \tag{4.40}$$

which we can substitute into Equation 4.39 to obtain

$$\frac{\partial \varepsilon}{\partial \mu_{\mathrm{a}}^k} = \phi^{\mathrm{T}} \left(\frac{\partial A}{\partial \mu_{\mathrm{a}}^k} \right)^{\mathrm{T}} \phi^* - \Phi^{\mathrm{T}} \left(\frac{\partial \mu_{\mathrm{a}}}{\partial \mu_{\mathrm{a}}^k} \right)^{\mathrm{T}} (h^{\mathrm{obs}} - h), \tag{4.41}$$

and so generally

$$\frac{\partial \varepsilon}{\partial \mu_{\mathrm{a}}} = \phi^{\mathrm{T}} \left(\frac{\partial A}{\partial \mu_{\mathrm{a}}} \right)^{\mathrm{T}} \phi^* - \Phi^{\mathrm{T}} (h^{\mathrm{obs}} - h). \tag{4.42}$$

This expression enables the functional gradient with respect to absorption to be calculated using only one run each of the forward and adjoint models.

4.1.5 Comparison with a finite difference calculation

Finite difference methods are a very accurate and robust way to approximate a derivative. We will therefore check that the above gradient calculations are correct by comparing

them to the derivative of the error functional calculated using a finite difference method. The derivative of the error functional with respect to a change in the absorption coefficient across the k^{th} element can be approximated by

$$\frac{\partial \varepsilon}{\partial \mu_{\text{a}}^k} \approx \frac{\varepsilon(\mu_{\text{a}}^k + \Delta\mu_{\text{a}}) - \varepsilon(\mu_{\text{a}}^k)}{\Delta\mu_{\text{a}}}, \tag{4.43}$$

where $\Delta\mu_{\text{a}}$ is some small, non-zero perturbation to μ_{a} (in this case we chose $\Delta\mu_{\text{a}} = 10^{-5}$ mm^{-1}). To evaluate the error functional due to the perturbed absorption coefficient, the forward RTE model must be solved to obtain the absorbed optical energy evaluated at the perturbed absorption coefficient. This process must be repeated for every element in the computational mesh to build up an image of the absorption gradient across the entire domain. This means that calculating the functional gradient with respect to absorption will require $N_e + 1$ evaluations of the forward model, where N_e is the number of elements in the computational mesh. Because of this, we have used a fairly coarse mesh, containing $N_e = 960$ elements, to perform the finite difference calculation. In practice, the number of mesh elements may be on the order of tens of thousands or more. Furthermore, the gradient of the error functional will need to be evaluated on each iteration of a gradient-based method. Using a finite difference method would therefore make the proposed gradient-based minimisation scheme entirely impractical. This highlights the usefulness of the adjoint-assisted gradient calculation presented in Section 6.2.1 as an efficient way to perform the gradient-based minimisation. Using the adjoint-assisted method, the functional gradient can be calculated using a single run each of the forward and adjoint models. The adjoint model is solved using the same FEM system matrix as the forward model, and so this is equivalent to two evaluations of the forward model.

The absorption and scattering coefficients and simulated absorbed energy distribution used in Section 3.3.3.1 (and shown in Figure 3.4) were used to calculate the gradients. The optical absorption coefficient consists of a homogeneous background of 0.01 mm^{-1} with two square absorbing inclusions with values of 0.2 mm^{-1} and 0.3 mm^{-1}. The optical scattering coefficient consists of a homogeneous background of 5 mm^{-1} with two square absorbing inclusions with values of 10 mm^{-1} and 15 mm^{-1}. Given these

absorption and scattering coefficients, the FE RTE model can be used to create a set of simulated PAT images which we will refer to as the measured data. Once this measured data h^{obs} has been simulated, an initial guess at the absorption and scattering can be made and used to simulate the absorbed energy h based on this initial guess. Here, initial guesses of homogeneous absorption and scattering coefficients set at their respective background values have been used. Now that we have measured data h^{obs} and an initial estimate h, the error functional 4.1 can then be calculated straightforwardly. The error functional gradient with respect to the absorption coefficient is then calculated using the adjoint-assisted method described in Section 4.1.3 and compared to the resulting functional gradient calculated using a finite difference method.

FIGURE 4.1: Error functional gradient with respect to absorption calculated using the adjoint-assisted method presented in Section 4.1.3, compared with those calculated using a finite difference method. The absorption and scattering coefficients are both heterogeneous and can be seen in , and the four source geometries are shown in . These give rise to a set of four measured absorbed energy images. Given an initial guess at the absorption coefficient, the error functional 4.1 can be calculated straightforwardly. The functional gradient with respect to absorption can then be calculated using the adjoint-assisted method (Equation 4.21) and also using a finite difference method. The figure below shows the functional gradient with respect to absorption calculated using (A) the adjoint-assisted method and (B) a finite difference method. The difference between the two is shown in (C) and a profile in the z-direction at $x = 1$ mm can be seen in (D).

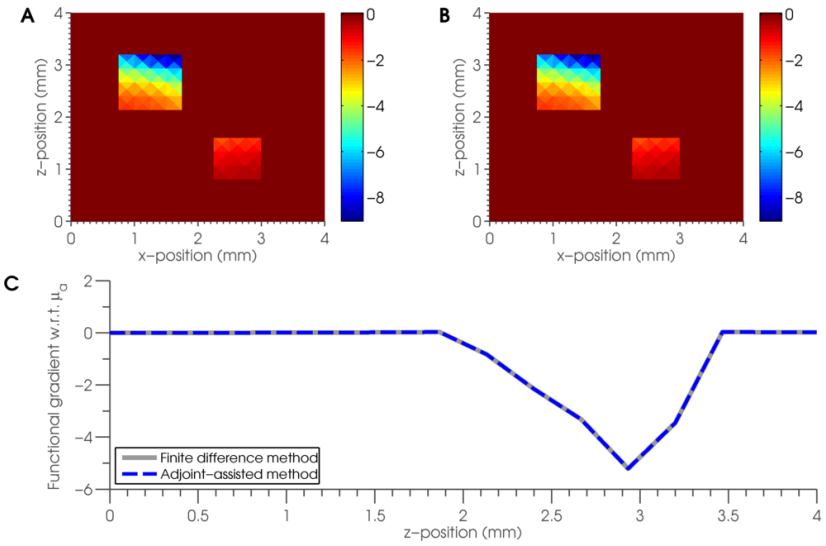

The results of these calculations are shown in Figure 4.1. Figure 4.1(A) shows the absorption gradient calculated using the adjoint-assisted method, and Figure 4.1(B) shows the absorption gradient calculated using a finite difference method. There is

excellent agreement between the two figures, which can be seen in the profile comparison in Figure 4.1(C). The relative error between the two methods can be calculated using

$$\varepsilon_{\mathrm{a}} = \frac{\left\| \left(\frac{\partial \varepsilon}{\partial \mu_{\mathrm{a}}}\right)_{\mathrm{FD}} - \left(\frac{\partial \varepsilon}{\partial \mu_{\mathrm{a}}}\right)_{\mathrm{adj}} \right\|}{\left\| \left(\frac{\partial \varepsilon}{\partial \mu_{\mathrm{a}}}\right)_{\mathrm{FD}} \right\|}, \tag{4.44}$$

where $(\partial\varepsilon/\partial\mu_{\mathrm{a}})_{\mathrm{FD}}$ and $(\partial\varepsilon/\partial\mu_{\mathrm{a}})_{\mathrm{adj}}$ are the functional gradients with respect to absorption calculated using the finite difference method and adjoint-assisted method, respectively. The error in this case was $\varepsilon_{\mathrm{a}} = 1.08 \times 10^{-4}$. Even for this small example, the advantages of using the adjoint-assisted method are clear; the finite difference calculation took approximately 43 minutes, compared with under 3 seconds to complete the adjoint-assisted method.

4.2 Numerical examples to recover absorption

In this section, the adjoint-assisted gradient-based method based on the RTE will be tested using 2D simulated PAT images. In Section 4.2.2, it is first assumed that the scattering coefficient is known, and we will look to recover a quantitatively accurate estimate of the absorption coefficient. The method will be tested using several different illumination positions and geometries, and the effects of including additive Gaussian noise to the simulated measurement data will be investigated. Section 4.2.4 will look at the sensitivity of the error in the absorption reconstruction to the initial guess at the absorption coefficient. Section 4.2.6 investigates the extent to which we can recover the absorption coefficient can be recovered when the scattering is unknown. In this case, it is assumed that the scattering coefficient is constant and fixed at an estimated value. Section 4.2.5 will look at the sensitivity of errors in the absorption estimate to the estimate of the scattering coefficient.

4.2.1 Simulation of measurement data

The gradient-based inversion will be performed using a variety of different source positions and geometries. Figures 4.2 and 4.3 show the six different source combinations used in Sections 4.2.2 and 4.2.6.

FIGURE 4.2: Multiple illumination positions from several different source geometries are used to investigate the performance of the gradient-based inversion method. In this section, the method will be tested using PAT images which have been simulated using a single point source, two point sources, and four point sources, placed in the positions shown by the red circles in the figure below.

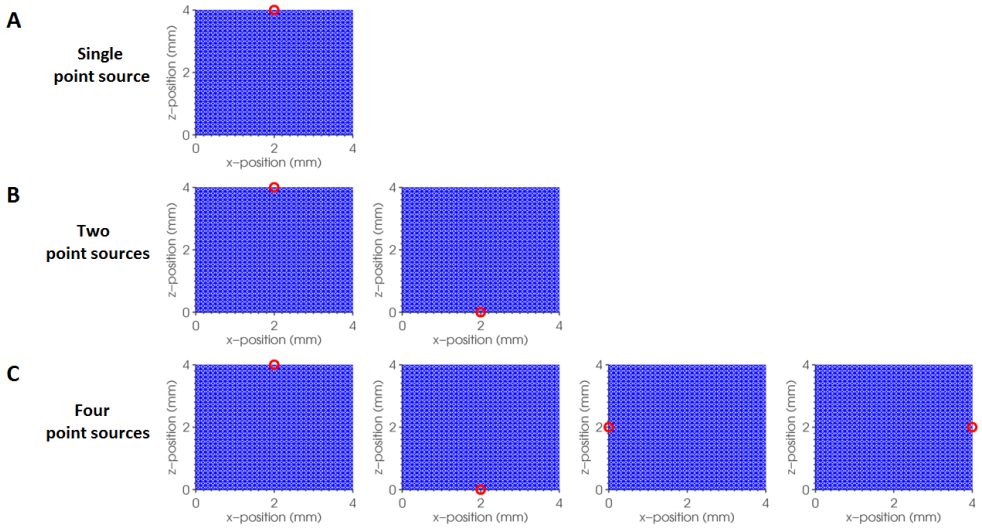

The optical coefficients are the same as those used to verify the gradients, and were defined in Section 3.3.3.1 and shown in Figures 3.4(A) and 3.4(B). As a reminder, the computational mesh was the 4 mm $\times$ 4 mm square $[0,4] \times [0,4]$ mm^2, consisting of $N_e = 3840$ triangular elements, $N_n = 1983$ nodes and an angular discretisation of $N_a = 16$ equal angles. The anisotropy factor was considered to be known and constant at $g = 0.8$, and the scattering coefficient μ_s was chosen such that $\mu_\mathrm{s}' = \mu_\mathrm{s}(1-g)$ varies between 1 mm^{-1} and 3 mm^{-1}, giving a background value of $\mu_\mathrm{s}^\mathrm{bg} = 5$ mm^{-1} and two non-smooth scattering inclusions of $\mu_\mathrm{s}^1 = 10$ mm^{-1} and $\mu_\mathrm{s}^2 = 15$ mm^{-1}. The absorption coefficient had a background value of $\mu_\mathrm{a}^\mathrm{bg} = 0.01$ mm^{-1} and two non-smooth absorbing inclusions of $\mu_\mathrm{a}^1 = 0.2$ mm^{-1} and $\mu_\mathrm{a}^2 = 0.3$ mm^{-1}. By solving Equation 4.24, the FE implementation of the RTE, using these coefficients and a particular source b, we obtain

the radiance $\phi = \phi(\mu_{\mathrm{a}}, \mu_{\mathrm{s}})$, and summing over all angles according to Equation 4.30 gives the fluence $\Phi(\mu_{\mathrm{a}}, \mu_{\mathrm{s}})$. The measured absorbed energy is then equal to the product of the absorption coefficient and the fluence, that is, $h^{\mathrm{obs}} = \mu_{\mathrm{a}}\Phi(\mu_{\mathrm{a}}, \mu_{\mathrm{s}})$. Noise can be added to this absorbed energy distribution to simulate the measurement noise which would be present in real photoacoustic data.

FIGURE 4.3: Multiple illumination positions from several different source geometries are used to investigate the performance of the gradient-based inversion method. In this section, the method will be tested using PAT images which have been simulated using a single line source, two line sources, and four line sources, placed in the positions shown by the red circles in the figure below.

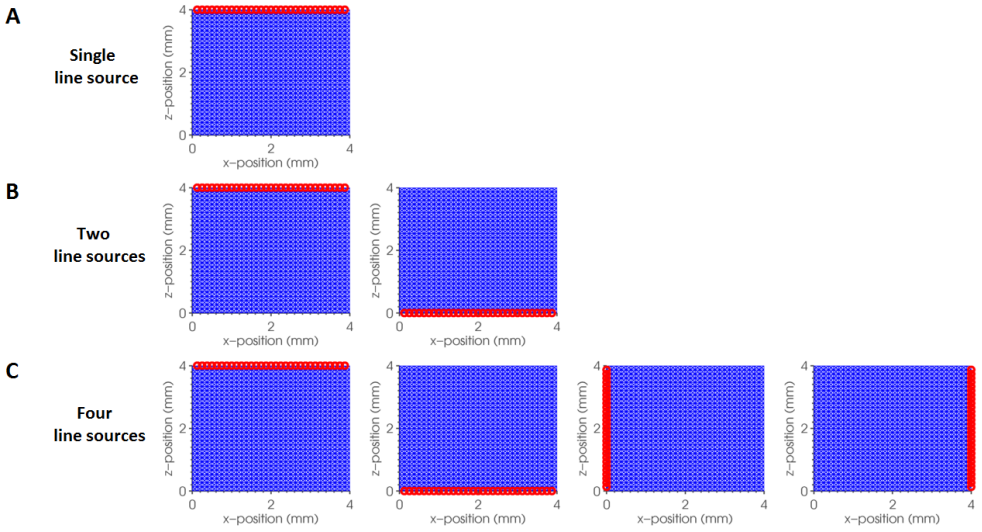

To perform the inversion, the functional gradients calculated in Section 4.1.3 are used in a quasi-Newton method. A quasi-Newton method well-suited to large-scale problems is the limited-memory BFGS method (l-BFGS), since it only requires a moderate amount of memory. The BFGS and l-BFGS methods are memory efficient since they never evaluate the Hessian directly and never have to store or invert it. Instead, an approximation to the inverse Hessian is iteratively improved using information about the gradient at each of the previous iteration steps. In the l-BFGS method, the user can define the number of previous steps used to inform the inverse Hessian approximation. Here, 15 iterations were stored according to advice found in [95]. To recover the optical coefficients, we first start with an initial guess. In this case, the background values of the coefficients were used, which are $\mu_a^{\mathrm{bg}} = 0.01$ mm^{-1} and $\mu_s^{\mathrm{bg}} = 5$ mm^{-1}. This initial approximation

to (μ_a, μ_s) is then passed to the l-BFGS method, which uses the error functional and the functional gradients to calculate an improved approximation. This is done by incrementally changing the approximation to (μ_a, μ_s) based on the gradient information and re-evaluating the model until the error functional has been reduced. This process is repeated until the value of the error functional falls below a user-defined tolerance. In this case the condition for terminating the iterative procedure was a change in ε less than 10^{-9} times its value due to the initial guess.

4.2.2 Inversions with known scattering

In these examples we will use the adjoint-assisted, gradient-based method proposed in Section 4.1.3 to obtain a quantitative estimate of the absorption coefficient given that the scattering is known *a priori*. To quantify the error in the reconstructions, we shall look at the percent relative error ϵ_{a}, which is calculated using

$$\epsilon_{\mathrm{a}} = \frac{\left\|\mu_{\mathrm{a}}^{\mathrm{true}} - \mu_{\mathrm{a}}^{\mathrm{approx}}\right\|}{\left\|\mu_{\mathrm{a}}^{\mathrm{true}}\right\|}, \tag{4.45}$$

where $\mu_{\mathrm{a}}^{\mathrm{true}}$ and $\mu_{\mathrm{a}}^{\mathrm{approx}}$ are the true and reconstructed absorption coefficients, respectively. We will begin by looking at the simplest case, where a single, collimated point source, placed at the centre of the top boundary of the domain, is used to illuminate the domain and simulate a PAT image. This source geometry can be seen in Figure 4.2(A).

4.2.2.1 Single point source

In this example we attempt to recover the absorption coefficient μ_{a} from a single PA image, which has been simulated using a numerical light model, as described in Section 4.2.1. The domain was illuminated using a single collimated point source at the centre of the top boundary (see Figure 4.2(A)). Using the error functional gradient calculated in Section 4.1.3, the limited-memory BFGS method was applied to the noise-free absorbed energy image and an estimate of the optical absorption coefficient was

obtained. The method was also applied to a noisy version of the image, which included additive Gaussian noise scaled to 5% of the mean absorbed energy. Figure 4.4 shows the recovered absorption coefficients after 874 iterations. Figure 4.4(A) shows the true absorption coefficient which is to be reconstructed. Figure 4.4(B) shows the reconstructed μ_{a} when using a noise-free absorbed energy image as the measurement data, and Figure 4.4(C) shows the μ_{a} reconstruction from the measurement data with added Gaussian noise. Figure 4.4(D) shows a profile through the x-direction at $z = 1.2$ mm comparing the true absorption, noise-free reconstruction and noisy reconstruction. The profile runs through the stronger absorbing of the two heterogeneities, which is furthest from the source. Figure 4.4(E) shows the per cent relative error in absorption, calculated using Equation 4.45, for each iteration of the l-BFGS method.

FIGURE 4.4: Reconstructed absorption coefficient when the scattering is known *a priori*. The domain was illuminated using a single point source, corresponding to Figure 4.2(A). (A) shows the true absorption coefficient, (B) shows the reconstructed absorption coefficient from noise-free data, and (C) shows the reconstructed absorption coefficient from data with 5% additive Gaussian noise. A profile comparison can be seen in (D), which compares the true absorption coefficient (grey solid), reconstructed absorption coefficient from noise-free data (blue dashed) and reconstructed absorption coefficient from noisy data (red dotted). The profile is taken in the x-direction at $z = 1.2$ mm. The percent relative error of the reconstructed absorption coefficients at each iteration can be seen in (E).

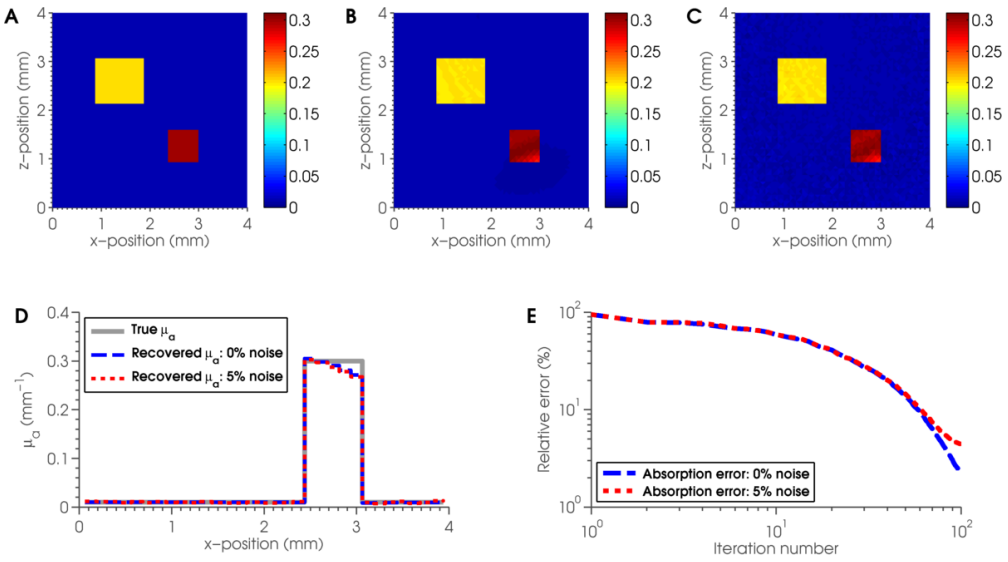

The percent relative error in the reconstructed absorption coefficient after 100 iterations were $\epsilon_{\mathrm{a}} = 2.24\%$ and $\epsilon_{\mathrm{a}} = 4.45\%$ for the noise-free and noisy cases, respectively. In both

the noise-free and noisy cases an accurate estimate of μ_{a} can be obtained, though errors appear in the absorbing heterogeneity farthest from the source, towards the $z = 0$ mm boundary. Figure 4.4(D) shows the underestimation of the absorption coefficient in this area. This is likely to be due to the fact that the signal-to-noise ratio is low in these areas. Figure 4.4(E) shows the percent relative error against iteration number, where it can be seen that the absorption reconstruction has not yet converged to a solution in either the noisy or noise-free case. The reconstruction may therefore improve if the number of iterations were to be increased. In the next section we will investigate whether accuracy in the reconstructions can be improved by increasing the number of sources along the top boundary, thereby increasing the signal to noise.

4.2.2.2 Single line source

The previous example demonstrated that the gradient-based method using the RTE, when using data generated from a single point source, can produce reasonably accurate reconstructions of μ_{a}, though the presence of noise in the measured data affects the reconstruction significantly, and a large number of iterations may be required even in the case of noise-free data. The accuracy of the reconstruction in the noisy case may be improved with an increase to the signal to noise by using a line array of collimated point sources along the top boundary to simulate the PA image, as in Figure 4.3(A). In this example the same optical coefficients are using to simulate the measured data, but now a line array of sources is used to simulate the measurement data. The simulated PAT images are obtained in the same way as in Section 4.2.2.1, that is, using the method described in Section 4.2.1.

Figure 4.5(A) shows the true absorption coefficient, Figure 4.5(B) and Figure 4.5(C) show the reconstructed absorption coefficients after 80 iterations from noise-free and noisy data, respectively. The percent relative errors of $\epsilon_{\mathrm{a}} = 7.9 \times 10^{-3}$ % and $\epsilon_{\mathrm{a}} = 5.46\%$ when using noise-free and noisy data, respectively. Using the line array of sources, we are able to improve significantly on the results obtained when using a single point source;

FIGURE 4.5: Reconstructed absorption coefficient when the scattering is known *a priori*. The domain was illuminated using a single line source, corresponding to Figure 4.3(A). (A) shows the true absorption coefficient, (B) shows the reconstructed absorption coefficient from noise-free data, and (C) shows the reconstructed absorption coefficient from data with 5% additive Gaussian noise. A profile comparison can be seen in (D), which compares the true absorption coefficient (grey solid), reconstructed absorption coefficient from noise-free data (blue dashed) and reconstructed absorption coefficient from noisy data (red dotted). The profile is taken in the x-direction at $z = 1.2$ mm. The percent relative error of the reconstructed absorption coefficients at each iteration can be seen in (E).

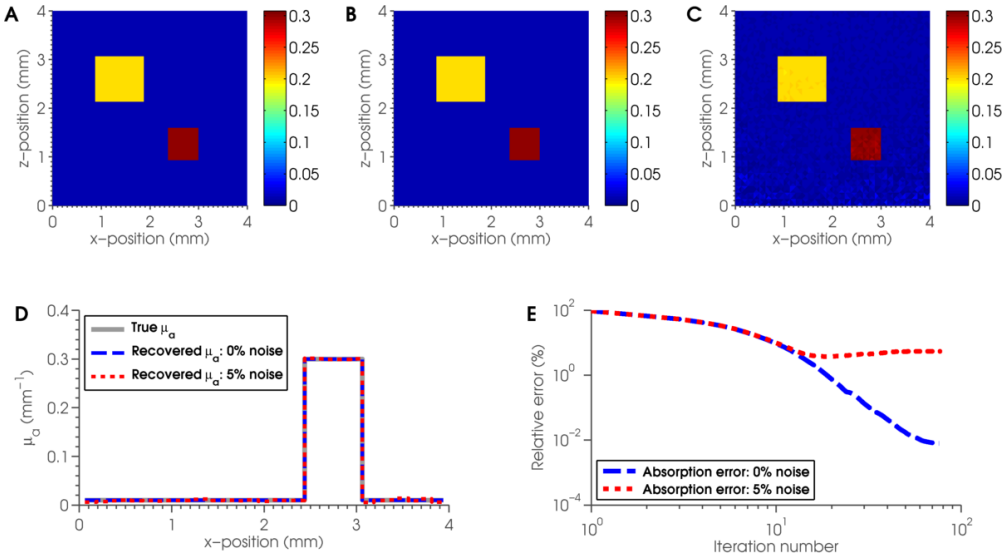

the inaccuracies in the reconstruction at regions far from the source which were present when using a single point source have been significantly improved. Figure 4.5(D) shows a profile comparison of the true absorption and the reconstructed images. In the noisy case, the error using a line source is larger than in the case where a single point source is used. This is perhaps misleading, as Figure 4.5(D) shows that the reconstruction is improved by using the line source. In this case, the errors in the image appear to be due to the amplification of errors due to noise in the inversion, particularly in areas farthest from the source where the signal to noise ratio is relatively low. Figure 4.5(E) shows the per cent relative error in the reconstructions with each iteration of the gradient-based method. Here we can see that the relative error in the reconstruction from noisy data begins to increase slightly after around 20 iterations. The reconstructions in the noisy case may therefore be aided by some appropriate regularisation to reduce the amplification of noise in the inversion.

4.2.3 Extension to multiple illumination directions

The results in Section 4.2.2.2 have demonstrated that the gradient-based method is able to produce accurate quantitative spatial maps of the absorption coefficient μ_{a} from 2D simulated absorbed energy data, even in the presence of 5% additive Gaussian noise. The inclusion of additional sources from the same illumination direction improved the reconstructions significantly when compared to Section 4.2.2.1. Another method that has been suggested to improve the stability of the reconstructions when using the RTE to model the light propagation is to use multiple illuminations directions [34]. In this case, two images illuminated from e.g. two opposite sides of the domain is used as the set of measurement data from which to reconstruct the absorption.

The inclusion of multiple PA images into the inversion requires the summation of the data over the number of sources. If N_s is the number of source positions, then the error functional becomes

$$\varepsilon = \sum_{p=1}^{N_s} \sum_{k=1}^{N_e} \frac{1}{2} (h_p^{\mathrm{obs}}(\mathbf{r}_k) - h_p(\mathbf{r}_k))^2, \tag{4.46}$$

where the subscript $\cdot_p$ denotes the quantity at the p^{th} source position. The error functional gradient must also be summed over the number of source positions, in which case we have

$$\frac{\partial \varepsilon}{\partial \mu_{\mathrm{a}}} = -\sum_{p=1}^{N_s} \Phi_j^{\mathrm{T}} (h_p^{\mathrm{obs}} - h_p) + \sum_{p=1}^{N_s} \phi_p^{\mathrm{T}} \left(\frac{\partial A}{\partial \mu_{\mathrm{a}}} \right)^{\mathrm{T}} \phi_p^*. \tag{4.47}$$

Numerical tests suggest that there is little difference performing the inversion with one image obtained with two simultaneous line sources (e.g. illumination from the top and bottom simultaneously) compared with those using two images (illuminating from the top and bottom separately). This means that information from multiple illumination directions could be incorporated without increasing the number of measurements required.

However, it is worth noting that, if reconstructing both absorption and scattering coefficients, as will be investigated later in Chapter 5, at least two images will be required to ensure a unique solution.

4.2.3.1 Two point sources

This example investigated whether the results in Section 4.2.2.1 can also be improved by including additional information from two simulated PAT images which have been obtained by illuminating the domain from two different directions. The single point source reconstruction in 4.2.2.1 resulted in errors in the reconstruction of μ_{a} at regions farthest from the source. In this example, a second image is obtained by illumination the domain using a point source placed at the opposite side of the computational mesh, at the $z = 0$ mm boundary. The domain is now illuminated using two point sources, as shown in Figure 4.2(B).

FIGURE 4.6: Reconstructed absorption coefficient when the scattering is known *a priori*. Two simulated PAT images were obtained by illuminating the domain using two point sources placed at different positions, corresponding to Figure 4.2(B). (A) shows the true absorption coefficient, (B) shows the reconstructed absorption coefficient from noise-free data, and (C) shows the reconstructed absorption coefficient from data with 5% additive Gaussian noise. A profile comparison can be seen in (D), which compares the true absorption coefficient (grey solid), reconstructed absorption coefficient from noise-free data (blue dashed) and reconstructed absorption coefficient from noisy data (red dotted). The profile is taken in the x-direction at $z = 1.2$ mm. The percent relative error of the reconstructed absorption coefficients at each iteration can be seen in (E).

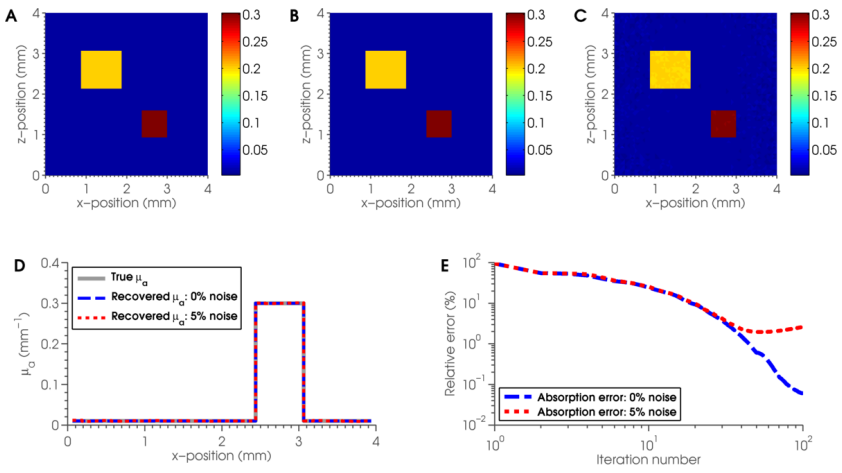

Figure 4.6 shows the results of the inversion after 100 iterations. Figure 4.6(A) shows the true absorption coefficient, Figure 4.6(B) and Figure 4.6(C) show the reconstructed absorption coefficients after 100 iterations from noise-free and noisy data, respectively. The percent relative error was $\epsilon_{\mathrm{a}} = 0.06\%$ and $\epsilon_{\mathrm{a}} = 2.55\%$ for the noise-free and noisy reconstructions, respectively. The illumination from two sides of the domain has improved the reconstruction compared to when a single point source was used, particularly where the absorption coefficient was underestimated towards the bottom of the domain. Figure 4.6(E) shows the percent relative error at each iteration of the reconstruction. In the case where noisy data was used, the error begins to increase after approximately 50 iterations. As in the previous example where a single point source was used, this effect is likely to be due to the amplification of high frequencies in the noise in areas where the signal to noise ration is relatively low. These areas are those furthest from a source, which in this case are the left- and right-hand edges of the domain, as seen in Figure 4.6(C). One method to reduce these errors could be to include a regularising term to penalise the amplification of noise in the inversion. Another method that may improve on these results might be to include information from additional sources. In the next example we will check whether the stability is furthered improved when four illumination directions are used.

4.2.3.2 Four point sources

In this example we will look at how well we can reconstruct the absorption coefficient if we include an additional two sources. Here, the measurement data consists of a set of four simulated PAT images obtained using four different illumination directions, namely a point source on each of the four sides of the domain, placed in the locations shown in Figure 4.2(C). The reconstructed absorption coefficient using this measurement data after 100 iterations can be seen in Figure 4.7.

The relative errors for the absorption reconstruction in this example are $\epsilon_{\mathrm{a}} = 0.03\%$ and $\epsilon_{\mathrm{a}} = 1.62\%$ from the noise-free and noisy measurement data, respectively. These have improved on the errors from the reconstructions using two point sources for the

FIGURE 4.7: Reconstructed absorption coefficient when the scattering is known *a priori*. Four simulated PAT images were obtained by illuminating the domain using four point sources placed at different positions, corresponding to Figure 4.2(C). (A) shows the true absorption coefficient, (B) shows the reconstructed absorption coefficient from noise-free data, and (C) shows the reconstructed absorption coefficient from data with 5% additive Gaussian noise. A profile comparison can be seen in (D), which compares the true absorption coefficient (grey solid), reconstructed absorption coefficient from noise-free data (blue dashed) and reconstructed absorption coefficient from noisy data (red dotted). The profile is taken in the x-direction at $z = 1.2$ mm. The percent relative error of the reconstructed absorption coefficients at each iteration can be seen in (E).

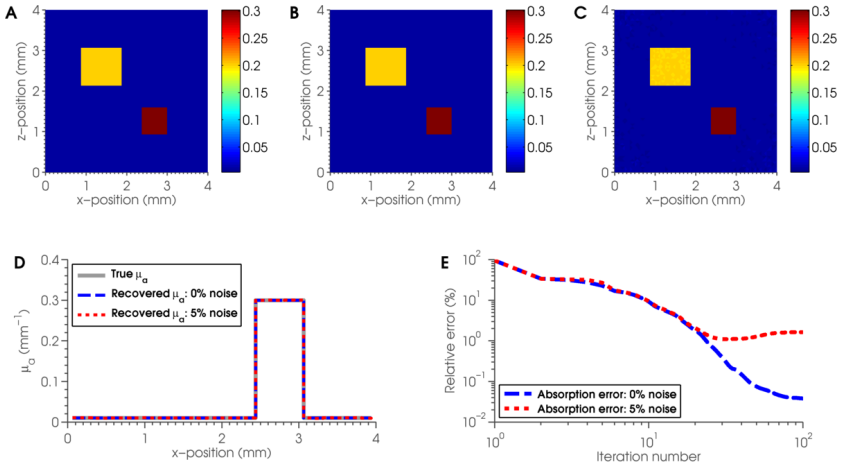

coarse mesh. The main improvement made by using the additional images appears in the reconstruction from noisy data, where the amplification of noise in the inversion has been reduced. As suggested by the theoretical results of [34], stability in the inversions is improved when multiple illuminations are used to obtained the measurement data. The incorporation of more than two illumination positions appears to further mitigate the errors due to noise in the inversion than when two illuminations are used.

4.2.3.3 Two line sources

In this example, two line sources, corresponding to Figure 4.3(B), are used to obtain a set of two simulated PAT images from which we look to reconstruct the absorption coefficient. Figure 4.8 shows the reconstructed absorption coefficient after 59 iterations. The results after 59 iterations are shown, as convergence on a solution was achieved and the reconstructions don't improve significantly past this point. In this case, the percent

relative errors for the noise-free and noisy reconstructions are $\epsilon_a = 7.5 \times 10^{-3}$ % and $\epsilon_a = 1.41\%$, respectively.

FIGURE 4.8: Reconstructed absorption coefficient when the scattering is known *a priori*. Two simulated PAT images were obtained by illuminating the domain using two line sources placed at different positions, corresponding to Figure 4.3(B). (A) shows the true absorption coefficient, (B) shows the reconstructed absorption coefficient from noise-free data, and (C) shows the reconstructed absorption coefficient from data with 5% additive Gaussian noise. A profile comparison can be seen in (D), which compares the true absorption coefficient (grey solid), reconstructed absorption coefficient from noise-free data (blue dashed) and reconstructed absorption coefficient from noisy data (red dotted). The profile is taken in the x-direction at $z = 2.5$ mm. The percent relative error of the reconstructed absorption coefficients at each iteration can be seen in (E).

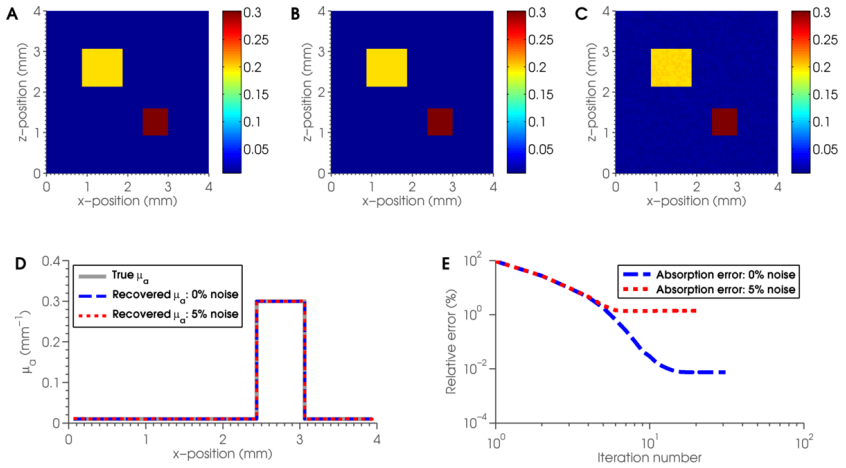

The use of two line sources enables the accurate reconstruction of the absorption coefficient to well within a 2% error, even in the presence of additive Gaussian noise. In the noise-free case the error in the absorption coefficient is comparable to the single line source case, however, the incorporation of an additional line source provides convergence to a solution after much fewer iterations (Figure 4.8 shows that the errors achieved in this example were obtained after around 10 iterations, compared to 80 iterations in the example using a single line source). This suggests that the incorporation of additional information from multiple illumination directions may not only improve stability but also the speed of convergence. The effects of additive noise in the measurement data can still be seen in the absorption reconstruction from noisy data (Figure 4.8(C)), though the incorporation of a second illumination position has helped to reduce the amplification of the high frequencies that appeared in Figure 4.5.

4.2.3.4 Four line sources

Since the accuracy and speed of convergence of the reconstructions continue to improve with the incorporation of additional sources, it is worth checking how well we can reconstruct the absorption coefficient using the gradient-based method when the domain is illuminated with line arrays of sources from all four directions. In this case, four images were simulated, each corresponding to a line source placed at either the top, bottom, left-hand side or right-hand side of the domain, as shown in Figure 4.3(C).

FIGURE 4.9: Reconstructed absorption coefficient when the scattering is known *a priori*. Four simulated PAT images were obtained by illuminating the domain using four line sources placed at different positions, corresponding to Figure 4.3(C). (A) shows the true absorption coefficient, (B) shows the reconstructed absorption coefficient from noise-free data, and (C) shows the reconstructed absorption coefficient from data with 5% additive Gaussian noise. A profile comparison can be seen in (D), which compares the true absorption coefficient (grey solid), reconstructed absorption coefficient from noise-free data (blue dashed) and reconstructed absorption coefficient from noisy data (red dotted). The profile is taken in the x-direction at $z = 1.2$ mm. The percent relative error of the reconstructed absorption coefficients at each iteration can be seen in (E).

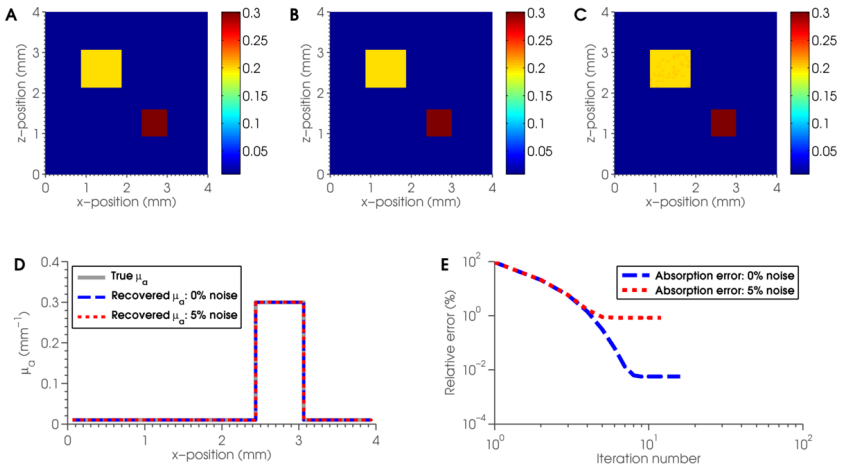

Figure 4.9 shows the reconstructed absorption coefficient when using this measurement data. The results after 20 iterations are shown as convergence on a solution was achieved and the reconstructions don't improve significantly past this point. In this case, the method is able to produce excellent quantitative estimates of the absorption coefficient, with errors of less than 1% even in the presence of 5% Gaussian noise; the percent relative errors for the noise-free and noisy reconstructions are $\epsilon_{\mathrm{a}} = 5.7 \times 10^{-3}$ % and $\epsilon_{\mathrm{a}} = 0.84\%$, respectively. Convergence to a solution in this case was obtained in only

20 iterations, which is a further improvement on both the case where four point sources where used and where two line sources were used. These results strongly suggest that it is worthwhile, if possible, to illuminate the domain as much as possible and use data from as many directions as possible when using the gradient-based method to perform the QPAT inversion.

4.2.4 Sensitivity to initial guess at absorption

The examples for reconstructing the optical absorption coefficient which have been presented so far have been performed by setting the initial guess at μ_{a} to the background value ($\mu_{\mathrm{a}}^{\mathrm{bg}} = 0.01$ mm $^{-1}$). In practice, the background absorption will not be known and will be difficult to measure. At best, we will be able to make a rough estimate based on the type of tissue we are measuring, provided that estimates of the absorption coefficient in that tissue have been made previously and are available in the literature. With this in mind, it will be useful to know how sensitive the reconstructed μ_{a} is to the initial guess at the absorption coefficient, and whether the method will perform successfully regardless of the initial guess.

To investigate the sensitivity to the initial guess at absorption, we will attempt to reconstruct the absorption coefficient using a range of initial guesses. The absorption and scattering coefficients are the same as in Section 4.2.2. The absorption coefficient is a homogeneous background with two absorbing heterogeneities, and has a background value of $\mu_{\mathrm{a}}^{\mathrm{bg}} = 0.01$ mm^{-1} with two non-smooth inclusions of $\mu_{\mathrm{a}}^{1} = 0.2$ mm^{-1} and $\mu_{\mathrm{a}}^{2} = 0.3$ mm^{-1}. The scattering coefficient has a similar structure, with a homogeneous background of $\mu_{\mathrm{s}}^{\mathrm{bg}} = 5$ mm^{-1} and two non-smooth scattering inclusions of $\mu_{\mathrm{s}}^{1} = 10$ mm^{-1} and $\mu_{\mathrm{s}}^{2} = 15$ mm^{-1}. Figures 3.4(A) and 3.4(B) show the 2D geometries of the optical absorption and scattering coefficients, respectively. The FE RTE model was used to simulate a measured absorbed energy map, which was obtained using a single point source. No noise was added to the image. The gradient-based inversion method was then used to recover the absorption coefficient using a range of initial guesses. These

FIGURE 4.10: Sensitivity of the absorption reconstruction to changes in the initial guess at absorption, assuming that scattering is known. In this case the inversion was performed using measurement data from a single image obtained using a single point source placed at the centre of the top boundary. The inversion was performed using a range of initial guesses at the absorption coefficient, beginning with 0 mm^{-1} up to 0.05 mm^{-1}, which is five times the background absorption coefficient $\mu_{\text{a}}^{\text{bg}} = 0.01$ mm^{-1}, the value of which has been indicated with an arrow. The percent relative error in the absorption reconstruction using this range of initial guesses is shown after 100 iterations (red solid), 150 iterations (green solid), 250 iterations (light blue dot-dash) and 500 iterations (dark blue dot-dash). Images of the reconstructed absorption at 100, 150, 250 and 500 iterations are shown on the right-hand side of the figure for the highest initial guess of 0.05 mm^{-1}.

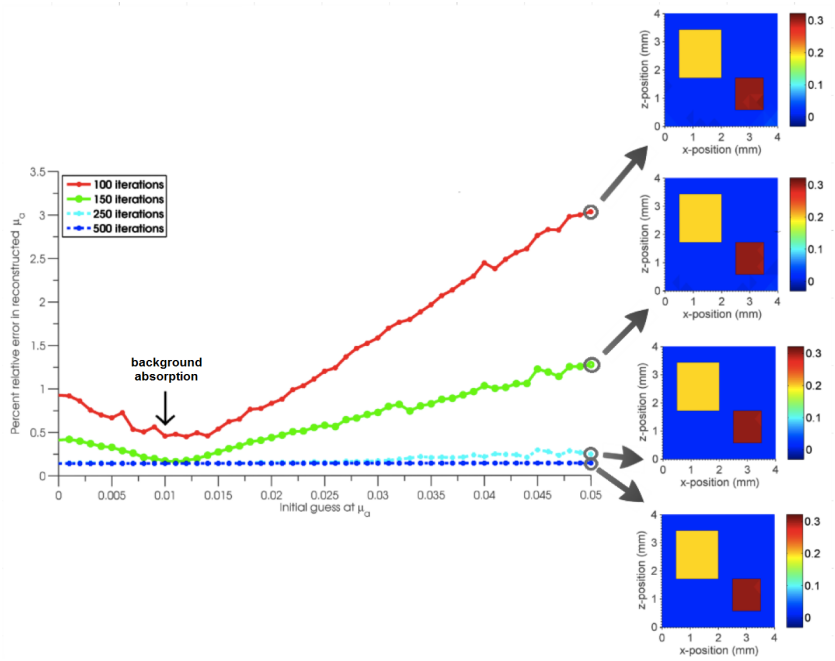

began at 0 mm^{-1} and moved in increments of 10^{-3} mm^{-1} up to 0.01 mm^{-1}, and then in larger increments of 0.05 mm^{-1} up to 0.1 mm^{-1}, which is 10 times the true background value, $\mu_{\text{a}}^{\text{bg}}$. For each initial guess at the absorption coefficient, the resulting relative error in the reconstructed absorption coefficient after 100, 150, 250 and 500 iterations of the l-BFGS method was recorded. The relative error was calculated using Equation 4.45. The results can be seen in Figure 4.10, where the arrow indicates the value of $\mu_{\text{a}}^{\text{bg}}$.

Figure 4.10 indicates that faster convergence will be provided if the initial guess at μ_{a} is around the background value $\mu_{\text{a}}^{\text{bg}}$. Convergence is also obtained quickly where the initial guess is lower than $\mu_{\text{a}}^{\text{bg}}$. The slower convergence as we increase the initial guess

is likely to be due to a loss of information resulting from the relatively strong absorption; overestimating the background means that the resulting fluence distribution decays more quickly. In the case where the initial guess is fairly high, the method does eventually recover a comparably accurate estimate of the absorption, though more iterations are required. This can be seen in the images on the right-hand side of Figure 4.10, which show the resulting absorption estimates for an initial guess of 0.05 mm^{-1} after 100, 150, 250 and 500 iterations. This result is encouraging, since it indicated that the method will be reliable regardless of the initial guess at the absorption coefficient, though it may take more time to complete the inversion. It also indicated that, in the case where the background absorption is unknown and it is difficult to make an estimate, starting with a small guess of, say, 10^{-3} mm is likely to provide convergence fairly quickly. Following these results, we will continue to use the background value of absorption as an initial guess.

4.2.5 Sensitivity to errors in the scattering

So far, we have seen that a gradient-based method which uses a numerical model of light transport based on the RTE can be used to obtain accurate quantitative estimates of the underlying absorption coefficient from 2D simulated absorbed energy images, given that the scattering is known *a priori*. In practice we will have a limited amount of information regarding the structure and absolute values of the scattering coefficient. Since this quantity is difficult to both measure and estimate, it is important to develop a method which is either relatively insensitive to errors in the estimation of the scattering coefficient, or otherwise does not rely on making an approximation at all. In this section, we will look at the former case, and investigate how accurately we can recover the absorption coefficient if we (incorrectly) assume that the scattering coefficient is homogeneous and fixed at some constant value. This is effectively what was performed in [79], where the homogeneous scattering coefficient was estimated through knowledge of the known homogeneous reduced scattering coefficient and a guess at the anisotropy factor g.

FIGURE 4.11: Sensitivity of the absorption reconstruction to errors in the scattering coefficient using a single point source. The graph shows the percent relative error in the reconstructed absorption coefficient after 50 iterations when assuming that scattering is fixed at a constant value, given by the x-axis. The labelled arrows indicate the value of the background scattering (5 mm^{-1}) and the mean scattering (5.55 mm^{-1}).

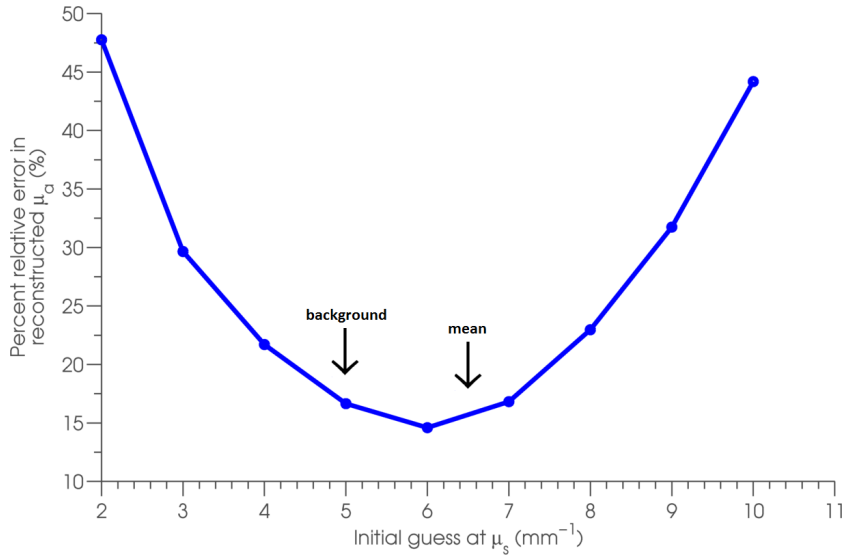

Incorrectly assuming the scattering distribution is homogeneous raises two questions regarding the determination of the absorption coefficient: (1) How sensitive is the method to errors in the scattering estimate?, and (2) What, if any, is the ideal constant value at which the scattering coefficient should be fixed? In Section 4.2.4, we investigated the sensitivity of the inversion to the initial guess at the absorption coefficient, and found that starting at its background value would provide the fastest convergence to the correct solution (though using a different initial guess will still converge to the correct solution eventually). To determine how sensitive the inversions are to errors in the scattering estimate, we will look at the percent relative error in the reconstructed absorption coefficient when there is a varying degree of error in the scattering coefficient.

To determine the ideal value at which to fix the scattering coefficient, a similar investigation to that performed in Section 4.2.4 was performed. Here, the optical coefficients were defined as in Section 4.2.1, and the measurement data was simulated using the two extremes in regards to the amount and number of illumination points: the first example uses a single point source, as in Section 4.2.2.1, and the second will use four line

FIGURE 4.12: Sensitivity of the absorption reconstruction to errors in the scattering coefficient using four line sources. The graph shows the percent relative error in the reconstructed absorption coefficient after 50 iterations when assuming that scattering is fixed at a constant value, given by the x-axis. The labelled arrows indicate the value of the background scattering (5 mm^{-1}) and the mean scattering (5.55 mm^{-1}).

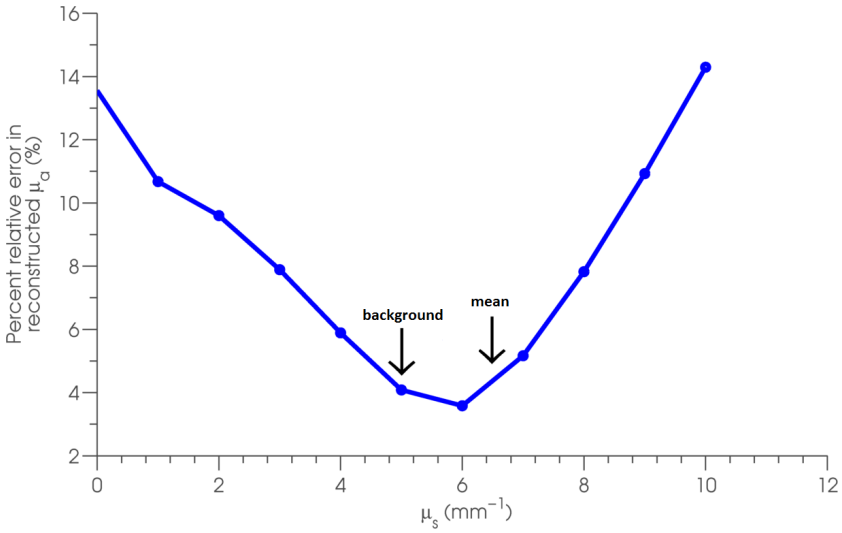

sources, as in Section 4.2.3.4. For each case, the inversions for the absorption coefficient were performed by assuming the scattering coefficient was homogeneous and fixed at a constant value of 0 mm^{-1}, and then again at increments of 0.25 mm^{-1} up to 10 mm^{-1}, which is twice the background scattering μ_s^{bg}. The resulting percent relative error in the absorption was calculated using Equation 4.45 and recorded for each change in the scattering value. The results can be seen in Figure 4.11 and Figure 4.12, where the background value and mean value of the scattering coefficient have been indicated by an arrow and labels.

In both cases, the inversion appears to perform better when the scattering is fixed around its background or mean value (in this case using either value will produce similar results since the mean scattering is relatively close to the background). Diverting from this value by either under- or overestimating the scattering results in much larger errors in the absorption reconstruction. This may suggest that the method will be sensitive to errors in the scattering estimate, however, it is worth noting that these are the results after 100 iterations, and it is possible that the result will improve with more iterations of the method (as in Section 4.2.4, where it was found that using a range of initial guesses

at the absorption coefficient would produce comparably accurate results, though the convergence may be slower). What is clear from these results is that, if the scattering is to be assumed homogeneous, fixing the scattering coefficient at its background or mean value appears to provide the fastest convergence to the correct absorption coefficient.

FIGURE 4.13: Improvement of errors in the absorption reconstruction when measurement data obtained using multiple illumination positions are used. Each line shows the sensitivity of the absorption reconstruction to errors in the scattering coefficient. Three sets of measured data were obtained using a single line source (green), two line sources (red) and four lines sources (blue). Resulting errors in the absorption reconstruction when using noise-free data are shown by dashed lines, and the errors from noisy data are shown by dotted lines.

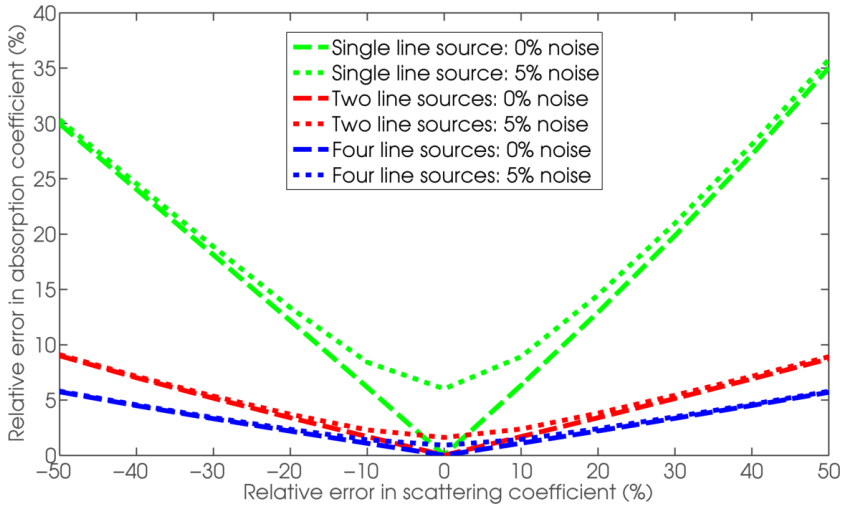

Section 4.2.2 has established that the incorporation of additional sources from multiple illumination positions is beneficial to the absorption reconstruction, either by improving the resulting estimate of μ_a or by improving the speed of convergence, or both. Figure 4.13 shows how the sensitivity to errors in the scattering is improved as more images are incorporated into the measurement data. Here, the scattering coefficient was scaled to between 50% and 150% of its true value, at increments of 10%, and the resulting error in the reconstructed absorption was recorded. This was done for three cases: a single line source, two line sources and four line sources. The results using noise-free and noisy data were recorded for each case. In the case where four line sources are used, the absorption coefficient can be recovered to within 6% even where the scattering estimate is underestimated by 50%. This is a promising result, though it should be considered with caution: the scattering coefficient has simply been scaled, so that the structure of

its heterogeneities are still intact. Indeed, it may be argued that there is some *a priori* knowledge about the scattering coefficient in this case.

FIGURE 4.14: Sensitivity of the absorption reconstruction to errors in the scattering coefficient using the fixed point iteration described in Section 3.3.3.1 and the gradient-based minimisation presented in Section 4.1.3. The measurement data has been obtained using a single point source. In the case of single-sided illumination, the gradient-based method performs comparably to the fixed point iteration.

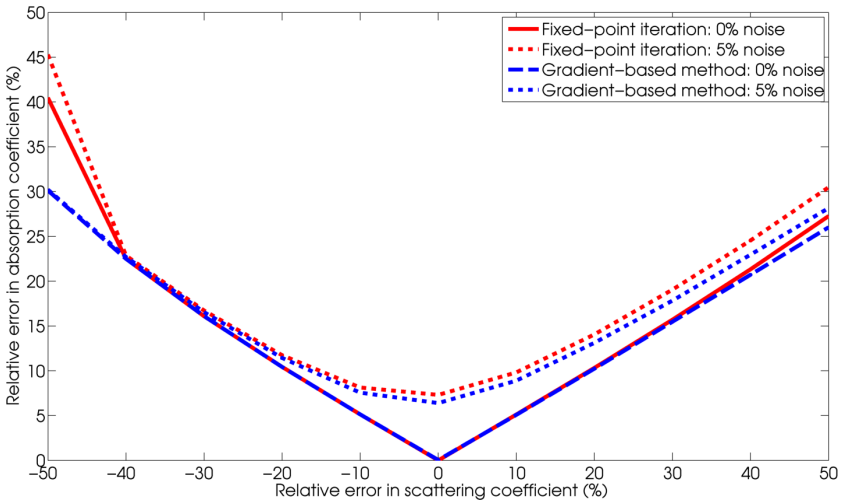

In Section 3.3.3.1 we discussed how the fixed-point iteration provides a useful tool where the scattering coefficient is known or can be estimated with some confidence. In the case where the scattering is assumed constant, and the measurement data has been obtained using a single illumination position, the fixed point iteration and the gradient-based method perform comparably. Figure 4.14 shows the resulting error in the absorption reconstruction when a single point source has been used to obtain the measured data. Due to the formulation of the fixed point iteration, however, data from multiple images cannot be incorporated, and the fixed point iteation does not therefore benefit from the improved accuracy and speed of convergence in the reconstruction provided by multiple illuminations.

Figure 4.15 shows the sensitivity to errors in the scattering using the fixed point iteration and the gradient-based method. A single line source has been used to obtain the results using the fixed point iteration, while four line sources are used to perform the

FIGURE 4.15: Sensitivity of the absorption reconstruction to errors in the scattering coefficient using the fixed point iteration described in Section 3.3.3.1 and the gradient-based minimisation presented in Section 4.1.3. The incorporation of additional information provided by multiple PAT obtained using multiple illumination positions improves the absorption reconstruction significantly. The fixed point iteration is unable to include these additional images into its framework, and is therefore unable to obtain a comparable estimate of absorption.

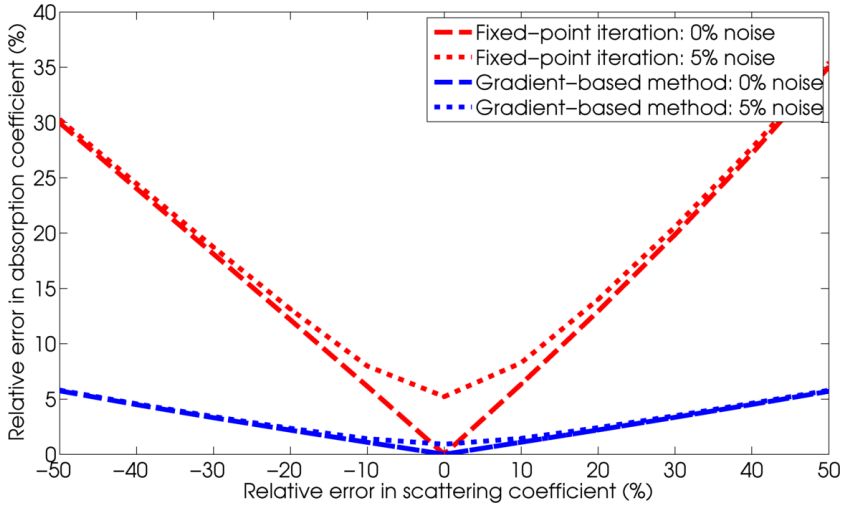

gradient-based method. These demonstrate the best-case scenario for each method. The gradient-based method performs comparably to the fixed point iteration where a single illumination is used, but significantly outperforms the fixed point iteration where multiple images can be obtained. If the scattering is known, or is to be assumed constant throughout the domain, the gradient-based method will therefore provide the best method for reconstructing the absorption coefficient.

These results suggest that fixing the scattering at some constant value may be enough to produce a sufficient estimate of the absorption coefficient for some applications. This is due to the relatively weak dependence of the data on the scattering coefficient; the absorbed energy density is the product of the absorption coefficient and the optical fluence, which is more strongly affected by absorption than scattering. The absorbed energy density is therefore much more strongly dependent on μ_a than μ_s. Given that it is likely that the scattering will be unknown, it will be useful to know how accurately we are able to recover μ_a if we are forced to use an estimate of the scattering coefficient.

4.2.6 Inversions with estimated scattering

The results in Section 4.2.5 suggest that, if we are to fix the scattering at some constant value, the background or mean value may produce the smallest error in the reconstructed absorption coefficient (or at least may provide faster convergence). In this section, we will therefore assume that the scattering coefficient is homogeneous and fixed at its mean value of $\mu_{\mathrm{s}} = 5.55$ mm^{-1}. Under this assumption, we will attempt to reconstruct quantitative estimates of the absorption coefficient. The simulated measurement data is obtained exactly as outlined in Section 4.2.1. Since the use of multiple illumination directions seems to improve the results more than simply increasing the signal to noise by including more source along the same boundary, we will now only consider the three cases using line sources, corresponding to Figure 4.3.

4.2.6.1 Single line source

In this first example, the data was obtained using a single line source, as shown in Figure 4.3(A). Figure 4.16 shows the results after 100 iterations. The percent relative errors in the absorption reconstructions were $\epsilon_{\mathrm{a}} = 8.53\%$ and $\epsilon_{\mathrm{a}} = 9.96\%$ for the noise-free and noisy data, respectively. Considering that the scattering is assumed to be completely homogeneous when in fact it has two strongly scattering heterogeneities, this result is encouraging. The structure of the heterogeneous absorption coefficient is recovered, and a reasonably small error is incurred. There is, however, a significant underestimation of the absorption coefficient in the two heterogeneities, and convergence to this incorrect solution is obtained in both the noisy and noise free case (in the noise-free case, the solution begins to diverge, but this would likely be remedied if some regularisation were used).

The corresponding example in the case where the scattering is known *a priori*, which was shown in Section 4.2.2.2, obtained relative errors of $\epsilon_{\mathrm{a}} = 7.9 \times 10^{-3}$ % and $\epsilon_{\mathrm{a}} = 5.46\%$

FIGURE 4.16: Reconstructed absorption coefficient when the scattering is fixed at its mean value. The domain was illuminated using a single line source, corresponding to Figure 4.3(A). (A) shows the true absorption coefficient, (B) shows the reconstructed absorption coefficient from noise-free data, and (C) shows the reconstructed absorption coefficient from data with 5% additive Gaussian noise. A profile comparison can be seen in (D), which compares the true absorption coefficient (grey solid), reconstructed absorption coefficient from noise-free data (blue dashed) and reconstructed absorption coefficient from noisy data (red dotted). The profile is taken in the x-direction at $z = 1.2$ mm. The percent relative error of the reconstructed absorption coefficients at each iteration can be seen in (E).

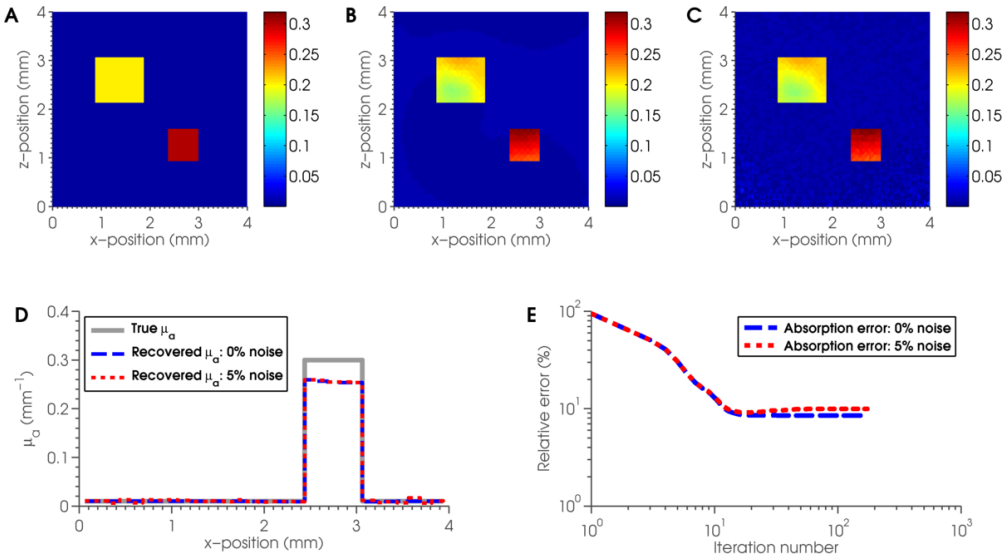

FIGURE 4.17: Comparison of the reconstructed absorption coefficients when the scattering is known *a priori* (left-hand image) and when it is fixed at its mean value (right-hand image). In this example, the domain was illuminated using a single line source, corresponding to Figure 4.3(A). The profile comparison compares the true absorption coefficient (grey solid), reconstructed absorption coefficient from noise-free data (blue dashed) and reconstructed absorption coefficient from noisy data (red dotted), and the profile is taken in the x-direction at $z = 1.2$ mm.

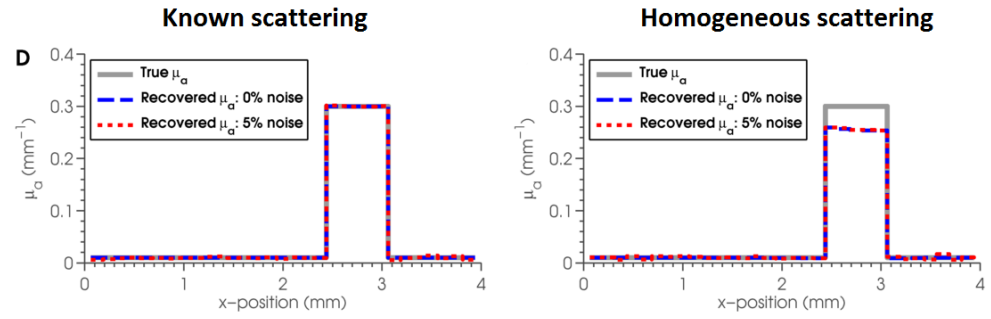

for the noise-free and noisy case, respectively. Whilst the latter error may seem significant, it is largely due to a low signal to noise ratio in regions far from the source causing the amplification of the noise in the inversion. Figure 4.17 shows a comparison of the reconstructed absorption coefficients obtained when the scattering is known *a priori* and when it is assumed to be homogeneous and fixed at its mean value. In the case where the scattering is known, the quantitative estimation of the absorption coefficient in the two heterogeneities is highly accurate in both the noise-free and noisy case. When fixed at its background value, the absorption coefficient in the heterogeneities is underestimated significantly.

4.2.6.2 Two line sources

FIGURE 4.18: Reconstructed absorption coefficient when the scattering is fixed at its mean value. The domain was illuminated using two line sources, corresponding to Figure 4.3(B). (A) shows the true absorption coefficient, (B) shows the reconstructed absorption coefficient from noise-free data, and (C) shows the reconstructed absorption coefficient from data with 5% additive Gaussian noise. A profile comparison can be seen in (D), which compares the true absorption coefficient (grey solid), reconstructed absorption coefficient from noise-free data (blue dashed) and reconstructed absorption coefficient from noisy data (red dotted). The profile is taken in the x-direction at $z = 1.2$ mm. The percent relative error of the reconstructed absorption coefficients at each iteration can be seen in (E).

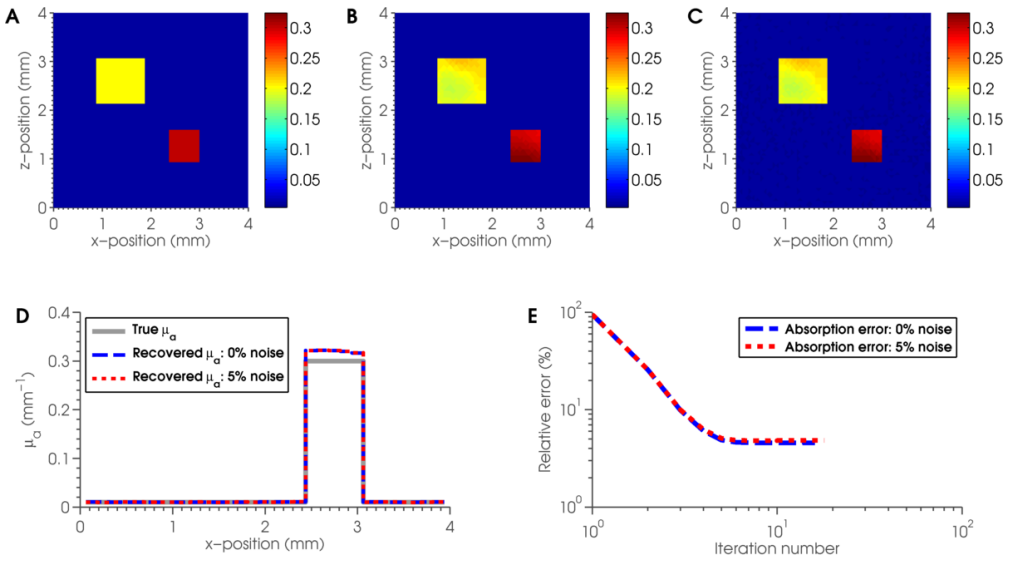

Here, the data was obtained using two line sources, corresponding to Figure 4.3(B). Figure 4.18 shows the results after 18 iterations. The results after 18 iterations are shown as the minimisation converged to a solution at this point. The per cent relative errors in the absorption reconstructions were $\epsilon_{\mathrm{a}} = 4.56\%$ and $\epsilon_{\mathrm{a}} = 4.84\%$ for the noise-free and noisy data, respectively. As in the known scattering case, the incorporation of an additional PAT image illuminated from a different direction has increased the accuracy of the resulting absorption estimate significantly. The speed of convergence has also improved significantly; an improved approximation to μ_{a} was obtained in only 18 iterations, compared with 100 iterations when using a single-sided illumination. In this example, the absorption has been overestimated in the two heterogeneities, though the incorporation of an additional image obtained using a different illumination position has helped to reduce the error in the absorption estimate.

FIGURE 4.19: Comparison of the reconstructed absorption coefficients when the scattering is known *a priori* (left-hand image) and when it is fixed at its mean value (right-hand image). In this example, the domain was illuminated using two line sources, corresponding to Figure 4.3(B). The profile comparison compares the true absorption coefficient (grey solid), reconstructed absorption coefficient from noise-free data (blue dashed) and reconstructed absorption coefficient from noisy data (red dotted), and the profile is taken in the x-direction at $z = 1.2$ mm.

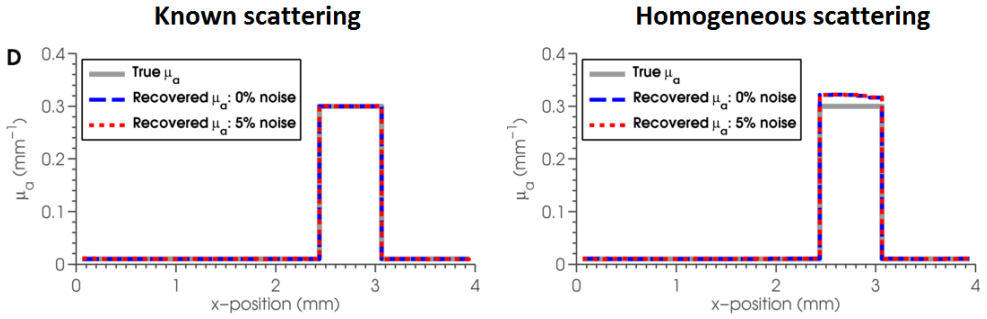

The corresponding example in the case where the scattering is known *a priori*, which was shown in Section 4.2.3.3, obtained relative errors of $\epsilon_{\mathrm{a}} = 7.5 \times 10^{-3}$ % and $\epsilon_{\mathrm{a}} = 1.41\%$ for the noise-free and noisy case, respectively. Figure 4.19 shows a comparison of the reconstructed absorption coefficients obtained when the scattering is known *a priori* and when it is assumed to be homogeneous and fixed at its mean value. As in the single-sided illumination example, the estimation of the absorption coefficient in the two heterogeneities when the scattering is known is highly accurate in both the noise-free

and noisy case. When the scattering is fixed at its background value, the absorption coefficient in the heterogeneities in this case has been overestimated. As in the single-sided illumination example, the minimisation when assuming the scattering is homogeneous has converged to the incorrect solution, suggesting that this is the best approximation to the absorption coefficient that may be obtained when the scattering is assumed to be homogeneous.

4.2.6.3 Four line sources

FIGURE 4.20: Reconstructed absorption coefficient when the scattering is fixed at its mean value. The domain was illuminated using four line sources, corresponding to Figure 4.3(C). (A) shows the true absorption coefficient, (B) shows the reconstructed absorption coefficient from noise-free data, and (C) shows the reconstructed absorption coefficient from data with 5% additive Gaussian noise. A profile comparison can be seen in (D), which compares the true absorption coefficient (grey solid), reconstructed absorption coefficient from noise-free data (blue dashed) and reconstructed absorption coefficient from noisy data (red dotted). The profile is taken in the x-direction at $z = 1.2$ mm. The percent relative error of the reconstructed absorption coefficients at each iteration can be seen in (E).

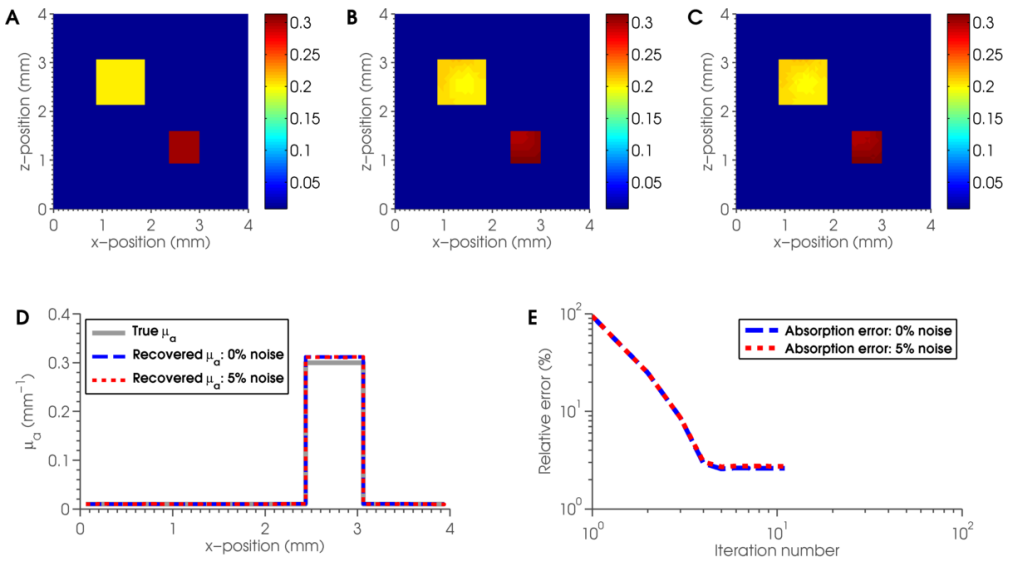

In this example, the data was obtained using four line sources, as can be seen in Figure 4.3(C). Figure 4.20 shows the results after 11 iterations. The results after 11 iterations are shown as the minimisation convergence to a solution at this point. The per cent relative errors in the absorption reconstructions were $\epsilon_{\mathrm{a}} = 2.62\%$ and $\epsilon_{\mathrm{a}} = 2.74\%$

for the noise-free and noisy data, respectively. As in the known scattering case, the incorporation of additional PAT images illuminated from different directions has further increased the accuracy of the resulting absorption estimate. The speed of convergence has also been improved when compared with the previous example; the improved approximation to μ_{a} was obtained in only 11 iterations. The absorption coefficient is now only slightly overestimated in the two heterogeneities, although the minimisation has again converged to this incorrect solution.

FIGURE 4.21: Comparison of the reconstructed absorption coefficients when the scattering is known *a priori* (left-hand image) and when it is fixed at its mean value (right-hand image). In this example, the domain was illuminated using four line sources, corresponding to Figure 4.3(C). The profile comparison compares the true absorption coefficient (grey solid), reconstructed absorption coefficient from noise-free data (blue dashed) and reconstructed absorption coefficient from noisy data (red dotted), and the profile is taken in the x-direction at $z = 1.2$ mm.

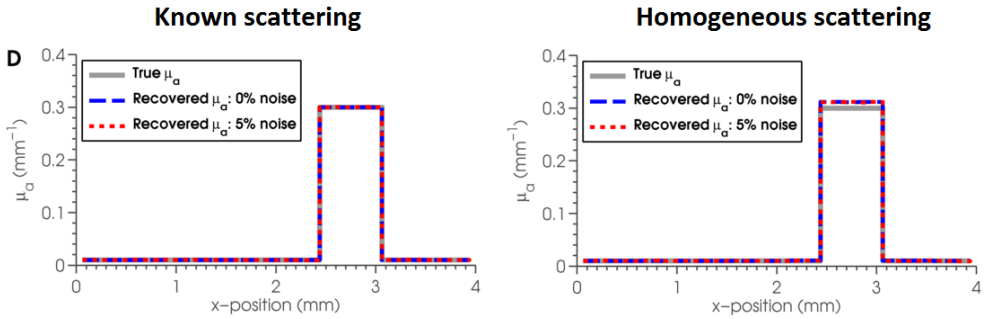

The corresponding example in the case where the scattering is known *a priori*, which was shown in Section 4.2.3.4, obtained relative errors of $\epsilon_{\mathrm{a}} = 5.7 \times 10^{-3}\%$ and $\epsilon_{\mathrm{a}} = 0.84\%$ for the noise-free and noisy case, respectively. Figure 4.21 shows a comparison of the reconstructed absorption coefficients obtained when the scattering is known *a priori* and when it is assumed to be homogeneous and fixed at its mean value. These results indicate that the gradient-based method is able to recover the absorption coefficient μ_{a} to within 3% of its true value, even where the scattering is unknown, or has been incorrectly assumed to be homogeneous and fixed at its mean value. Incorrectly approximating the scattering does result in an under- or overestimation in the recovered absorption coefficient, but the heterogeneous structure is preserved and a good quantitative estimate can be obtained, particularly when measured data obtained using multiple illumination

positions is available.

In Section 4.2.5, we investigated the sensitivity of the absorption estimate to changes in the value at which the scattering coefficient is fixed. Figures 4.11 and 4.12 showed the resulting error in the absorption estimate when the scattering is assumed to be homogeneous and is fixed at a range of values. These results indicated that the fastest convergence to the correct solution would be provided if we choose to assume the scattering coefficient is homogeneous and equal to its mean. Following this, we have attempted to recover the absorption coefficient for three different source geometries, and have found that a reasonably accurate quantitative estimate of the absorption coefficient can be found if the scattering is fixed at its mean value. The results of these inversions have also shown that, in the case where the scattering coefficient is incorrectly assumed to be homogeneous, the minimisation will converge to an under- or overestimation of the absorption coefficient, and do not improve with more iterations of the method. Considering this, Figures 4.11 and 4.12, which show the error in the absorption coefficient after 100 iterations, may indicate that moving away from the mean or background value scattering will produce significantly larger errors in the resulting absorption estimate. If this is the case, then the choice of the mean value could perhaps be considered a best-case scenario. Indeed, it could be argued that considerable *a priori* knowledge has been used to perform the inversion.

Let us reconsider the example presented above (see Figure 4.21), where the scattering was assumed to be homogeneous and fixed at its mean value, and four line sources were used to obtain the measured data. In this example, the percent relative errors in the absorption reconstructions were $\epsilon_{\mathrm{a}} = 2.62\%$ and $\epsilon_{\mathrm{a}} = 2.74$ for the noise-free and noisy data, respectively. We will now consider the same measurement data, but instead we will assume that the scattering distribution is entirely unknown, and so we are forced to choose a value at which to fix the scattering coefficient. We now incorrectly choose the mean scattering to be twice its true value, that is, $\mu_{\mathrm{s}} = 11.1$ mm^{-1}, and attempt to reconstruct the absorption coefficient using the gradient-based minimisation scheme. Figure 4.22 shows the results after 11 iterations, when convergence to a solution

was achieved. In this case, the percent relative errors in the reconstructed absorption coefficient were $\epsilon_{\mathrm{a}} = 13.2\%$ for both the reconstructions from noise-free and noisy data. Even in the ideal scenario where four line sources have been used to obtain the measurement data, overestimation of the scattering mean has led to overestimation of the reconstructed absorption coefficient, resulting in a significant increase in the percent relative error.

FIGURE 4.22: Reconstructed absorption coefficient when the scattering is fixed at twice its mean value ($\mu_{\mathrm{s}} = 11.1$ mm^{-1}). The domain was illuminated using four line sources, corresponding to Figure 4.3(C). (A) shows the true absorption coefficient, (B) shows the reconstructed absorption coefficient from noise-free data, and (C) shows the reconstructed absorption coefficient from data with 5% additive Gaussian noise. A profile comparison can be seen in (D), which compares the true absorption coefficient (grey solid), reconstructed absorption coefficient from noise-free data (blue dashed) and reconstructed absorption coefficient from noisy data (red dotted). The profile is taken in the x-direction at $z = 1.2$ mm. The percent relative error of the reconstructed absorption coefficients at each iteration can be seen in (E). Overestimation of the scattering mean has resulted in significantly larger errors than the results shown in Figure 4.20.

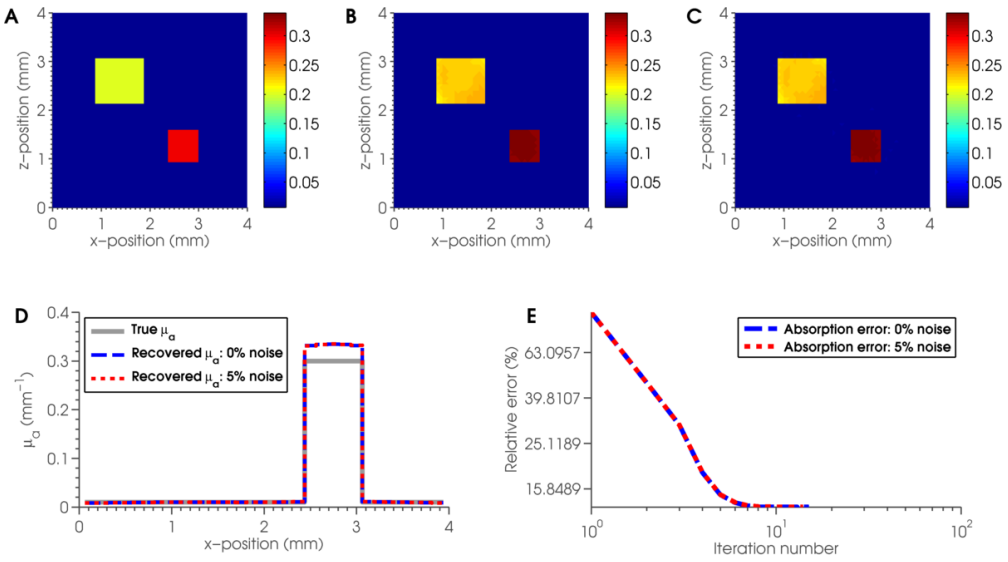

4.3 Conclusions

○ *In this chapter, we have proposed, derived and implemented an adjoint-assisted gradient-based minimisation method which uses the full RTE to recover quantitative estimates of the optical absorption coefficient from simulated PAT images.*

The absorption and scattering coefficients consisted of a homogeneous background with two non-smooth heterogeneities. The anisotropy factor was constant with $g = 0.8$ for all simulations. The numerical examples presented here can be placed into two categories: known scattering and estimated scattering. A number of different source geometries were considered for each scattering scenario. 2D simulated PAT images were obtained using a FE implementation of the RTE. The FE mesh consisted of $N_e = 3840$ triangular elements, $N_n = 1983$ nodes and an angular discretisation of $N_a = 16$ equal angles. For each example, the gradient-based RTE method was used to reconstruct the absorption coefficient from both noise-free data and data with additive Gaussian noise scaled to 5% of the mean absorbed energy density. Table 4.1 summarises the results of the numerical examples.

◦ *When the scattering coefficient is known a priori, highly accurate quantitative estimates of the optical absorption coefficient can be recovered.*

In Section 4.2.2, we assumed that the scattering coefficient was known. The first example considered a single PAT image obtained using a single point source. Using this measurement data, a good approximation to the absorption coefficient was obtained, though there was some underestimation of μ_{a} in areas far from the source where the signal to noise ratio was relatively low. Increasing the signal by using a line array of sources along the same boundary improved the approximation significantly, producing an error of less than 0.01% in the noise-free case. The reconstructions using a single illumination and noisy data still experienced errors due to the amplification of noise in the inversion process. The inclusion of additional information from simulated PAT images obtained using multiple illumination positions reduced the amplification of noise, improved the accuracy of the reconstructed absorption, and also improved the speed of convergence to a solution. Using multiple illumination, highly accurate estimates of the absorption coefficient were obtained in both the noise-free and noisy cases.

◦ *When the scattering coefficient is unknown, choosing the mean scattering is good place to start.*

TABLE 4.1: Summary of the results of the gradient-based inversions presented in Chapter 4. Two situations were investigated: the first considered the scattering to be known *a priori*, and the second incorrectly estimated the scattering to be homogeneous, and fixed at its mean value. A variety of source geometries were considered in each case, corresponding to Figures 4.2 and 4.3. The two right-hand columns show the percent relative error in the absorption coefficient from data which included 0% and 5% noise.

Scattering	Source	Distribution	0% noise	5% noise
Known	Point	Top	2.24	4.45
		Top and bottom	0.06	2.55
		Top, bottom, left and right	0.03	1.62
	Line	Top	7.9×10^{-3}	5.46
		Top and bottom	7.5×10^{-3}	1.41
		Top, bottom, left and right	5.7×10^{-3}	0.84
Estimated (Fixed at mean)	Line	Top	8.53	9.96
		Top and bottom	4.56	4.84
		Top, bottom, left and right	2.62	2.74

In practice, the scattering coefficient is not likely to be known *a priori*, and so it is necessary to develop a technique which can deal with an unknown scattering coefficient, or is relatively insensitive to errors in its estimation. In PAT, the measurement data is relatively weakly dependent on the scattering coefficient compared to the absorption coefficient. Considering this, in Section 4.2.6 we investigated whether a crude estimate of the scattering coefficient can be used to successfully reconstruct an accurate quantitative estimate of μ_{a}. In these examples, the heterogeneous scattering coefficient was incorrectly considered to be homogeneous, and was fixed to its mean value. The estimation that the scattering is homogeneous was able to provide reasonable estimates of the absorption coefficient, with percent relative errors as small as 2.62% when measurement data obtained using four illumination positions was used. However, Section 4.2.5 indicated that knowledge of the mean value of the scattering coefficient is likely to be considerably important *a priori* knowledge, as the method appears to be sensitive to the scattering estimate and the reconstructions are less accurate as the scattering estimate moves away from its mean value.

◦ *Multiple images obtained using different illumination directions can be used to improve the reconstructions.*

The absorption reconstructions can be improved using three methods: including a regularisation term to penalise the amplification of high frequencies in the data; increasing the number of sources along the boundaries which already contain a source in order to increase the signal to noise ratio; increasing the number of illumination directions, e.g. illumination from all four sides of the domain. Using this gradient-based minimisation method, these techniques could all be used simultaneously, for example, the domain could be illuminated using an array of line sources at each boundary of the domain, and regularisation could be added when performing the inversion. In practice, the choice of these methods will depend on the application and the experimental setup available, since it may not be possible to illuminate from more than one direction with a particular setup or for a particular target. Where additional sources are unavailable, it will always be possible to include regularisation when using this type of iterative minimisation scheme. Despite some small errors due to noise, the reconstruction of the absorption coefficient appears to be stable, and so a regularisation term has not been included in these examples, but the incorporation of an appropriate regularisation method could be used to improve the reconstructions from noisy data.

◦ *Unless there is confidence in the scattering mean, it is likely that both optical coefficients will need to be reconstructed.*

In practice, the scattering coefficient is likely to be heterogeneous and unknown. If little information is known about the rough values of the scattering coefficient for a given target, then estimating its mean value will be difficult. The incorrect estimation of the scattering coefficient as a homogeneous distribution is therefore likely to limit the ability to reconstruct the absorption coefficient significantly. Even in the case where there is confidence in the mean value of the scattering and the multiple illuminations are available, the absorption coefficient can only be reconstructed to within around 5% of its true value. In practice, a blind guess at the scattering mean is more likely to result in errors of around 10 - 15% or higher, as in the example shown in Figure 4.22. If the scattering

distribution is entirely unknown, and there is little confidence in the estimated mean value, the gradient-based method presented here can be extended to reconstruct both absorption and scattering coefficients simultaneously. In the next chapter, we will extend the adjoint-assisted gradient-based method to the case where both optical coefficients are heterogeneous and unknown.

Chapter 5

Gradient-based QPAT using the RTE 2: recovering absorption and scattering

In Chapter 4, we proposed the use of a gradient-based method based on the RTE for recovering quantitative estimates of the optical absorption coefficient. This inversion method, which uses the full RTE to model the propagation of light within the tissue, was used to reconstruct highly accurate quantitative estimates of the absorption coefficient from 2D simulated PAT images when the scattering is known *a priori*. Section 4.2.6 investigated how well the absorption coefficient can be reconstructed if the scattering coefficient is incorrectly assumed to be a homogeneous distribution. In this case, good quantitative estimates of absorption can be found if there is confidence in the estimation of the mean scattering and if multiple illumination positions are used to obtain the measurement data, however, the method is sensitive to errors in the scattering estimate. Generally in QPAT, the scattering coefficient μ_{s} will be heterogeneous and will not be known in advance. It will therefore be difficult to estimate its mean value or distribution. In this case, it is necessary to recover both the absorption and scattering coefficients simultaneously. Following the uniqueness results discussed in Section 3.4.1, multiple illuminations positions are used to ensure a unique solution, however, we will

first consider the case of a single PAT image before extending the method to the multiple illumination case.

5.0.1 Functional gradient with respect to the scattering coefficient

We now seek to minimise the error functional with respect to both the absorption and scattering coefficients, that is, we wish to solve

$$\begin{aligned} \underset{\mu_{\mathrm{a}},\mu_{\mathrm{s}}}{\operatorname{argmin}} \quad \varepsilon &= \frac{1}{2}\left\| h^{\mathrm{obs}} - h(\mu_{\mathrm{a}},\mu_{\mathrm{s}}) \right\|^2 \\ &= \frac{1}{2}\int_{\Omega} (h^{\mathrm{obs}} - h(\mu_{\mathrm{a}},\mu_{\mathrm{s}}))^2 \,\mathrm{d}\Omega. \end{aligned} \tag{5.1}$$

The fact that the scattering is now considered unknown does not change the calculation of the functional gradient with respect to absorption presented in Section 4.1.3. We now only need to consider the functional gradient with respect to the scattering coefficient.

Consider the scattering coefficient μ_{s} at a point $\mathbf{r}_i \in \Omega$, which we will denote by $\mu_{\mathrm{s}}^i := \mu_{\mathrm{s}}(\mathbf{r}_i)$. To calculate the scattering gradient of the objective function, differentiate Equation 5.1 with respect to μ_{s}^i to obtain

$$\frac{\partial \varepsilon}{\partial \mu_{\mathrm{s}}^i} = -\int_{\Omega} \frac{\partial h}{\partial \mu_{\mathrm{s}}^i}(h^{\mathrm{obs}} - h)\,\mathrm{d}\Omega. \tag{5.2}$$

Since $h = \mu_{\mathrm{a}}\Phi$, this can be written equivalently as

$$\frac{\partial \varepsilon}{\partial \mu_{\mathrm{s}}^i} = -\int_{\Omega} \frac{\partial \Phi}{\partial \mu_{\mathrm{s}}^i}\mu_{\mathrm{a}}(h^{\mathrm{obs}} - h)\,\mathrm{d}\Omega. \tag{5.3}$$

Now recall that the time-independent RTE is given by

$$(\hat{\mathbf{s}}\cdot\nabla + \mu_{\mathrm{a}}(\mathbf{r}) + \mu_{\mathrm{s}}(\mathbf{r}))\phi(\mathbf{r},\hat{\mathbf{s}}) = \mu_{\mathrm{s}}(\mathbf{r})\int_{S^{n-1}} \Theta(\hat{\mathbf{s}},\hat{\mathbf{s}}')\phi(\mathbf{r},\hat{\mathbf{s}}')\,\mathrm{d}\hat{\mathbf{s}}' + q(\mathbf{r},\hat{\mathbf{s}}). \tag{5.4}$$

The sensitivity of the fluence Φ to changes in the scattering coefficient can be found by differentiating the RTE with respect to μ_{s}^i, which yields

$$\begin{aligned}(\hat{\mathbf{s}}\cdot\nabla+\mu_{\mathrm{a}}+\mu_{\mathrm{s}})\frac{\partial\phi}{\partial\mu_{\mathrm{s}}^i}-\mu_{\mathrm{s}}\int_{S^{n-1}}\Theta(\hat{\mathbf{s}},\hat{\mathbf{s}}')\frac{\partial\phi(\hat{\mathbf{s}}')}{\partial\mu_{\mathrm{s}}^i}\,\mathrm{d}\hat{\mathbf{s}}'\\ =\left(\int_{S^{n-1}}\Theta(\hat{\mathbf{s}},\hat{\mathbf{s}}')\frac{\partial\phi(\hat{\mathbf{s}}')}{\partial\mu_{\mathrm{s}}^i}\,\mathrm{d}\hat{\mathbf{s}}'-\phi(\hat{\mathbf{s}})\right)\delta(\mathbf{r}-\mathbf{r}_i).\end{aligned}\tag{5.5}$$

Similarly to Section 4.1.3, an adjoint model is introduced to assist the gradient calculation. The adjoint RTE model is defined by

$$(-\hat{\mathbf{s}}\cdot\nabla+\mu_{\mathrm{a}}+\mu_{\mathrm{s}})\phi^*(\hat{\mathbf{s}})-\mu_{\mathrm{s}}\int_{S^{n-1}}\Theta(\hat{\mathbf{s}},\hat{\mathbf{s}}')\phi^*(\hat{\mathbf{s}}')\,\mathrm{d}\hat{\mathbf{s}}'=\mu_{\mathrm{a}}(h^{\mathrm{obs}}-h),\tag{5.6}$$

and has solution ϕ^*, the adjoint radiance. Evaluating $\phi^*\times$(5.5) $-(\partial\phi/\partial\mu_{\mathrm{s}}^i)\times$(5.6) yields

$$\begin{aligned}&\phi^*(\hat{\mathbf{s}})(\hat{\mathbf{s}}\cdot\nabla)\frac{\partial\phi(\hat{\mathbf{s}})}{\partial\mu_{\mathrm{s}}^i}+\frac{\partial\phi(\hat{\mathbf{s}})}{\partial\mu_{\mathrm{s}}^i}(\hat{\mathbf{s}}\cdot\nabla)\phi^*(\hat{\mathbf{s}})\\ &\quad-\phi^*(\hat{\mathbf{s}})\mu_{\mathrm{s}}\int_{S^{n-1}}\Theta(\hat{\mathbf{s}},\hat{\mathbf{s}}')\frac{\partial\phi(\hat{\mathbf{s}}')}{\partial\mu_{\mathrm{s}}^i}\,\mathrm{d}\hat{\mathbf{s}}'+\frac{\partial\phi(\hat{\mathbf{s}})}{\partial\mu_{\mathrm{s}}^i}\mu_{\mathrm{s}}\int_{S^{n-1}}\Theta(\hat{\mathbf{s}},\hat{\mathbf{s}}')\phi^*(\hat{\mathbf{s}}')\,\mathrm{d}\hat{\mathbf{s}}'\\ &\quad=\left(\int_{S^{n-1}}\Theta(\hat{\mathbf{s}},\hat{\mathbf{s}}')\phi^*(\hat{\mathbf{s}})\phi(\hat{\mathbf{s}}')\,\mathrm{d}\hat{\mathbf{s}}'-\phi^*(\hat{\mathbf{s}})\phi(\hat{\mathbf{s}})\right)\delta(\mathbf{r}-\mathbf{r}_i)-\frac{\partial\phi(\hat{\mathbf{s}})}{\partial\mu_{\mathrm{s}}^i}\mu_{\mathrm{a}}(h^{\mathrm{obs}}-h).\end{aligned}\tag{5.7}$$

Similarly to Equation 4.10 in the absorption case, this equation can be reduced significantly by integrating over all angles $\hat{\mathbf{s}}\in S^{n-1}$ and over the domain Ω to obtain

$$\begin{aligned}&\int_\Omega\int_{S^{n-1}}\phi^*(\hat{\mathbf{s}})(\hat{\mathbf{s}}\cdot\nabla)\frac{\partial\phi(\hat{\mathbf{s}})}{\partial\mu_{\mathrm{s}}^i}\,\mathrm{d}\hat{\mathbf{s}}\,\mathrm{d}\Omega+\int_\Omega\int_{S^{n-1}}\frac{\partial\phi(\hat{\mathbf{s}})}{\partial\mu_{\mathrm{s}}^i}(\hat{\mathbf{s}}\cdot\nabla)\phi^*(\hat{\mathbf{s}})\,\mathrm{d}\hat{\mathbf{s}}\,\mathrm{d}\Omega\\ &\quad-\int_\Omega\mu_{\mathrm{s}}\int_{S^{n-1}}\phi^*(\hat{\mathbf{s}})\int_{S^{n-1}}\Theta(\hat{\mathbf{s}},\hat{\mathbf{s}}')\frac{\partial\phi(\hat{\mathbf{s}}')}{\partial\mu_{\mathrm{s}}^i}\,\mathrm{d}\hat{\mathbf{s}}'\,\mathrm{d}\hat{\mathbf{s}}\,\mathrm{d}\Omega\\ &\quad+\int_\Omega\mu_{\mathrm{s}}\int_{S^{n-1}}\frac{\partial\phi(\hat{\mathbf{s}})}{\partial\mu_{\mathrm{s}}^i}\int_{S^{n-1}}\Theta(\hat{\mathbf{s}},\hat{\mathbf{s}}')\phi^*(\hat{\mathbf{s}}')\,\mathrm{d}\hat{\mathbf{s}}'\,\mathrm{d}\hat{\mathbf{s}}\,\mathrm{d}\Omega\\ &\quad=\int_\Omega\int_{S^{n-1}}\left(\int_{S^{n-1}}\Theta(\hat{\mathbf{s}},\hat{\mathbf{s}}')\phi^*(\hat{\mathbf{s}})\phi(\hat{\mathbf{s}}')\,\mathrm{d}\hat{\mathbf{s}}'-\phi^*(\hat{\mathbf{s}})\phi(\hat{\mathbf{s}})\right)\mathrm{d}\hat{\mathbf{s}}\,\delta(\mathbf{r}-\mathbf{r}_i)\,\mathrm{d}\Omega\\ &\qquad-\int_\Omega\mu_{\mathrm{a}}(h^{\mathrm{obs}}-h)\int_{S^{n-1}}\frac{\partial\phi(\hat{\mathbf{s}})}{\partial\mu_{\mathrm{s}}^i}\,\mathrm{d}\hat{\mathbf{s}}\,\mathrm{d}\Omega.\end{aligned}\tag{5.8}$$

The divergence theorem, given by Equation 4.12, is used again to replace the first two terms of Equation 5.8 with an integral over the boundary $\partial\Omega$:

$$\begin{aligned}&\int_\Omega \int_{S^{n-1}} \phi^*(\hat{\mathbf{s}})(\hat{\mathbf{s}}\cdot\nabla)\frac{\partial\phi(\hat{\mathbf{s}})}{\partial\mu_\mathrm{s}^i}\,\mathrm{d}\hat{\mathbf{s}}\,\mathrm{d}\Omega + \int_\Omega \int_{S^{n-1}} \frac{\partial\phi(\hat{\mathbf{s}})}{\partial\mu_\mathrm{s}^i}(\hat{\mathbf{s}}\cdot\nabla)\phi^*(\hat{\mathbf{s}})\,\mathrm{d}\hat{\mathbf{s}}\,\mathrm{d}\Omega \\ &\quad = \int_{\partial\Omega}\int_{S^{n-1}} (\hat{\mathbf{s}}\cdot\hat{\mathbf{n}})\phi^*(\hat{\mathbf{s}})\frac{\partial\phi(\hat{\mathbf{s}})}{\partial\mu_\mathrm{s}^i}\,\mathrm{d}\hat{\mathbf{s}}\,\mathrm{d}\Omega. \end{aligned} \tag{5.9}$$

It is now clear that this single term equates to zero, since both $\phi^* \to 0$ and $\partial\phi/\partial\mu_\mathrm{s}^i \to 0$ on $\partial\Omega$. Equation 4.11 therefore reduces to

$$\begin{aligned}&\int_\Omega \mu_\mathrm{s} \int_{S^{n-1}}\int_{S^{n-1}} \Theta(\hat{\mathbf{s}},\hat{\mathbf{s}}')\phi^*(\hat{\mathbf{s}})\frac{\partial\phi(\hat{\mathbf{s}}')}{\partial\mu_\mathrm{s}^i}\,\mathrm{d}\hat{\mathbf{s}}'\,\mathrm{d}\hat{\mathbf{s}}\,\mathrm{d}\Omega \\ &\quad - \int_\Omega \mu_\mathrm{s} \int_{S^{n-1}}\int_{S^{n-1}} \Theta(\hat{\mathbf{s}},\hat{\mathbf{s}}')\phi^*(\hat{\mathbf{s}}')\frac{\partial\phi(\hat{\mathbf{s}})}{\partial\mu_\mathrm{s}^i}\,\mathrm{d}\hat{\mathbf{s}}'\,\mathrm{d}\hat{\mathbf{s}}\,\mathrm{d}\Omega \\ &\quad = \int_\Omega \int_{S^{n-1}} \left(\phi^*(\hat{\mathbf{s}})\phi(\hat{\mathbf{s}}) - \int_{S^{n-1}} \Theta(\hat{\mathbf{s}},\hat{\mathbf{s}}')\phi^*(\hat{\mathbf{s}})\phi(\hat{\mathbf{s}}')\,\mathrm{d}\hat{\mathbf{s}}'\right)\,\mathrm{d}\hat{\mathbf{s}}\,\delta(\mathbf{r}-\mathbf{r}_i)\,\mathrm{d}\Omega \\ &\qquad + \int_\Omega \mu_\mathrm{a}(h^\mathrm{obs}-h)\int_{S^{n-1}} \frac{\partial\phi(\hat{\mathbf{s}})}{\partial\mu_\mathrm{s}^i}\,\mathrm{d}\hat{\mathbf{s}}\,\mathrm{d}\Omega. \end{aligned} \tag{5.10}$$

Since Θ is a symmetric function, the left-hand side of Equation 5.10 also equates to zero, leaving us with

$$\begin{aligned}&-\int_\Omega \mu_\mathrm{a}(h^\mathrm{obs}-h)\int_{S^{n-1}} \frac{\partial\phi(\hat{\mathbf{s}})}{\partial\mu_\mathrm{a}^i}\,\mathrm{d}\hat{\mathbf{s}}\,\mathrm{d}\Omega \\ &\quad = \int_\Omega \int_{S^{n-1}} \left(\phi^*(\hat{\mathbf{s}})\phi(\hat{\mathbf{s}}) - \int_{S^{n-1}} \Theta(\hat{\mathbf{s}},\hat{\mathbf{s}}')\phi^*(\hat{\mathbf{s}})\phi(\hat{\mathbf{s}}')\,\mathrm{d}\hat{\mathbf{s}}'\right)\,\mathrm{d}\hat{\mathbf{s}}\,\delta(\mathbf{r}-\mathbf{r}_i)\,\mathrm{d}\Omega. \end{aligned} \tag{5.11}$$

The fluence Φ is equal to the integral over all directions $\hat{\mathbf{s}}$ of the time-integrated radiance ϕ, that is,

$$\Phi(\mathbf{r}) = \int_{S^{n-1}} \phi(\mathbf{r},\hat{\mathbf{s}})\mathrm{d}\hat{\mathbf{s}}. \tag{5.12}$$

It therefore follows that

$$\frac{\partial\Phi}{\partial\mu_\mathrm{s}^i} = \int_{S^{n-1}} \frac{\partial\phi(\hat{\mathbf{s}})}{\partial\mu_\mathrm{s}^i}\mathrm{d}\hat{\mathbf{s}}, \tag{5.13}$$

and hence Equation 5.11 can be written as

$$
\begin{aligned}
&-\int_{\Omega} \frac{\partial \Phi}{\partial \mu_{\mathrm{s}}^{i}} \mu_{\mathrm{a}}(h^{\mathrm{obs}} - h)\, \mathrm{d}\Omega \\
&\quad = \left[\int_{S^{n-1}} \phi^{*}(\hat{\mathbf{s}}) \phi(\hat{\mathbf{s}})\, \mathrm{d}\hat{\mathbf{s}} \right]_{\mathbf{r}=\mathbf{r}_i} \\
&\qquad - \left[\int_{S^{n-1}} \int_{S^{n-1}} \Theta(\hat{\mathbf{s}}, \hat{\mathbf{s}}') \phi^{*}(\hat{\mathbf{s}}) \phi(\hat{\mathbf{s}}')\, \mathrm{d}\hat{\mathbf{s}}'\, \mathrm{d}\hat{\mathbf{s}} \right]_{\mathbf{r}=\mathbf{r}_i}.
\end{aligned} \tag{5.14}
$$

We can now equate Equation 5.14 and Equation 5.3 to obtain an expression for the scattering gradient

$$
\begin{aligned}
\frac{\partial \varepsilon}{\partial \mu_{\mathrm{s}}^{i}} &= \left[\int_{S^{n-1}} \phi^{*}(\hat{\mathbf{s}}) \phi(\hat{\mathbf{s}})\, \mathrm{d}\hat{\mathbf{s}} \right]_{\mathbf{r}=\mathbf{r}_i} \\
&\quad - \left[\int_{S^{n-1}} \int_{S^{n-1}} \Theta(\hat{\mathbf{s}}, \hat{\mathbf{s}}') \phi^{*}(\hat{\mathbf{s}}) \phi(\hat{\mathbf{s}}')\, \mathrm{d}\hat{\mathbf{s}}'\, \mathrm{d}\hat{\mathbf{s}} \right]_{\mathbf{r}=\mathbf{r}_i}.
\end{aligned} \tag{5.15}
$$

It then follows that, in general, the error functional gradient with respect to the scattering coefficient is given by

$$
\frac{\partial \varepsilon}{\partial \mu_{\mathrm{s}}} = \int_{S^{n-1}} \phi^{*}(\hat{\mathbf{s}}) \phi(\hat{\mathbf{s}})\, \mathrm{d}\hat{\mathbf{s}} - \int_{S^{n-1}} \int_{S^{n-1}} \Theta(\hat{\mathbf{s}}, \hat{\mathbf{s}}') \phi^{*}(\hat{\mathbf{s}}) \phi(\hat{\mathbf{s}}')\, \mathrm{d}\hat{\mathbf{s}}' \mathrm{d}\hat{\mathbf{s}}. \tag{5.16}
$$

5.0.2 Implementation

As in Section 4.1.4, the least-squares error functional (Equation 5.1) can be written in vector notation as

$$
\varepsilon(\mu_{\mathrm{a}}, \mu_{\mathrm{s}}) = \frac{1}{2} (h^{\mathrm{obs}} - h)^{\mathrm{T}} (h^{\mathrm{obs}} - h), \tag{5.17}
$$

and its derivative with respect to μ_{s}^k, the absorption over the k^{th} element, as

$$\begin{aligned} \frac{\partial \varepsilon}{\partial \mu_{\mathrm{s}}^k} &= -\left(\frac{\partial h}{\partial \mu_{\mathrm{s}}^k}\right)^{\mathrm{T}} (h^{\mathrm{obs}} - h) \\ \Rightarrow \frac{\partial \varepsilon}{\partial \mu_{\mathrm{s}}^k} &= -\left(\mu_{\mathrm{a}} \frac{\partial \Phi}{\partial \mu_{\mathrm{s}}^k}\right)^{\mathrm{T}} (h^{\mathrm{obs}} - h) \\ \Rightarrow \frac{\partial \varepsilon}{\partial \mu_{\mathrm{s}}^k} &= -\left(\mu_{\mathrm{a}} M \frac{\partial \phi}{\partial \mu_{\mathrm{s}}^k}\right)^{\mathrm{T}} (h^{\mathrm{obs}} - h). \end{aligned} \tag{5.18}$$

The sensitivity of the radiance to changes in the scattering coefficient is found by differentiating the FE model of the RTE, given by

$$A\phi = b, \tag{5.19}$$

with respect to μ_{s}^k. Doing so and applying the product rule, we obtain

$$\begin{aligned} \frac{\partial A}{\partial \mu_{\mathrm{s}}^k}\phi + A\frac{\partial \phi}{\partial \mu_{\mathrm{s}}^k} &= 0 \\ \Rightarrow \frac{\partial \phi}{\partial \mu_{\mathrm{s}}^k} &= -A^{-1}\left(\frac{\partial A}{\partial \mu_{\mathrm{s}}^k}\right)\phi. \end{aligned} \tag{5.20}$$

Substituting this into Equation 5.18 then gives

$$\begin{aligned} \frac{\partial \varepsilon}{\partial \mu_{\mathrm{s}}^k} &= \left(\mu_{\mathrm{a}} M A^{-1}\left(\frac{\partial A}{\partial \mu_{\mathrm{s}}^k}\right)\phi\right)^{\mathrm{T}} (h^{\mathrm{obs}} - h) \\ \Rightarrow \frac{\partial \varepsilon}{\partial \mu_{\mathrm{s}}^k} &= \phi^{\mathrm{T}}\left(\frac{\partial A}{\partial \mu_{\mathrm{a}}^k}\right)^{\mathrm{T}} (A^{\mathrm{T}})^{-1}(\mu_{\mathrm{a}} M)^{\mathrm{T}}(h^{\mathrm{obs}} - h), \end{aligned} \tag{5.21}$$

where $\partial A/\partial \mu_{\mathrm{s}}^k$ is the gradient of the FE system matrix, given by Equation 4.25, with respect to the scattering coefficient. For each element $k = 1, \ldots, N_e$, this is given by

$$\begin{aligned} \frac{\partial A}{\partial \mu_{\mathrm{s}}^k} = &\int_\Omega \chi_k(\mathbf{r})\psi_j(\mathbf{r})\psi_{j'}(\mathbf{r})\,\mathrm{d}\mathbf{r} \int_{S^{n-1}} \psi_l(\hat{\mathbf{s}})\psi_{l'}(\hat{\mathbf{s}})\,\mathrm{d}\hat{\mathbf{s}} \\ &- \int_\Omega \chi_k(\mathbf{r})\psi_j(\mathbf{r})\psi_{j'}(\mathbf{r})\,\mathrm{d}\mathbf{r} \int_{S^{n-1}} \int_{S^{n-1}} \Theta(\hat{\mathbf{s}}, \hat{\mathbf{s}}')\psi_l(\hat{\mathbf{s}}')\,\mathrm{d}\hat{\mathbf{s}}'\ \psi_{l'}(\hat{\mathbf{s}})\,\mathrm{d}\hat{\mathbf{s}}. \end{aligned} \tag{5.22}$$

The FE RTE adjoint model corresponding to Equation 4.9 is given by

$$A^{\mathrm{T}}\phi^* := (\mu_{\mathrm{a}}M)^{\mathrm{T}}(h^{\mathrm{obs}} - h), \tag{5.23}$$

which we can substitute into Equation 5.21 to obtain

$$\frac{\partial\varepsilon}{\partial\mu_{\mathrm{s}}^k} = \phi^{\mathrm{T}}\left(\frac{\partial A}{\partial\mu_{\mathrm{s}}^k}\right)^{\mathrm{T}}\phi^*. \tag{5.24}$$

This leads to a general expression for the gradient of the error functional with respect to the scattering coefficient

$$\frac{\partial\varepsilon}{\partial\mu_{\mathrm{s}}} = \phi^{\mathrm{T}}\left(\frac{\partial A}{\partial\mu_{\mathrm{s}}}\right)^{\mathrm{T}}\phi^*. \tag{5.25}$$

The gradient of the error functional with respect to the absorption coefficient was calculated in Section 4.1.3, and so we now have expressions for the functional gradients with respect to both coefficients

$$\frac{\partial\varepsilon}{\partial\mu_{\mathrm{a}}} = \phi^{\mathrm{T}}\left(\frac{\partial A}{\partial\mu_{\mathrm{a}}}\right)^{\mathrm{T}}\phi^* - \Phi^{\mathrm{T}}(h^{\mathrm{obs}} - h), \tag{5.26}$$

$$\frac{\partial\varepsilon}{\partial\mu_{\mathrm{s}}} = \phi^{\mathrm{T}}\left(\frac{\partial A}{\partial\mu_{\mathrm{s}}}\right)^{\mathrm{T}}\phi^*. \tag{5.27}$$

Since the forward and adjoint fluences are the same in both the absorption and scattering case, we can now calculate both functional gradients with one run each of the two models.

5.0.2.1 Extension to multiple illumination positions

The inclusion of multiple PA images into the inversion requires the summation of the data over the number of sources. If N_s is the number of source positions, then the error

functional becomes

$$\varepsilon = \sum_{p=1}^{N_s} \sum_{k=1}^{N_e} \frac{1}{2} (h_p^{\text{obs}}(\mathbf{r}_k) - h_p(\mathbf{r}_k))^2, \tag{5.28}$$

where the subscript $\cdot_p$ denotes the quantity at the p^{th} source position. The error functional gradients must also be summed over the number of source positions, in which case we have

$$\frac{\partial \varepsilon}{\partial \mu_{\text{a}}} = -\sum_{p=1}^{N_s} \Phi_p^{\text{T}} (h_p^{\text{obs}} - h_p) + \sum_{p=1}^{N_s} \phi_p^{\text{T}} \left(\frac{\partial A}{\partial \mu_{\text{a}}} \right)^{\text{T}} \phi_p^* \tag{5.29}$$

and

$$\frac{\partial \varepsilon}{\partial \mu_{\text{s}}} = \sum_{p=1}^{N_s} \phi_p^{\text{T}} \left(\frac{\partial A}{\partial \mu_{\text{s}}} \right)^{\text{T}} \phi_p^*. \tag{5.30}$$

5.0.3 Comparison with finite difference calculation

We discussed in Section 4.1.5 that finite difference methods can be used to approximate the error functional gradients. The method, though robust and accurate, can be time-consuming; calculating the functional gradient with respect to absorption will require $N_e + 1$ evaluations of the forward model, where N_e is the number of elements in the computational mesh. Calculating the functional gradient with respect to the scattering coefficient will demand a further N_e evaluations of the forward model. Determining both functional gradients using a finite difference method will therefore require $2N_e + 1$ evaluations of the forward model. On the other hand, the adjoint-assisted method can be used to calculate both functional gradients with respect to absorption and scattering using only a single run each of the forward and adjoint models, equivalent to two evaluations of the forward model.

FIGURE 5.1: Error functional gradient with respect to scattering calculated using the adjoint-assisted method presented in Section 5.0.1, compared with those calculated using a finite difference method. The absorption and scattering coefficients are both heterogeneous and can be seen in Figures 3.4(A) and 3.4(B). Given an initial guess at the absorption coefficient, the error functional 5.1 can be calculated straightforwardly. The functional gradient with respect to scattering can then be calculated using the adjoint-assisted method (Equation 5.26) and also using a finite difference method. The figure below shows the functional gradient with respect to absorption calculated using (A) the adjoint-assisted method and (B) a finite difference method. The difference between the two is shown in (C) and a profile in the z-direction at $x = 1$ mm can be seen in (D).

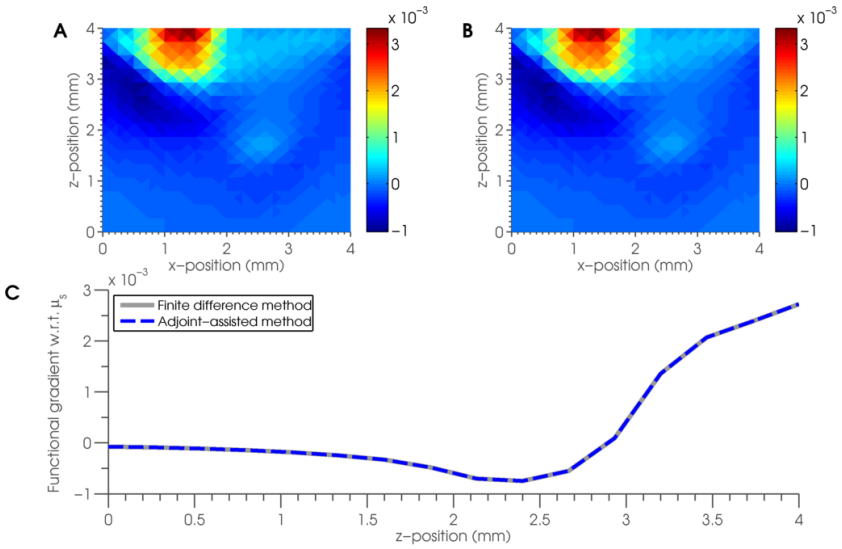

In Section 4.1.5, we verified that the adjoint-assisted calculation for the functional gradient with respect to absorption is correct. We will now use a finite difference calculation to verify the adjoint-assisted calculation for the functional gradient with respect to the scattering coefficient. The absorption and scattering coefficients and absorbed energy distribution are the same as used in Section 4.1.5. Figure 5.1(A) shows the absorption gradient calculated using the adjoint-assisted method, and Figure 5.1(B) shows the absorption gradient calculated using a finite difference method. As in the absorption case, there is excellent agreement between the two figures. A profile comparison is shown in Figure 5.1(C). The relative error for the scattering coefficient can be calculated using

$$\varepsilon_{\mathrm{s}} = \frac{\left\| \left(\frac{\partial \varepsilon}{\partial \mu_{\mathrm{s}}} \right)_{\mathrm{FD}} - \left(\frac{\partial \varepsilon}{\partial \mu_{\mathrm{s}}} \right)_{\mathrm{adj}} \right\|}{\left\| \left(\frac{\partial \varepsilon}{\partial \mu_{\mathrm{s}}} \right)_{\mathrm{FD}} \right\|}, \tag{5.31}$$

where $(\partial \varepsilon / \partial \mu_{\mathrm{s}})_{\mathrm{FD}}$ and $(\partial \varepsilon / \partial \mu_{\mathrm{s}})_{\mathrm{adj}}$ are the functional gradients with respect to scattering

calculated using the finite difference method and adjoint-assisted method, respectively. The relative error in this case was $\varepsilon_{\mathrm{a}} = 2.59 \times 10^{-5}$ %, and the finite difference calculation took approximately 1 hour 26 minutes to calculate both the absorption and scattering gradients, compared with under 6 seconds to complete the adjoint-assisted method.

5.0.4 Regularisation

In Section 3.4.1, we discussed how the second-order dependence of the measurement data on the scattering coefficient can lead to the amplification of high frequencies in the scattering inversion. To mitigate these effects, a first order Tikhonov regularisation penalty term is added to the error functional whenever noise is present in the simulated measurement data. This has a smoothing effect on the solution to the scattering coefficient. A large amount of literature on regularisation techniques for inverse problems exists, e.g. [89–94], and other forms of regularisation could easily be incorporated into this inversion scheme. The inclusion of a Tikhonov penalty term means that the error functional is now given by

$$\varepsilon = \sum_{p=1}^{N_p} \sum_{k=1}^{N} \frac{1}{2} (h_p^{\mathrm{obs}}(\mathbf{r}_k) - h_p(\mathbf{r}_k))^2 + \frac{1}{2} \beta \left| \nabla \mu_{\mathrm{s}} \right|^2 , \tag{5.32}$$

where β is a constant scaling factor. This additional term changes the functional gradient for the scattering, which now includes the additional term

$$\frac{\partial \varepsilon}{\partial \mu_{\mathrm{s}}} = \sum_{p=1}^{N_p} \phi_p^{\mathrm{T}} \left(\frac{\partial A}{\partial \mu_{\mathrm{s}}} \right)^{\mathrm{T}} \phi_p^* + \beta \nabla^2 \mu_{\mathrm{s}}. \tag{5.33}$$

The effect of adjusting the regularisation parameter β can be seen in Figure 5.2. In this left-hand column of this figure, (A) shows the true absorption coefficient, and (B)-(E) show the reconstructed absorption coefficient using $\beta = 1$, $\beta = 10^{-3}$, $\beta = 10^{-6}$ and $\beta = 10^{-8}$, respectively. In the right-hand column of Figure 5.2, figure (F) shows the true

FIGURE 5.2: The effect of varying the regularisation parameter β on the reconstructed optical coefficients. (A) shows the true absorption coefficient, and (B)-(E) show the reconstructed absorption coefficient using $\beta = 1$, $\beta = 10^{-3}$, $\beta = 10^{-6}$ and $\beta = 10^{-8}$, respectively. (F) shows the true scattering coefficient, and (G)-(J) show the reconstructed scattering coefficient using $\beta = 1$, $\beta = 10^{-3}$, $\beta = 10^{-6}$ and $\beta = 10^{-8}$, respectively.

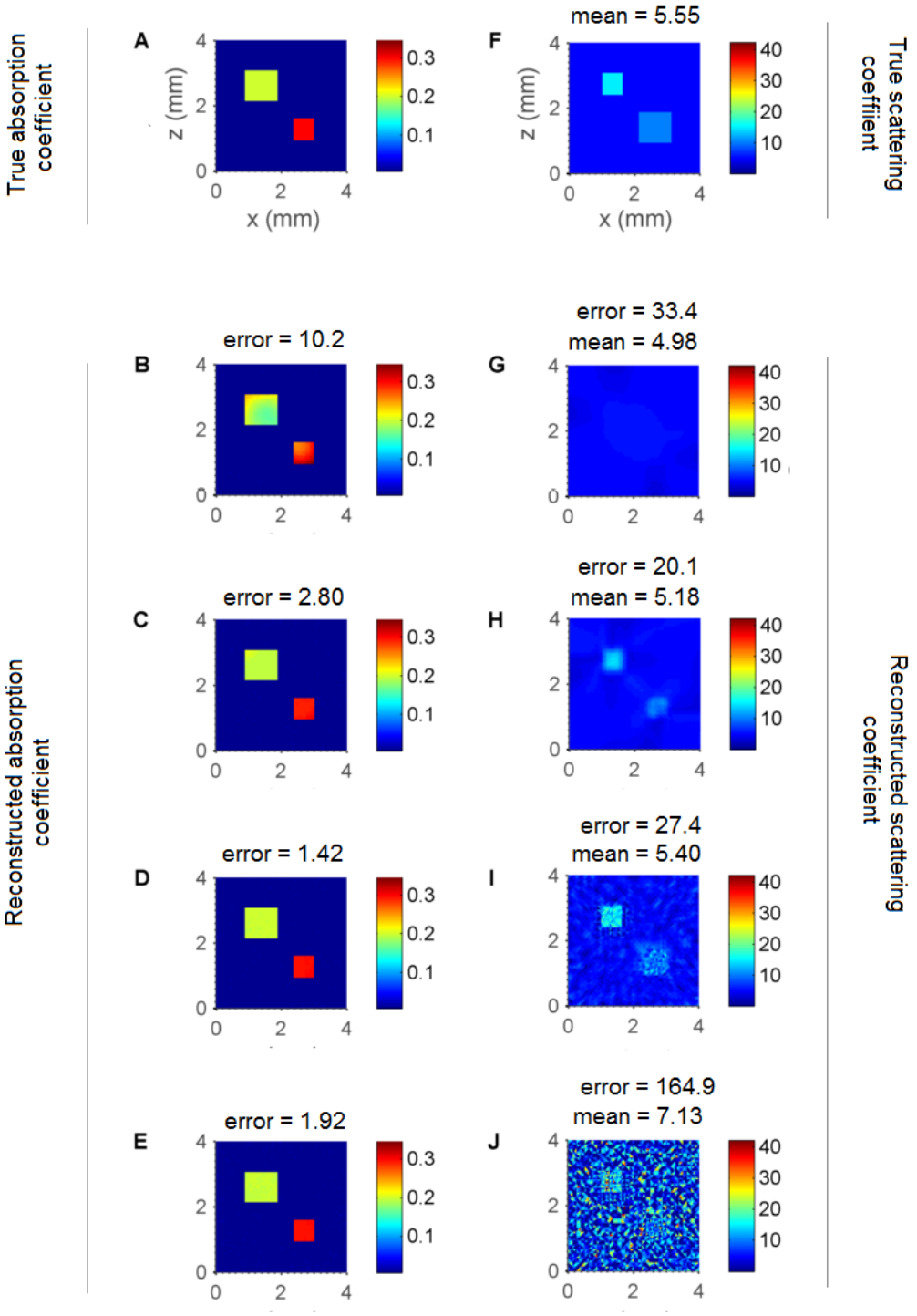

scattering coefficient, and (G)-(J) show the reconstructed scattering coefficient using $\beta = 1$, $\beta = 10^{-3}$, $\beta = 10^{-6}$ and $\beta = 10^{-8}$, respectively. In the case where $\beta = 1$, the largest amount of regularisation used here, the reconstructed scattering coefficient is smoothed out almost entirely to the background value. As we decrease the amount of regularisation to 10^{-3} and then to 10^{-6}, the heterogeneities in the scattering coefficient can be seen and the reconstruction begins to improve. However, reducing β to as small as 10^{-8} removes the effect of the regularisation, and allows the high frequency components of the noise to be amplified and produce very large errors in the scattering reconstruction. It is worth nothing, however, that the instability and errors which appear in the scattering reconstruction when very little regularisation is applied do not produce comparable errors in the reconstructed absorption coefficient, and actually under-regularising produces a better absorption estimate than over-regularising and fully smoothing out the scattering. The ability to produce a good quantitative estimate of absorption without including any regularisation at all would be particularly beneficial if little is known about the underlying structure and quantitative values of the optical coefficients, and the choice of an appropriate regularisation scheme and appropriate regularisation parameter is therefore unclear.

Choosing $\beta = 10^{-3}$ results in a smoother reconstruction and a smaller scattering error than when $\beta = 10^{-6}$. However, this smoothing results in an underestimation of the scattering heterogeneities, and therefore produces a larger error in the resulting absorption coefficient ($\epsilon_{\mathrm{a}} = 2.80\%$ compared to $\epsilon_{\mathrm{a}} = 1.42\%$). This can be seen in the profile comparison shown in Figure 5.3. Using $\beta = 10^{-6}$ provides a better quantitative reconstruction in the scattering heterogeneities, though the instability due to the noise is more apparent than when $\beta = 10^{-3}$. The mean scattering, however, is closer to the true scattering mean in the former case, indicating that the noise present in the scattering reconstruction may not adversely affect the resulting absorption estimate provided that the mean of the reconstructed scattering is close to the scattering coefficient's true mean. Following these results, the examples presented in the remainder of these chapter were obtained using a regularisation parameter of $\beta = 10^{-6}$.

FIGURE 5.3: Profile comparison showing the effect of varying the regularisation parameter β on the reconstructed optical coefficients. (A) shows a profile of the true and reconstructed absorption coefficients at $z = 1$ mm, while (B) shows a profile of the true and reconstructed scattering coefficients at $z = 3$ mm. The grey solid lines show the true absorption (A) and scattering (B) coefficients. The reconstructed coefficients using $\beta = 1$ (red dashed), $\beta = 10^{-3}$ (blue dotted), $\beta = 10^{-6}$ (green dashed) and $\beta = 10^{-8}$ (pink dotted).

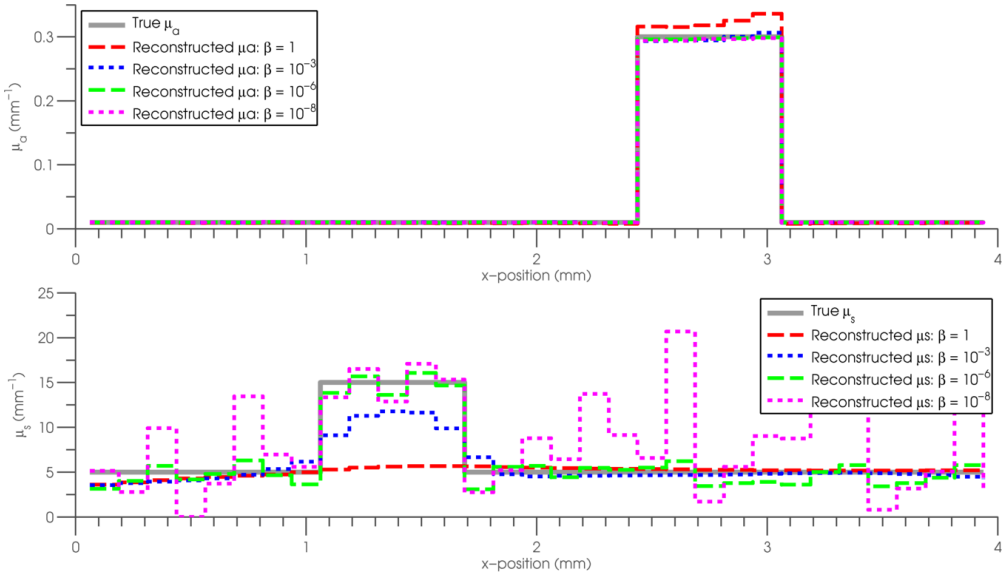

5.1 Numerical examples recovering absorption and scattering

In this section, the gradient-based method which uses the full RTE will be used to recover both optical absorption and scattering simultaneously from 2D simulated PAT images. The method will be tested using several different illumination positions, and the effects of including additive Gaussian noise to the simulated measurement data will be investigated.

5.1.1 Simulation of measurement data

To simulate the measurement data, the same computational mesh, illumination positions and optical properties that were used in Section 4.2.1 are used in this section. The optical properties are shown in Figures 3.4(A) and 3.4(B). This provides consistency

and allows us to compare the results in this chapter with the results obtained for the known- or constant-scattering case. As a reminder, and to provide easier reference for the reader, we will restate these properties here. The computational mesh, used for all the simulations in this chapter, was a 4 mm $\times$ 4 mm square, consisting of $N_e = 3840$ triangular elements, $N_n = 1983$ nodes and a discretisation of $N_a = 16$ equal angles. The anisotropy factor was considered to be known and constant at $g = 0.8$, and the scattering coefficient μ_s was chosen such that $\mu_\mathrm{s}' = \mu_\mathrm{s}(1-g)$ varies between 1 mm^{-1} and 3 mm^{-1}, giving a background value of $\mu_\mathrm{s}^\mathrm{bg} = 5$ mm^{-1} and two non-smooth scattering inclusions of $\mu_\mathrm{s}^1 = 10$ mm^{-1} and $\mu_\mathrm{s}^2 = 15$ mm^{-1}. The absorption coefficient had a background value of $\mu_\mathrm{a}^\mathrm{bg} = 0.01$ mm^{-1} and two non-smooth absorbing inclusions of $\mu_\mathrm{a}^1 = 0.2$ mm^{-1} and $\mu_\mathrm{a}^2 = 0.3$ mm^{-1}.

The source geometries used in Section 4.2.2 were also used to perform these inversions. These can be seen in Figures 4.2 and 4.3. Since multiple illuminations are required to guarantee a unique solution when recovering absorption and scattering simultaneously, inversions using a single point source and single line source (Figures 4.2(A) and 4.3(A)) are omitted.

By solving Equation 4.24, the FE implementation of the RTE, for a particular source b, we obtain the radiance $\phi = \phi(\mu_\mathrm{a}, \mu_\mathrm{s})$, and summing over all angles according to Equation 4.30 gives the fluence $\Phi(\mu_\mathrm{a}, \mu_\mathrm{s})$. The measured absorbed energy is then equal to the product of the absorption coefficient and the fluence, that is, $h^\mathrm{obs} = \mu_\mathrm{a}\Phi(\mu_\mathrm{a}, \mu_\mathrm{s})$. Additive Gaussian noise, scaled to 5% of the mean absorbed energy density, was added to this absorbed energy distribution to simulate the measurement noise which would be present in real photoacoustic data. In each example, the results using noise-free and noisy data are shown.

The background values are used as an initial guess to begin the iterative procedure. To quantify the error in the reconstructions, we shall look at the per cent relative error ϵ_a

and ϵ_{s}, calculated using

$$\epsilon_{\mathrm{a}} = \frac{\left\|\mu_{\mathrm{a}}^{\mathrm{true}} - \mu_{\mathrm{a}}^{\mathrm{approx}}\right\|}{\left\|\mu_{\mathrm{a}}^{\mathrm{true}}\right\|} \tag{5.34}$$

and

$$\epsilon_{\mathrm{s}} = \frac{\left\|\mu_{\mathrm{s}}^{\mathrm{true}} - \mu_{\mathrm{s}}^{\mathrm{approx}}\right\|}{\left\|\mu_{\mathrm{s}}^{\mathrm{true}}\right\|}. \tag{5.35}$$

A positivity constraint was added to threshold the values of the optical coefficients which fall below zero, a reasonable constraint since these values do not make physical sense.

5.1.2 Inversion results: recovering absorption and scattering

5.1.2.1 Two point sources

FIGURE 5.4: Reconstructed absorption and scattering coefficients when using two point sources, corresponding to Figure 4.2(B). (A) shows the true absorption coefficient, (B) shows the reconstructed absorption coefficient from noise-free data, and (C) shows the reconstructed absorption coefficient from data with 5% additive Gaussian noise. (D) shows the true scattering coefficient, (E) shows the reconstructed scattering coefficient from noise-free data, and (F) shows the reconstructed scattering coefficient from data with 5% additive Gaussian noise.

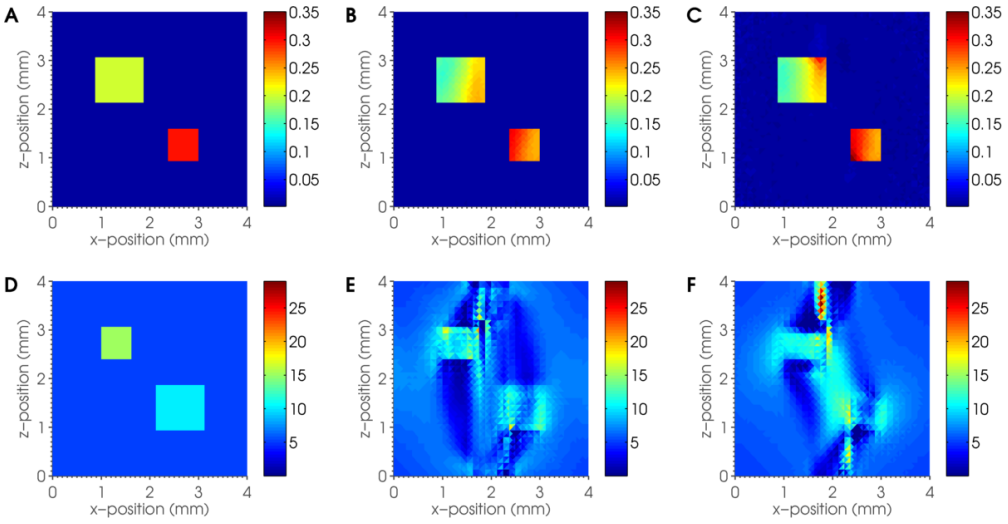

In this example, a set of two images were obtained using two point sources, as shown in Figure 4.2(B). Figure 5.4 shows the recovered absorption and scattering after 1000

FIGURE 5.5: Simultaneous recovery of absorption and scattering coefficients using two point sources. A profile comparison of the reconstructed absorption coefficient can be seen in (A), which compares the true absorption coefficient (grey solid), reconstructed absorption coefficient from noise-free data (blue dashed) and reconstructed absorption coefficient from noisy data (red dotted). The profile is taken in the x-direction at $z = 1.2$ mm. A profile comparison of the reconstructed scattering coefficient can be seen in (B), which compares the true scattering coefficient (grey solid), reconstructed scattering coefficient from noise-free data (blue dashed) and reconstructed scattering coefficient from noisy data (red dotted). The profile is taken in the x-direction at $z = 2.4$ mm. The percent relative errors of the reconstructed absorption (blue) and scattering (red) coefficients at each iteration can be seen in (E).

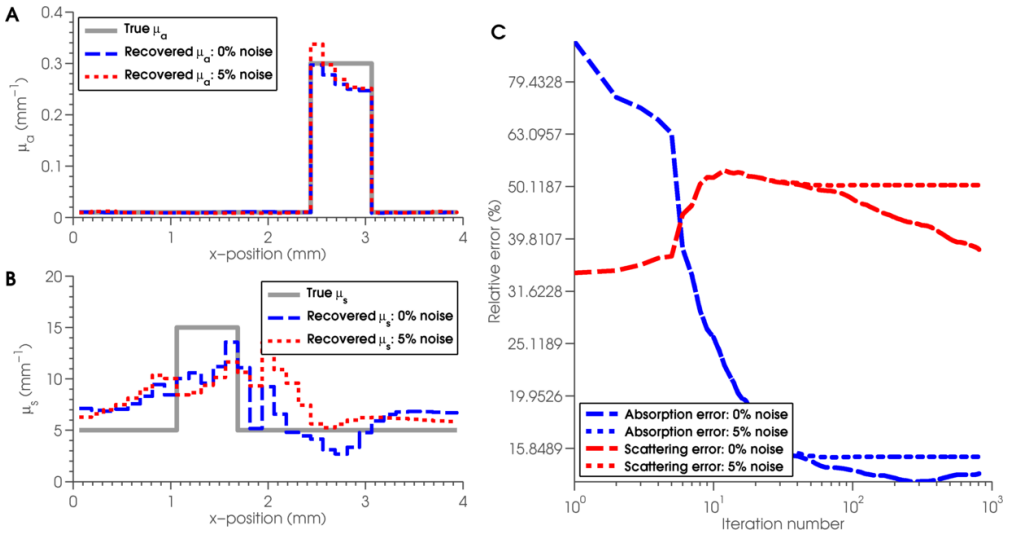

iterations of the l-BFGS method. The percent relative error in the reconstructed absorption for the noise-free and noisy cases are $\epsilon_{\mathrm{a}} = 14.2\%$ and $\epsilon_{\mathrm{a}} = 15.3\%$, respectively. The percent relative error in the reconstructed absorption for the noise-free and noisy cases are $\epsilon_{\mathrm{s}} = 37.9\%$ and $\epsilon_{\mathrm{s}} = 50.4\%$, respectively. The difficulties in recovering the scattering coefficient due to the ill-posedness of the problem, which were discussed in Section 3.4.1, can be seen in the results of this inversion. The reconstruction of the scattering coefficient is quite poor, however, the data is so insensitive to the scattering coefficient that a reasonably good estimate of the absorption coefficient can still be obtained. Figure 5.5 shows a profile comparison of the true and reconstructed absorption and scattering coefficients for this example. The relative error in the reconstructed absorption and scattering coefficients at each iteration can be seen in Figure 5.5(C). The scattering error has increased significantly at around the tenth iteration, even in the noise-free case, indicating that the inversion for the scattering coefficient has been fairly unstable. Despite this, the error in the absorption coefficient continued to decrease, and

a good approximation to the structure and quantitative values in the heterogeneities is obtained, although the error begins to increase towards the boundaries that do not contain a source. As in the previous chapter, it is likely that these results will improve with the incorporation of additional sources along the boundary, or information from additional illumination directions.

5.1.2.2 Two line sources

FIGURE 5.6: Reconstructed absorption and scattering coefficients when using two line sources, corresponding to Figure 4.3(B). (A) shows the true absorption coefficient, (B) shows the reconstructed absorption coefficient from noise-free data, and (C) shows the reconstructed absorption coefficient from data with 5% additive Gaussian noise. (D) shows the true scattering coefficient, (E) shows the reconstructed scattering coefficient from noise-free data, and (F) shows the reconstructed scattering coefficient from data with 5% additive Gaussian noise.

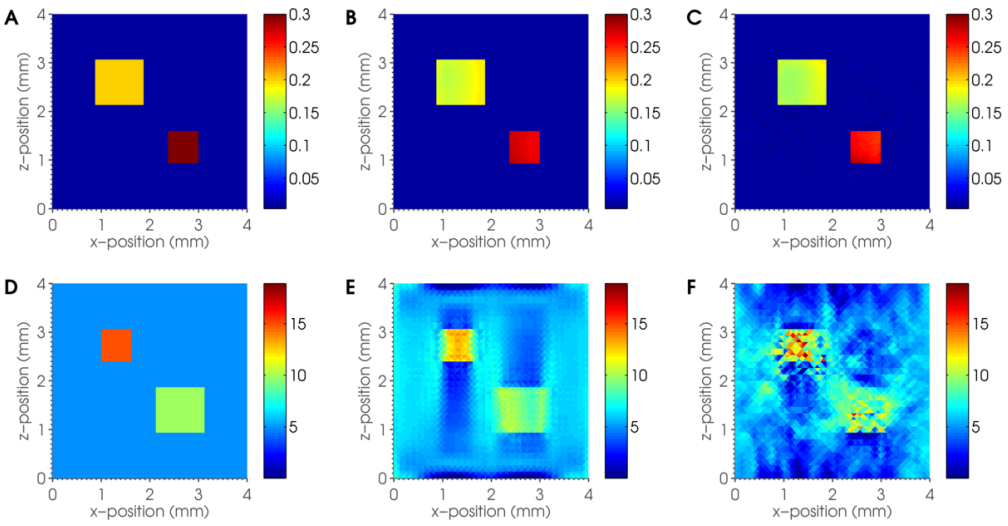

In this example, two images were simulated, with each corresponding to a line source placed at either the top or bottom edge of the domain, as shown in Figure 4.3(B). Figure 5.6 shows the recovered absorption and scattering after 1000 iterations. In this case, the percent relative errors in the absorption coefficient for the noise-free and noisy reconstructions are $\epsilon_{\mathrm{a}} = 10.6\%$ and $\epsilon_{\mathrm{a}} = 15.1\%$, respectively. The percent relative error in the reconstructed absorption for the noise-free and noisy cases are $\epsilon_{\mathrm{s}} = 25.2\%$ and $\epsilon_{\mathrm{s}} = 33.1\%$, respectively. The inclusion of additional sources along the boundary when obtaining the two simulated images has improved the reconstructions significantly. In

FIGURE 5.7: Simultaneous recovery of absorption and scattering coefficients using two line sources. A profile comparison of the reconstructed absorption coefficient can be seen in (A), which compares the true absorption coefficient (grey solid), reconstructed absorption coefficient from noise-free data (blue dashed) and reconstructed absorption coefficient from noisy data (red dotted). The profile is taken in the x-direction at $z = 1.2$ mm. A profile comparison of the reconstructed scattering coefficient can be seen in (B), which compares the true scattering coefficient (grey solid), reconstructed scattering coefficient from noise-free data (blue dashed) and reconstructed scattering coefficient from noisy data (red dotted). The profile is taken in the x-direction at $z = 2.4$ mm. The percent relative errors of the reconstructed absorption (blue) and scattering (red) coefficients at each iteration can be seen in (C).

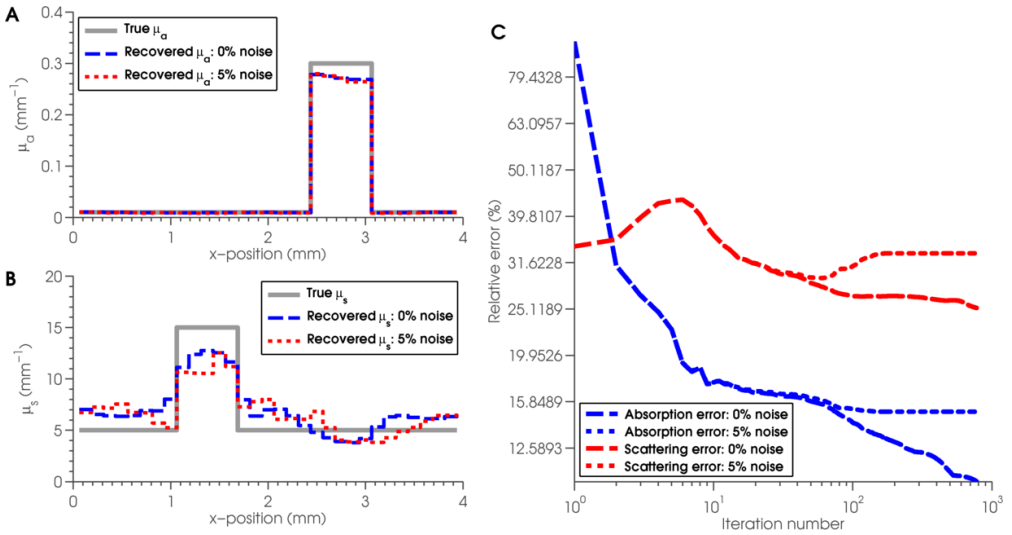

particular, the structure of the scattering coefficient is much more clear, though the values in the two heterogeneities are underestimated significantly. A profile comparison of the true and reconstructed optical coefficients can be seen in Figure 5.7. The absorption coefficient is slightly underestimated, but the correct structure is preserved even without regularisation to the absorption reconstruction, and a good estimate to the quantities in the two heterogeneities is obtained. Figure 5.7 shows a profile comparison of the true and reconstructed absorption and scattering coefficients for this example. The underestimation of the scattering coefficient could be due to the smoothing effect of the Tikhonov regularisation. This type of regularisation is not particularly appropriate for non-smooth parameters such as these, and so the estimation of the scattering coefficient and hence the absorption estimate would likely improve with the incorporation of an edge-preserving regularisation scheme, e.g. total variation [94]. The relative error in the reconstructed absorption and scattering coefficients at each iteration can be seen in Figure 5.7(C). The errors in the reconstructed scattering coefficient using noisy data

show the amplification of noise, and indicate again that the regularisation of the inversion could be improved. The absorption error continually decreases, and has still not converged after as many as 1000 iterations. This suggests that, should better regularisation be applied to the inversion, the reconstructed coefficients might improve if the minimisation is continued for a larger number of iterations.

5.1.2.3 Four point sources

FIGURE 5.8: Reconstructed absorption and scattering coefficients when using four point sources, corresponding to Figure 4.2(C). (A) shows the true absorption coefficient, (B) shows the reconstructed absorption coefficient from noise-free data, and (C) shows the reconstructed absorption coefficient from data with 5% additive Gaussian noise. (D) shows the true scattering coefficient, (E) shows the reconstructed scattering coefficient from noise-free data, and (F) shows the reconstructed scattering coefficient from data with 5% additive Gaussian noise.

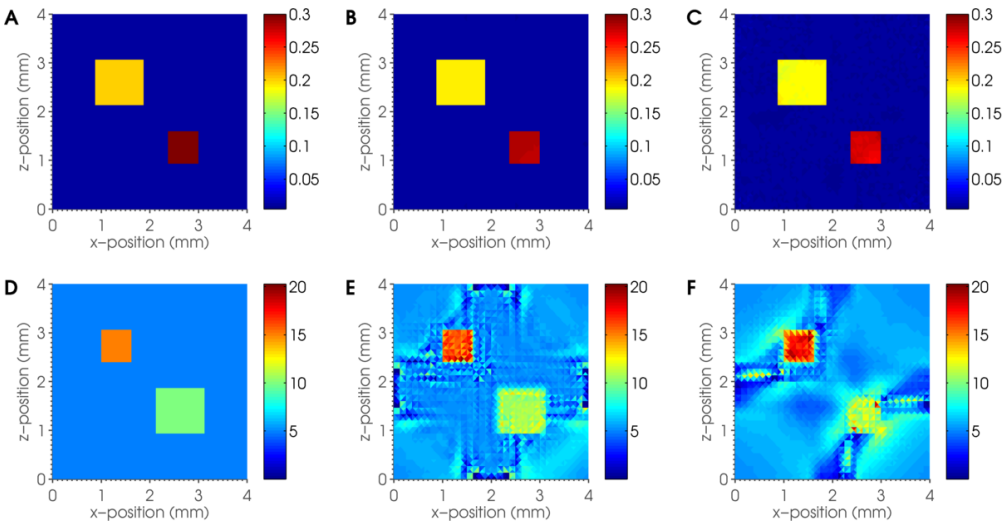

Since the reconstructions in Section 4.2 improved with the incorporation of additional sources, we shall now investigate how well the absorption coefficient can be recovered using the gradient-based method when the domain is illuminated from all four directions. In this case, four images were simulated, each corresponding to a point source placed at either the top, bottom, left-hand side or right-hand side of the domain. We again investigated both the noise-free and noisy scenarios, with 5% Gaussian noise being added to the measurement data in the noisy case. Figure 5.8 shows the reconstructed absorption and scattering coefficients when using these data. In this case, the percent relative errors in the absorption coefficient for the noise-free and noisy reconstructions

FIGURE 5.9: Simultaneous recovery of absorption and scattering coefficients using four point sources. A profile comparison of the reconstructed absorption coefficient can be seen in (A), which compares the true absorption coefficient (grey solid), reconstructed absorption coefficient from noise-free data (blue dashed) and reconstructed absorption coefficient from noisy data (red dotted). The profile is taken in the x-direction at $z = 1.2$ mm. A profile comparison of the reconstructed scattering coefficient can be seen in (B), which compares the true scattering coefficient (grey solid), reconstructed scattering coefficient from noise-free data (blue dashed) and reconstructed scattering coefficient from noisy data (red dotted). The profile is taken in the x-direction at $z = 2.4$ mm. The percent relative errors of the reconstructed absorption (blue) and scattering (red) coefficients at each iteration can be seen in (C).

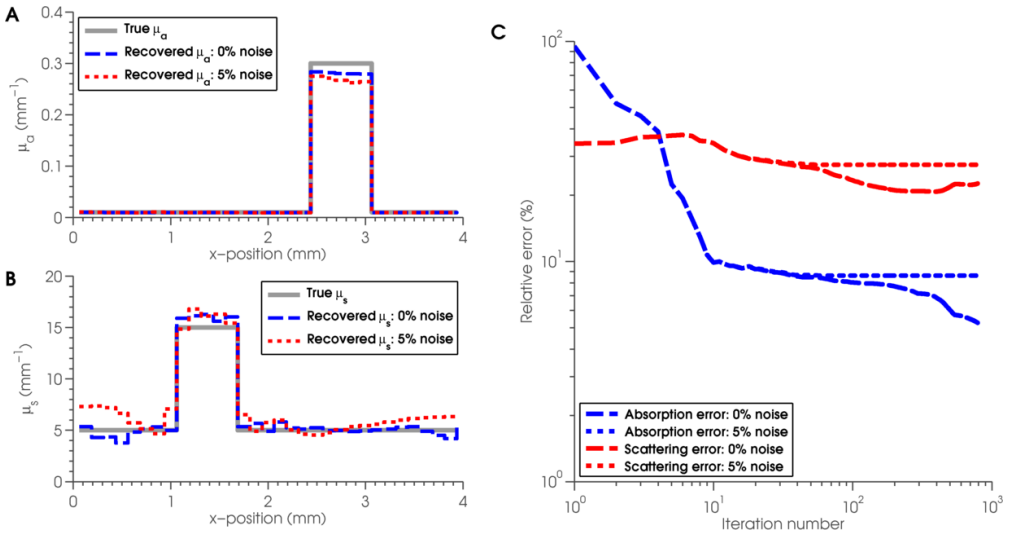

are $\epsilon_{\mathrm{a}} = 5.26\%$ and $\epsilon_{\mathrm{a}} = 8.62\%$, respectively, and the percent relative error in the reconstructed absorption for the noise-free and noisy cases are $\epsilon_{\mathrm{s}} = 22.6\%$ and $\epsilon_{\mathrm{s}} = 27.5\%$, respectively. Interestingly, illuminating from four directions using point sources produces a more accurate quantitative reconstruction in both optical coefficients than when using two line sources, suggesting that it might be preferable to illuminate from more directions with fewer sources than to illuminate from fewer directions with a line array of sources. In this example, accurate quantitative estimate of both optical coefficients are obtained, and again it is likely that better regularisation could improve these further. A profile comparison of the true and reconstructed optical coefficients can be seen in Figure 5.9. Figure 5.9 shows a profile comparison of the true and reconstructed absorption and scattering coefficients for this example. There is now only a small underestimation of the absorption coefficient, and a small overestimation of the scattering coefficient. The relative error in the reconstructed absorption and scattering coefficients at each iteration can be seen in Figure 5.9(C). These errors behave much

more conventionally than in the previous two examples. The absorption error continues to descend even after 1000 iterations, suggesting that the estimate shown here might improve given more iterations.

5.1.2.4 Four line sources

FIGURE 5.10: Reconstructed absorption and scattering coefficients when using four line sources, corresponding to Figure 4.3(C). (A) shows the true absorption coefficient, (B) shows the reconstructed absorption coefficient from noise-free data, and (C) shows the reconstructed absorption coefficient from data with 5% additive Gaussian noise. (D) shows the true scattering coefficient, (E) shows the reconstructed scattering coefficient from noise-free data, and (F) shows the reconstructed scattering coefficient from data with 5% additive Gaussian noise.

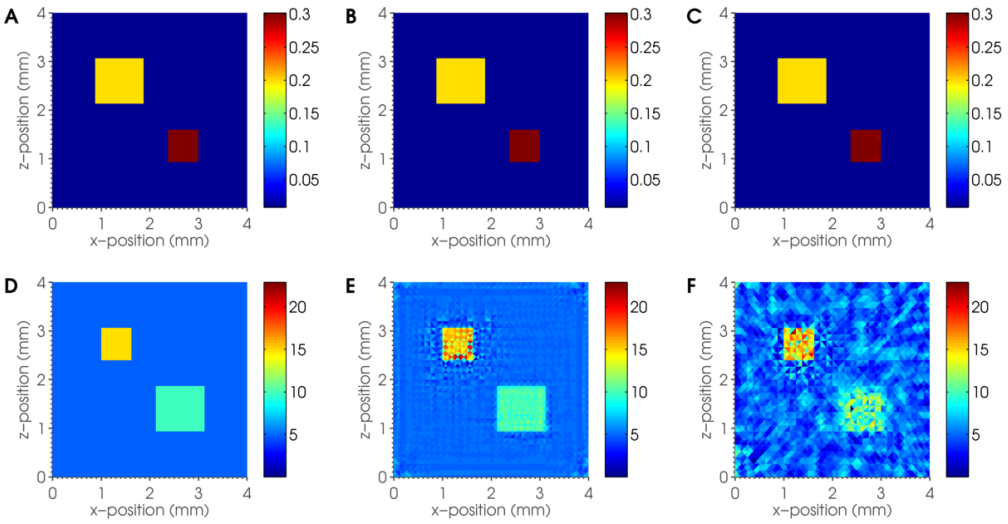

In this example, four images were simulated, each corresponding to a line source placed at either the top, bottom, left-hand side or right-hand side of the domain. Again, we investigated both the noise-free and noisy scenarios, with 5% Gaussian noise being added to the measurement data in the noisy case. Figure 5.10 shows the reconstructed absorption and scattering coefficients when using these data. In this case, the method is able to produce excellent quantitative estimates of the absorption coefficient, even in the presence of 5% Gaussian noise; the percent relative errors in the absorption coefficient for the noise-free and noisy reconstructions are $\epsilon_{\mathrm{a}} = 0.08\%$ and $\epsilon_{\mathrm{a}} = 1.16\%$, respectively, and the percent relative errors in the scattering coefficient are $\epsilon_{\mathrm{s}} = 11.6\%$ and $\epsilon_{\mathrm{s}} = 28.3\%$ for the noise-free and noisy reconstructions, respectively. A profile comparison of the true and reconstructed optical coefficients can be seen in Figure 5.11. Using four line

FIGURE 5.11: Simultaneous recovery of absorption and scattering coefficients using four line sources. A profile comparison of the reconstructed absorption coefficient can be seen in (A), which compares the true absorption coefficient (grey solid), reconstructed absorption coefficient from noise-free data (blue dashed) and reconstructed absorption coefficient from noisy data (red dotted). The profile is taken in the x-direction at $z = 1.2$ mm. A profile comparison of the reconstructed scattering coefficient can be seen in (B), which compares the true scattering coefficient (grey solid), reconstructed scattering coefficient from noise-free data (blue dashed) and reconstructed scattering coefficient from noisy data (red dotted). The profile is taken in the x-direction at $z = 2.4$ mm. The percent relative errors of the reconstructed absorption (blue) and scattering (red) coefficients at each iteration can be seen in (C).

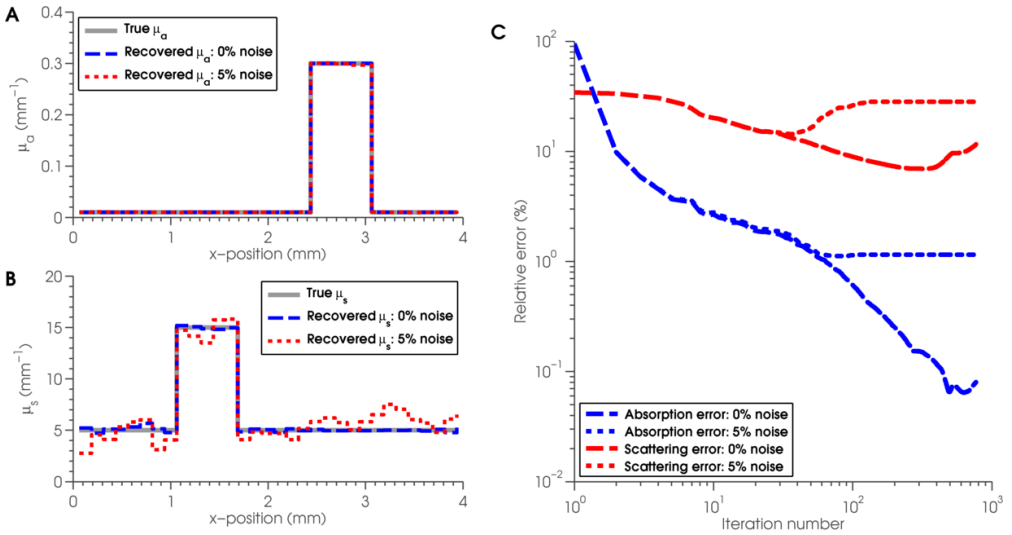

sources produces an almost exact reconstruction of the absorption coefficient. Figure 5.11 shows a profile comparison of the true and reconstructed absorption and scattering coefficients for this example. The relative error in the reconstructed absorption and scattering coefficients at each iteration can be seen in Figure 5.11(C). Here, it is clear that errors due to noise have propagated in the inversion from noisy data, which can be seen in the reconstructed scattering coefficient in Figure 5.10(F). Despite this, a good estimate of the scattering coefficient is still obtained, which in turn produces a highly accurate quantitative reconstruction of the absorption coefficient.

5.2 Conclusions

○ *In this chapter, we have extended the gradient-based minimisation method based on the RTE to enable the simultaneous recovery of quantitative estimates of the optical absorption*

and scattering coefficients from simulated PAT images.

The absorption and scattering coefficients consisted of a homogeneous background with two non-smooth heterogeneities. The anisotropy factor was constant with $g = 0.8$ for all simulations. A number of different source geometries were considered. 2D simulated PAT images were obtained using a FE implementation of the RTE, in which the FE mesh consisted of $N_e = 3840$ triangular elements, $N_n = 1983$ nodes and an angular discretisation of $N_a = 16$ equal angles. For each example, the gradient-based RTE method was used to reconstruct the absorption coefficient from both noise-free data and data with additive Gaussian noise scaled to 5% of the mean absorbed energy density. Reconstructing both optical coefficients simultaneously from simulated PAT images is challenging for a number of reasons. Firstly, reconstructing $(\mu_{\mathrm{a}}, \mu_{\mathrm{s}})$ from a single PAT image does not necessarily have a unique solution, and so additional information must be incorporated to guarantee uniqueness. In the examples presented in this chapter, multiple illumination positions were used, whereby a set of simulated PAT images are obtained by illuminating the domain from different directions. Secondly, reconstructing the scattering coefficient from a PAT image is more challenging than reconstructing the absorption coefficient, since the data is only dependent upon the scattering coefficient through its effect on the optical fluence. The fluence therefore acts as a low pass filter to reduce the amplitudes of the high frequency components of the scattering distribution. Consequently, inverting for the scattering coefficient will grow the high frequency components, which will also have the effect of amplifying noise in the measured data. The examples presented in this chapter have shown that the gradient-based method using the RTE can be extended to the case where the scattering is unknown, and can successfully recover quantitative estimates of both optical coefficients from simulated PAT images.

◦ *It is not necessary that the details of the scattering reconstruction are accurate to obtain a quantitative estimate of absorption, however, it is is necessary that the mean value of that estimate is close to the true scattering mean.*

When using two point sources, the estimate of the scattering coefficient was poor, resulting in some errors in the reconstruction of the absorption coefficient. However, despite the significant errors in the reconstructed scattering coefficient, the background

value and structure of the absorption coefficient was obtained accurately; with only small under- or over-estimations of the values in the heterogeneities. This suggests that the details, pixel-by-pixel, of the scattering coefficient are not highly relevant to the estimate of μ_{a}. The correct estimation of the mean properties of the scattering appear to be more important to the absorption reconstruction. The results using two line sources improved the reconstruction of both coefficients, producing only a slight underestimation in the absorbing heterogeneity and an accurate estimation of the background value. Illuminating the domain from all four directions produced significantly better quantitative results than when fewer directions were used, and in this case, accurate quantitative reconstructions of both optical coefficients were found. In the case of four line sources, the absorption coefficient was reconstructed to within 1% of its true value in the noise-free case, and 1.15% in the noise-free case.

◦ *In the case where data from only two illumination directions was used, determination of the scattering coefficient proved to be challenging.*

In the case where four multiple illuminations are not available, incorporating information from multiple wavelength as well as multiple illumination positions could into the gradient-based minimisation scheme could improve the reconstructions further. Another method to improve stability in the reconstructions could be to scale the data, e.g. by using the logarithm of the data, so that $h^{\mathrm{obs}} = \ln h^{\mathrm{obs}}$. This method is often used in optical tomography, since the dynamic range of the measured light intensities can be very large [98, 99]. Preliminary results using a logarithmic scaling of the data are shown in Appendix A.

The use of the full RTE rather than the DA means that few approximations to the propagation of light within the tissue are made, and so the method will be applicable to real PAT data. The use of a gradient-based method means that the method is memory-efficient, and so the extension to a large-scale 3D problem is possible. The remaining drawback here is that solving the RTE for a large-scale 3D problem is itself computationally intensive, and so performing a full 3D inversion using the RTE is likely to be extremely

time-consuming. In the following chapter, we propose the use of the δ-Eddington approximation to the RTE to improve the computational efficiency of the model.

Chapter 6

Gradient-based QPAT using the δ-Eddington approximation

In previous chapters, we have discussed the importance of accounting for the dependence of the transportation of light in biological tissue on both optical absorption and optical scattering when attempting to determine quantitative estimates of tissue optical properties from measured PAT images. We have also motivated the use of iterative minimisation schemes for tackling the full and general problem of quantitative photoacoustic tomography (QPAT), in which the optical absorption and scattering coefficients are heterogeneous and unknown. We addressed the challenges of applying a Jacobian-based minimisation method to real PAT images, and based on these conclusions we proposed the use of a gradient-based minimisation scheme to provide a much less memory-intensive method, enabling the application of the method to large-scale, three-dimensional (3D) data sets. These minimisation schemes require an accurate computational model of light transport, and in Chapter 5 we demonstrated that the radiative transfer equation (RTE) provides an accurate model of light transport which can be incorporated into a gradient-based minimisation scheme to produce accurate quantitative estimate of optical absorption from two-dimensional (2D) simulated PAT images when the scattering coefficient was known. In Chapter 5 we demonstrated that this type of gradient-based minimisation scheme can be used to successfully recover quantitative estimates of the unknown optical

absorption and optical scattering coefficients from 2D simulated PAT images. Since, in practice, PAT images will be large-scale and 3D, the next step is to extend this work to 3D simulated PAT images.

For a large-scale, 3D problem, a numerical solution to the RTE will require significant computational memory and time due to the angular dependence of the phase function; the solution $\phi(\mathbf{r}, \hat{\mathbf{s}})$ is a function of angle at each point within the domain, so that the 3D problem essentially becomes a four-dimensional problem. The gradient-based method presented in Chapter 5 will require one evaluation each of the forward and adjoint models per iteration. Since it is possible that hundreds of iterations may be required to obtain a sufficiently accurate estimate of optical absorption, an RTE-based iterative method is likely to be extremely time-consuming for a typical QPAT problem, and hence may not be a particularly practical method for the full and general problem. As in the choice of Jacobian-based vs. gradient-based methods, we once again find ourselves in a trade-off between accuracy and practicality. The RTE provides us with an accurate model, but its complexity may prove it to be an infeasible choice for a practical solution method. In Section 2.4.4 we discussed how the diffusion approximation (DA) to the RTE can be used to derive a much simpler, more efficient model of light transport than the full RTE. To derive the DA, it is assumed that the transportation of light is dominated by scattering ($\mu_{\mathrm{a}} \ll \mu_{\mathrm{s}}$), and that the scattering is only weakly isotropic. Whilst the former is typically true for biological tissue, the latter is violated in regions close to boundaries and sources. This is due to the fact that scattering of light in biological tissue is highly forward-peaked, and will only behave diffusely once a few scattering events have occurred. This move into the diffusive regime occurs around a few transport mean free paths away from the source, where a transport mean free path is given by $l = (\mu_{\mathrm{a}} + \mu_{\mathrm{s}}')^{-1}$. The DA therefore breaks down at regions within a few transport mean free paths from any light sources. In biological tissue, a transport mean free path may be on the order of 1 mm, and can therefore constitute a significantly large portion of a PAT image. This region may also contain information of great interest. The DA is therefore unsuitable for the quantitative modelling of PAT images, and using the DA in an inversion scheme will not recover sufficiently accurate estimates of optical absorption for QPAT. The tractability of the DA,

however, is extremely desirable; the removal of angular dependence makes the DA much simpler and quicker to solve, and its incorporation into this type of iterative minimisation scheme for QPAT would provide a practical solution method even for large-scale, 3D data sets. In this chapter we will introduce another approximation to the RTE, called the δ-Eddington approximation [54]. The δ-Eddington approximation is similar to the DA, in that it removes the dependence on scattering angle which makes the RTE difficult and time-consuming to solve, whilst retaining accuracy where the DA breaks down. This is achieved by improving the approximation to the scattering phase function by incorporating a strongly forward-peaked component, and also by modelling the ballistic (unscattered) portion of light resulting from the boundary source. This collimated part of the fluence field then provides the source term to a diffusion equation to model the scattered field, meaning that the resulting model can be solved as quickly and efficiently as the DA. The improved approximation to the transportation of light in biological tissue and comparable tractability to the DA mean that the δ-Eddington approximation may provide the ideal light model for solving the full and general problem of QPAT.

6.1 The δ-Eddington approximation

In Chapter 2 we derived the time-independent RTE (Equation 2.30), which is given by

$$(\hat{\mathbf{s}} \cdot \nabla + \mu_{\mathrm{a}} + \mu_{\mathrm{s}})\phi(\mathbf{r}, \hat{\mathbf{s}}) = \mu_{\mathrm{s}} \int_{S^{n-1}} \Theta(\hat{\mathbf{s}}, \hat{\mathbf{s}}')\phi(\mathbf{r}, \hat{\mathbf{s}}') \, \mathrm{d}\hat{\mathbf{s}}' + q, \tag{6.1}$$

and is solved for $\phi(\mathbf{r}, \hat{\mathbf{s}})$, the radiance at position $\mathbf{r}$ travelling in the direction of the unit vector $\hat{\mathbf{s}}$. The RTE is based on the principle of energy conservation, and describes how optical energy in some control volume may be lost due to absorption or scattering out of the direction of interest, or gained through scattering into the direction of interest or from a source of energy $q = q(\mathbf{r}, \hat{\mathbf{s}})$. In Equation 6.1, $\mu_{\mathrm{a}} = \mu_{\mathrm{a}}(\mathbf{r})$ and $\mu_{\mathrm{s}} = \mu_{\mathrm{s}}(\mathbf{r})$ are the optical absorption and scattering coefficients, respectively, and $\Theta(\hat{\mathbf{s}}, \hat{\mathbf{s}}')$ is the scattering phase function, which represents the fraction of light scattering from a direction $\hat{\mathbf{s}}'$ into a direction $\hat{\mathbf{s}}$. The scattering phase function is a probability density function, and is

normalised such that

$$\int_{S^{n-1}} \Theta(\hat{\mathbf{s}}, \hat{\mathbf{s}}') \, \mathrm{d}\hat{\mathbf{s}}' = 1. \tag{6.2}$$

In Section 2.4.3 we discussed that the RTE can be simplified by expressing the directional dependence as a sum of spherical harmonics [47]. In this case, the quantities in Equation 6.1 are expressed as

$$\phi(\mathbf{r}, \hat{\mathbf{s}}) = \sum_{l}^{\infty} \sum_{m=-l}^{l} \left(\frac{2l+1}{4\pi} \right)^{\frac{1}{2}} \Psi_{l,m}(\mathbf{r}) Y_{l,m}(\hat{\mathbf{s}}), \tag{6.3}$$

$$q(\mathbf{r}, \hat{\mathbf{s}}) = \sum_{l}^{\infty} \sum_{m=-l}^{l} \left(\frac{2l+1}{4\pi} \right)^{\frac{1}{2}} q_{l,m}(\mathbf{r}) Y_{l,m}(\hat{\mathbf{s}}), \tag{6.4}$$

where the terms $\Psi_{l,m}$ and $Y_{l,m}$ are spherical harmonics of order l and degree m, depending on the associated Legendre polynomials. The phase function can also be expressed using spherical harmonics, as

$$\Theta(\hat{\mathbf{s}}, \hat{\mathbf{s}}') = \sum_{l}^{\infty} \left(\frac{2l+1}{4\pi} \right) \Theta_l P_l(\cos\theta), \tag{6.5}$$

where P_l are the associated Legendre polynomials of order l, and $\cos\theta$ is the angle between the unit vectors $\hat{\mathbf{s}}$ and $\hat{\mathbf{s}}'$. The Henyey-Greenstein phase function uses $\Theta_l = g^l$ to model the scattering of light in biological tissue, and so the Henyey-Greenstein phase function to also be written in terms of spherical harmonics:

$$\Theta_{\mathrm{HG}}(\hat{\mathbf{s}}, \hat{\mathbf{s}}') = \sum_{l=0}^{\infty} \frac{2l+1}{4\pi} g^l P_l(\cos\theta). \tag{6.6}$$

These expressions can be substituted into 6.1 and, after some algebra, we are left with an infinite set of coupled equations known as the P_N approximations to the RTE. The DA can be derived by assuming that $\Psi_{l,m} = 0$ for $l > 1$, and hence the DA is sometimes referred to as the P_1 approximation.

The truncation of the infinite sums describing the radiance, scattering phase function and source term leaves only the first two terms for each quantity, which has the effect

of leaving only weak-anisotropy in the resulting light model. The first two Legendre polynomials can be calculated easily, since $P_0(x) = 1$ and $P_1(x) = x$. Substituting these into 6.6 and 6.3 leaves two important terms used to derive the DA, which will be used analogously in this chapter to derive the δ-Eddington approximation. The first is a truncated phase function, sometimes known as the Eddington phase function, which (in the 3D case) is given by

$$\Theta_{\mathrm{E}}(\hat{\mathbf{s}}, \hat{\mathbf{s}}') = \frac{1}{4\pi}\left(1 + 3g\cos\theta\right). \tag{6.7}$$

The second is an expression for the P_1 approximation to the radiance, which can be found by substituting the Legendre polynomials and manipulating Equation 6.3 above to give

$$\phi(\mathbf{r}, \hat{\mathbf{s}}') = \frac{1}{4\pi}\Phi(\mathbf{r}) + \frac{3}{4\pi}(\hat{\mathbf{s}} \cdot \mathbf{J}(\mathbf{r})), \tag{6.8}$$

where Φ is the optical fluence and $\mathbf{J}$ is the radiant flux. Equations 6.7 and 6.8 can then be substituted into Equation 6.1 and manipulated to obtain the DA.

The DA assumes that the scattering of light within the domain is only weakly anisotropic, however, light scattering in biological tissue is typically highly anisotropic, which means that the DA breaks down close to sources, where the light is strongly forward-directed and has not been scattered enough to behave diffusely. The DA can be improved by incorporating an extra term into the scattering phase function, thereby shifting a portion f of the light into the forward direction to better model the forward-peaked scattering of biological tissue. To obtain the δ-Eddington approximation, the phase function Θ_{E} is replaced by the δ-Eddington phase function $\Theta_{\delta-\mathrm{E}}$ of Joseph *et al* [54], given by

$$\Theta_{\delta-\mathrm{E}} = \frac{1}{4\pi}\left\{2f\delta(1 - (\hat{\mathbf{s}} \cdot \hat{\mathbf{s}}')) + (1-f)(1 + 3\hat{g}(\hat{\mathbf{s}} \cdot \hat{\mathbf{s}}'))\right\}. \tag{6.9}$$

The modified anisotropy factor $\hat{g}$ can be found by considering that, in turbid media, the DA is valid at depths greater than a few transport mean free paths. In this region, the scattering of light is characterised solely by the reduced scattering coefficient $\mu_{\mathrm{s}}' =$

$\mu_{\mathrm{s}}(1-g)$ [66]. If we define the modified reduced scattering coefficient $\hat{\mu}'_{\mathrm{s}} = \hat{\mu}_{\mathrm{s}}(1-\hat{g})$ and enforce the requirement that this parameter remain unchanged, we obtain an expression for the modified anisotropy factor $\hat{g}$:

$$\begin{aligned} \hat{\mu}'_{\mathrm{s}} &= \mu'_{\mathrm{s}} \\ \Rightarrow \mu_{\mathrm{s}}(1-f)(1-\hat{g}) &= \mu_{\mathrm{s}}(1-g) \\ \Rightarrow \hat{g} &= \frac{g-f}{1-f} \end{aligned} \tag{6.10}$$

The parameter f can be chosen to best match an appropriate scattering phase function. For example, an empirical formula for calculating f as a function of g ($f = 0.026094g^3 + 0.023597g^2 + 0.13572g + 0.60366$) was determined by comparison with Monte Carlo simulations [100], while comparison with the first n terms of the Henyey-Greenstein phase function results in a choice of $f = g^n$.

Given a suitable choice of f, the approximation to the phase function $\Theta \approx \Theta_{\delta-\mathrm{E}}$ can be substituted into the RTE (Equation 6.1) to give

$$(\hat{\mathbf{s}} \cdot \nabla + \mu_{\mathrm{a}} + \hat{\mu}_{\mathrm{s}})\phi(\mathbf{r}, \hat{\mathbf{s}}) = \frac{\hat{\mu}_{\mathrm{s}}}{4\pi} \int_{4\pi} (1 + 3\hat{g}(\hat{\mathbf{s}} \cdot \hat{\mathbf{s}}'))\phi(\mathbf{r}, \hat{\mathbf{s}}') \, \mathrm{d}\hat{\mathbf{s}}', \tag{6.11}$$

where $\hat{\mu}_{\mathrm{s}} = (1-f)\mu_{\mathrm{s}}$. The radiance may be separated into its collimated (ϕ_{c}) and scattered (ϕ_{s}) components

$$\phi(\mathbf{r}, \hat{\mathbf{s}}) = \phi_{\mathrm{c}}(\mathbf{r}, \hat{\mathbf{s}}) + \phi_{\mathrm{s}}(\mathbf{r}, \hat{\mathbf{s}}), \tag{6.12}$$

and hence the fluence can be separated similarly, since

$$\begin{aligned} \Phi(\mathbf{r}) &= \int_{4\pi} \phi(\mathbf{r}, \hat{\mathbf{s}}) \, \mathrm{d}\hat{\mathbf{s}} \\ \Rightarrow \Phi(\mathbf{r}) &= \int_{4\pi} \phi_{\mathrm{c}}(\mathbf{r}, \hat{\mathbf{s}}) \, \mathrm{d}\hat{\mathbf{s}} + \int_{4\pi} \phi_{\mathrm{s}}(\mathbf{r}, \hat{\mathbf{s}}) \, \mathrm{d}\hat{\mathbf{s}} \\ \Rightarrow \Phi(\mathbf{r}) &= \Phi_{\mathrm{c}}(\mathbf{r}) + \Phi_{\mathrm{s}}(\mathbf{r}), \end{aligned} \tag{6.13}$$

where Φ_{c} and Φ_{s} denote the collimated and scattered fluence, respectively. Substituting 6.12 and 6.13 into 6.11 gives

$$\begin{aligned}
&(\hat{\mathbf{s}}\cdot\nabla+\mu_{\mathrm{a}}+\hat{\mu}_{\mathrm{s}})\phi_{\mathrm{s}}(\mathbf{r},\hat{\mathbf{s}})\\
&\quad=-(\hat{\mathbf{s}}\cdot\nabla+\mu_{\mathrm{a}}+\hat{\mu}_{\mathrm{s}})\phi_{\mathrm{c}}(\mathbf{r},\hat{\mathbf{s}})\\
&\quad+\frac{\hat{\mu}_{\mathrm{s}}}{4\pi}(\Phi_{\mathrm{c}}(\mathbf{r})+\Phi_{\mathrm{s}}(\mathbf{r}))\\
&\quad+\frac{3\hat{g}\hat{\mu}_{\mathrm{s}}}{4\pi}\int_{4\pi}(\hat{\mathbf{s}}\cdot\hat{\mathbf{s}}')(\phi_{\mathrm{c}}(\mathbf{r},\hat{\mathbf{s}}')\\
&\quad+\phi_{\mathrm{s}}(\mathbf{r},\hat{\mathbf{s}}'))\,\mathrm{d}\hat{\mathbf{s}}'.
\end{aligned}\tag{6.14}$$

The collimated radiance includes both unscattered light and light scattered into the forward direction $\hat{\mathbf{z}}$, and is hence attenuated at a rate proportional to the modified transport coefficient $\hat{\mu}_{\mathrm{t}}=\mu_{\mathrm{a}}+\hat{\mu}_{\mathrm{s}}$, that is,

$$(\hat{\mathbf{s}}\cdot\nabla)\phi_{\mathrm{c}}(\mathbf{r},\hat{\mathbf{s}})=-\hat{\mu}_{\mathrm{t}}\phi_{\mathrm{c}}(\mathbf{r},\hat{\mathbf{s}}).\tag{6.15}$$

This can then be used to reduce Equation 6.14 to

$$\begin{aligned}
&(\hat{\mathbf{s}}\cdot\nabla+\mu_{\mathrm{a}}+\hat{\mu}_{\mathrm{s}})\phi_{\mathrm{s}}(\mathbf{r},\hat{\mathbf{s}})\\
&\quad=\frac{\hat{\mu}_{\mathrm{s}}}{4\pi}(\Phi_{\mathrm{c}}(\mathbf{r})+\Phi_{\mathrm{s}}(\mathbf{r}))\\
&\quad+\frac{3\hat{g}\hat{\mu}_{\mathrm{s}}}{4\pi}\int_{4\pi}(\hat{\mathbf{s}}\cdot\hat{\mathbf{s}}')(\phi_{\mathrm{c}}(\mathbf{r},\hat{\mathbf{s}}')\\
&\quad+\phi_{\mathrm{s}}(\mathbf{r},\hat{\mathbf{s}}'))\,\mathrm{d}\hat{\mathbf{s}}'.
\end{aligned}\tag{6.16}$$

If the source is considered to be a monodirectional flux $I_0(\mathbf{r})$ incident in the positive z-direction, the solution to Equation 6.15 is given by

$$\phi_{\mathrm{c}}(\mathbf{r},\hat{\mathbf{s}})=I_0(\mathbf{r})\exp\left(-\int_{z_0}^{z}\hat{\mu}_{\mathrm{t}}(z')\,\mathrm{d}z'\right)\delta(1-(\hat{\mathbf{s}}\cdot\hat{\mathbf{z}})),\tag{6.17}$$

where $\hat{\mathbf{z}}$ is a unit vector in the z-direction, which means the collimated fluence can be written as

$$\begin{aligned} \Phi_{\mathrm{c}}(\mathbf{r}) &= \int_{4\pi} \phi_{\mathrm{c}}(\mathbf{r},\hat{\mathbf{s}})\mathrm{d}\hat{\mathbf{s}} \\ \Rightarrow \Phi_{\mathrm{c}}(\mathbf{r}) &= I_0(\mathbf{r}) \exp\left(-\int_{z_0}^{z} \hat{\mu}_{\mathrm{t}}(z')\,\mathrm{d}z'\right). \end{aligned} \tag{6.18}$$

Substituting 6.17 and 6.18 into 6.16 then gives

$$\begin{aligned} &(\hat{\mathbf{s}}\cdot\nabla + \mu_{\mathrm{a}} + \hat{\mu}_{\mathrm{s}})\phi_{\mathrm{s}}(\mathbf{r},\hat{\mathbf{s}}) \\ &\quad = \frac{\hat{\mu}_{\mathrm{s}}}{4\pi}(\Phi_{\mathrm{c}}(\mathbf{r}) + \Phi_{\mathrm{s}}(\mathbf{r})) \\ &\quad + \frac{3\hat{g}\hat{\mu}_{\mathrm{s}}}{4\pi}\left\{\Phi_{\mathrm{c}}(\mathbf{r})(\hat{\mathbf{s}}\cdot\hat{\mathbf{z}}) + \int_{4\pi}(\hat{\mathbf{s}}\cdot\hat{\mathbf{s}}')\phi_{\mathrm{s}}(\mathbf{r},\hat{\mathbf{s}}')\,\mathrm{d}\hat{\mathbf{s}}'\right\}. \end{aligned} \tag{6.19}$$

Recall from Equation 6.8 that the scattered radiance can be written as

$$\phi_{\mathrm{s}}(\mathbf{r},\hat{\mathbf{s}}) = \frac{1}{4\pi}\Phi_{\mathrm{s}}(\mathbf{r}) + \frac{3}{4\pi}(\hat{\mathbf{s}}\cdot\mathbf{J}_{\mathrm{s}}(\mathbf{r})), \tag{6.20}$$

where Φ_{s} is the scattered fluence and $\mathbf{J}_{\mathrm{s}}$ is the scattered radiant flux. This is substituted into Equation 6.19 to give

$$\begin{aligned} &(\hat{\mathbf{s}}\cdot\nabla)\Phi_{\mathrm{s}} + \mu_{\mathrm{a}}\Phi_{\mathrm{s}} + 3(\hat{\mathbf{s}}\cdot\nabla)(\mathbf{J}_{\mathrm{s}}\cdot\hat{\mathbf{s}}) + 3(\mu_{\mathrm{a}} + \hat{\mu}_{\mathrm{s}})(\mathbf{J}_{\mathrm{s}}\cdot\hat{\mathbf{s}}) \\ &\quad = \hat{\mu}_{\mathrm{s}}\Phi_{\mathrm{c}} + 3\hat{g}\hat{\mu}_{\mathrm{s}}\Phi_{\mathrm{c}}(\hat{\mathbf{s}}\cdot\hat{\mathbf{z}}) \\ &\qquad + \frac{3\hat{g}\hat{\mu}_{\mathrm{s}}}{4\pi}\left(\Phi_{\mathrm{s}}\int_{4\pi}(\hat{\mathbf{s}}\cdot\hat{\mathbf{s}}')\,\mathrm{d}\hat{\mathbf{s}}' + 3\int_{4\pi}(\hat{\mathbf{s}}\cdot\hat{\mathbf{s}}')(\mathbf{J}_{\mathrm{s}}\cdot\hat{\mathbf{s}}')\,\mathrm{d}\hat{\mathbf{s}}'\right). \end{aligned} \tag{6.21}$$

To progress from here, we will take two approaches to derive two expressions for the divergence of the scattered flux $\nabla\cdot\mathbf{J}_{\mathrm{s}}$, which we can equate to obtain one single equation and remove the scattered flux entirely. The following solid angle vector identities will be

useful:

$$\int_{4\pi} \mathrm{d}\hat{\mathbf{s}} = 4\pi, \tag{6.22}$$

$$\int_{4\pi} \hat{\mathbf{s}}\, \mathrm{d}\hat{\mathbf{s}} = 0 \tag{6.23}$$

$$\int_{4\pi} \hat{\mathbf{s}} \cdot \mathbf{A}\, \mathrm{d}\hat{\mathbf{s}} = 0, \tag{6.24}$$

$$\int_{4\pi} (\hat{\mathbf{s}} \cdot \mathbf{A})\hat{\mathbf{s}}\, \mathrm{d}\hat{\mathbf{s}} = \frac{4\pi}{3}\mathbf{A}, \tag{6.25}$$

$$\int_{4\pi} (\hat{\mathbf{s}} \cdot \mathbf{A})(\hat{\mathbf{s}} \cdot \mathbf{B})\, \mathrm{d}\hat{\mathbf{s}} = \frac{4\pi}{3}(\mathbf{A} \cdot \mathbf{B}), \tag{6.26}$$

$$\int_{4\pi} \hat{\mathbf{s}}(\hat{\mathbf{s}} \cdot \mathbf{A})(\hat{\mathbf{s}} \cdot \mathbf{B})\, \mathrm{d}\hat{\mathbf{s}} = 0, \tag{6.27}$$

which hold for arbitrary vectors $\mathbf{A}$ and $\mathbf{B}$. To obtain the first expressions for $\nabla \cdot \mathbf{J}_\mathrm{s}$, we integrate Equation 6.21 over all angles $\hat{\mathbf{s}} \in S^{n-1}$, giving

$$\begin{aligned}
&\int_{4\pi} (\hat{\mathbf{s}} \cdot \nabla)\Phi_\mathrm{s}\, \mathrm{d}\hat{\mathbf{s}} + \mu_\mathrm{a}\Phi_\mathrm{s} \int_{4\pi} \mathrm{d}\hat{\mathbf{s}} + 3\int_{4\pi} (\hat{\mathbf{s}} \cdot \nabla)(\hat{\mathbf{s}} \cdot \mathbf{J}_\mathrm{s})\, \mathrm{d}\hat{\mathbf{s}} \\
&\quad + 3(\mu_\mathrm{a} + \hat{\mu}_\mathrm{s}) \int_{4\pi} (\hat{\mathbf{s}} \cdot \mathbf{J}_\mathrm{s})\, \mathrm{d}\hat{\mathbf{s}} \\
&\quad = \hat{\mu}_\mathrm{s}\Phi_\mathrm{c} \int_{4\pi} \mathrm{d}\hat{\mathbf{s}} + 3\hat{g}\hat{\mu}_\mathrm{s}\Phi_\mathrm{c} \int_{4\pi} (\hat{\mathbf{s}} \cdot \hat{\mathbf{z}})\, \mathrm{d}\hat{\mathbf{s}} \\
&\qquad + \frac{3\hat{g}\hat{\mu}_\mathrm{s}}{4\pi}\Phi_\mathrm{s} \int_{4\pi}\int_{4\pi} (\hat{\mathbf{s}} \cdot \hat{\mathbf{s}}')\, \mathrm{d}\hat{\mathbf{s}}'\, \mathrm{d}\hat{\mathbf{s}} \\
&\qquad + \frac{9\hat{g}\hat{\mu}_\mathrm{s}}{4\pi} \int_{4\pi}\int_{4\pi} (\hat{\mathbf{s}} \cdot \hat{\mathbf{s}}')(\mathbf{J}_\mathrm{s} \cdot \hat{\mathbf{s}}')\, \mathrm{d}\hat{\mathbf{s}}'\, \mathrm{d}\hat{\mathbf{s}}.
\end{aligned} \tag{6.28}$$

Using the solid angle vector integral identities 6.22, 6.24 and 6.26, Equation 6.28 reduces to the first equation for the divergence of $\mathbf{J}_\mathrm{s}$:

$$\nabla \cdot \mathbf{J}_\mathrm{s} = \hat{\mu}_\mathrm{s}\Phi_\mathrm{c} - \mu_\mathrm{a}\Phi_\mathrm{s}. \tag{6.29}$$

To obtain the second expression, we return to Equation 6.21 and instead we first multiply by $\hat{\mathbf{s}}$ before integrating over all angles to obtain

$$\begin{aligned}
&\Phi_{\mathrm{s}} \int_{4\pi} \hat{\mathbf{s}}(\hat{\mathbf{s}} \cdot \nabla)\, \mathrm{d}\hat{\mathbf{s}} + \mu_{\mathrm{a}} \Phi_{\mathrm{s}} \int_{4\pi} \hat{\mathbf{s}}\, \mathrm{d}\hat{\mathbf{s}} + 3 \int_{4\pi} \hat{\mathbf{s}}(\hat{\mathbf{s}} \cdot \nabla)(\hat{\mathbf{s}} \cdot \mathbf{J}_{\mathrm{s}})\, \mathrm{d}\hat{\mathbf{s}} \\
&\quad + 3(\mu_{\mathrm{a}} + \hat{\mu}_{\mathrm{s}}) \int_{4\pi} \hat{\mathbf{s}}(\hat{\mathbf{s}} \cdot \mathbf{J}_{\mathrm{s}})\, \mathrm{d}\hat{\mathbf{s}} \\
&\quad = \hat{\mu}_{\mathrm{s}} \Phi_{\mathrm{c}} \int_{4\pi} \hat{\mathbf{s}}\, \mathrm{d}\hat{\mathbf{s}} + 3\hat{g}\hat{\mu}_{\mathrm{s}} \Phi_{\mathrm{c}} \int_{4\pi} \hat{\mathbf{s}}(\hat{\mathbf{s}} \cdot \hat{\mathbf{z}})\, \mathrm{d}\hat{\mathbf{s}} \\
&\qquad + \frac{3\hat{g}\hat{\mu}_{\mathrm{s}}}{4\pi} \int_{4\pi} \int_{4\pi} (\hat{\mathbf{s}} \cdot \hat{\mathbf{s}}')\, \mathrm{d}\hat{\mathbf{s}}' \hat{\mathbf{s}}\, \mathrm{d}\hat{\mathbf{s}} \\
&\qquad + \frac{9\hat{g}\hat{\mu}_{\mathrm{s}}}{4\pi} \int_{4\pi} \int_{4\pi} (\hat{\mathbf{s}}' \cdot \hat{\mathbf{s}})(\hat{\mathbf{s}}' \cdot \mathbf{J}_{\mathrm{s}})\, \mathrm{d}\hat{\mathbf{s}}' \hat{\mathbf{s}}\, \mathrm{d}\hat{\mathbf{s}}.
\end{aligned} \tag{6.30}$$

Using the identities 6.23, 6.25 and 6.27, we find this reduces to

$$\frac{1}{3} \nabla \Phi_{\mathrm{s}} + (\mu_{\mathrm{a}} + \hat{\mu}_{\mathrm{s}}(1 - \hat{g})) \mathbf{J}_{\mathrm{s}} = 3\hat{g}\hat{\mu}_{\mathrm{s}} \Phi_{\mathrm{c}} \hat{\mathbf{z}}, \tag{6.31}$$

or equivalently,

$$\mathbf{J}_{\mathrm{s}}(\mathbf{r}) = 3\hat{g}\hat{\kappa}\hat{\mu}_{\mathrm{s}} \Phi_{\mathrm{c}}(\mathbf{r}) \hat{\mathbf{z}} - \kappa \nabla \Phi_{\mathrm{s}}(\mathbf{r}), \tag{6.32}$$

where $\hat{\kappa}(\mathbf{r}) = (3(\mu_{\mathrm{a}} + \hat{\mu}_{\mathrm{s}}(1 - \hat{g})))^{-1}$. Taking the divergence of 6.32 gives a second equation for the divergence of $\mathbf{J}_{\mathrm{s}}$:

$$\nabla \cdot \mathbf{J}_{\mathrm{s}}(\mathbf{r}) = -\nabla \cdot \hat{\kappa} \nabla \Phi_{\mathrm{s}}(\mathbf{r}) - 3\hat{g}\hat{\kappa}\hat{\mu}_{\mathrm{t}}\hat{\mu}_{\mathrm{s}} \Phi_{\mathrm{c}}(\mathbf{r}). \tag{6.33}$$

We can now equate 6.29 and 6.33 to obtain a diffusion equation for the scattered fluence

$$(\nabla \cdot \kappa \nabla - \mu_{\mathrm{a}}) \Phi_{\mathrm{s}}(\mathbf{r}) = -(1 + 3\hat{g}\hat{\kappa}\hat{\mu}_{\mathrm{t}}) \hat{\mu}_{\mathrm{s}} \Phi_{\mathrm{c}}(\mathbf{r}), \tag{6.34}$$

where the right-hand side represents the collimated source. Thus, having found the collimated fluence Φ_{c} using Equation 6.17, the scattered fluence Φ_{s} can be found by solving the diffusion equation 6.34, and the total fluence found using $\Phi = \Phi_{\mathrm{c}} + \Phi_{\mathrm{s}}$. The reduction to a diffusion equation means that the δ-Eddington approximation is comparative to the DA in its computational efficiency, while the improved approximation to the

scattering phase function and its ability to model a collimated light source improves the accuracy at regions close to the source.

6.1.1 Model verification

To verify that the FE δ-Eddington model has been implemented correctly, we will calculate its solution for a given tissue geometry and compare it with the 'gold standard' model of light transport, the Monte Carlo (MC) method. MC methods simulate the delivery of a large number of packets of energy into a computational domain with some given optical properties. Each packet's journey through the tissue is tracked until either its energy is depleted due to absorption or it leaves the domain. The random walks that these energy packets take are decided by sampling probability distributions for step length and angular deflection per scattering event. This process is then repeated for a large number of energy packets until a sufficiently with sufficiently low variance is obtained. For a given problem, the number of energy packets required will depend on several factors, including domain size and mesh element size, and can be found in much the same way as determining how fine a mesh to use for a FE problem; the number of energy packets used in the forward model is gradually increased until convergence in the resulting solution is obtained.

We have discussed how the δ-Eddington approximation can model light transport more accurately than the DA in the low-scattering case and in regions of the domain where the DA breaks down. To demonstrate this, we will also compare the results of the MC and δ-Eddington models with the DA. To assess the performance of the δ-Eddington model, the three models (MC, δ-Eddington and DA) were used to simulate the transportation of light within the square domain $[0, 15] \times [0, 15]$ mm^2. These particular implementations of the MC and δ-Eddington models require two different types of mesh elements, rectangular (MC) and triangular (δ-Eddington). The two meshes were chosen so that the nodes of the mesh coincided exactly, with each square element of the MC mesh being split into two triangular elements to create the δ-Eddington mesh. The MC model requires a structured

FIGURE 6.1: Absorbed optical energy calculated using three different computational light models and three different values of optical scattering. In each case, a line array of sources was used to illuminate the domain from the top boundary ($z = 15$ mm)s. The optical absorption coefficient was heterogeneous, with two absorbing inclusions over a background absorption, and remained the same for each simulation. The three columns show the resulting absorbed optical energy calculated using the Monte Carlo method (left column), the δ-Eddington approximation (centre column) and the diffusion approximation (right column). Each row represents a different value of homogeneous scattering coefficient. The images show that the δ-Eddington approximation gives a good approximation for each scattering case, while the diffusion approximation, though accurate in the far-field, is unable to model the absorbed energy accurately in regions close to the source, particularly in the low-scattering case.

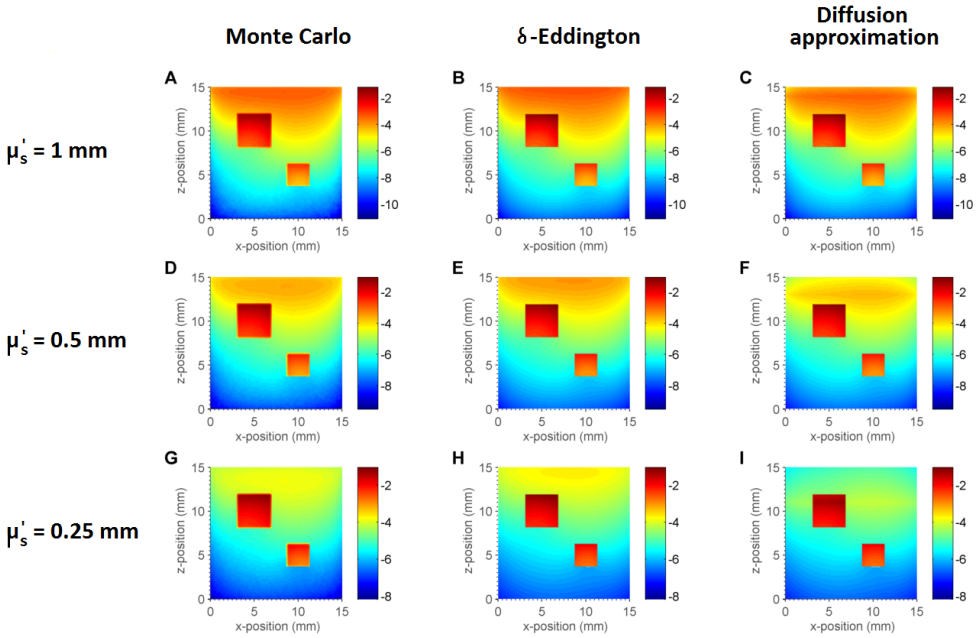

rectangular mesh, and in this case the mesh contained 16384 square elements, while the DA and δ-Eddington models were solved on a structured triangular mesh containing 32768 triangular elements. A line array of collimated sources, placed at each mesh node along the top boundary, was used to illuminate the domain. The absorption coefficient was heterogeneous, with a background value of 0.01 mm^{-1} and two square absorbing inclusions placed at $(5, 10)$ and $(10, 5)$, with absorption coefficients of 0.2 mm^{-1} and 0.3 mm^{-1}, respectively. The anisotropy factor was chosen to be $g = 0.95$, and the factor f of light scattered into the forward direction for the δ-Eddington approximation was chosen to be $f = 0.026094g^3 + 0.023597g^2 + 0.13572g + 0.60366$, a polynomial in g found to best match MC simulations when using the Henyey-Greenstein phase function for biological

tissue [100]. The scattering coefficient μ_s is considered to be constant throughout the entire domain for all simulations in this section. Three different values of μ_s have been used to demonstrate the breakdown of the DA as the scattering becomes weak. These were $\mu_s = 20$ mm^{-1}, $\mu_s = 10$ mm^{-1} and $\mu_s = 5$ mm^{-1}, resulting in reduced scattering coefficients of $\mu_s' = 1$ mm^{-1}, $\mu_s' = 0.5$ mm^{-1} and $\mu_s' = 0.25$ mm^{-1}. A line array of sources was placed along the top boundary ($z = 15$ mm). Since the DA cannot describe collimated sources correctly [49], a common approach is to simulate a collimated pencil beam by placing an isotropic source at a depth of $1/\mu_s'$ below the tissue surface. This enables the DA to produce accurate results at depths more than one mean free path from the source.

Figure 6.1 shows the resulting absorbed optical energy densities calculated using the MC method, δ-Eddington approximation and DA for three different cases of optical scattering. The three rows represent the different values of scattering coefficient, while the three columns represent the three different computational light models. These images demonstrate that the DA, though accurate in the far-field, breaks down significantly in regions close to the source and becomes significantly worse as the scattering coefficient decreases. The δ-Eddington approximation performs well in all three scattering cases, closely matching the MC solution throughout the whole domain. Figure 6.2 shows a profile comparison of the light models in each of the three scattering cases. The profile is in the z-direction at $x = 5$ mm, running through the centre of one of the absorbing inclusions. These profiles show more clearly the breakdown of the DA close to the source. The δ-Eddington approximation provides a better approximation to the MC solution than the DA in all areas of the domain, though the approximation breaks down in a small region very close the source. The profiles also show that there is a discrepancy between the models at the boundary farthest from the source, which is due to the fact that not enough photons have reached that area when running the MC simulation. Increasing the number of photons used to obtain the MC solution would remove this drop-off. To obtain the MC solution, the simulation of 10^6 energy packets was used; a higher number would have produced a smoother solution by reducing the variance (MC noise) and removing the drop-off found in regions farther from the source, however, the model that has been used to produce this forward solution has not been optimised, and increasing

FIGURE 6.2: Profiles of the absorbed optical energy calculated using three different computational light models and three different values of optical scattering. In each case, a line array of sources was used to illuminate the domain from the top boundary ($z = 15$ mm). The optical absorption coefficient was heterogeneous, with two absorbing inclusions over a background absorption, and remained the same for each simulation. The three figures show profiles in the z-direction at $x = 5$ mm of the absorbed optical energy calculated using three different values of homogeneous reduced scattering coefficient; (A) 1 mm^{-1}, (B) 0.5 mm^{-1} and (C) 0.25 mm^{-1}. Each figure compares the three light models; the Monte Carlo method (red dash), the δ-Eddington approximation (blue dot-dash) and the diffusion approximation (green dots). The profiles show that the δ-Eddington approximation gives a good approximation for each scattering case, and highlight that the diffusion approximation, though accurate in the far-field, is unable to model the absorbed energy accurately in regions close to the source, particularly in the low-scattering case (C).

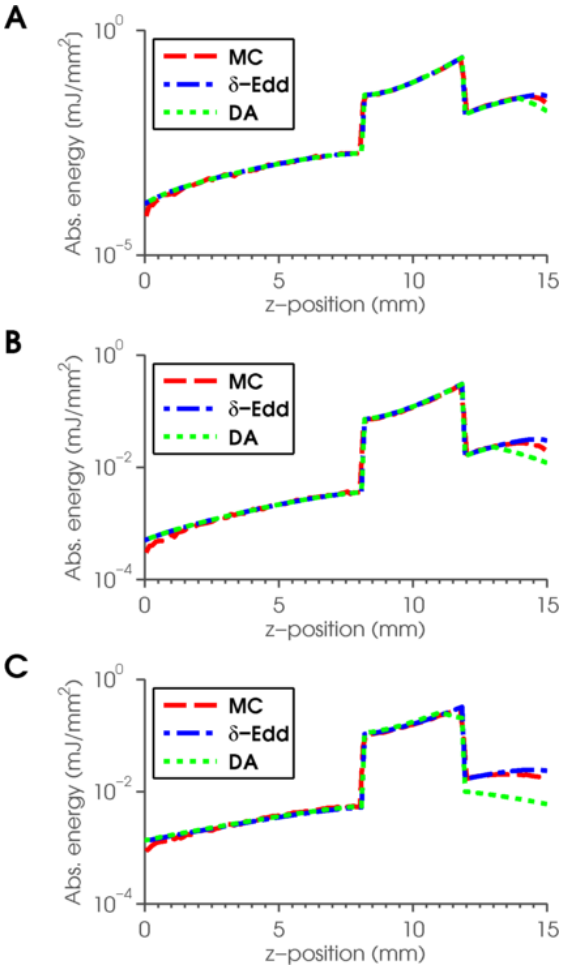

this number significantly would be very time-consuming. The number of photons used was considered to be sufficient enough to obtain a reasonably accurate solution and demonstrate the behaviour of the solution in the near-field and through the absorbing inclusion.

6.2 Incorporation into a gradient-based minimisation scheme

Now that we have verified that the δ-Eddington approximation derived above is able to model the transportation of light accurately, we can use the model to produce accurate simulations of PAT images and incorporate it into the gradient-based minimisation scheme discussed in Chapter 5. We will assume that the PA efficiency parameter is known and constant such that $\hat{\Gamma}(\mathbf{r}) = 1 \ \forall \mathbf{r} \in \Omega$, and hence

$$p_0 = h = \mu_\mathrm{a}\Phi = \mu_\mathrm{a}(\Phi_\mathrm{c} + \Phi_\mathrm{s}). \tag{6.35}$$

We therefore seek a solution to

$$\underset{\mu_\mathrm{a},\mu_\mathrm{s}}{\text{argmin}} \quad \varepsilon = \frac{1}{2}(h^\mathrm{obs} - h(\mu_\mathrm{a},\mu_\mathrm{s}))^\mathrm{T}(h^\mathrm{obs} - h(\mu_\mathrm{a},\mu_\mathrm{s})), \tag{6.36}$$

where h^obs and h are the measured and modelled PAT images, respectively. To employ a gradient-based minimisation scheme, we will need to obtain an expression for the gradient of 6.36 with respect to $(\mu_\mathrm{a},\mu_\mathrm{s})$. We will move straight to the case where the model has been implemented using the finite element method (FEM), i.e. the diffusion equation for the scattered fluence (6.34) has been converted to its weak formulation and the domain is constructed from continuous piecewise linear basis functions $\psi_j(\mathbf{r})$, $j = 1,\ldots,N$, so that the scattered fluence can be written as

$$\Phi_\mathrm{s}(\mathbf{r}) \approx \Phi_\mathrm{s}^h(\mathbf{r}) = \sum_{i=1}^{N} \Phi_\mathrm{s}^i \psi^i(\mathbf{r}). \tag{6.37}$$

The absorption and scattering coefficients are also defined using a piecewise linear basis:

$$\mu_{\mathrm{a}}(\mathbf{r}) \approx \mu_{\mathrm{a}}^{h}(\mathbf{r}) = \sum_{i=1}^{N} \mu_{\mathrm{a}}^{i} \psi^{i}(\mathbf{r}), \quad \mu_{\mathrm{s}}(\mathbf{r}) \approx \mu_{\mathrm{s}}^{h}(\mathbf{r}) = \sum_{i=1}^{N} \mu_{\mathrm{s}}^{i} \psi^{i}(\mathbf{r}). \tag{6.38}$$

This means that μ_{a} and Φ are now defined in the same basis, removing the need to interpolate the fluence to the elements to calculate the product $h = \mu_{\mathrm{a}}\Phi$, as in the RTE case. Having noted that these parameters are now expressed in this form, we will drop the superscript $(.)^{h}$ for notational convenience. More information on the numerical implementation of the diffusion equation using the FEM can be found in the literature, e.g. [48, 49, 101].

6.2.1 Functional gradient for the absorption coefficient

Applying the FEM allows us to write Equation 6.34 in the matrix form

$$A\Phi_{\mathrm{s}} = b, \tag{6.39}$$

which is solved for $\Phi_{\mathrm{s}}(\mathbf{r}) = \sum_{i=1}^{N} \Phi_{\mathrm{s}}^{i} \psi^{i}(\mathbf{r})$, where A is the FE system matrix with entries

$$A_{jk} = \int_{\Omega} \hat{\kappa}(\mathbf{r})\, \nabla\psi^{k}(\mathbf{r}) \cdot \nabla\psi^{j}(\mathbf{r})\, \mathrm{d}\Omega + \int_{\Omega} \mu_{\mathrm{a}}(\mathbf{r})\, \psi^{k}(\mathbf{r}) \cdot \psi^{j}(\mathbf{r})\, \mathrm{d}\Omega, \tag{6.40}$$

and b is the FE source vector with entries

$$b_{k} = \int_{\Omega} (1 + 3\hat{g}\kappa(\mathbf{r})\hat{\mu}_{\mathrm{t}}(\mathbf{r}))\hat{\mu}_{\mathrm{s}}(\mathbf{r})\Phi_{\mathrm{c}}(\mathbf{r})\psi^{k}(\mathbf{r})\, \mathrm{d}\Omega, \tag{6.41}$$

for $j = 1, \ldots, N$, $k = 1, \ldots, N$. We now consider the gradient of the error functional 6.36 with respect to the absorption coefficient μ_{a}. Differentiating Equation 6.36 with respect to μ_{a} at a point $\mathbf{r}_i$ is given by

$$\frac{\partial \varepsilon}{\partial \mu_{\mathrm{a}}^{i}} = -\left(\frac{\partial h}{\partial \mu_{\mathrm{a}}^{i}}\right)^{\mathrm{T}} (h^{\mathrm{obs}} - h), \tag{6.42}$$

where $\mu_{\mathrm{a}}^i = \mu_{\mathrm{a}}(\mathbf{r}_i)$. The derivative of h with respect to μ_{a}^i is given by

$$\frac{\partial h}{\partial \mu_{\mathrm{a}}^i} = \frac{\partial \mu_{\mathrm{a}}}{\partial \mu_{\mathrm{a}}^i}\Phi + \mu_{\mathrm{a}}\frac{\partial \Phi_{\mathrm{c}}}{\partial \mu_{\mathrm{a}}^i} + \mu_{\mathrm{a}}\frac{\partial \Phi_{\mathrm{s}}}{\partial \mu_{\mathrm{a}}^i}. \tag{6.43}$$

Substituting this into Equation 6.42 and using the property of matrix transposes

$$(A_1 A_2 \dots A_n)^{\mathrm{T}} = A_n^{\mathrm{T}} \dots A_2^{\mathrm{T}} A_1^{\mathrm{T}}, \tag{6.44}$$

we find that

$$\begin{aligned}\frac{\partial \varepsilon}{\partial \mu_{\mathrm{a}}^i} = &-\Phi^{\mathrm{T}}\left(\frac{\partial \mu_{\mathrm{a}}}{\partial \mu_{\mathrm{a}}^i}\right)^{\mathrm{T}}(h^{\mathrm{obs}} - h) \\ &-\left(\frac{\partial \Phi_{\mathrm{c}}}{\partial \mu_{\mathrm{a}}^i}\right)^{\mathrm{T}}\mu_{\mathrm{a}}^{\mathrm{T}}(h^{\mathrm{obs}} - h) \\ &-\left(\frac{\partial \Phi_{\mathrm{s}}}{\partial \mu_{\mathrm{a}}^i}\right)^{\mathrm{T}}\mu_{\mathrm{a}}^{\mathrm{T}}(h^{\mathrm{obs}} - h).\end{aligned} \tag{6.45}$$

The first term can be calculated directly, and the second term requires differentiating 6.18 with respect to μ_{a}^i, which is simply the derivative of an exponentially decaying function. The third term requires the derivative of the scattered fluence, which we do not have a direct expression for. To obtain this, we differentiate 6.39 with respect to μ_{a}^i to obtain

$$\begin{aligned}\frac{\partial (A\Phi_{\mathrm{s}})}{\partial \mu_{\mathrm{a}}^i} &= \frac{\partial b}{\partial \mu_{\mathrm{a}}^i} \\ \Rightarrow \frac{\partial A}{\partial \mu_{\mathrm{a}}^i}\Phi_{\mathrm{s}} + A\frac{\partial \Phi_{\mathrm{s}}}{\partial \mu_{\mathrm{a}}^i} &= \frac{\partial b}{\partial \mu_{\mathrm{a}}^i} \\ \Rightarrow \frac{\partial \Phi_{\mathrm{s}}}{\partial \mu_{\mathrm{a}}^i} &= A^{-1}\left(\frac{\partial b}{\partial \mu_{\mathrm{a}}^i} - \frac{\partial A}{\partial \mu_{\mathrm{a}}^i}\Phi_{\mathrm{s}}\right).\end{aligned} \tag{6.46}$$

Substituting this into 6.45 gives

$$\begin{aligned}\frac{\partial\varepsilon}{\partial\mu_{\mathrm{a}}^{i}} = & - \Phi^{\mathrm{T}}\left(\frac{\partial\mu_{\mathrm{a}}}{\partial\mu_{\mathrm{a}}^{i}}\right)^{\mathrm{T}}(h^{\mathrm{obs}}-h) - \left(\frac{\partial\Phi_{\mathrm{c}}}{\partial\mu_{\mathrm{a}}^{i}}\right)^{\mathrm{T}}\mu_{\mathrm{a}}^{\mathrm{T}}(h^{\mathrm{obs}}-h) \\ & - \left(\frac{\partial b}{\partial\mu_{\mathrm{a}}^{i}}\right)^{\mathrm{T}}(A^{-1})^{\mathrm{T}}\mu_{\mathrm{a}}^{\mathrm{T}}(h^{\mathrm{obs}}-h) \\ & + \Phi_{\mathrm{s}}^{\mathrm{T}}\left(\frac{\partial A}{\partial\mu_{\mathrm{a}}^{i}}\right)^{\mathrm{T}}(A^{-1})^{\mathrm{T}}\mu_{\mathrm{a}}^{\mathrm{T}}(h^{\mathrm{obs}}-h), \end{aligned} \tag{6.47}$$

and, since $(A^{-1})^{\mathrm{T}} = (A^{\mathrm{T}})^{-1}$,

$$\begin{aligned}\frac{\partial\varepsilon}{\partial\mu_{\mathrm{a}}^{i}} = & - \Phi^{\mathrm{T}}\left(\frac{\partial\mu_{\mathrm{a}}}{\partial\mu_{\mathrm{a}}^{i}}\right)^{\mathrm{T}}(h^{\mathrm{obs}}-h) - \left(\frac{\partial\Phi_{\mathrm{c}}}{\partial\mu_{\mathrm{a}}^{i}}\right)^{\mathrm{T}}\mu_{\mathrm{a}}^{\mathrm{T}}(h^{\mathrm{obs}}-h) \\ & - \left(\frac{\partial b}{\partial\mu_{\mathrm{a}}^{i}}\right)^{\mathrm{T}}(A^{\mathrm{T}})^{-1}\mu_{\mathrm{a}}^{\mathrm{T}}(h^{\mathrm{obs}}-h) \\ & + \Phi_{\mathrm{s}}^{\mathrm{T}}\left(\frac{\partial A}{\partial\mu_{\mathrm{a}}^{i}}\right)^{\mathrm{T}}(A^{\mathrm{T}})^{-1}\mu_{\mathrm{a}}^{\mathrm{T}}(h^{\mathrm{obs}}-h). \end{aligned} \tag{6.48}$$

By defining the adjoint fluence Φ^{*} to be the solution to another diffusion equation

$$\begin{aligned} A^{\mathrm{T}}\Phi^{*} &:= \mu_{\mathrm{a}}^{\mathrm{T}}(h^{\mathrm{obs}}-h) \\ \Rightarrow \Phi^{*} &= (A^{\mathrm{T}})^{-1}\mu_{\mathrm{a}}^{\mathrm{T}}(h^{\mathrm{obs}}-h), \end{aligned} \tag{6.49}$$

we can substitute 6.49 into Equation 6.48 to obtain an expression for the absorption gradient:

$$\begin{aligned}\frac{\partial\varepsilon}{\partial\mu_{\mathrm{a}}^{i}} = & -\Phi^{\mathrm{T}}\left(\frac{\partial\mu_{\mathrm{a}}}{\partial\mu_{\mathrm{a}}^{i}}\right)^{\mathrm{T}}(h^{\mathrm{obs}}-h) - \left(\frac{\partial\Phi_{\mathrm{c}}}{\partial\mu_{\mathrm{a}}^{i}}\right)^{\mathrm{T}}\mu_{\mathrm{a}}^{\mathrm{T}}(h^{\mathrm{obs}}-h) \\ & - \left(\frac{\partial b}{\partial\mu_{\mathrm{a}}^{i}}\right)^{\mathrm{T}}\Phi^{*} + \Phi_{\mathrm{s}}^{\mathrm{T}}\left(\frac{\partial A}{\partial\mu_{\mathrm{a}}^{i}}\right)^{\mathrm{T}}\Phi^{*}. \end{aligned} \tag{6.50}$$

The gradient of the FEM system matrix can be calculated from

$$\frac{\partial A_{jk}}{\partial \mu_{\mathrm{a}}^i} = \int_\Omega \frac{\partial \hat{\kappa}}{\partial \mu_{\mathrm{a}}^i} \nabla\psi^k(\mathbf{r}) \cdot \nabla\psi^j(\mathbf{r}) \, \mathrm{d}\Omega + \int_\Omega \frac{\partial \mu_{\mathrm{a}}}{\partial \mu_{\mathrm{a}}^i} \psi^k(\mathbf{r}) \cdot \psi^j(\mathbf{r}) \, \mathrm{d}\Omega, \tag{6.51}$$

where

$$\frac{\partial \hat{\kappa}(\mathbf{r})}{\partial \mu_{\mathrm{a}}^i} = -3\hat{\kappa}(\mathbf{r}_i)^2. \tag{6.52}$$

The gradient of the source vector b with respect to μ_{a}^i is given by

$$\begin{aligned} \frac{\partial b}{\partial \mu_{\mathrm{a}}^i} &= \frac{\partial}{\partial \mu_{\mathrm{a}}^i}\left((1 + 3\hat{g}\kappa\hat{\mu}_{\mathrm{t}})\hat{\mu}_{\mathrm{s}}\Phi_{\mathrm{c}}\right) \\ \Rightarrow \frac{\partial b}{\partial \mu_{\mathrm{a}}^i} &= (1 + 3\hat{g}\kappa\hat{\mu}_{\mathrm{t}})\hat{\mu}_{\mathrm{s}}\frac{\partial \Phi_{\mathrm{c}}}{\partial \mu_{\mathrm{a}}^i} + 3\hat{g}\kappa\hat{\mu}_{\mathrm{s}}(1 - 3\kappa\hat{\mu}_{\mathrm{t}}\Phi_{\mathrm{c}}), \end{aligned} \tag{6.53}$$

and the derivative of the collimated fluence with respect to μ_{a}^i can be calculated from

$$\frac{\partial \Phi_{\mathrm{c}}}{\partial \mu_{\mathrm{a}}^i} = -\Phi_{\mathrm{c}} \int_{z_0}^{z} \frac{\partial \mu_{\mathrm{a}}(z')}{\partial \mu_{\mathrm{a}}^i} \, \mathrm{d}z'. \tag{6.54}$$

6.2.2 Functional gradient for the scattering coefficient

The gradient for the scattering coefficient can be found analogously, and is given by

$$\frac{\partial \varepsilon}{\partial \mu_{\mathrm{s}}^i} = -\left(\frac{\partial \Phi_{\mathrm{c}}}{\partial \mu_{\mathrm{s}}^i}\right)^{\mathrm{T}} \mu_{\mathrm{a}}^{\mathrm{T}}(h^{\mathrm{obs}} - h) - \left(\frac{\partial b}{\partial \mu_{\mathrm{s}}^i}\right)^{\mathrm{T}} \Phi^* + \Phi_{\mathrm{s}}^{\mathrm{T}} \left(\frac{\partial A}{\partial \mu_{\mathrm{s}}^i}\right)^{\mathrm{T}} \Phi^*, \tag{6.55}$$

with

$$\frac{\partial A_{jk}}{\partial \mu_{\mathrm{s}}^i} = \int_\Omega \frac{\partial \hat{\kappa}}{\partial \mu_{\mathrm{s}}^i} \nabla\psi^k(\mathbf{r}) \cdot \nabla\psi^j(\mathbf{r}) \, \mathrm{d}\Omega + \int_\Omega \frac{\partial \mu_{\mathrm{a}}}{\partial \mu_{\mathrm{s}}^i} \psi^k(\mathbf{r}) \cdot \psi^j(\mathbf{r}) \, \mathrm{d}\Omega, \tag{6.56}$$

where the derivative of the diffusion coefficient can be calculated using

$$\frac{\partial\hat{\kappa}(\mathbf{r})}{\partial\mu_{\mathrm{s}}^{i}} = -3(1-f)(1-\hat{g})\hat{\kappa}(\mathbf{r}_i)^2. \tag{6.57}$$

The derivative of the source vector with respect to μ_{s}^{i} is given by

$$\begin{aligned} \frac{\partial b}{\partial\mu_{\mathrm{s}}^{i}} &= \frac{\partial}{\partial\mu_{\mathrm{s}}^{i}}\left((1+3\hat{g}\kappa\hat{\mu}_{\mathrm{t}})\hat{\mu}_{\mathrm{s}}\Phi_{\mathrm{c}}\right) \\ \Rightarrow \frac{\partial b}{\partial\mu_{\mathrm{s}}^{i}} &= (1+3\hat{g}\kappa\hat{\mu}_{\mathrm{t}})\hat{\mu}_{\mathrm{s}}\frac{\partial\Phi_{\mathrm{c}}}{\partial\mu_{\mathrm{s}}^{i}} \\ &\quad + (1+3\hat{g}\kappa(\hat{\mu}_{\mathrm{t}}+\hat{\mu}_{\mathrm{s}}-3(1-\hat{g})\kappa\hat{\mu}_{\mathrm{t}}\hat{\mu}_{\mathrm{s}}))(1-f)\Phi_{\mathrm{c}}, \end{aligned} \tag{6.58}$$

and the derivative of the collimated fluence with respect to μ_{s}^{i} is found from

$$\frac{\partial\Phi_{\mathrm{c}}}{\partial\mu_{\mathrm{s}}^{i}} = -\int_{z_0}^{z}\frac{\partial\hat{\mu}_{\mathrm{s}}(z')}{\partial\mu_{\mathrm{s}}^{i}}\,\mathrm{d}z'\Phi_{\mathrm{c}}. \tag{6.59}$$

As with the RTE-based minimisation scheme, the incorporation of the adjoint model means that both functional gradients can be calculated using only one run each of the forward and adjoint model.

6.2.3 Verification of functional gradient calculations

Though a finite difference calculation might be time-consuming, it is also a very accurate and robust way to approximate a derivative. We will therefore check that the above gradient calculations are correct by comparing them to the derivative of the error functional calculated using a finite difference method. The derivative of the error functional with respect to the absorption coefficient at a particular point $\mathbf{r}_i$, denoted by $\mu_{\mathrm{a}}^{i} = \mu_{\mathrm{a}}(\mathbf{r}_i)$, can be approximated by

$$\frac{\partial\varepsilon}{\partial\mu_{\mathrm{a}}^{i}} \approx \frac{\varepsilon(\mu_{\mathrm{a}}^{i}+\Delta\mu_{\mathrm{a}}) - \varepsilon(\mu_{\mathrm{a}}^{i})}{\Delta\mu_{\mathrm{a}}}, \tag{6.60}$$

and with respect to the scattering coefficient at $\mathbf{r}_i$, denoted by $\mu_{\mathrm{s}}^i = \mu_{\mathrm{s}}(\mathbf{r}_i)$, by

$$\frac{\partial \varepsilon}{\partial \mu_{\mathrm{s}}^i} \approx \frac{\varepsilon(\mu_{\mathrm{s}}^i + \Delta\mu_{\mathrm{s}}) - \varepsilon(\mu_{\mathrm{s}}^i)}{\Delta\mu_{\mathrm{s}}}, \tag{6.61}$$

where $\Delta\mu_{\mathrm{a}}$ and $\Delta\mu_{\mathrm{s}}$ are some small, non-zero perturbations to μ_{a} and μ_{s}, respectively. In this case we chose $\Delta\mu_{\mathrm{a}} = 10^{-5}$ mm^{-1} and $\Delta\mu_{\mathrm{s}} = 5 \times 10^{-3}$ mm^{-1}. To evaluate the error functional at the perturbed absorption coefficient, the forward δ-Eddington model must be solved to obtain the absorbed optical energy evaluated at the perturbed absorption coefficient. This process must be repeated for every node in the computational mesh to build up an image of the absorption and scattering gradients across the entire domain. This means that calculating the functional gradients with respect to absorption and scattering will require $2N_n + 1$ evaluations of the forward model, where N_n is the number of nodes in the computational mesh. Using the adjoint-assisted method presented in Section 6.2.1, both functional gradients can be calculated using a single run each of the forward and adjoint models, equivalent to two runs of the forward model. This will speed up the gradient calculation significantly, even for a very coarse mesh. If we consider that the functional gradients will be evaluated at each iteration of a gradient-based minimisation method, the incorporation of the adjoint-assisted calculation makes the use of a gradient-based method much more practical.

FIGURE 6.3: Absorption and scattering coefficients used to compare the error functional gradients calculated using the adjoint-assisted method to a finite difference calculation. The optical absorption coefficient consists of a homogeneous background of 0.01 mm^{-1} with two square absorbing inclusions with values of 0.2 mm^{-1} and 0.3 mm^{-1}. The optical scattering coefficient consists of a homogeneous background of 5 mm^{-1} with two square absorbing inclusions with values of 10 mm^{-1} and 15 mm^{-1}.

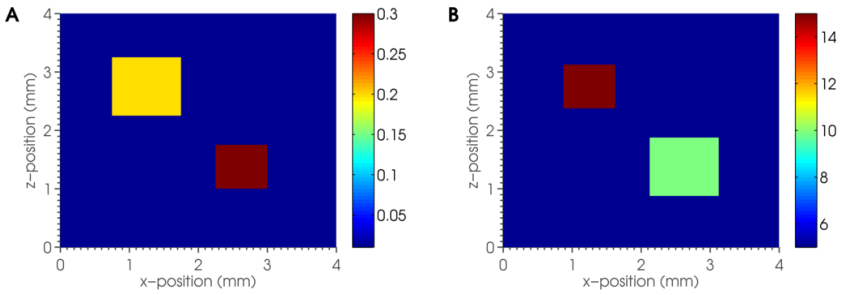

A structured triangular mesh consisting of $N_n = 1089$ nodes and $N_e = 2048$ triangular

elements was used to perform the simulations in this section. The absorption and scattering coefficients are shown in Figure 6.3. The optical absorption coefficient consists of a homogeneous background of 0.01 mm^{-1} with two square absorbing inclusions with values of 0.2 mm^{-1} and 0.3 mm^{-1}. The optical scattering coefficient consists of a homogeneous background of 5 mm^{-1} with two square absorbing inclusions with values of 10 mm^{-1} and 15 mm^{-1}. Given these absorption and scattering coefficients, the δ-Eddington approximation can be used to create a set of simulated PAT images (see Section 6.3.1 for more details), which we will refer to as the measured data. Additive Gaussian noise can be added to these images to simulate the noise that would be present in a real PAT image. Once this measured data h^{obs} has been simulated, an initial guess at the absorption and scattering can be made and used to simulate the absorbed energy h based on this initial guess. Here, initial guesses of homogeneous absorption and scattering coefficients set at their respective background values have been used. Now that we have measured data h^{obs} and an initial estimate h, the error functional 6.36 can then be calculated straightforwardly. The error functional gradients with respect to absorption and scattering can then be calculated using the adjoint-assisted method (Equation 6.50) and compared to the resulting functional gradients calculated using a finite difference method.

FIGURE 6.4: The error functional gradient with respect to the absorption coefficient is calculated using (A) the adjoint-assisted method presented in Section 6.2.1 and compared with (B) a finite difference calculation. A profile comparison in the z-direction at $x = 1$ mm can be seen in (C).

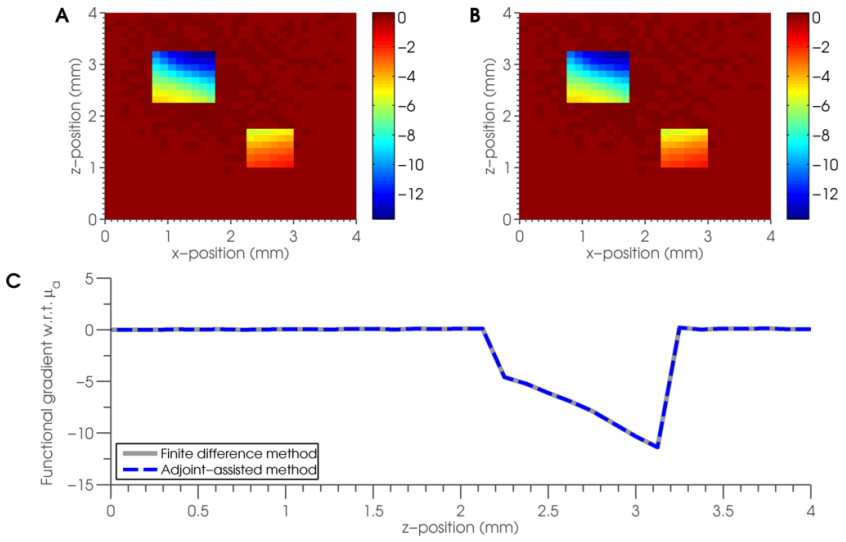

FIGURE 6.5: The error functional gradient with respect to the scattering coefficient is calculated using (A) the adjoint-assisted method presented in Section 6.2.1 and compared with (B) a finite difference calculation. A profile comparison in the z-direction at $x = 1$ mm can be seen in (C).

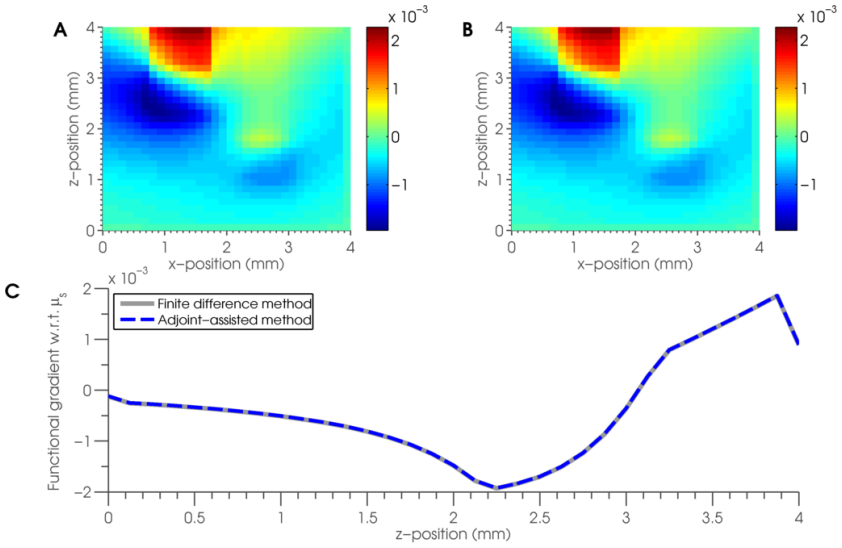

Figures 6.4 and 6.5 show the results for the absorption and scattering gradients, respectively. In both cases, the functional gradients calculated using the adjoint-assisted method show excellent agreement with the corresponding finite difference calculation. Analogously to Sections 4.1.5 and 5.0.3, the relative errors in the gradients can be calculated using

$$\varepsilon_{\mathrm{a}} = \frac{\left\| \left(\frac{\partial \varepsilon}{\partial \mu_{\mathrm{a}}}\right)_{\mathrm{FD}} - \left(\frac{\partial \varepsilon}{\partial \mu_{\mathrm{a}}}\right)_{\mathrm{adj}} \right\|}{\left\| \left(\frac{\partial \varepsilon}{\partial \mu_{\mathrm{a}}}\right)_{\mathrm{FD}} \right\|} \tag{6.62}$$

and

$$\varepsilon_{\mathrm{s}} = \frac{\left\| \left(\frac{\partial \varepsilon}{\partial \mu_{\mathrm{s}}}\right)_{\mathrm{FD}} - \left(\frac{\partial \varepsilon}{\partial \mu_{\mathrm{s}}}\right)_{\mathrm{adj}} \right\|}{\left\| \left(\frac{\partial \varepsilon}{\partial \mu_{\mathrm{s}}}\right)_{\mathrm{FD}} \right\|}, \tag{6.63}$$

where $\left(\frac{\partial \varepsilon}{\partial \mu_{\mathrm{a}}}\right)_{\mathrm{FD}}$ and $\left(\frac{\partial \varepsilon}{\partial \mu_{\mathrm{a}}}\right)_{\mathrm{adj}}$ are the functional gradients with respect to absorption calculated using the finite difference method and adjoint-assisted method, respectively, and $\left(\frac{\partial \varepsilon}{\partial \mu_{\mathrm{s}}}\right)_{\mathrm{FD}}$ and $\left(\frac{\partial \varepsilon}{\partial \mu_{\mathrm{s}}}\right)_{\mathrm{adj}}$ are the functional gradients with respect to scattering calculated using the finite difference method and adjoint-assisted method, respectively. In this case,

the errors were $\varepsilon_{\mathrm{a}} = 4.09 \times 10^{-6}$ and $\varepsilon_{\mathrm{s}} = 6.5 \times 10^{-3}$. The finite difference calculation took approximately 7 minutes to calculate both the absorption and scattering gradients, compared with less than half a second to complete the adjoint-assisted calculation.

6.3 Numerical examples using 2D simulated data

In this section, the adjoint-assisted quasi-Newton scheme based on the δ-Eddington approximation to the RTE will be used to recover quantitative estimates of the optical absorption coefficient from 2D simulated PAT images. Section 6.3.2 will assume that the scattering coefficient is known *a priori* in order to demonstrate that a highly accurate quantitative estimate of the absorption coefficient can be found using the above algorithm. Section 6.3.3 will assume that the absorption coefficient is known *a priori* and attempt to recover the scattering coefficient. Section 6.3.4 will look to reconstruct both optical coefficients simultaneously for three different sets of measured PAT data obtained using three different source geometries. Each example will show the reconstructed coefficients using noise-free simulated data and data including additive Gaussian noise.

6.3.1 Simulation of 2D PAT images

The computational mesh, used for all the simulations in this section was a triangulation of the square domain $[0, 4] \times [0, 4]$ mm^2, consisting of $N_e = 2048$ triangular elements and $N_n = 1089$ nodes. The anisotropy factor was considered to be known and constant at $g = 0.8$, and the factor f of light scattered into the forward direction was chosen to be $f = 0.026094g^3 + 0.023597g^2 + 0.13572g + 0.60366$ to maintain correspondence with the Monte Carlo forward solution [100]. The optical coefficients were the same as those used to verify the functional gradient calculation in Section 6.2.3, as shown in Figure 6.3. The scattering coefficient μ_{s} was chosen such that $\mu_{\mathrm{s}}' = \mu_{\mathrm{s}}(1 - g)$ varied between 1 mm^{-1} and 3 mm^{-1}, which is typical of biological tissue. μ_{s} consisted of a background value of $\mu_{\mathrm{s}}^{\mathrm{bg}} = 5$ mm^{-1} and two non-smooth scattering inclusions of $\mu_{\mathrm{s}}^{1} = 10$ mm^{-1}

and $\mu_{\mathrm{s}}^2 = 15$ mm^{-1}. The absorption coefficient had a background value of $\mu_{\mathrm{a}}^{\mathrm{bg}} = 0.01$ mm^{-1} and two non-smooth absorbing inclusions of $\mu_{\mathrm{a}}^1 = 0.2$ mm^{-1} and $\mu_{\mathrm{a}}^2 = 0.3$ mm^{-1}.

As in Chapters 4 and 5, multiple images were used to perform the inversion, obtained using combinations of different source geometries. These were arrays of point sources placed to create either a line across the domain boundary, or a 'top hat' beam profile with a width of 0.5 mm at the centre of each boundary. Top hat sources were used to avoid some instability in the solution which results from using a single point source. Figure 6.6 shows the four illuminations positions for the line source arrays, and Figure 6.7 shows the four illumination positions of the top hat arrays.

FIGURE 6.6: Mesh structure and source geometry used to perform the gradient-based QPAT inversion which incorporates the δ-Eddington approximation. Four illumination positions containing four different line source arrays are used to create sets of simulated PAT images.

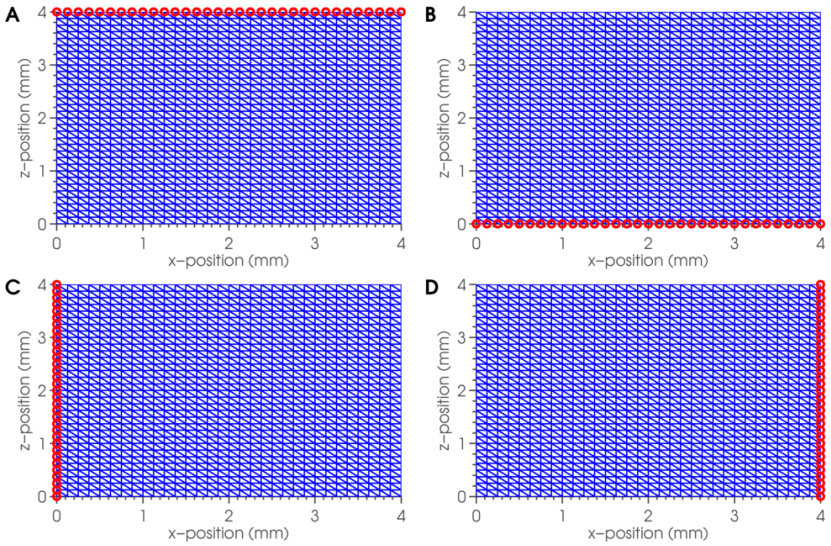

Given that we have now defined our optical coefficients, source geometry and other important constants, we can now solve Equation 6.18 for the collimated fluence distribution Φ_{c}. This is then used to calculate the source term for the diffusion equation 6.34, which is solved for the scattered fluence Φ_{s}. The total fluence distribution Φ is then equal to the sum of the collimated and scattered fields, and the measured absorbed optical energy density is calculated from $h^{\mathrm{obs}} = \mu_{\mathrm{a}}\Phi + \eta$, where η represents additive Gaussian

FIGURE 6.7: Mesh structure and source geometry used to perform the gradient-based QPAT inversion which incorporates the δ-Eddington approximation. Four illumination positions containing four different 'top hat' source arrays are used to create sets of simulated PAT images.

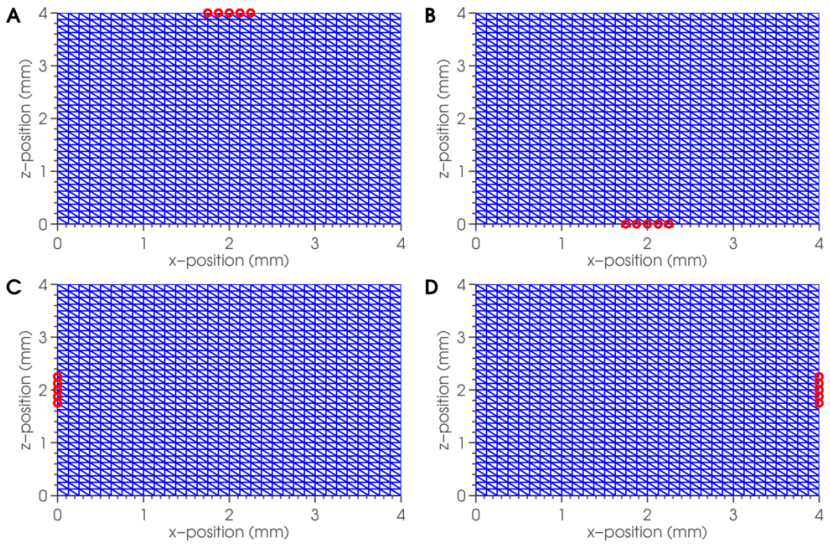

noise. Figure 6.8 shows (A) the collimated fluence, (B) the scattered fluence, (C) the total fluence, and (D) the measured absorbed optical energy density with additive noise scaled to 5% of the mean absorbed energy. These images result from a line source array placed along the top boundary ($z = 4$ mm), as shown in Figure 6.6(A).

Using this set of measured absorbed energy images, we can proceed to apply a gradient-based method using the functional gradient calculations derived in Section 6.2.1. For all of the results in this chapter, as in previous chapters, the limited memory BFGS (l-BFGS) method was used to perform the inversion. The l-BFGS method saves gradient information from a user-defined number of previous iterations to build an approximation to the inverse Hessian matrix (see Appendix D for more details). Here, 15 previous iterations were stored, following advice found in the literature [95]. The l-BFGS method was performed for a maximum of 2500 iterations. The background values of the optical coefficients to be recovered are used as an initial starting guess to begin the iterative scheme.

FIGURE 6.8: Forward data calculated using the δ-Eddington approximation to the RTE. The absorption and scattering coefficients are both heterogeneous, consisting of two square inclusions placed in a homogeneous background, and can be seen in Figure 6.3. The source is a line source array placed along the top boundary ($z = 4$ mm), as shown in Figure 6.6(A). Given these optical coefficients and source geometry, a PAT image can be simulated using the δ-Eddington approximation by calculating (A) the collimated fluence, (B) the scattered fluence, (C) the total fluence, and finally (D) the measured absorbed optical energy density, to which additive Gaussian noise may be added. In (D), noise scaled to 5% of the mean absorbed energy has been included.

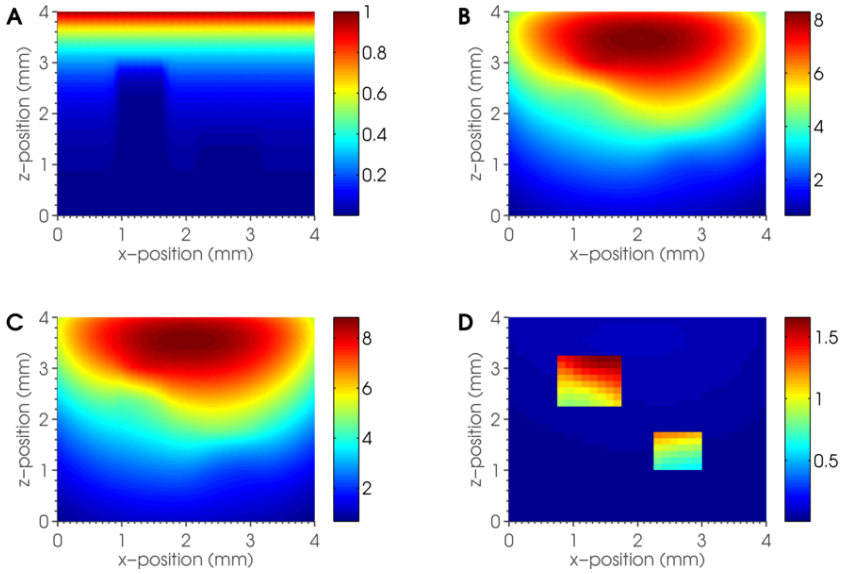

6.3.2 Inversion for absorption coefficient

In this example, the gradient-based method incorporating the δ-Eddington approximation is demonstrated by recovering a quantitatively accurate estimate of the optical absorption coefficient from a set of 2D simulated PAT images when the optical scattering coefficient is considered to be known *a priori*. Four line sources, as shown in Figure 6.6, were used to simulate the 2D measured data. Two sets of measurement data were obtained; one without any additive noise and another with additive Gaussian noise scaled to 5% of the mean absorbed optical energy density. The background absorption coefficient was used as an initial guess to begin the iterative inversion. To quantify the error in the absorption reconstruction, we shall look at the per cent relative error ϵ_{a}, calculated using

$$\epsilon_{\mathrm{a}} = \frac{\left\| \mu_{\mathrm{a}}^{\mathrm{true}} - \mu_{\mathrm{a}}^{\mathrm{approx}} \right\|}{\left\| \mu_{\mathrm{a}}^{\mathrm{true}} \right\|}, \tag{6.64}$$

where $\mu_{\mathrm{a}}^{\mathrm{true}}$ is the true absorption coefficient, seen in Figure 6.3(A), and $\mu_{\mathrm{a}}^{\mathrm{approx}}$ is the reconstructed absorption coefficient.

FIGURE 6.9: Reconstructed absorption coefficient using the gradient-based method based on the δ-Eddington approximation from 2D simulated data when the scattering is known *a priori*. (A) True absorption coefficient; (B) Reconstructed absorption coefficient from noise-free data; (C) Reconstructed absorption coefficient from data including 5% additive Gaussian noise.

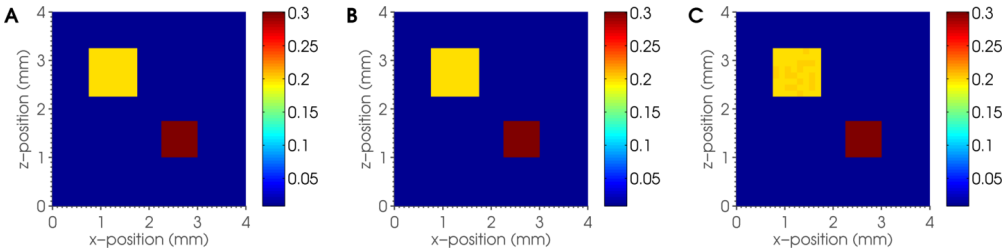

Figure 6.9 show the results of the reconstruction for the optical absorption coefficient after 35 iterations. Figure 6.9(A) shows the true absorption coefficient, Figure 6.9(B) shows the reconstructed absorption coefficient from the noise-free data, and Figure 6.9(C) shows the reconstructed absorption coefficient from the noisy data. The percent relative errors in the absorption reconstructions were $\epsilon_{\mathrm{a}} = 2.8 \times 10^{-12}\%$ and $\epsilon_{\mathrm{a}} = 0.8\%$ for reconstructions from noise-free and noisy data, respectively.

FIGURE 6.10: (A) shows a profile comparison corresponding to the results shown in Figure 6.9, the reconstructed absorption coefficient when the scattering is known *a priori*. The profiles compare the true absorption coefficient (solid grey) and the reconstructed absorption coefficients from noise-free (blue dashed) and noisy (red dotted) simulated 2D images. The profile is in the x-direction at $z = 1.2$ mm. (B) shows the percent relative errors in the reconstructed absorption coefficient from noise-free (blue dashed) and noisy (blue dotted) data at each iteration of the method.

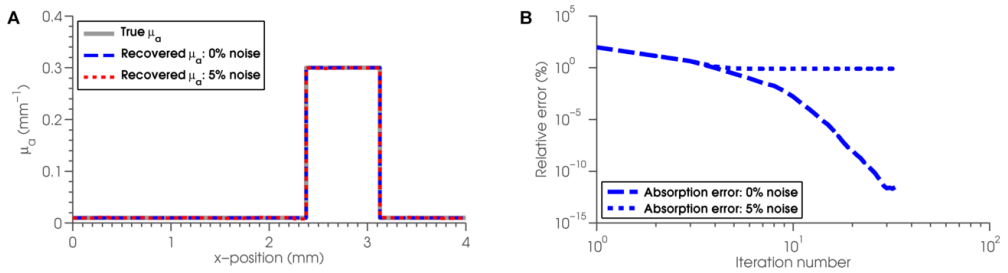

A profile comparison in the x-direction at $z = 1.2$ mm, which is through the smaller, stronger absorbing inclusion, can be seen in Figure 6.10(A). Figure 6.10(B) shows a plot

of the percent relative error ϵ_{a} at each iteration. Both cases show excellent agreement with the true absorption coefficient in all areas of the domain after only 35 iterations. In both cases, a relative error less than 1% is achieved after 10 iterations. In the noisy case, the solution converges to an error of $\epsilon_{\mathrm{a}} = 0.8\%$, and does not improve with more iterations of the method. Though this is only a small error, it is likely that it may be improved by the inclusion of an appropriate regularisation scheme for non-smooth data was included, e.g. total variation regularisation.

6.3.3 Inversion for scattering coefficient

In this example, we assume the optical absorption coefficient is known *a priori* and investigate how well we can recover a quantitatively accurate estimate of the optical scattering coefficient. The simulated data is obtained as outlined in Section 6.3.3, and the background scattering coefficient is used as an initial guess to begin the iterative inversion. The sensitivity to noise is more apparent when reconstructing the scattering coefficient, and so first-order Tikhonov regularisation was added to the error functional, which has the effect of smoothing the solution. To quantify the error in the scattering reconstruction, we shall look at the per cent relative error ϵ_{s}, which is analogous to Equation 6.64 and is calculated using

$$\epsilon_{\mathrm{s}} = \frac{\left\| \mu_{\mathrm{s}}^{\mathrm{true}} - \mu_{\mathrm{s}}^{\mathrm{approx}} \right\|}{\left\| \mu_{\mathrm{s}}^{\mathrm{true}} \right\|}, \tag{6.65}$$

where $\mu_{\mathrm{s}}^{\mathrm{true}}$ is the true scattering coefficient, seen in Figure 6.3(B), and $\mu_{\mathrm{s}}^{\mathrm{approx}}$ is the reconstructed scattering coefficient.

Figure 6.11 show the results of the reconstruction for the optical scattering coefficient after 500 iterations. Figure 6.11(A) shows the true scattering coefficient, Figure 6.11(B) shows the reconstructed scattering coefficient from the noise-free data, and Figure 6.11(C) shows the reconstructed scattering coefficient from the noisy data. The percent relative errors in the scattering reconstructions were $\epsilon_{\mathrm{s}} = 1.95\%$ and $\epsilon_{\mathrm{s}} = 14.32\%$

FIGURE 6.11: Reconstructed scattering coefficient using the gradient-based method based on the δ-Eddington approximation from 2D simulated data. (A) True scattering coefficient; (B) Reconstructed scattering coefficient from noise-free data; (C) Reconstructed scattering coefficient from data including 5% additive Gaussian noise.

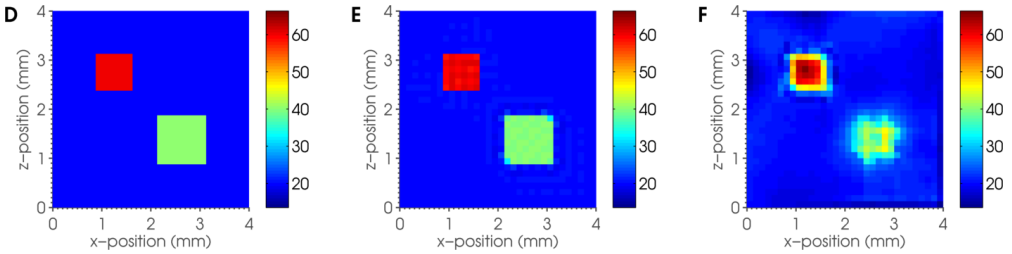

for reconstructions from noise-free and noisy data, respectively. A profile comparison in the x-direction at $z = 2.4$ mm, through the smaller, stronger scattering inclusion, can be seen in Figure 6.12(A). Figure 6.12(B) shows a plot of the percent relative error ϵ_s at each iteration.

FIGURE 6.12: (A) shows a profile comparison corresponding to the results shown in Figure 6.11, the inversion results using the gradient-based method which incorporates the δ-Eddington approximation to reconstruct the scattering coefficient from 2D simulated data. The profiles compare the true scattering coefficient (solid grey) and the reconstructed scattering coefficients from noise-free (blue dashed) and noisy (red dotted) simulated 2D images. The profile is in the x-direction at $z = 2.4$ mm. The profile is in the x-direction at $z = 1.2$ mm. (B) shows the percent relative errors in the reconstructed absorption coefficient from noise-free (red dashed) and noisy (red dotted) data at each iteration of the method.

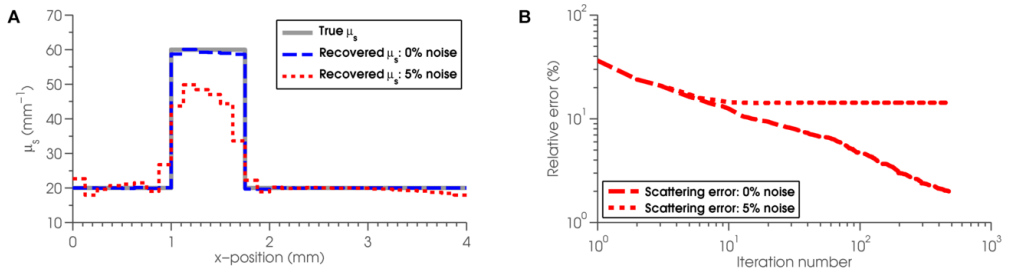

These results demonstrate that the relatively weak dependence of the data on the optical scattering coefficient means that the recovery of μ_s is much more challenging than the recovery of μ_a; even in the case where the μ_a is known *a priori*, and there is no noise present in the simulated data, convergence to the correct μ_s is much slower than when convergence to the correct μ_a. Obtaining a scattering estimate which is comparably accurate to the absorption estimate obtained in Section 6.3.2 takes a significantly larger

number of iterations of the method. For the noise-free case, an error of $\epsilon_{\mathrm{s}} = 1.95\%$ was found after 500 iterations. The error plot in Figure 6.12(B) suggests that this will continue to improve if a larger number of iterations are used, however, when recovering for μ_{a} in Section 6.3.2, an error of $\epsilon_{\mathrm{a}} = 0.1\%$ was found in only 10 iterations. In the case where noisy data is used, the reconstructed scattering eventually converges to an underestimation of the true scattering at the inclusion locations, though this may be partly due to the smoothing effect of the added Tikhonov regularisation. Regularisation based on prior knowledge of the optical coefficients will always provide an improved reconstruction, and so in this case, where the optical coefficients are discontinuous, an edge-preserving regularisation method such as total variation would likely improve the reconstructions. However, in general, the structure of the optical coefficients will not be known, and so that prior information will not be available.

6.3.4 Inversion for absorption and scattering

In this section it is assumed that both optical coefficients are unknown, and we attempt to recover both optical absorption and scattering coefficients simultaneously. The true absorption scattering coefficients can be seen in Figure 6.3. Three examples will be investigated, corresponding to three different sets of simulated data obtained using different source geometries. In each example we show the reconstructed optical coefficients recovered from noise-free and noisy data. Wherever noisy data has been used, Tikhonov regularisation is included to reduce the amplification of noise in the scattering inversion.

6.3.4.1 Example using two line sources

The first example will consider the case where two PAT images have been simulated using two line source arrays, one from the top of the domain and one from the bottom of the domain, as can be seen in Figures 6.7(A) and 6.7(B).

FIGURE 6.13: Reconstructed absorption and scattering coefficients using the gradient-based method incorporating the δ-Eddington approximation from 2D simulated data obtained using two line sources. (A) True absorption coefficient; (B) Reconstructed absorption coefficient from noise-free data; (C) Reconstructed absorption coefficient from data including 5% additive Gaussian noise. (D) True scattering coefficient; (E) Reconstructed scattering coefficient from noise-free data; (F) Reconstructed scattering coefficient from data including 5% additive Gaussian noise.

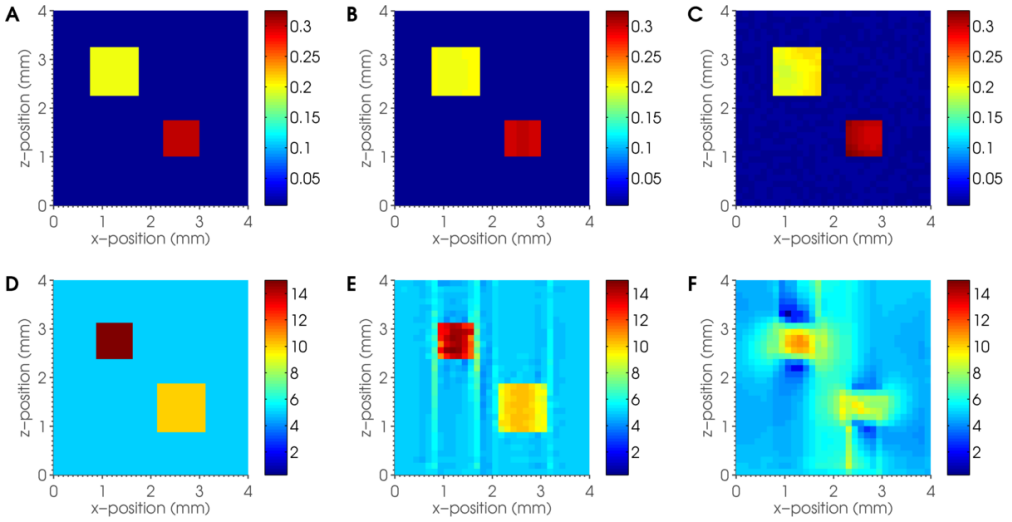

FIGURE 6.14: Profile comparison of the inversion results corresponding to Figure 6.13. (A) Profile comparison of the true absorption coefficient (solid grey) and the reconstructed absorption coefficients from noise-free (blue dashed) and noisy (red dotted) simulated 2D images. The profile is in the x-direction at $z = 1.2$ mm. (B) Profile comparison of the true scattering coefficient (solid grey) and the reconstructed scattering coefficients from noise-free (blue dashed) and noisy (red dotted) simulated 2D images. The profile is in the x-direction at $z = 2.4$ mm. (C) shows the percent relative errors in the reconstructed absorption and scattering coefficients at each iteration; absorption error from noise-free data (blue dashed); absorption error from noisy (blue dotted) data; scattering error from noise-free data (red dashed); scattering error from noisy data (red dotted).

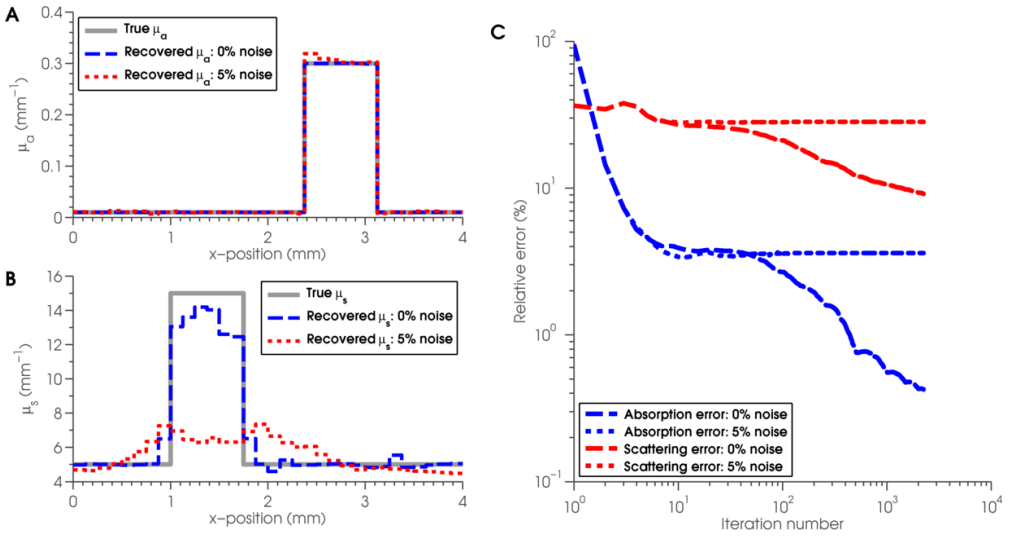

6.3.4.2 Example using four top hat sources

This second example recovering both absorption and scattering simultaneously will consider the case where four PAT images have been simulated using four top hat source arrays, one from each of the four sides of the domain, as can be seen in Figures 6.7(A-D).

FIGURE 6.15: Reconstructed absorption and scattering coefficients using the gradient-based method incorporating the δ-Eddington approximation from 2D simulated data obtained using four top-hat sources. (A) True absorption coefficient; (B) Reconstructed absorption coefficient from noise-free data; (C) Reconstructed absorption coefficient from data including 5% additive Gaussian noise. (D) True scattering coefficient; (E) Reconstructed scattering coefficient from noise-free data; (F) Reconstructed scattering coefficient from data including 5% additive Gaussian noise.

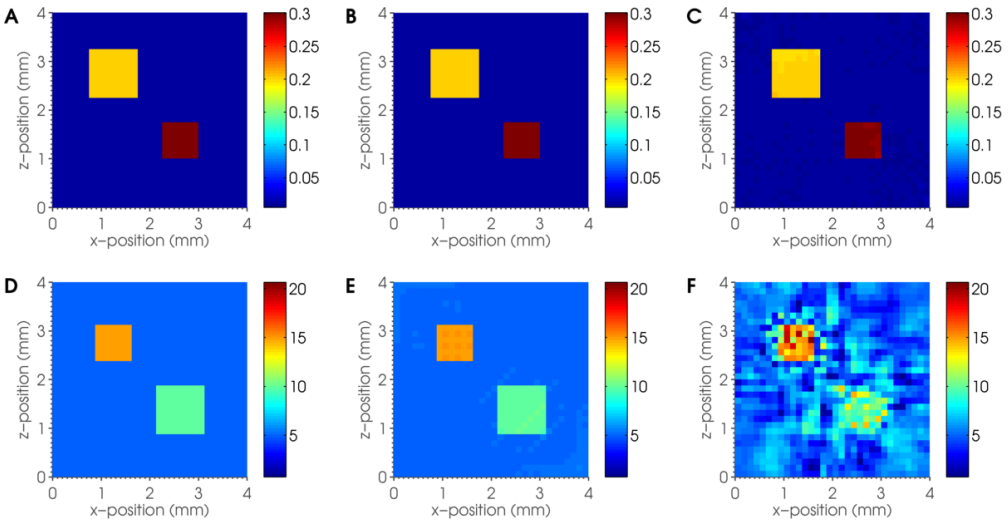

Figure 6.15(A) shows the true absorption coefficient, Figure 6.15(B) shows the reconstructed absorption coefficient from the noise-free data after 2227 iterations, and Figure 6.15(C) shows the reconstructed absorption coefficient from the noisy data after 100 iterations. The percent relative errors in the absorption reconstructions were $\epsilon_{\mathrm{a}} = 0.08\%$ and $\epsilon_{\mathrm{a}} = 1.63\%$ for reconstructions from noise-free and noisy data, respectively. Figure 6.15(D) shows the true scattering coefficient, Figure 6.15(E) shows the reconstructed scattering coefficient from the noise-free data, and Figure 6.15(F) shows the reconstructed scattering coefficient from the noisy data. The percent relative errors in the scattering reconstructions were $\epsilon_{\mathrm{s}} = 1.29\%$ and $\epsilon_{\mathrm{s}} = 28.66\%$ for reconstructions

from noise-free and noisy data, respectively.

FIGURE 6.16: Profile comparison of the inversion results corresponding to Figure 6.15. (A) Profile comparison of the true absorption coefficient (solid grey) and the reconstructed absorption coefficients from noise-free (blue dashed) and noisy (red dotted) simulated 2D images. The profile is in the x-direction at $z = 1.2$ mm. (B) Profile comparison of the true scattering coefficient (solid grey) and the reconstructed scattering coefficients from noise-free (blue dashed) and noisy (red dotted) simulated 2D images. The profile is in the x-direction at $z = 2.4$ mm. (C) shows the percent relative errors in the reconstructed absorption and scattering coefficients at each iteration; absorption error from noise-free data (blue dashed); absorption error from noisy (blue dotted) data; scattering error from noise-free data (red dashed); scattering error from noisy data (red dotted).

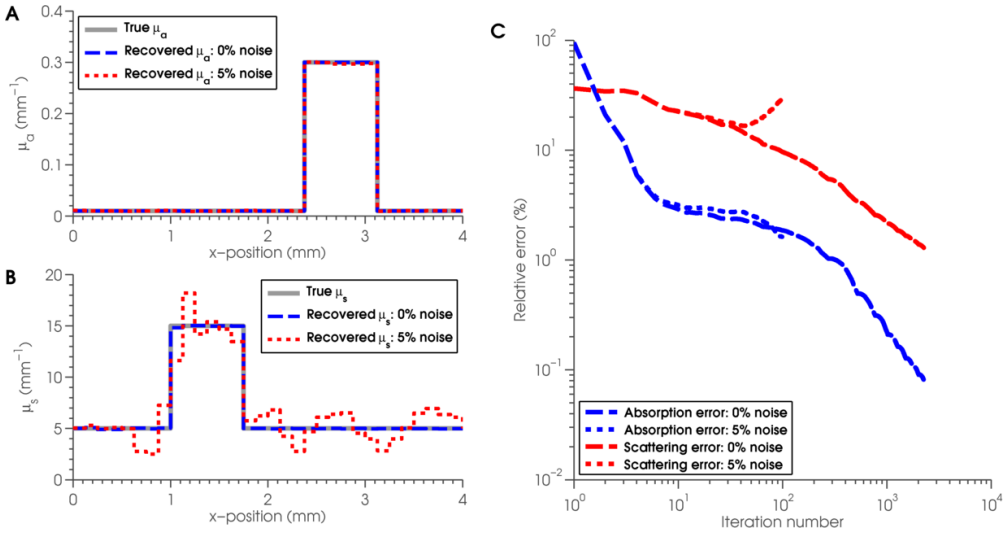

Profile comparisons in the x-direction can be seen in Figure 6.16. Figure 6.16(A) shows a profile at $z = 1.2$ mm comparing the true and reconstructed absorption coefficients, and Figure 6.16(B) shows a profile at $z = 2.4$ mm comparing the true and reconstructed scattering coefficients. Figure 6.16(C) shows a plot of the percent relative errors ϵ_{a} and ϵ_{s} at each iteration.

6.3.4.3 Example using four line sources

This first example will consider the case where four PAT images have been simulated using four line source arrays, one from each of the four sides of the domain, as can be

seen in Figures 6.6(A-D).

FIGURE 6.17: Reconstructed absorption and scattering coefficients using the gradient-based method incorporating the δ-Eddington approximation from 2D simulated data obtained using four line sources. (A) True absorption coefficient; (B) Reconstructed absorption coefficient from noise-free data; (C) Reconstructed absorption coefficient from data including 5% additive Gaussian noise. (D) True scattering coefficient; (E) Reconstructed scattering coefficient from noise-free data; (F) Reconstructed scattering coefficient from data including 5% additive Gaussian noise.

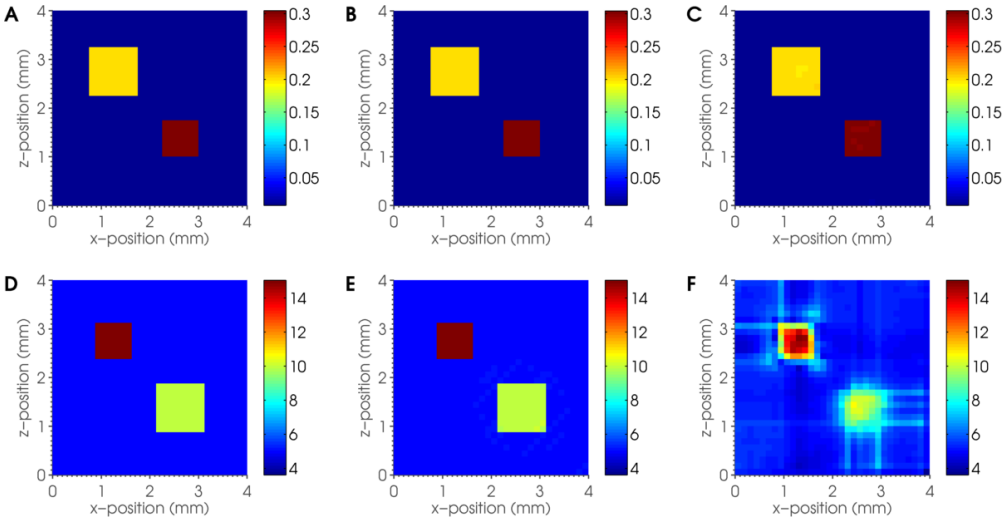

Figure 6.17 show the results of the reconstruction after 2270 iterations. Figure 6.17(A) shows the true absorption coefficient, Figure 6.17(B) shows the reconstructed absorption coefficient from the noise-free data, and Figure 6.17(C) shows the reconstructed absorption coefficient from the noisy data. The percent relative errors in the absorption reconstructions were $\epsilon_{\mathrm{a}} = 7.7 \times 10^{-4}\%$ and $\epsilon_{\mathrm{a}} = 1.12\%$ for reconstructions from noise-free and noisy data, respectively. Figure 6.17(D) shows the true scattering coefficient, Figure 6.17(E) shows the reconstructed scattering coefficient from the noise-free data, and Figure 6.17(F) shows the reconstructed scattering coefficient from the noisy data. The percent relative errors in the scattering reconstructions were $\epsilon_{\mathrm{s}} = 0.44\%$ and $\epsilon_{\mathrm{s}} = 17.09\%$ for reconstructions from noise-free and noisy data, respectively.

Profile comparisons in the x-direction can be seen in Figure 6.18. Figure 6.18(A) shows a profile at $z = 1.2$ mm comparing the true and reconstructed absorption coefficients, and Figure 6.18(B) shows a profile at $z = 2.4$ mm comparing the true and reconstructed

FIGURE 6.18: Profile comparison of the inversion results corresponding to Figure 6.17. (A) Profile comparison of the true absorption coefficient (solid grey) and the reconstructed absorption coefficients from noise-free (blue dashed) and noisy (red dotted) simulated 2D images. The profile is in the x-direction at $z = 1.2$ mm. (B) Profile comparison of the true scattering coefficient (solid grey) and the reconstructed scattering coefficients from noise-free (blue dashed) and noisy (red dotted) simulated 2D images. The profile is in the x-direction at $z = 2.4$ mm. (C) shows the percent relative errors in the reconstructed absorption and scattering coefficients at each iteration: the absorption error from noise-free data (blue dashed); the absorption error from noisy (blue dotted) data; the scattering error from noise-free data (red dashed); the scattering error from noisy data (red dotted).

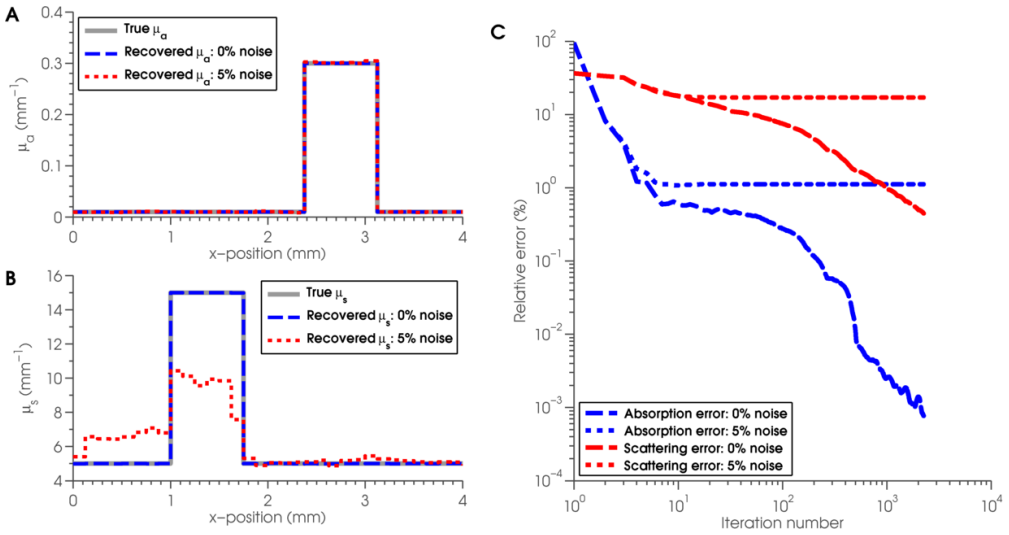

scattering coefficients. Figure 6.18(C) shows a plot of the percent relative errors ϵ_{a} and ϵ_{s} at each iteration. In both cases, highly accurate reconstructions of the absorption coefficient can be recovered; an error of less than 2% is achieved in 10 iterations, which improves considerably more in the case where noise-free data is used. As may be expected from the previous sections, the scattering estimate is slower to converge. A highly accurate estimate of the scattering coefficient, with $\epsilon_{\mathrm{s}} = 0.44\%$, is recovered in the noise-free case. This estimate is more accurate than the result obtained in Section 6.3.3 after 500 iterations, confirming the previous thought that the estimate would improve if the minimisation had completed a larger number of iterations. In the case where noisy data has been used, a good estimate of the scattering coefficient is recovered, though it is underestimated and smoothed. This is also in line with the results from Section 6.3.3, and is again likely to be an effect of the Tikhonov regularisation.

6.4 Simulating PAT images using the Monte Carlo method

In the numerical examples presented so far, the simulation of the measurement data has been performed using the δ-Eddington approximation. Whilst the δ-Eddington is a good approximation to the behaviour of light in tissue, it is still an approximation, and will not therefore be an exact representation of the measurement data that would be obtained in practice. In this section, we will use a highly accurate model of light transport to obtain the measurement data in order to provide a more accurate simulation of a PAT image. Using this data, we will then apply the gradient-based method using the δ-Eddington approximation to reconstruct the optical coefficients.

To simulate the forward data we used the MC method, which was used to verify the δ-Eddington model in Section 6.1.1. The MC model requires a structured rectangular mesh. The mesh to calculate the forward data contained 16384 square elements. The mesh to perform the inversion was a structured triangular mesh containing 32768 triangular elements. The measured data was a set of simulated PAT images obtained using four illumination positions. For each image, the domain was illuminated using a line array of collimated sources, placed at each mesh node along one of the domain edges. The MC method used $N_p = 10^6$ photon packets to obtained the measurement data for each illumination. The absorption coefficient was heterogeneous, with a background value of 0.01 mm^{-1} and two square absorbing inclusions with absorption coefficients of 0.2 mm^{-1} and 0.3 mm^{-1}, respectively. This is the same absorption coefficient used in previous examples in this chapter, and can be seen in Figure 6.3(A). The anisotropy factor was chosen to be $g = 0.95$, and the factor f of light scattered into the forward direction for the δ-Eddington approximation was chosen to be $f = 0.026094g^3 + 0.023597g^2 + 0.13572g + 0.60366$, a polynomial in g found to best match MC simulations when using the Henyey-Greenstein phase function for biological tissue [100]. This particular implementation of the Monte Carlo allows only homogeneous scattering. The scattering coefficient μ_s is therefore considered to be constant throughout the entire domain, with $\mu_\mathrm{s} = 20$ mm^{-1}. Additional noise has not been added to the measured data, since the interpolation between the mesh used for the forward simulation and the mesh used for the inverse simulation should

provide a reasonable amount of error between the two cases. Furthermore, the model used to produce the forward data is entirely unrelated to the model used to perform the inversion. The inverse crime has therefore been entirely avoided.

6.4.1 Inversion for absorption coefficient

This example first looks to reconstruct the optical absorption coefficient when the scattering is known. Figure 6.19 shows the reconstructed μ_{a} after 19 iterations of the l-BFGS method. In this case, an excellent quantitative approximation to the absorption coefficient can be obtained, although there is a slight underestimation in the two absorbing heterogeneities and in regions close to boundaries, as can be seen in the profile Figure 6.19(C). The percent relative error in the reconstruction was $\epsilon_{\mathrm{a}} = 4.14\%$.

FIGURE 6.19: Reconstructed absorption coefficient using the gradient-based δ-Eddington minimisation where the forward data is simulated using the MC method. The measurement data was obtained using four illumination positions. The scattering coefficient was assumed to be known and homogeneous. (A) shows the true absorption coefficient. (B) shows the reconstructed absorption coefficient after 19 iterations. (C) shows a profile comparison in the x-direction of the true (grey solid) and reconstructed (blue dashed) absorption coefficients at $z = 1.2$ mm. (D) shows the percent relative error in the reconstruction at each iteration.

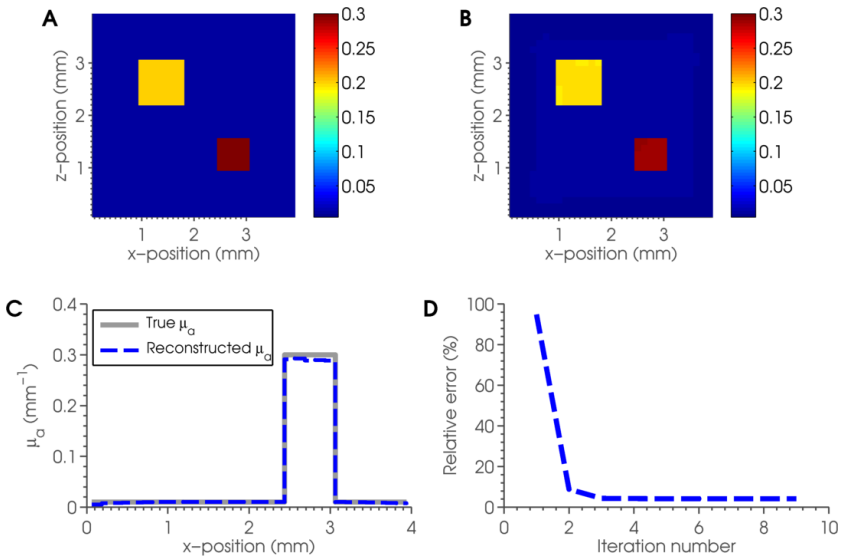

6.4.2 Inversion for absorption and scattering

In this example we will attempt to recover both absorption and scattering coefficients from the multiple-illumination PAT images simulated using the MC method. Unlike in previous examples, the scattering coefficient is homogeneous, with $\mu_{\mathrm{s}} = 20$ mm^{-1}. The initial guess at absorption was chosen to be the background value, $\mu_{\mathrm{a}}^{\mathrm{bg}} = 0.01$ mm^{-1}, and the initial guess at the scattering coefficient was chosen to be $\mu_{\mathrm{s}} = 5$ mm^{-1}. Figure 6.20 shows the results of the reconstruction for both coefficients after 73 iterations. In this case, the reconstructed absorption coefficient, shown in Figure 6.20(B), is actually more accurate than in the case when the scattering is known *a priori*. This is likely to be due to the fact that the minimisation ran for a larger number of iterations. The percent relative error in the absorption and scattering reconstructions were $\epsilon_{\mathrm{a}} = 3.31\%$ and $\epsilon_{\mathrm{s}} = 29.4\%$, respectively. Significant cross-talk can be seen in the scattering reconstruction in Figure 6.20(D), where the structure of the absorption coefficient is clear in the scattering reconstruction. This may be due to the fact that the scattering is homogeneous, and so the gradient-based method struggles to produce an entirely flat reconstruction from the heterogeneous gradient. A profile comparison of the true and reconstructed absorption and scattering coefficients can be seen in Figure 6.21. Although the reconstructed scattering coefficient does not accurately represent the true, homogeneous scattering, the reconstruction has moved the initial guess of 5 mm^{-1} up to its correct value of 20 mm^{-1} in significantly large portions of the domain.

6.5 Numerical examples using 3D simulated data

The efficiency of the δ-Eddington model compared to the full RTE enables the practical extension of the gradient-based technique to 3D data whilst still maintaining sufficient accuracy in the computational light model. In this section, the adjoint-assisted quasi-Newton scheme based on the δ-Eddington approximation to the RTE is used to recover the absorption and scattering coefficients from 3D simulated PAT images. Section 6.5.1

FIGURE 6.20: Reconstructed absorption coefficient using the gradient-based δ-Eddington minimisation where the forward data is simulated using the MC method. The measurement data was obtained using four illumination positions.

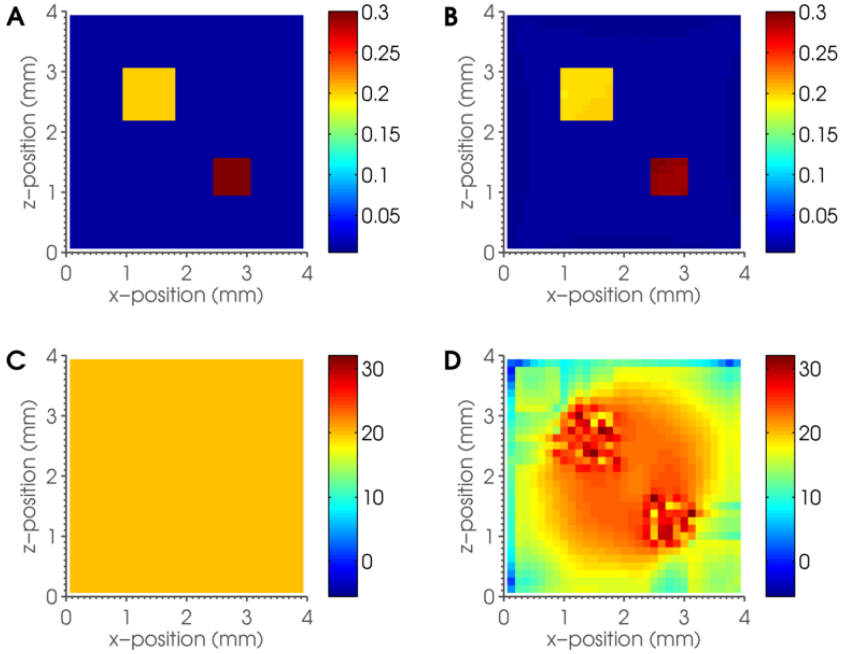

FIGURE 6.21: Reconstructed absorption coefficient using the gradient-based δ-Eddington minimisation where the forward data is simulated using the MC method. The measurement data was obtained using four illumination positions.

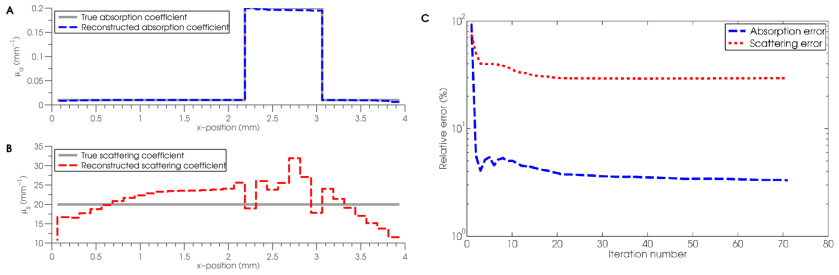

describes how the 3D data is simulated, and Section 6.5.2 shows the results of the inversion when recovering both optical coefficients simultaneously from 3D PAT images using multiple illumination positions.

6.5.1 Simulation of 3D PAT images

The computational mesh used in this section was a structured 3D mesh of the cubic domain $[0,4] \times [0,4] \times [0,4]$ mm^3, consisting of $N_e = 3375$ elements and $N_n = 4096$ nodes. The anisotropy factor was considered to be known and constant at $g = 0.8$, and the factor f of light scattered into the forward direction was chosen to be $f = 0.026094g^3 + 0.023597g^2 + 0.13572g + 0.60366$. As in Section 6.3.1, the scattering coefficient μ_s was chosen such that $\mu_\mathrm{s}' = \mu_\mathrm{s}(1-g)$ varied between 1 mm^{-1} and 3 mm^{-1}, which is typical of biological tissue. μ_s therefore consisted of a background value of $\mu_\mathrm{s}^\mathrm{bg} = 5$ mm^{-1} and a non-smooth scattering inclusions of $\mu_\mathrm{s}^1 = 15$ mm^{-1}. The absorption coefficient had a background value of $\mu_\mathrm{a}^\mathrm{bg} = 0.01$ mm^{-1} and a non-smooth absorbing inclusions of $\mu_\mathrm{a}^1 = 0.3$ mm^{-1}. Figure 6.22 shows the 3D geometries of the optical coefficients used in the numerical simulations.

FIGURE 6.22: Optical absorption and scattering coefficients used to simulate 3D PAT images. The optical absorption coefficient consists of a homogeneous background of 0.01 mm^{-1} with a cubic absorbing inclusion with a value of 0.3 mm^{-1}. The optical scattering coefficient consists of a homogeneous background of 5 mm^{-1} with a cubic absorbing inclusion with a value of 15 mm^{-1}. (A) A slice at $x = 1.2$ mm of the optical absorption coefficient. (B) A slice at $x = 2.4$ mm of the optical scattering coefficient. The units of the colorbar are mm^{-1}.

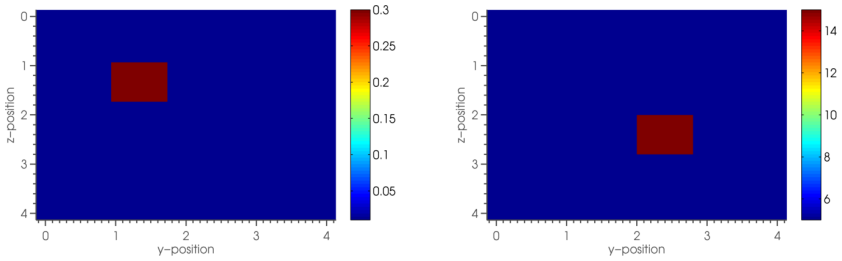

For the 3D examples, the domain was illuminated with a planar source array placed at one of the six sides of the domain to create a simulated 3D PAT image. This was done for four sides, corresponding to $z = 0$ mm, $z - 4$ mm, $y = 0$ mm and $y = 4$ mm, which created a set of four simulated PAT images.Equation 6.18 is then solved for the collimated fluence distribution Φ_c, which is used to calculate the source term for the diffusion equation 6.34. This equation is solved for the scattered fluence Φ_s, and the total fluence distribution Φ is then calculated from $\Phi = \Phi_\mathrm{c} + \Phi_\mathrm{s}$. The measured absorbed

optical energy density can then be calculated from $h^{\text{obs}} = \mu_{\text{a}}\Phi + \eta$, where η represents additive Gaussian noise. Figure 6.23 shows (A) the collimated fluence, (B) the scattered fluence, (C) the total fluence, and (D) the absorbed optical energy density with additive noise scaled to 5% of the mean absorbed energy. These images result from a planar source array placed along the top edge of the domain ($z = 4$ mm).

FIGURE 6.23: Forward data calculated using the 3D δ-Eddington approximation to the RTE. The absorption and scattering coefficients are both heterogeneous, each consisting of a cubic inclusion placed in a homogeneous background, and can be seen in Figure 6.22. The source is a planar source array placed along the top boundary ($z = 4$ mm). Given these optical coefficients and source geometry, a 3D PAT image can be simulated using the δ-Eddington approximation by calculating (A) the collimated fluence, (B) the scattered fluence, (C) the total fluence, and finally (D) the measured absorbed optical energy density, to which additive Gaussian noise may be added. In (D), noise scaled to 5% of the mean absorbed energy has been included.

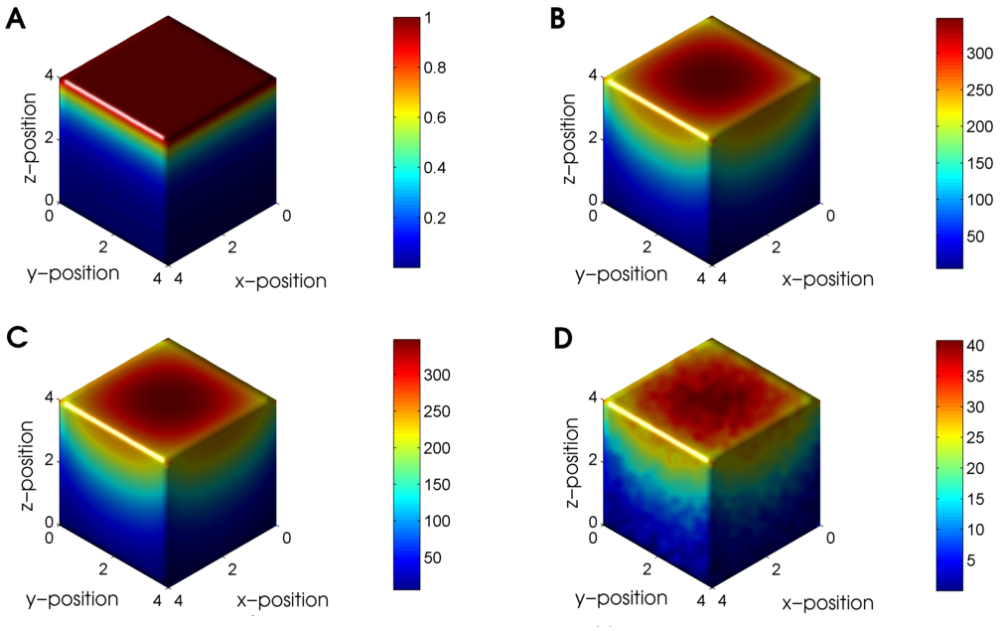

Using this set of measured absorbed energy images, we can proceed to apply a the l-BFGS method using the functional gradient calculations derived in Section 6.2.1. As in the 2D case, 15 previous iterations were stored, and the method was performed for a maximum of 2500 iterations. The background values of the optical coefficients to be recovered are used as an initial starting guess to begin the iterative scheme.

FIGURE 6.24: Profiles of the forward data calculated using the 3D δ-Eddington approximation to the RTE, corresponding to Figure 6.23. The profiles are in the z-direction and run through the absorbing heterogeneity at $x = 1.2$ mm and $y = 1.2$ mm. The profiles show (A) the collimated fluence, (B) the scattered fluence, (C) the total fluence, and (D) the measured absorbed optical energy density.

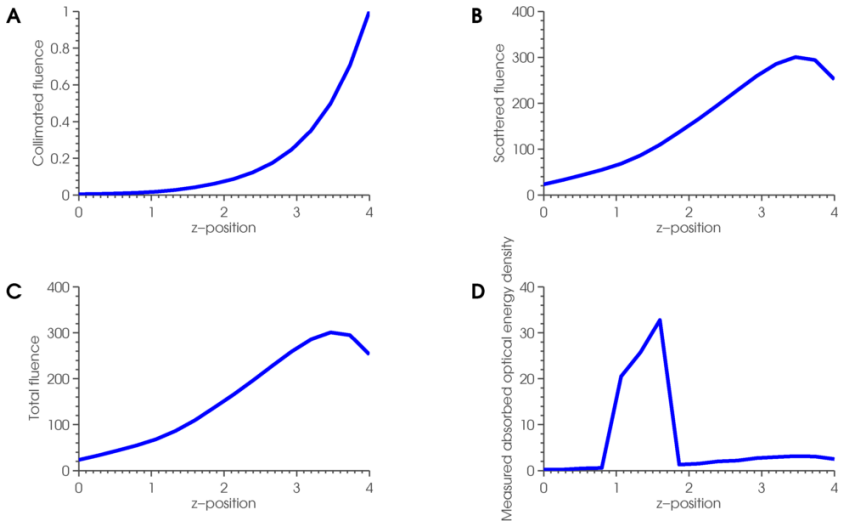

6.5.2 Inversion for absorption and scattering

In this section we will demonstrate the ability of the method to recover the optical absorption and scattering coefficients simultaneously from a set of simulated 3D PAT images. The measured data was simulated using the δ-Eddington approximation with four planar source arrays; a planar source array placed at a different edge of the domain ($z = 0$ mm, $z = 4$ mm, $y = 0$ mm, $y = 4$ mm) gave rise to a different simulated 3D PAT image. Two sets of measurement data were obtained; one without any additive noise and another with additive Gaussian noise scaled to 5% of the mean absorbed optical energy density. Tikhonov regularisation has been included in the scattering reconstruction in the case of noisy data. The background absorption and scattering coefficients were used as an initial guess to begin the iterative inversion. To quantify the error in the reconstructions, we shall look at the per cent relative errors ϵ_{a} and ϵ_{s} that we used in the 2D inversions, which are calculated using

$$\epsilon_{\mathrm{a}} = \frac{\left\| \mu_{\mathrm{a}}^{\mathrm{true}} - \mu_{\mathrm{a}}^{\mathrm{approx}} \right\|}{\left\| \mu_{\mathrm{a}}^{\mathrm{true}} \right\|}, \tag{6.66}$$

FIGURE 6.25: Slices of the true and reconstructed optical absorption coefficient recovered from simulated 3D PAT data obtained using four planar sources. The optical coefficients are heterogeneous, and can be seen in Figure 6.22. The slices are taken at $x = 1.2$ mm, $x = 1.4$ mm and $x = 1.6$ mm, where the absorbing inclusion is placed. The left-hand column shows the true absorption coefficient, the centre column shows the reconstructed absorption coefficient from noise-free data, and the right-hand column shows the reconstructed absorption coefficient from noisy data.

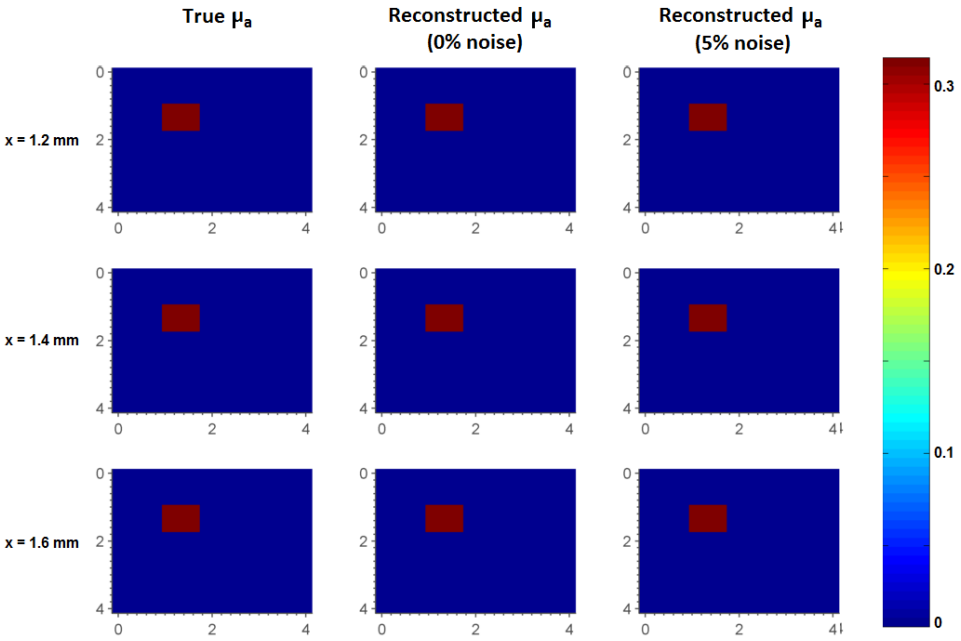

where $\mu_{\mathrm{a}}^{\mathrm{true}}$ is the true absorption coefficient and $\mu_{\mathrm{a}}^{\mathrm{approx}}$ is the reconstructed absorption coefficient, and

$$\epsilon_{\mathrm{s}} = \frac{\left\|\mu_{\mathrm{s}}^{\mathrm{true}} - \mu_{\mathrm{s}}^{\mathrm{approx}}\right\|}{\left\|\mu_{\mathrm{s}}^{\mathrm{true}}\right\|}, \tag{6.67}$$

where $\mu_{\mathrm{s}}^{\mathrm{true}}$ is the true scattering coefficient and $\mu_{\mathrm{s}}^{\mathrm{approx}}$ is the reconstructed scattering coefficient.

Slices through the true and reconstructed absorption coefficients can be seen in Figure 6.25, and slices through the true and reconstructed scattering coefficients can be seen in Figure 6.26. These are the results after 2270 iterations of the l-BFGS method. Using this measurement data, the gradient-based method is able to recover a highly accurate quantitative estimate of the absorption coefficient in both the noise-free and

FIGURE 6.26: Slices of the true and reconstructed optical scattering coefficients recovered from simulated 3D PAT data obtained using four planar sources. The optical coefficients are heterogeneous, and can be seen in Figure 6.22. The slices are taken at $x = 2.2$ mm, $x = 2.4$ mm and $x = 2.6$ mm, where the scattering inclusion is placed. The left-hand column shows the true scattering coefficient, the centre column shows the reconstructed scattering coefficient from noise-free data, and the right-hand column shows the reconstructed scattering coefficient from noisy data.

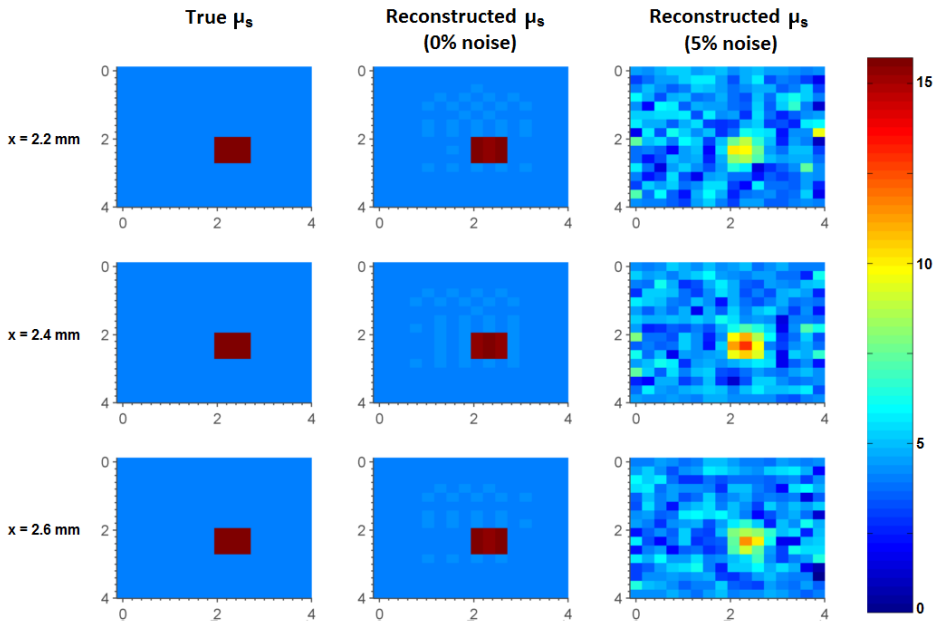

noisy cases. The percent relative errors in the reconstructed absorption coefficients are $\epsilon_{\mathrm{a}} = 5.8 \times 10^{-3}$ % and $\epsilon_{\mathrm{a}} = 1.92\%$ for the reconstructions from noise-free and noisy data, respectively. The percent relative errors in the reconstructed scattering coefficients are $\epsilon_{\mathrm{s}} = 0.19\%$ and $\epsilon_{\mathrm{s}} = 22.4\%$ for the reconstructions from noise-free and noisy data, respectively. A highly accurate reconstruction of the scattering coefficient was obtained in the noise-free case, though the propagation of errors due to noise are apparent in the reconstruction from noisy data. This reconstruction also produces an underestimation of the scattering coefficient. This is possibly due to the smoothing effect of the regularisation, and may be improved if a more appropriate regularisation method were used. A profile comparison of the true and reconstructed coefficients can be seen in Figure 6.27. The relative errors in the reconstruction at each iteration are plotted in Figure 6.27(C).

As we have seen in previous examples, these plots show that errors due to noise have been amplified in the reconstructions from noisy data. Although the underestimation of the scattering is significant, recovering for both optical coefficients simultaneously enables a reconstruction of the scattering coefficient which is accurate enough to produce an extremely accurate reconstruction of μ_{a} in both the noise-free and noisy case.

FIGURE 6.27: Profiles of the true and reconstructed optical absorption and scattering coefficients recovered from simulated 3D PAT data obtained using four planar sources. The optical coefficients are heterogeneous, and can be seen in Figure 6.22. (A) shows a profile comparison of the true absorption coefficient (solid grey), the reconstructed absorption coefficient from noise-free data (blue dashed), and the reconstructed absorption coefficient from noisy data (red dotted). The profiles are taken at $x = 1.4$ mm, $y = 1.4$ mm, through the absorbing inclusion. (B) shows a profile comparison of the true scattering coefficient (solid grey), the reconstructed scattering coefficient from noise-free data (blue dashed), and the reconstructed scattering coefficient from noisy data (red dotted). The profiles are taken at $x = 2.4$ mm, $y = 2.4$ mm, through the absorbing inclusion. (C) shows the percent relative error in the reconstructed absorption (blue) and scattering (red) coefficient from noise-free (dashed) and noisy (dotted) data at each iteration.

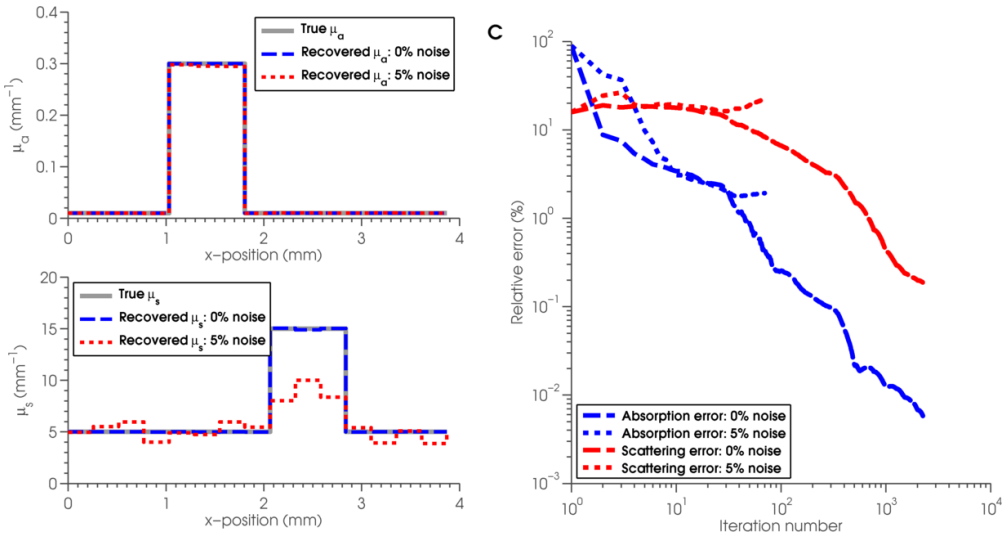

6.6 Conclusions

○ *The δ-Eddington approximation provides a more accurate light model than the DA, and has been incorporated into an adjoint-assisted gradient-based minimisation scheme for QPAT.*

Section 6.1 derived the δ-Eddington approximation for modelling light transport in biological tissue, and Section 6.1.1 verified the model against a Monte Carlo method. We also demonstrated the increased accuracy of the δ-Eddington approximation over the DA for three cases of scattering. In Section 6.2 we have shown that the δ-Eddington approximation can be successfully incorporated into the adjoint-assisted, gradient-based minimisation scheme presented in Chapters 4 and 5, and we verified the adjoint-assisted gradient calculations against a finite different calculation. Section 6.3 demonstrated the ability of the method to recover highly accurate quantitative estimates of optical absorption and scattering coefficients from simulated 2D PAT images. The results were achieved by using the model derived in Section 6.1 and the gradient calculations outlined in Section 6.2 to perform a limited-memory BFGS minimisation [95].

◦ *The gradient-based method using the δ-Eddington approximation can be used to recover the optical coefficients from 2D simulated PAT images.*

In the 2D reconstructions, the reconstruction of the absorption coefficient is reasonably stable even where additive noise is present in the measured data and no regularisation has been used to assist the inversion. When reconstructing the scattering coefficient, a first-order Tikhonov regularising penalty term, which depends only on the scattering coefficient, was added to the error functional, and subsequently the scattering functional gradient. In the reconstructions from noisy data, the inversion for the scattering coefficient was underestimated significantly more than the inversions from noise-free data. This smoothing effect of the reconstructed scattering coefficient when reconstructing from noisy data could be remedied by the inclusion of a more appropriate regularisation technique; Tikhonov regularisation looks to smooth out the solution, and will not preserve the sharp edges of the scattering coefficients used in these simulations. The total variation method, an edge-preserving regularisation technique, would have been a more appropriate regularisation technique for these particular scattering coefficients. Including total variation regularisation may therefore improve the scattering reconstruction, and subsequently the absorption reconstruction. In practice, however, the optimal regularisation scheme to use will ultimately depend on the geometry of the target. Given that the target may be unknown, it is encouraging at least that the absorption reconstruction

is not particularly sensitive to the method or inclusion of regularisation.

The use of the MC method to simulate the forward data is a good test for the accuracy of the δ-Eddington model. The use of a more accurate forward model that is entirely different to the model used in the inversion method avoids the inverse crime entirely. In Section 6.4, we demonstrated that highly accurate quantitative estimates of the absorption coefficient can be obtained even where MC is used to generate the simulated 2D PAT images. In these examples, the scattering coefficient was homogeneous. In the case of unknown scattering, the absorption coefficient was recovered despite the fact that the estimate of the scattering coefficient was quite poor, and significant absorption-scattering cross-talk could be seen in the reconstruction. However, the estimate was still roughly around the mean value of the scattering coefficient, which provides another example of how it may not be important to recover the scattering distribution pixel-by-pixel, but rather ensure its mean value is obtained. These results may be improved if the MC solution was obtained by simulating the delivery of a larger number of photon packets. Section 6.1.1 showed that the δ-Eddington provides a good approximation to the MC model, with a small error close to the source. Larger errors could be seen close to the boundary farthest from the source due to the fact that the number of photons N_p used to obtain the MC solution was not large enough to reduce the variance in the solution. In these examples, $N_p = 10^6$ photon packets were used to obtain a solution for four illumination positions. Running the MC method for, say, $N_p = 10^7$ photon packets would have therefore been impractical, but might have improved the reconstructions significantly.

◦ *It has been demonstrated that the gradient-based method using the δ-Eddington approximation can be extended to recover the optical coefficients from 3D simulated PAT images.*

The most significant advantage of using the δ-Eddington approximation is the ability to use the gradient-based method to obtain quantitative reconstructions from 3D data in a reasonable amount of time even for large-scale data sets. Section 6.5 demonstrated that the method can be successfully applied to 3D data sets obtained using multiple

illumination positions. In this case, highly accurate quantitative estimates of both absorption and scattering coefficients were obtained. A significant number of iterations were required to obtain the results presented in Sections 6.3 and 6.5 (typically around 2250 iterations). This is due to the slow convergence of the scattering coefficient. Whilst this number may seem large, the efficiency of the δ-Eddington model means that many more iterations can be used to perform the minimisation in less time than when using the full RTE for a problem of the same size. The reconstruction of the absorption and scattering coefficients are more accurate than the corresponding 2D RTE reconstructions, which may be due to the increase in the number of iterations taken to obtain the presented solutions. This presents another advantage of using the δ-Eddington approximation for QPAT, in that it will be able to perform a large enough number of iterations to produce convergence to a solution in a practical amount of time even for 3D data sets.

Chapter 7

Conclusions

The aim of this thesis has been to develop an accurate and practical method for determining chromophore concentrations from PAT images. By accurate, we mean a method which solves the full and general problem, in which there are no restrictions to the tissue geometry, and the optical absorption and scattering coefficients are unknown and may vary spatially. It will also be important that the light model is sufficiently accurate to perform a quantitative inversion. By practical, we mean a method which can remain computationally efficient when applied to large-scale, 3D data sets. This means that both the inversion scheme and the light model must be efficient for data sets of this size.

The difficulty in determining chromophore concentrations from PAT images is due to the non-linear dependence of the image on the concentrations themselves. Obtaining quantitatively accurate maps of chromophore concentrations requires the removal of the effects of the unknown light fluence, which varies both spatially and with wavelength, so that the problem is a non-linear inverse problem. Various approaches to tackling QPAT have been proposed. Early suggestions have involved invasive or clinically inapplicable methods such as tissue excision [56] or the embedding of absorbers beneath the skin [57]. Others have required additional information, such as the incorporation of contrast agents [58] or the use of measurements obtained using another imaging modality, e.g. optical tomography [59]. This thesis has focused on developing a method for QPAT

which avoids these limitations; the technique uses a mathematical representation of light transport in biological tissue to formulate a numerical model which can accurately simulate multi-wavelength PAT images. To obtain the chromophore concentration maps, the parameters of interest within the model are varied until the difference between the measured images and those predicted by the numerical model is minimised. This approach is non-invasive, does not require any additional hardware or changes to the usual experimental setup, and is applicable to any tissue geometry or type. However, for 3D data sets, model-based minimisation schemes can quickly become impractical; the chosen minimisation scheme may require so much computational memory for a 3D inversion that its implementation is unfeasible, or the complexity of the numerical model may mean that such an inversion is extremely time-consuming. Since PAT images are inherently 3D, these limitations must be overcome before a model-based inversion scheme can be successfully and routinely applied to experimental data. This thesis has demonstrated a practical inversion method for the full and general QPAT problem, in which the tissue geometry is arbitrary, the optical coefficients are unknown and the data is large-scale.

The majority of proposed methods for QPAT assume that the light field can be modelled using the diffusion approximation (DA) to the radiative transfer equation (RTE) [88]. Since the DA is not accurate close to the tissue surface, which is a region-of-interest in PAT, a more accurate model of light transport is required. This thesis initially proposed and implemented a practical inversion scheme which employs the full RTE. In Chapter 4 we derived a gradient-based minimisation scheme, in which the gradients of a non-linear least squares error functional with respect to the desired model parameters are calculated and used to step down towards the minimum. Calculating the gradients is straightforward if we employ a finite difference method, however, this would require N runs of the light model per iteration, where N is the number of unknowns in the problem (potentially millions for 3D data). The efficiency of this method was greatly improved by incorporating an adjoint light model; this allows the gradients to be calculated using only two runs of the model per iteration. Thus, while the time taken to solve the forward model may increase with the number of unknowns, the number of

evaluations of the forward model per iteration will remain the same. This means that, while a gradient-based minimisation will typically require a larger number of iterations than a corresponding Jacobian-based method such as the Gauss-Newton method, the time required per iteration will scale much more favourably. It is therefore likely that, even if it became possible to store the Jacobian matrix for a large data set, it will take significantly less time to perform an adjoint-assisted gradient-based method than a corresponding Jacobian-based method.

7.1 Known scattering

In our first approach, we have proposed, derived and implemented an adjoint-assisted, minimisation-based approach to recover quantitative estimates of the optical absorption coefficient from simulated PAT images. The method incorporates the full radiative transfer equation (RTE) to accurately model the propagation of light within biological tissue. In Section 4.2.2, we demonstrated the ability of the adjoint-assisted gradient-based method to reconstruct highly accurate estimates of the heterogeneous absorption coefficient from 2D simulated images when the scattering is known *a priori*. We first considered a single PAT image obtained using a single point source which illuminated a square domain from the top boundary. Using this measurement data, a good quantitative estimate of the absorption coefficient was obtained, though there was some underestimation of μ_{a} in areas far from the source where the signal-to-noise ratio (SNR) was relatively low. The results were improved significantly by increasing the SNR using a line array of sources along the same boundary; the percent relative error was less than 0.01% in the noise-free case. In the case where the measurement data included Gaussian noise, the reconstruction contained errors due to the amplification of noise in area where the SNR is low. To remedy this, additional information from multiple simulated PAT images obtained using multiple illumination positions was incorporated, and was shown to not only improve the accuracy of the reconstructed absorption, but also the speed of convergence to a solution. Using this multiple illumination approach, the proposed adjoint-assisted, gradient-based method can produce highly accurate estimates of the

absorption coefficient in both the noise-free and noisy cases.

In the inversions described above, the background absorption coefficient was used as an initial guess at the absorption coefficient, required to begin the iterative minimisation. A thorough investigation into the effect of changing the initial guess at the absorption coefficient on the absorption reconstruction was performed in Section 4.2.4. In the case where the initial guess is far from the background absorption, comparable quantitative estimates of the true absorption coefficient can still be found, although the number of iterations required to perform the inversion may increase. The results of this section therefore indicate that the background absorption provides the best starting point for the minimisation, however, the method should still converge to a correct solution should the background absorption be known.

The results in Section 4.2.2 assume *a priori* knowledge of the scattering coefficient. Since this quantity is difficult to both measure and estimate, it is important to develop a method which is either relatively insensitive to errors in the estimation of the scattering coefficient, or one that does not rely on making an approximation at all. In Section 4.2.5, we investigated how accurately we can recover the absorption coefficient if we were to incorrectly assume that the scattering coefficient is homogeneous and fixed at some constant value. The results in this section suggest that making this assumption of constant scattering when the true scattering coefficient is heterogeneous can produce reasonable accurate quantitative results when the scattering is fixed around its mean value. Diverting from this value by either under- or overestimating the scattering mean results in much larger errors in the absorption reconstruction, and will not be suitable for providing quantitatively accurate results. Assuming the scattering is homogeneous therefore requires a different kind of *a priori* knowledge, in the form of the scattering mean, which is unlikely to be available or easy to measure in practice.

7.2 Homogeneous scattering

The results in Section 4.2.5 suggest that fixing the scattering at its mean value may be enough to produce a sufficient estimate of the absorption coefficient for some applications. This is due to the relatively weak dependence of the data on the scattering coefficient; the absorbed energy density is the product of the absorption coefficient and the optical fluence, which is more strongly affected by absorption than scattering. Although the scattering is unlikely to be known in practice, there may be cases where a reasonable estimate of the scattering mean can be provided, in which case it will be useful to know how accurate a quantitative estimate we can obtain should this information be available. Section 4.2.6 looked at how accurately we are able to recover μ_{a} if we assume the heterogeneous scattering coefficient is considered homogeneous and is fixed at its mean value, where we found that reasonable estimates of the absorption coefficient can be determined, with percent relative errors as small as 2.62% when measurement data obtained using four illumination positions was used. However, Section 4.2.5 indicated that knowledge of the mean value of the scattering coefficient is likely to be considerably important *a priori* knowledge, since the errors in the reconstructions are significantly worse as the value at which the scattering is fixed moves away from the scattering mean. The accuracy of this method will therefore be directly related to the confidence in the true scattering mean, and, unfortunately, few situations arise in practice where the scattering mean is known or can be measured with accuracy.

7.3 Unknown scattering

If the scattering distribution is entirely unknown, and there is little confidence in the estimated mean value, the gradient-based method presented in Chapter 4 can be extended to reconstruct both absorption and scattering coefficients simultaneously. Reconstructing both optical coefficients simultaneously from simulated PAT images is challenging for a number of reasons. Firstly, reconstructing $(\mu_{\mathrm{a}}, \mu_{\mathrm{s}})$ from a single PAT image does not necessarily have a unique solution, and so additional information must be incorporated to

guarantee uniqueness. In the examples presented in this chapter, multiple illumination positions were used, whereby a set of simulated PAT images are obtained by illuminating the domain from different directions. Secondly, reconstructing the scattering coefficient from a PAT image is more challenging than reconstructing the absorption coefficient, since the data is only dependent upon the scattering coefficient through its effect on the optical fluence. The fluence therefore acts as a low pass filter to reduce the amplitudes of the high frequency components of the scattering distribution. Consequently, inverting for the scattering coefficient will grow the high frequency components, which will also have the effect of amplifying noise in the measured data.

In Chapter 5, we extended the adjoint-assisted, gradient-based method to the case where both optical coefficients are heterogeneous and unknown. In this case, it was shown that both optical coefficients can be simultaneously reconstructed from a set of 2D simulated images obtained using multiple illumination positions. When using two point sources, the estimate of the scattering coefficient was poor, resulting in some errors in the reconstruction of the absorption coefficient. However, despite the significant errors in the reconstructed scattering coefficient, the background value and structure of the absorption coefficient was obtained accurately; with only small under- or over-estimations of the values in the heterogeneities. This suggests that the details, pixel-by-pixel, of the scattering coefficient are not highly relevant to the estimate of μ_{a}. The correct estimation of the mean properties of the scattering appear to be more important to the absorption reconstruction. The results using two line sources improved the reconstruction of both coefficients, producing only a slight underestimation in the absorbing heterogeneity and an accurate estimation of the background value. Illuminating the domain from all four directions produced significantly better quantitative results than when fewer directions were used, and in this case, accurate quantitative reconstructions of both optical coefficients were found. In the case of four line sources, the absorption coefficient was reconstructed to within 1% of its true value in the noise-free case, and 1.15% in the noise-free case.

The approach presented here relies on the fact that data can be obtained using multiple illumination positions. Highly accurate estimates of the absorption coefficient when using four illumination positions can be obtained, but reconstructions from two illumination positions resulted in some over- or under-estimation of the absorption coefficient which may be significant in some applications. In the case where only two illumination positions are available, it is possible that the incorporation of additional information using multiple wavelengths could improve the reconstructions. This information could be easily incorporated into the gradient-based minimisation approach presented here, and may then provide enough information to produce results which are comparable with those using four illumination positions. An alternative approach could be to use the logarithm of the measured data to scale the dynamic range; preliminary results using this method can be found in Appendix A.

7.4 The δ-Eddington approximation

The gradient-based minimisation scheme presented in this thesis has demonstrated that it is possible to determine highly accurate quantitative estimates of the absorption coefficient in the case where there is no *a priori* knowledge of the optical coefficients. The use of a gradient-based method means that the method is memory-efficient, and so the extension to a large-scale 3D problem is possible. Furthermore, the use of the full RTE rather than the DA means that few approximations to the propagation of light within the tissue have been made, enabling accurate quantitative results to be obtained. However, since the RTE explicitly considers the light as a function of angle at every position, its solution is considerably more computationally expensive. 3D inversions using the RTE will therefore be time-consuming. To tackle this, we proposed the use of the δ-Eddington approximation to the RTE in a gradient-based minimisation scheme for QPAT. The δ-Eddington approximation first models the collimated light, found straightforwardly using the Beer-Lambert law, and uses this as the source term to determine the scattered light, which is the solution to a diffusion equation. The sum of the collimated and scattered

fields then provides the total field, which more accurately models the light in those regions where the DA breaks down. The δ-Eddington approximation is therefore a more suitable model for QPAT, since it is simultaneously accurate and tractable enough to use in a 3D gradient-based minimisation scheme.

A full and rigorous derivation of the δ-Eddington approximation to the RTE was included in Chapter 6, and the model was implemented in 2D and 3D. We then incorporated the δ-Eddington approximation into the adjoint-assisted gradient-based minimisation scheme described above. We showed that the adjoint-assisted gradient-based minimisation method using the δ-Eddington approximation can be used to reconstruct both optical coefficients simultaneously from 2D and 3D simulated PAT images.

In the 2D reconstructions, the reconstruction of the absorption coefficient is reasonably stable even where additive noise is present in the measured data and no regularisation has been used to assist the inversion. When reconstructing the scattering coefficient, a first-order Tikhonov regularising penalty term, which depends only on the scattering coefficient, was added to the error functional, and subsequently the scattering functional gradient. In the reconstructions from noisy data, the inversion for the scattering coefficient was underestimated significantly more than the inversions from noise-free data. This smoothing effect of the reconstructed scattering coefficient when reconstructing from noisy data could be remedied by the inclusion of a more appropriate regularisation technique; Tikhonov regularisation looks to smooth out the solution, and will not preserve the sharp edges of the scattering coefficients used in these simulations. The total variation method, an edge-preserving regularisation technique, would have been a more appropriate regularisation technique for these particular scattering coefficients. Including total variation regularisation may therefore improve the scattering reconstruction, and subsequently the absorption reconstruction. In practice, however, the optimal regularisation scheme to use will ultimately depend on the geometry of the target. Given that the target may be unknown, it is encouraging at least that the absorption reconstruction is not particularly sensitive to the method or inclusion of regularisation.

It was also demonstrated that the δ-Eddington-based minimisation can recover accurate quantitative estimates of the absorption coefficient from 2D data simulated using a Monte Carlo method, establishing that the δ-Eddington approximation will be applicable to real PAT data. The use of the MC method to simulate the forward data is a good test for the accuracy of the δ-Eddington model. The use of a more accurate forward model that is entirely different to the model used in the inversion method avoids the inverse crime entirely. In Section 6.4, we demonstrated that highly accurate quantitative estimates of the absorption coefficient can be obtained even where MC is used to generate the simulated 2D PAT images. In these examples, the scattering coefficient was homogeneous. In the case of unknown scattering, the absorption coefficient was recovered despite the fact that the estimate of the scattering coefficient was quite poor, and significant absorption-scattering cross-talk could be seen in the reconstruction. However, the estimate was still roughly around the mean value of the scattering coefficient, which provides another example of how it may not be important to recover the scattering distribution pixel-by-pixel, but rather ensure its mean value is obtained. These results may be improved if the MC solution was obtained by simulating the delivery of a larger number of photon packets. Section 6.1.1 showed that the δ-Eddington provides a good approximation to the MC model, with a small error close to the source. Larger errors could be seen close to the boundary farthest from the source due to the fact that the number of photons N_p used to obtain the MC solution was not large enough to reduce the variance in the solution. In these examples, $N_p = 10^6$ photon packets were used to obtain a solution for four illumination positions. Running the MC method for, say, $N_p = 10^7$ photon packets would have therefore been impractical, but might have improved the reconstructions significantly.

The most significant advantage of using the δ-Eddington approximation is the ability to use the gradient-based method to obtain quantitative reconstructions from 3D data in a reasonable amount of time even for large-scale data sets. Section 6.5 demonstrated that the method can be successfully applied to 3D data sets obtained using multiple illumination positions. In this case, highly accurate quantitative estimates of both absorption and scattering coefficients were obtained. A significant number of iterations

were required to obtain the results presented in Sections 6.3 and 6.5 (typically around 2250 iterations). This is due to the slow convergence of the scattering coefficient. Whilst this number may seem large, the efficiency of the δ-Eddington model means that many more iterations can be used to perform the minimisation in less time than when using the full RTE for a problem of the same size. The reconstruction of the absorption and scattering coefficients are more accurate than the corresponding 2D RTE reconstructions, which may be due to the increase in the number of iterations taken to obtain the presented solutions. This presents another advantage of using the δ-Eddington approximation for QPAT, in that it will be able to perform a large enough number of iterations to produce convergence to a solution in a practical amount of time even for 3D data sets.

7.5 Future work

Some very basic questions, such as the conditions under which QPAT is possible at all, even in principal, have only been answered since beginning the work in this thesis, and my contribution has been to devise the first, and so far only, algorithm which is simultaneously both sufficiently computationally efficient and accurate (in terms of the physics) to be applicable to experimental data. However, to take this very good start and translate it into something that would be useful to practitioners and transform preclinical practice requires several additional problems to be solved, which could form the programme for future work.

My suggestion for the advancement of this research is to apply the presented model-based inversion technique to *in vivo* 3D PAT images, with the aim of solving the remaining problems of QPAT. Some achievable specific objectives could be:

(1) To determine absolute blood oxygen saturation (sO_2) from *in vivo* 3D PAT images of the blood vasculature.

(2) To determine chromophore concentrations from *in vivo* 3D PAT images of the blood vasculature.

(3) To extend the inversion method to the limited-view case, thereby broadening the range of clinical applications.

These objectives correspond to three scenarios with increasing generality and difficulty due to the reduction of available information. Since blood sO_2 is calculated as a ratio of concentrations, it will remove the difficulties related to the calibration of the system and the unknown Gruneisen parameter. Methods developed during my PhD can therefore be extended straightforwardly to the multiwavelength case and used to solve (1). Objective (2) will require calibration of the system and must address the unknown Grüneisen parameter, and (3) will consider the case where there is a limited amount of data available (e.g. one-sided illumination).

7.5.0.1 Determining absolute blood oxygen saturation

The inversion algorithms presented here could be adapted to multiwavelength data to determine blood sO_2 from experimentally obtained images. The first of these experiments could be to acquire PA images of simple tissue phantoms using nickel chloride and copper chloride, in order to determine a concentration ratio analogous to sO_2. *In vivo* experimental data using measurements made in the mouse leg or tail could then be used to apply the proposed inversion method to determine quantitative estimates of oxy- and deoxyhaemoglobin, hence providing quantitative 3D spatial maps of absolute blood sO_2 from *in vivo* PAT images. To verify these results, the true sO_2 could be established by extracting arterial and venous blood immediately following the scan. Extension of the method to the multiwavelength case would be straightforward, and since sO_2 is a ratio, the main difficulty I foresee is in ensuring that the parameters in the model are correct, e.g. the way the illumination is modelled, especially for the case of *in vivo* data, where the mouse will have a curved surface.

7.5.0.2 Recovery of chromophore concentrations

Experimentalist collaborators within the Photoacoustic Imaging Group at UCL are just completing a system that will enable detection over a V-shaped array. This will, in principle, allow exact images to be reconstructed within the V-shape, though no algorithm that can do it has yet been devised which can account for the reflections between the array surfaces. It may therefore be useful to explore the use of an iterated time reversal reconstruction [102] in this setting. Having a data set that is free of artifacts takes QPAT to within one step of applying the methods developed in this thesis. The remaining challenges are the unknown calibration factor and Grüneisen parameter. Preliminary theoretical analysis [28] has suggested that the use of multiwavelength data can ensure uniqueness when determining the optical properties and the Grüneisen parameter simultaneously. By incorporating multiwavelength data and inverting for the parameters of interest and the unknown calibration factor simultaneously, a self-calibrating inversion can be performed. An alternative approach could be to extend the vector-field approach [28] from the diffusion equation to the closely-related δ-Eddington approximation.

7.5.0.3 Limited-view data

It is not always possible to obtain a full data set because of a lack of access to all sides of the region of interest. This is especially true when imaging humans, e.g. head and neck tumours or skin cancers. Developing a method for QPAT which uses limited-view data would therefore provide flexibility in the data acquisition process and significantly broaden the range of clinical applications. A future project could therefore be to apply the recently-proposed artifact-minimising approach [103] to image reconstructions with both the Universal Backprojection formula and time-reversal (using a k-space acoustic propagation model), and explore the use of penalty terms which incorporate prior knowledge to remove image artifacts [104]. While a full Bayesian inversion is out of reach for computational reasons, one could nevertheless ameliorate the uncertainty in the most troublesome parameters [87].

As well as providing useful information about the molecular structure of the imaged region, the model and inversion scheme could also be used to inform the experimental design. For example, in practice there will be constraints on the number of wavelengths and/or a limitation on the wavelength range. The model/inversion scheme might therefore be used to identify the optimum wavelengths, assess the uncertainty in the known input parameters or investigate the impact of errors in the reconstructed PA images.

Appendix A

Scaling the measured data

The results in Section 3.4.1.5 suggest that it may be worthwhile to use a different type of error functional in order to increase the sensitivity of the error functional to changes in the scattering coefficient. The use of a different error functional will subsequently change the gradient calculation shown in Section 4.1.4, and so a new calculation based on the new error functional is required. In optical tomography, the dynamic range of the light fluence is very large, and so the data is often scaled to ensure numerical stability of the optimisation problem [98]. Tarvainen *et al*. [30] suggested the use of this kind of scaling for QPAT, and used a Gauss-Newton method to recover the optical coefficients from the logarithm of the measured data.

Section 3.4.1.5 demonstrated that the error functional is relatively insensitive to the scattering coefficient. (see Figure A.1), suggesting that reconstruction of the scattering coefficient might be difficult. By scaling the measured data so that $h^{\text{obs}} = \ln(h^{\text{obs}})$, the sensitivity to the scattering coefficient can be improved. Figure A.2 shows the improvement to the sensitivity of the error functional when logarithmic data is used.

Here, we demonstrate that the logarithmic scaling of the data may be incorporated into the presented gradient-based minimisation scheme and used to improve the reconstructed absorption and scattering coefficients.

FIGURE A.1: (A) Contour and (B) surface plot showing the sensitivity of the error functional to changes in the absorption and scattering coefficients. The error map reaches its absolute minimum of zero at the correct perturbation data set, when $\mu_{\mathrm{a}}^{\mathrm{pert}} = 0.3\ \mathrm{mm}^{-1}$ and $\mu_{\mathrm{s}}^{\mathrm{pert}} = 15\ \mathrm{mm}^{-1}$, which is indicated by a blue cross. The error functional ε is much less sensitive to changes in the scattering coefficient than changes in the absorption coefficient.

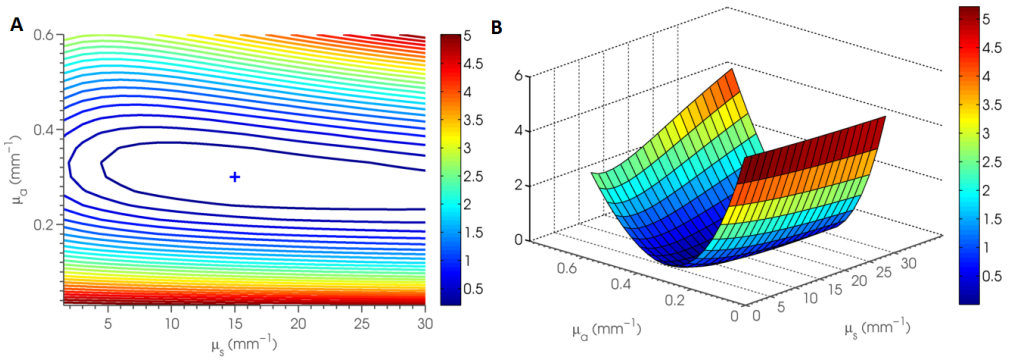

FIGURE A.2: (A) Contour and (B) surface plot showing the improved sensitivity of the error functional to changes in the absorption and scattering coefficients when using logarithmic data. The error map reaches its absolute minimum of zero at the correct perturbation data set, when $\mu_{\mathrm{a}}^{\mathrm{pert}} = 0.3\ \mathrm{mm}^{-1}$ and $\mu_{\mathrm{s}}^{\mathrm{pert}} = 15\ \mathrm{mm}^{-1}$, which is indicated by a blue cross.

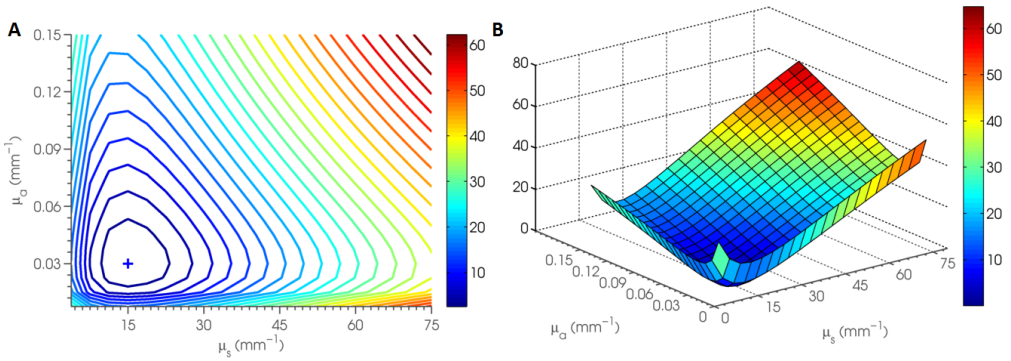

A.0.1 Functional gradients using logarithmic data

If the measured absorbed optical energy density h^{obs} is scaled such that $h^{\mathrm{obs}} = \ln h^{\mathrm{obs}}$, the error functional is given by

$$\varepsilon = \sum_{i=1}^{N} \frac{1}{2}(\ln(h^{\mathrm{obs}}) - \ln(h_i))^2, \tag{A.1}$$

where $h_i = \mu_{\mathrm{a}}(x_i)\Phi(\mu_{\mathrm{a}}(x_i), \mu_{\mathrm{s}}(x_i))$, which can be written in vector notation as

$$\frac{1}{2}(\ln(h^{\mathrm{obs}}) - \ln(h))^T(\ln(h^{\mathrm{obs}}) - \ln(h)). \tag{A.2}$$

Recall from Section 5.0.2 that the finite element light transport model can be written as

$$A\phi = b, \tag{A.3}$$

where the intention is to solve for the radiance ϕ. The light fluence is the sum of the radiance over all angles, and is calculated from

$$\Phi = M\phi, \tag{A.4}$$

where M is some measurement matrix. If the measured absorbed optical energy density h^{obs} is scaled such that $h^{\text{obs}} = \ln h^{\text{obs}}$, the error functional is given by

$$\varepsilon = \sum_{i=1}^{N} \frac{1}{2}(\ln(h^{\text{obs}}) - \ln(h_i))^2, \tag{A.5}$$

where $h_i = \mu_{\text{a}}(x_i)\Phi(\mu_{\text{a}}(x_i), \mu_{\text{s}}(x_i))$, which can be written in vector notation as

$$\frac{1}{2}(\ln(h^{\text{obs}}) - \ln(h))^T(\ln(h^{\text{obs}}) - \ln(h)). \tag{A.6}$$

Before continuing, first recall some established properties of the logarithm function:

- For a function f, the logarithmic derivative is given by

$$(\ln(f))' = \frac{f'}{f}. \tag{A.7}$$

- For functions f and g, the logarithmic derivative of their product is the sum of their logarithmic derivates (follows from the product rule):

$$(\ln(fg))' = \frac{(fg)'}{fg} = \frac{f'g + fg'}{fg} = \frac{f'}{f} + \frac{g'}{g} = (\ln(f))' + (\ln(g))'. \tag{A.8}$$

To differentiate Equation (A.6) with respect to the absorption coefficient we apply these properties to obtain

$$\begin{aligned}
\frac{\partial \varepsilon}{\partial \mu_{\mathrm{a}}} &= -\frac{\partial(\ln(h))}{\partial \mu_{\mathrm{a}}}(\ln(h^{\mathrm{obs}}) - \ln(h)) \\
&= -\frac{\partial(\ln(\mu_{\mathrm{a}}\Phi))}{\partial \mu_{\mathrm{a}}}(\ln(h^{\mathrm{obs}}) - \ln(h)) \\
&= -\left(\frac{\partial(\ln(\mu_{\mathrm{a}}) + \ln(\Phi))}{\partial \mu_{\mathrm{a}}}\right)(\ln(h^{\mathrm{obs}}) - \ln(h)) \\
&= -\left(\frac{\partial(\ln(\mu_{\mathrm{a}}))}{\partial \mu_{\mathrm{a}}} + \frac{\partial(\ln(\Phi))}{\partial \mu_{\mathrm{a}}}\right)(\ln(h^{\mathrm{obs}}) - \ln(h)) \\
&= \left(\frac{1}{\mu_{\mathrm{a}}} + \frac{1}{\Phi}\frac{\partial \Phi}{\partial \mu_{\mathrm{a}}}\right)(\ln(h^{\mathrm{obs}}) - \ln(h)).
\end{aligned} \tag{A.9}$$

To calculate the sensitivity of the fluence with respect to the absorption, first differentiating (A.4) with respect to μ_{a} gives

$$\frac{\partial \Phi}{\partial \mu_{\mathrm{a}}} = M\frac{\partial \phi}{\partial \mu_{\mathrm{a}}}, \tag{A.10}$$

and to calculate this we differentiate (A.3) with respect to μ_{a} to arrive at

$$\begin{aligned}
\frac{\partial(A\phi)}{\partial \mu_{\mathrm{a}}} &= \frac{\partial b}{\partial \mu_{\mathrm{a}}} \\
\Rightarrow \frac{\partial A}{\partial \mu_{\mathrm{a}}}\Phi + A\frac{\partial \phi}{\partial \mu_{\mathrm{a}}} &= 0 \\
\Rightarrow \frac{\partial \phi}{\partial \mu_{\mathrm{a}}} &= -A^{-1}\frac{\partial A}{\partial \mu_{\mathrm{a}}}\phi.
\end{aligned} \tag{A.11}$$

Substituting (A.11) into (A.10) then gives

$$\frac{\partial \Phi}{\partial \mu_{\mathrm{a}}} = -MA^{-1}\frac{\partial A}{\partial \mu_{\mathrm{a}}}\phi, \tag{A.12}$$

and substituting this into (A.9) gives

$$\begin{aligned}
\frac{\partial \varepsilon}{\partial \mu_{\mathrm{a}}} &= -\left(\frac{1}{\mu_{\mathrm{a}}} - \frac{1}{\Phi} M A^{-1} \frac{\partial A}{\partial \mu_{\mathrm{a}}} \phi\right)^T (\ln(h^{\mathrm{obs}}) - \ln(h)) \\
&= -\left(\frac{1}{\mu_{\mathrm{a}}}\right)^T (\ln(h^{\mathrm{obs}}) - \ln(h)) + \left(\frac{1}{\Phi} M A^{-1} \frac{\partial A}{\partial \mu_{\mathrm{a}}} \phi\right)^T (\ln(h^{\mathrm{obs}}) - \ln(h)) \\
&= -\left(\frac{1}{\mu_{\mathrm{a}}}\right)^T (\ln(h^{\mathrm{obs}}) - \ln(h)) \\
&\quad + \left(\frac{\partial A}{\partial \mu_{\mathrm{a}}} \phi\right)^T \left(\frac{1}{\Phi} M A^{-1}\right)^T (\ln(h^{\mathrm{obs}}) - \ln(h)) \\
&= -\left(\frac{1}{\mu_{\mathrm{a}}}\right)^T (\ln(h^{\mathrm{obs}}) - \ln(h)) \\
&\quad + \phi^T \left(\frac{\partial A}{\partial \mu_{\mathrm{a}}}\right)^T (A^T)^{-1} \left(\frac{1}{\Phi} M\right)^T (\ln(h^{\mathrm{obs}}) - \ln(h)). \qquad \text{(A.13)}
\end{aligned}$$

(A.14)

The adjoint solution is then defined by

$$\phi^* = (A^T)^{-1} \left(\frac{1}{\Phi} M\right)^T (\ln(h^{\mathrm{obs}}) - \ln(h)) \qquad \text{(A.15)}$$

$$\Rightarrow A^T \phi^* = \left(\frac{1}{\Phi} M\right)^T (\ln(h^{\mathrm{obs}}) - \ln(h)), \qquad \text{(A.16)}$$

so that the error functional gradient is given by

$$\frac{\partial \varepsilon}{\partial \mu_{\mathrm{a}}} = -\left(\frac{1}{\mu_{\mathrm{a}}}\right)^T (\ln(h^{\mathrm{obs}}) - \ln(h)) + \phi^T \left(\frac{\partial A}{\partial \mu_{\mathrm{a}}}\right)^T \phi^*. \qquad \text{(A.17)}$$

Similarly, the functional gradient for the scattering coefficient is given by

$$\frac{\partial \varepsilon}{\partial \mu_{\mathrm{s}}} = \phi^T \left(\frac{\partial A}{\partial \mu_{\mathrm{s}}}\right)^T \phi^*. \qquad \text{(A.18)}$$

These adjoint-assisted functional gradients can be calculated efficiently, using only one run each of the forward and adjoint models. The gradients can then be used in a quasi-Newton scheme to obtain an estimate of the optical coefficients.

A.1 Numerical example using two line sources

In Chapter 5, the gradient-based method was used to reconstruct the unknown absorption and scattering coefficients simultaneously. Where only two illumination positions were used (Section 5.1.2.2), the method produced relative errors in the reconstructions of $\epsilon_{\mathrm{a}} = 10.6\%$ and $\epsilon_{\mathrm{s}} = 15.1\%$. Here, the same example was performed, but this time logarithmic data and the corresponding gradients were used to perform the inversion. Figure A.3 shows the reconstruced absorption coefficients from noise-free data. The percent relative errors in these reconstructions are $\epsilon_{\mathrm{a}} = 6.31\%$ and $\epsilon_{\mathrm{s}} = 24.63\%$. A profile comparison can be seen in Figure A.4. Using this data, the estimation of the absorption coefficient is significantly improved. The reconstructed scattering coefficient is also improved. The values of the reconstructed scattering in the two heterogeneities are much closer to the true scattering, though the relative error has increased. This is possible due to errors in the background close to the boundary. These preliminary results suggest that the use of logarithmic data can improve the quality of the reconstructions, and may aid the inversions in the case where a larger number of multiple illuminations are unavailable.

FIGURE A.3: Reconstructed absorption and scattering coefficients from logarithmic data when using two line sources, corresponding to Figure 4.3(B). (A) shows the true absorption coefficient, (B) shows the reconstructed absorption coefficient from noise-free data. (C) shows the true scattering coefficient, and (D) shows the reconstructed scattering coefficient from noise-free data. The use of logarithmic data has improved the reconstruction of the optical absorption coefficient.

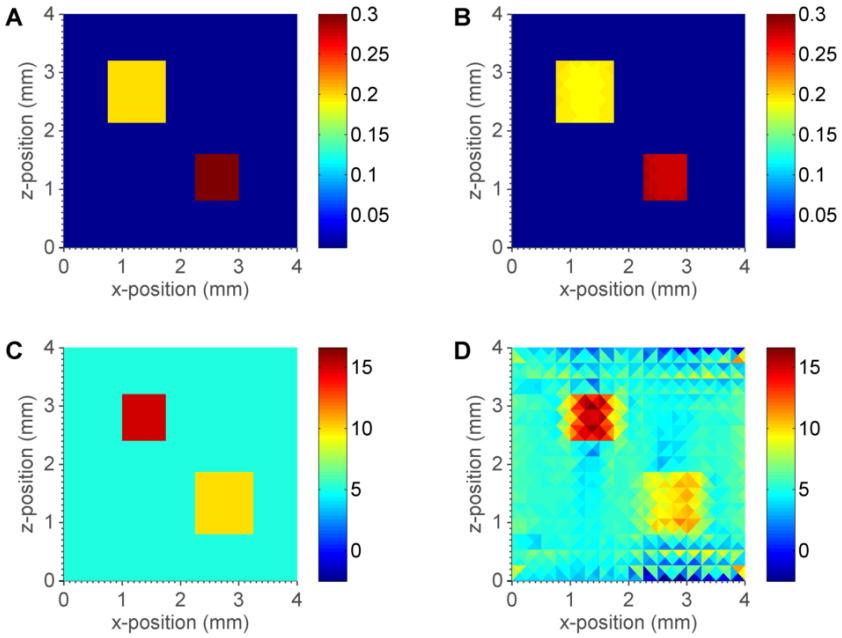

FIGURE A.4: Simultaneous recovery of absorption and scattering coefficients from logarithmic data using two line sources. A profile comparison of the reconstructed absorption coefficient can be seen in (A), which compares the true absorption coefficient (grey solid) and the reconstructed absorption coefficient from noise-free data (red dashed). The profile is taken in the x-direction at $z = 1.2$ mm. A profile comparison of the reconstructed scattering coefficient can be seen in (B), which compares the true scattering coefficient (grey solid) and the reconstructed scattering coefficient from noise-free data (blue dashed). The profile is taken in the x-direction at $z = 2.4$ mm. The percent relative errors of the reconstructed absorption (blue) and scattering (red) coefficients at each iteration can be seen in (C).

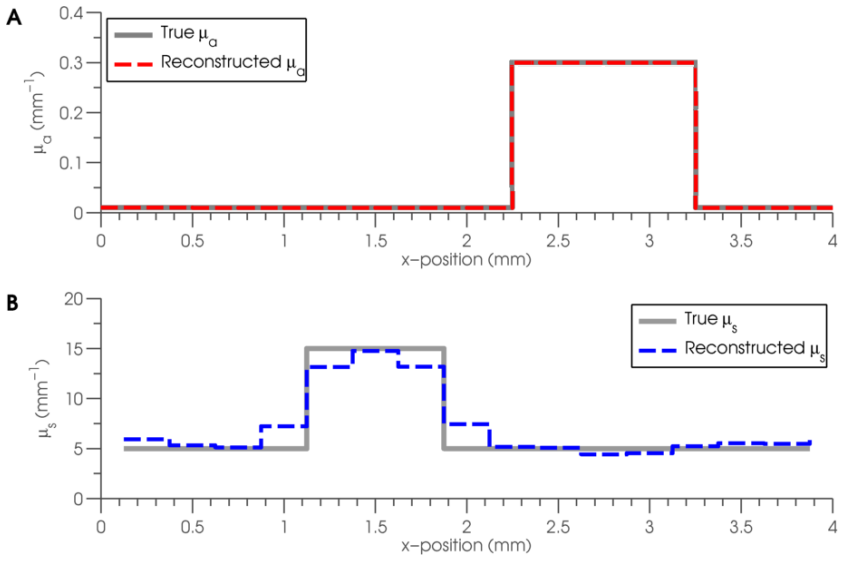

Appendix B

Using quotient data to remove the PA efficiency

In quantitative photoacoustic tomography (QPAT), the photoacoustic (PA) efficiency parameter, $\hat{\Gamma}$, is typically assumed to be known *a priori*. In practice, it is not likely that this will be the case, nor is it likely that $\hat{\Gamma}$ will be easy to estimate or to measure. It is likely then, that we may require a reconstruct method which can simultaneously recover the absorption coefficient μ_{a}, the scattering coefficient μ_{s} and the PA efficiency $\hat{\Gamma}$. However, Bal *et al*. have shown that, using the multiple illumination approach described in Section 3.4.1.1, only two out of the three parameters may be reconstructed uniquely, regardless of the number of different illuminations used [34]. Since $\hat{\Gamma}$ is independent of wavelength, it is possible that this may be remedied by incorporating measurement data obtained using multiple illumination positions *and* multiple wavelengths. Another approach was taken by Zemp [25], who tackled this problem by using a quotient of two PA images obtained using different illumination positions. Since the PA efficiency is independent of the source position, this removes $\hat{\Gamma}$ from the problem entirely. The method in [25] uses a linearisation technique which only allows the recovery of small perturbations to the optical coefficients. Here, we propose the incorporation of the 'quotient' type data into the gradient-based minimisation scheme for QPAT that has been demonstrated in this thesis.

B.1 Quotient data type using multiple illumination positions

To remove the PA efficiency parameter $\hat{\Gamma}$, we construct a new data type

$$d = \frac{p_1}{p_2} = \frac{\hat{\Gamma} h_1}{\hat{\Gamma} h_2} = \frac{\hat{\Gamma} \mu_{\mathrm{a}} \Phi_1}{\hat{\Gamma} \mu_{\mathrm{a}} \Phi_2}, \tag{B.1}$$

where h_1 and h_2 denote two PA images of a region of tissue illuminated with sources q_1 and q_2, respectively. Similarly, Φ_1 and Φ_2 denote the two fluences arising from the sources q_1 and q_2, respectively. Because $\hat{\Gamma}$ and μ_{a} do not change when the position of the source is altered, their product cancels out of the above equation, and we are left with

$$d = \frac{\Phi_1}{\Phi_2}. \tag{B.2}$$

The error functional to be minimised now becomes

$$\varepsilon = \frac{1}{2} \int_{\Omega} \left(\frac{\Phi_1}{\Phi_2} - d \right)^2 \, \mathrm{d}\Omega, \tag{B.3}$$

and, using the quotient rule, the functional gradients with respect to the absorption and scattering coefficients can be written as

$$\frac{\partial \varepsilon}{\partial \mu_{\mathrm{a}}} = \int_{\Omega} \left(\frac{\Phi_2 \frac{\partial \Phi_1}{\partial \mu_{\mathrm{a}}} - \Phi_1 \frac{\partial \Phi_2}{\partial \mu_{\mathrm{a}}}}{(\Phi_2)^2} \right) \left(\frac{\Phi_1}{\Phi_2} - d \right) \, \mathrm{d}\Omega \tag{B.4}$$

and

$$\frac{\partial \varepsilon}{\partial \mu_{\mathrm{s}}} = \int_{\Omega} \left(\frac{\Phi_2 \frac{\partial \Phi_1}{\partial \mu_{\mathrm{s}}} - \Phi_1 \frac{\partial \Phi_2}{\partial \mu_{\mathrm{s}}}}{(\Phi_2)^2} \right) \left(\frac{\Phi_1}{\Phi_2} - d \right) \, \mathrm{d}\Omega, \tag{B.5}$$

or equivalently

$$\frac{\partial \varepsilon}{\partial \mu_{\mathrm{a}}} = \int_{\Omega} \left(\frac{\partial \Phi_1}{\partial \mu_{\mathrm{a}}} \left(\frac{1}{\Phi_2} \right) \left(\frac{\Phi_1}{\Phi_2} - d \right) - \frac{\partial \Phi_2}{\partial \mu_{\mathrm{a}}} \left(\frac{\Phi_1}{(\Phi_2)^2} \right) \left(\frac{\Phi_1}{\Phi_2} - d \right) \right) \, \mathrm{d}\Omega \tag{B.6}$$

and

$$\frac{\partial \varepsilon}{\partial \mu_{\mathrm{s}}} = \int_{\Omega} \left(\frac{\partial \Phi_1}{\partial \mu_{\mathrm{s}}} \left(\frac{1}{\Phi_2} \right) \left(\frac{\Phi_1}{\Phi_2} - d \right) - \frac{\partial \Phi_2}{\partial \mu_{\mathrm{s}}} \left(\frac{\Phi_1}{(\Phi_2)^2} \right) \left(\frac{\Phi_1}{\Phi_2} - d \right) \right) \, \mathrm{d}\Omega. \tag{B.7}$$

An adjoint model can be used to assist the calculation of the functional gradients. The choice of adjoint model will depend on the choice of forward model used to perform the inversion. Here we will use the full radiative transfer equation (RTE) to demonstrate how the functional gradients can be calculated using a quotient data type. We define two RTE adjoint models

$$(-\hat{\mathbf{s}}\cdot\nabla+\mu_{\mathrm{a}}+\mu_{\mathrm{s}})\phi_1^*(\hat{\mathbf{s}})-\mu_{\mathrm{s}}\int_{S^{n-1}}\Theta(\hat{\mathbf{s}},\hat{\mathbf{s}}')\phi_1^*(\hat{\mathbf{s}}')\,\mathrm{d}\hat{\mathbf{s}}'=\frac{1}{\Phi_2}\left(\frac{\Phi_1}{\Phi_2}-d\right) \tag{B.8}$$

and

$$(-\hat{\mathbf{s}}\cdot\nabla+\mu_{\mathrm{a}}+\mu_{\mathrm{s}})\phi_2^*(\hat{\mathbf{s}})-\mu_{\mathrm{s}}\int_{S^{n-1}}\Theta(\hat{\mathbf{s}},\hat{\mathbf{s}}')\phi_2^*(\hat{\mathbf{s}}')\,\mathrm{d}\hat{\mathbf{s}}'=\frac{\Phi_1}{(\Phi_2)^2}\left(\frac{\Phi_1}{\Phi_2}-d\right), \tag{B.9}$$

which will be used to assist the gradient calculations with respect to the absorption and scattering coefficients.

B.1.1 Functional gradient for the absorption coefficient

The functional gradients for the absorption and scattering coefficients can be expressed in terms of the solutions of the adjoint models. For $i=1,2$, the RTE is given by

$$(\hat{\mathbf{s}}\cdot\nabla+\mu_{\mathrm{a}}+\mu_{\mathrm{s}})\phi_i(\hat{\mathbf{s}})=\mu_{\mathrm{s}}\int_{S^{n-1}}\Theta(\hat{\mathbf{s}},\hat{\mathbf{s}}')\phi_i(\hat{\mathbf{s}}')\,\mathrm{d}\hat{\mathbf{s}}'+q_i(\hat{\mathbf{s}}), \tag{B.10}$$

and differentiating with respect to $\mu_{\mathrm{a}}(\mathbf{r}')$ gives

$$(\hat{\mathbf{s}}\cdot\nabla+\mu_{\mathrm{a}}+\mu_{\mathrm{s}})\frac{\partial\phi_i(\hat{\mathbf{s}})}{\partial\mu_{\mathrm{a}}(\mathbf{r}')}-\mu_{\mathrm{s}}\int_{S^{n-1}}\Theta(\hat{\mathbf{s}},\hat{\mathbf{s}}')\frac{\partial\phi_i(\hat{\mathbf{s}}')}{\partial\mu_{\mathrm{a}}(\mathbf{r}')}\,\mathrm{d}\hat{\mathbf{s}}'=-\phi_i(\hat{\mathbf{s}})\delta(\mathbf{r}-\mathbf{r}'). \tag{B.11}$$

We now compute $(\phi_1^* \times B.6) - (\partial\phi_1/\partial\mu_\mathrm{a} \times B.8)$ with $i = 1$ to obtain

$$\begin{aligned}
&\Phi_1^*(\hat{\mathbf{s}}\cdot\nabla)\frac{\partial\Phi_1}{\partial\mu_\mathrm{a}} - \frac{\partial\Phi_1}{\partial\mu_\mathrm{a}}(\hat{\mathbf{s}}\cdot\nabla)\Phi_1^* \\
&\quad - \Phi_1^*\mu_\mathrm{s}\int_{S^{n-1}}\Theta(\hat{\mathbf{s}},\hat{\mathbf{s}}')\frac{\partial\Phi_1(\hat{\mathbf{s}}')}{\partial\mu_\mathrm{a}}\,\mathrm{d}\hat{\mathbf{s}}' \\
&\quad + \frac{\partial\Phi_1}{\partial\mu_\mathrm{a}}\mu_\mathrm{s}\int_{S^{n-1}}\Theta(\hat{\mathbf{s}},\hat{\mathbf{s}}')\Phi_1^*(\hat{\mathbf{s}}')\,\mathrm{d}\hat{\mathbf{s}}' \\
&\quad = -\Phi_1^*\Phi_1\delta(\mathbf{r}-\mathbf{r}') - \frac{\partial\Phi_1}{\partial\mu_\mathrm{a}}\left(\frac{1}{\Phi_2}\right)\left(\frac{\Phi_1}{\Phi_2}-d\right).
\end{aligned} \tag{B.12}$$

We now integrate over all angles $\hat{\mathbf{s}} \in S^{n-1}$ and over a volume Ω, use the identity 4.12, and note that $\partial\phi/\partial\mu_\mathrm{a} \to 0$ on the boundary $\partial\Omega$ to arrive at

$$\int_\Omega\int_{S^{n-1}}\frac{\partial\Phi_1}{\partial\mu_\mathrm{a}}\left(\frac{1}{\Phi_2}\right)\left(\frac{\Phi_1}{\Phi_2}-d\right)\,\mathrm{d}\hat{\mathbf{s}}\,\mathrm{d}\Omega = -\left[\int_{S^{n-1}}\Phi_1^*\Phi_1\,\mathrm{d}\hat{\mathbf{s}}\right]_{\mathbf{r}=\mathbf{r}'}. \tag{B.13}$$

If we now substitute this into Equation 4.6, we have

$$\frac{\partial\varepsilon}{\partial\mu_\mathrm{a}} = -\left[\int_{S^{n-1}}\Phi_1^*\Phi_1\,\mathrm{d}\hat{\mathbf{s}}\right]_{\mathbf{r}=\mathbf{r}'} - \frac{\partial\Phi_2}{\partial\mu_\mathrm{a}}\left(\frac{\Phi_1}{(\Phi_2)^2}\right)\left(\frac{\Phi_1}{\Phi_2}-d\right)\,\mathrm{d}\Omega. \tag{B.14}$$

We now compute $(\phi_2^* \times 4.6) - (\partial\phi_2/\partial\mu_\mathrm{a} \times B.8)$ with $i = 2$ to obtain

$$\begin{aligned}
&\Phi_2^*(\hat{\mathbf{s}}\cdot\nabla)\frac{\partial\Phi_2}{\partial\mu_\mathrm{a}} - \frac{\partial\Phi_2}{\partial\mu_\mathrm{a}}(\hat{\mathbf{s}}\cdot\nabla)\Phi_2^* \\
&\quad - \Phi_2^*\mu_\mathrm{s}\int_{S^{n-1}}\Theta(\hat{\mathbf{s}},\hat{\mathbf{s}}')\frac{\partial\Phi_2(\hat{\mathbf{s}}')}{\partial\mu_\mathrm{a}}\,\mathrm{d}\hat{\mathbf{s}}' \\
&\quad + \frac{\partial\Phi_2}{\partial\mu_\mathrm{a}}\,\mu_\mathrm{s}\int_{S^{n-1}}\Theta(\hat{\mathbf{s}},\hat{\mathbf{s}}')\Phi_2^*(\hat{\mathbf{s}}')\,\mathrm{d}\hat{\mathbf{s}}' \\
&\quad = -\Phi_2^*\Phi_2\delta(\mathbf{r}-\mathbf{r}') - \frac{\partial\Phi_2}{\partial\mu_\mathrm{a}}\left(\frac{\Phi_1}{(\Phi_2)^2}\right)\left(\frac{\Phi_1}{\Phi_2}-d\right).
\end{aligned} \tag{B.15}$$

Integrating over all angles $\hat{\mathbf{s}} \in S^{n-1}$ and over a volume Ω, using the identity 4.12 and noting that $\partial\phi/\partial\mu_\mathrm{a} \to 0$ on the boundary $\partial\Omega$ yields

$$\int_\Omega\int_{S^{n-1}}\frac{\partial\Phi_2}{\partial\mu_\mathrm{a}}\left(\frac{\Phi_1}{(\Phi_2)^2}\right)\left(\frac{\Phi_1}{\Phi_2}-d\right)\,\mathrm{d}\hat{\mathbf{s}}\mathrm{d}\Omega = -\left[\int_{S^{n-1}}\Phi_2^*\Phi_2\,\mathrm{d}\hat{\mathbf{s}}\right]_{\mathbf{r}=\mathbf{r}'}. \tag{B.16}$$

This can be substituted into Equation B.14 to obtain an expression for the functional gradient for the absorption at a point $\mathbf{r} = \mathbf{r}'$, given by

$$\frac{\partial \varepsilon}{\partial \mu_{\mathrm{a}}} = -\left[\int_{S^{n-1}} \Phi_1^* \Phi_1 \, \mathrm{d}\hat{\mathbf{s}}\right]_{\mathbf{r}=\mathbf{r}'} + \left[\int_{S^{n-1}} \Phi_2^* \Phi_2 \, \mathrm{d}\hat{\mathbf{s}}\right]_{\mathbf{r}=\mathbf{r}'}, \tag{B.17}$$

and hence, in general,

$$\frac{\partial \varepsilon}{\partial \mu_{\mathrm{a}}} = \int_{S^{n-1}} \Phi_2^* \Phi_2 - \Phi_1^* \Phi_1 \, \mathrm{d}\hat{\mathbf{s}}. \tag{B.18}$$

B.1.2 Functional gradient for the scattering coefficient

Differentiating Equation B.10 with respect to $\mu_{\mathrm{s}}(\mathbf{r}')$ gives

$$\begin{aligned}
&(\hat{\mathbf{s}} \cdot \nabla + \mu_{\mathrm{a}} + \mu_{\mathrm{s}}) \frac{\partial \phi_i(\hat{\mathbf{s}})}{\partial \mu_{\mathrm{s}}(\mathbf{r}')} - \mu_{\mathrm{s}} \int_{S^{n-1}} \Theta(\hat{\mathbf{s}}, \hat{\mathbf{s}}') \frac{\partial \phi_i(\hat{\mathbf{s}}')}{\partial \mu_{\mathrm{s}}(\mathbf{r}')} \mathrm{d}\hat{\mathbf{s}}' \\
&\quad = \left(\int_{S^{n-1}} \Theta(\hat{\mathbf{s}}, \hat{\mathbf{s}}') \Phi_i \, \mathrm{d}\hat{\mathbf{s}}' - \phi_i(\hat{\mathbf{s}}) \right) \delta(\mathbf{r} - \mathbf{r}'),
\end{aligned} \tag{B.19}$$

for $i = 1, 2$. Evaluating $(\phi_1^* \times B.7) - (\partial \phi_1 / \partial \mu_{\mathrm{s}} \times B.8)$ with $i = 1$ yields

$$\begin{aligned}
&\Phi_1^* (\hat{\mathbf{s}} \cdot \nabla) \frac{\partial \Phi_1}{\partial \mu_{\mathrm{s}}} - \frac{\partial \Phi_1}{\partial \mu_{\mathrm{s}}} (\hat{\mathbf{s}} \cdot \nabla) \Phi_1^* \\
&\quad - \Phi_1^* \mu_{\mathrm{s}} \int_{S^{n-1}} \Theta(\hat{\mathbf{s}}, \hat{\mathbf{s}}') \frac{\partial \Phi_1(\hat{\mathbf{s}}')}{\partial \mu_{\mathrm{s}}} \, \mathrm{d}\hat{\mathbf{s}}' + \frac{\partial \Phi_1}{\partial \mu_{\mathrm{s}}} \mu_{\mathrm{s}} \int_{S^{n-1}} \Theta(\hat{\mathbf{s}}, \hat{\mathbf{s}}') \Phi_1^*(\hat{\mathbf{s}}') \, \mathrm{d}\hat{\mathbf{s}}' \\
&\quad = \Phi_1^* \left(\int_{S^{n-1}} \Theta(\hat{\mathbf{s}}, \hat{\mathbf{s}}') \Phi_i \, \mathrm{d}\hat{\mathbf{s}}' - \phi_i(\hat{\mathbf{s}}) \right) \delta(\mathbf{r} - \mathbf{r}') - \frac{\partial \Phi_1}{\partial \mu_{\mathrm{s}}} \left(\frac{1}{\Phi_2} \right) \left(\frac{\Phi_1}{\Phi_2} - d \right),
\end{aligned} \tag{B.20}$$

and, analogous to the absorption case, this reduces to

$$\begin{aligned}
&\int_\Omega \frac{\partial \Phi}{\partial \mu_{\mathrm{s}}} \left(\frac{1}{\Phi_1} \right) \left(\frac{\Phi_1}{\Phi_2} \right) \mathrm{d}\Omega \\
&\quad = \int_{S^{n-1}} \int_{S^{n-1}} \Theta(\hat{\mathbf{s}}, \hat{\mathbf{s}}') \phi_1^*(\hat{\mathbf{s}}) \phi_1(\hat{\mathbf{s}}') \, \mathrm{d}\hat{\mathbf{s}}' \mathrm{d}\hat{\mathbf{s}} - \int_{S^{n-1}} \phi_1^*(\hat{\mathbf{s}}) \phi_1(\hat{\mathbf{s}}) \, \mathrm{d}\hat{\mathbf{s}}.
\end{aligned} \tag{B.21}$$

Similarly, for the second illumination position we have

$$\begin{aligned}
&\int_\Omega \frac{\partial \Phi}{\partial \mu_{\mathrm{s}}} \left(\frac{\Phi_1}{(\Phi_2)^2} \right) \left(\frac{\Phi_1}{\Phi_2} \right) \mathrm{d}\Omega \\
&\quad = \int_{S^{n-1}} \int_{S^{n-1}} \Theta(\hat{\mathbf{s}}, \hat{\mathbf{s}}') \phi_2^*(\hat{\mathbf{s}}) \phi_2(\hat{\mathbf{s}}') \, \mathrm{d}\hat{\mathbf{s}}' \mathrm{d}\hat{\mathbf{s}} - \int_{S^{n-1}} \phi_2^*(\hat{\mathbf{s}}) \phi_2(\hat{\mathbf{s}}) \, \mathrm{d}\hat{\mathbf{s}},
\end{aligned} \tag{B.22}$$

and substituting these into Equation B.7, we arrive at

$$\frac{\partial \varepsilon}{\partial \mu_{\mathrm{s}}} = \int_{S^{n-1}} \int_{S^{n-1}} \Theta(\hat{\mathbf{s}}, \hat{\mathbf{s}}') \left(\phi_1^*(\hat{\mathbf{s}}) \phi_1(\hat{\mathbf{s}}') - \phi_2^*(\hat{\mathbf{s}}) \phi_2(\hat{\mathbf{s}}') \right) \, \mathrm{d}\hat{\mathbf{s}}' \mathrm{d}\hat{\mathbf{s}} + \int_{S^{n-1}} \left(\phi_2^*(\hat{\mathbf{s}}) \phi_2(\hat{\mathbf{s}}) - \phi_1^*(\hat{\mathbf{s}}) \phi_1(\hat{\mathbf{s}}) \right) \, \mathrm{d}\hat{\mathbf{s}}. \tag{B.23}$$

The data is also less dependent on the absorption coefficient, which may mean that the scattering coefficient is recovered more easily.

B.2 Implementation

When using a finite element (FE) model to solve the RTE, the numerical implementation of the model must be accounted for when calculating the functional gradients. Recall from Equation 4.24 that the FE RTE model calculates the radiance ϕ by solving

$$A\phi^h = b, \tag{B.24}$$

where A is the FE system matrix representing the terms in the RTE and b is the source term. Translating this to the multiple illumination case, the two fluences can be calculated from

$$A\phi_1 = b_1, \qquad \Phi_1 = M\phi_1, \tag{B.25}$$

$$A\phi_2 = b_2, \qquad \Phi_2 = M\phi_2, \tag{B.26}$$

where ϕ_1 and ϕ_2 are the radiance arising from two different source vectors b_1 and b_2, and M is a measurement matrix which performs the summation over all angles. The error functional in vector notation becomes

$$\varepsilon = \frac{1}{2} \left(\frac{\Phi_1}{\Phi_2} - d \right)^{\mathrm{T}} \left(\frac{\Phi_1}{\Phi_2} - d \right). \tag{B.27}$$

B.2.1 Functional gradient for absorption

The absorption gradient is calculated by differentiating Equation B.27 with respect to $\mu'_{\mathrm{a}} = \mu_{\mathrm{a}}(\mathbf{r}')$ to obtain

$$\frac{\partial \varepsilon}{\partial \mu'_{\mathrm{a}}} = \left(\frac{\partial \left(\frac{\Phi_1}{\Phi_2} \right)}{\partial \mu'_{\mathrm{a}}} \right)^{\mathrm{T}} \left(h_m - \frac{\Phi_1}{\Phi_2} \right). \tag{B.28}$$

Using the quotient rule, this can be written as

$$\begin{aligned} \frac{\partial \varepsilon}{\partial \mu'_{\mathrm{a}}} &= \left(\frac{\Phi_2 \frac{\partial \Phi_1}{\partial \mu'_{\mathrm{a}}} - \Phi_1 \frac{\partial \Phi_2}{\partial \mu'_{\mathrm{a}}}}{(\Phi_2)^2} \right)^{\mathrm{T}} \left(d - \frac{\Phi_1}{\Phi_2} \right) \\ &= \left(\frac{1}{\Phi_2} \frac{\Phi_1}{(\Phi_2)^2} \frac{\partial \Phi_1}{\partial \mu'_{\mathrm{a}}} \right)^{\mathrm{T}} \left(h_m - \frac{\Phi_1}{\Phi_2} \right) - \left(\frac{\partial \Phi_2}{\partial \mu'_{\mathrm{a}}} \right)^{\mathrm{T}} \left(h_m - \frac{\Phi_1}{\Phi_2} \right). \end{aligned} \tag{B.29}$$

The gradients of the radiances ϕ_1 and ϕ_2 with respect to the absorption coefficient at $\mathbf{r}'$ are given by

$$\frac{\partial \Phi_1}{\partial \mu'_{\mathrm{a}}} = -MA^{-1} \frac{\partial A}{\partial \mu'_{\mathrm{a}}} \phi_1, \tag{B.30}$$

$$\text{and} \quad \frac{\partial \Phi_2}{\partial \mu'_{\mathrm{a}}} = -MA^{-1} \frac{\partial A}{\partial \mu'_{\mathrm{a}}} \phi_2. \tag{B.31}$$

Substituting these into Equation (B.29) gives

$$\frac{\partial \varepsilon}{\partial \mu'_{\mathrm{a}}} = -\left(\frac{1}{\Phi_2} MA^{-1} \frac{\partial A}{\partial \mu'_{\mathrm{a}}} \phi_1 \right)^{\mathrm{T}} \left(h_m - \frac{\Phi_1}{\Phi_2} \right) + \left(\frac{\Phi_1}{(\Phi_2)^2} MA^{-1} \frac{\partial A}{\partial \mu'_{\mathrm{a}}} \phi_2 \right)^{\mathrm{T}} \left(h_m - \frac{\Phi_1}{\Phi_2} \right), \tag{B.32}$$

which can be rearranged (using the identity $(AB \dots N)^{\mathrm{T}} = N^{\mathrm{T}} \dots B^{\mathrm{T}} A^{\mathrm{T}}$ and the fact that $(A^{-1})^{\mathrm{T}} = (A^{\mathrm{T}})^{-1}$) to give

$$\frac{\partial \varepsilon}{\partial \mu'_{\mathrm{a}}} = -\phi_1^{\mathrm{T}} \left(\frac{\partial A}{\partial \mu'_{\mathrm{a}}} \right)^{\mathrm{T}} \phi_1^* + \phi_2^{\mathrm{T}} \left(\frac{\partial A}{\partial \mu'_{\mathrm{a}}} \right)^{\mathrm{T}} \phi_2^*, \tag{B.33}$$

where ϕ_1^* and ϕ_2^* are the solutions to the adjoint models

$$\begin{aligned} A^{\mathrm{T}}\phi_1^* &= M^{\mathrm{T}}\left(\frac{1}{\Phi_2}\right)^{\mathrm{T}}\left(h_m - \frac{\Phi_1}{\Phi_2}\right) \\ \text{and} \qquad A^{\mathrm{T}}\phi_2^* &= M^{\mathrm{T}}\left(\frac{\Phi_1}{(\Phi_2)^2}\right)^{\mathrm{T}}. \end{aligned} \tag{B.34}$$

Similarly, the scattering gradient uses the same adjoint models, and is given by

$$\frac{\partial \varepsilon}{\partial \mu_{\mathrm{s}}} = -\phi_1^{\mathrm{T}}\left(\frac{\partial A}{\partial \mu_{\mathrm{s}}}\right)^{\mathrm{T}}\phi_1^* + \phi_2^{\mathrm{T}}\left(\frac{\partial A}{\partial \mu_{\mathrm{s}}}\right)^{\mathrm{T}}\phi_2^*. \tag{B.35}$$

These gradients and the error functional (B.27) can be used in the same quasi-Newton algorithm as the previous results in this thesis to provide an efficient minimisation technique to recover the optical coefficients that does not require knowledge or estimation of the Grüneisen parameter. Because of the division of data involved in construction this quotient of photoacoustic images, there may be problems at points in the region where the fluence is low. One way to tackle this problem could be to add in a regularising term whenever the fluence falls below some threshold value.

Appendix C

Including the acoustic propagation and reconstruction

All of the methods to solve the optical inverse problem presented so far have assumed that the acoustic inverse problem has been solved, and an exact reconstruction of the initial pressure distribution p_0 has been obtained. To simulate the noise present in the measured data, Gaussian noise has been added by scaling a distribution of pseudorandom numbers from a normal distribution with mean 0 and standard deviation 0.25 by a percentage of the mean value of the true absorbed energy. For example, after setting some optical coefficients $\mu_{\mathrm{a}}, \mu_{\mathrm{s}}$ and calculating $\Phi(\mu_{\mathrm{a}}, \mu_{\mathrm{s}})$ with a numerical light model, the true absorbed energy distribution h_t is found from

$$h_t = \mu_{\mathrm{a}}\Phi. \tag{C.1}$$

If we wish to add 5% Gaussian noise, then the noise term is then calculated from

$$\eta = 0.05 \times \max(h_t) \times \mathcal{N}(0, (0.25)^2), \tag{C.2}$$

where $\mathcal{N}(0, (0.25)^2$ is the normal distribution with mean 0 and standard deviation 0.25. This choice of mean and standard deviation means that the pseudorandom numbers come from a normal distribution between -1 and 1, so that the maximum additive noise

is 5% of the true absorbed energy. Although the addition of this type of noise might be a good indicator of how well each method will stand up when using real photoacoustic data, it is not representative of the artifacts and noise present in a real photoacoustic (PA) image, which is the solution to another inverse problem. When using simulated data, it may therefore be useful to simulate a more realistic noise model by including the acoustic propagation and inversion procedure into the simulation of PA images.

The acoustic inverse problem takes the boundary pressure measurements resulting from the propagation of a PA wave following the absorption of a light pulse and reconstructs the initial pressure using time-reversal methods, back-projection methods or fourier series expansion methods, all of which will results in different artifacts in the presence of noise and possibly under-estimate, over-estimate or completely remove parts of the data depending on the ultrasound detector geometry [21]. Simulating the forward and inverse acoustic problems will describe more closely the types of noise, artifacts and data problems that may appear in a real PA image and the resulting initial pressure distribution measurements that constitute the measured data of the optical inverse problem. The following publications demonstrate the adjoint-assisted gradient-based method using the RTE and the δ-Eddington approximation, and have included the acoustic propagation and reconstruction in the simulation of the measurement data.

Appendix D

Newton and quasi-Newton methods

In the late seventeenth century, Sir Isaac Newton developed a simple method for approximating the roots of polynomials. The method shows that, given a function $f(x)$, its derivative $f'(x)$ and some current approximation to a root x_n, a better approximation x_{n+1} can be found by calculating

$$x_{n+1} = x_n - \frac{f(x_n)}{f'(x_n)}. \tag{D.1}$$

In the mid-eighteenth century, Thomas Simpson realised that the method is not restricted to finding roots of polynomials, but can be used to solve general nonlinear equations. Simpson also noted that, since the derivative of a function is zero at its extrema, by applying Newton's method to the derivative of the function the method can also be used for solving optimisation problems.

D.1 Newton's method in optimisation

We first expand the obejctive function f by its Taylor series about some current approximation x_n, so that

$$f(x_n + \Delta x) \cong f(x_n) + f'(x_n)\Delta x + \frac{1}{2}f''(x_n)(\Delta x)^2. \tag{D.2}$$

This function attains its extremum when its derivative is equal to zero, i.e. when

$$f'(x_n + \Delta x) \cong f'(x_n) + f''(x_n)\Delta x = 0, \tag{D.3}$$

or equivalently

$$\Delta x = -\frac{f'(x_n)}{f''(x_n)}. \tag{D.4}$$

This gives the iterative update

$$x_{n+1} = x_n - \frac{f'(x_n)}{f''(x_n)}. \tag{D.5}$$

This method can be generalised to several dimensions by replacing the derivative with the gradient vector

$$\nabla f(x_n) = g(x_n) = \left[\frac{\partial f}{\partial x_1}, \ldots, \frac{\partial f}{\partial x_N}\right]^T \tag{D.6}$$

and the second derivative with the Hessian matrix

$$\nabla^2 f(x_n) = H(x_n) = \begin{bmatrix} \frac{\partial^2 f}{\partial x_1^2} & \cdots & \frac{\partial^2 f}{\partial x_1 \partial x_N} \\ \vdots & \ddots & \vdots \\ \frac{\partial^2 f}{\partial x_1 \partial x_N} & \cdots & \frac{\partial^2 f}{\partial x_N^2} \end{bmatrix}, \tag{D.7}$$

in which case the update is

$$x_{n+1} = x_n - H_n^{-1} g_n, \tag{D.8}$$

where $g_n = g(x_n)$ and $H_n = H(x_n)$. The term $-H_n^{-1} g_n$ is referred to as the Newton direction, and is often denoted by $p_n = -H_n^{-1} g_n$. Newton's method is a powerful technique, with quadratic convergence guaranteed in many cases.

D.1.1 Line search methods

At each iteration, the Newton direction p_n is calculated and a line search is performed to determine how far along the search direction should be moved to give an appropriate reduction in the objective function. The iteration is therefore given by

$$x_{n+1} = x_n + \alpha_n p_n, \tag{D.9}$$

where α is the step length. In computing an appropriate step length there is often a trade-off between accuracy and efficiency. Although the step length which produces the biggest reduction in the objective function is desireable, it is not often worthwhile to spend a lot of time determining which step length that may be. For example, it may be that the most accurate method to find α involves a gradient calculation, but since this may be much more expensive than evaluation of the objective function only, it may be more efficient to perform multiple function evaluations to improve the estimate of α than it is to use the gradient. Most line search implementations of Newton's method use the unit step $\alpha = 1$, with adjustments only when there is an unsatisfactory reduction in the value of f [95]. In this work, α was found by calculating the objective function at three different step lengths $\alpha_0 = 0, \alpha_1$ and α_2, *i.e.* by evaluating

$$f_0 = f(x_n), \tag{D.10}$$

$$f_1 = f(x_n + \alpha_1 p), \tag{D.11}$$

$$f_2 = f(x_n + \alpha_2 p). \tag{D.12}$$

The initial value of α_2 will depend on the typical values of the objective function, and we take $\alpha_1 = \alpha_2/2$. If f_1 results in a lower value than f_0 or f_2, then we take α_1 to be the appropriate step length. If f_2 produces the greatest reduction in f, then we attempt to find a bigger reduction than that and increase the bracket by setting $f_1 = f_2$ and $f_2 = 2f_2$. In the case that f_0 provides the greatest reduction, the bracket is reduced by setting $f_2 = f_1$ and $f_1 = f_1/2$. This method can then be repeated until it is f_1 produces the greatest decrease in f or until α_1 has fallen below some minimum step length.

Whilst Newton methods are an extremely efficient way of finding the minimise of a function, their main drawback is that finding the inverse of the Hessian matrix can be an expensive and error-prone operation. Because of this, efforts have been made to find accurate, computationally cheap approximations to the Hessian inverse.

D.2 Quasi-Newton methods

Instead of performing the laborious Hessian calculation and inversion, quasi-Newton methods use an approximation to the inverse Hessian by calculating the gradient g and making use of the fact that changes in the gradient provide information about the second derivative of f. This can be seen by using a Taylor series expansion of the gradient about the current approximation x_n, which gives

$$\nabla f(x_n + \Delta x) \cong \nabla f(x_n) + \nabla^2 f(x_n)\Delta x. \tag{D.13}$$

By defining $\Delta x := x_{n+1} - x_n$ and employing the notation defined earlier, this can be equivalently written as

$$H_n(x_{n+1} - x_n) \cong g_{n+1} - g_n, \tag{D.14}$$

which is often written as

$$H_n s_n \approx y_n, \tag{D.15}$$

where

$$s_n = x_{n+1} - x_n \quad \text{and} \quad y_n = g_{n+1} - g_n. \tag{D.16}$$

Quasi-Newton methods keep a rolling estimate of the Hessian matrix by improving the approximation at each iteration using the new gradient information. One of the most popular quasi-Newton methods is the Broyden-Fletcher-Goldfarb-Shanno method (BFGS). The BFGS algorithm begins by making an initial guess x_0 and initial approximation to the

Hessian matrix B_0 (often the identity matrix). By calculating the gradient information g_0, the Newton direction p_0 can be found from

$$p_0 = -B_0^{-1} g_0. \tag{D.17}$$

An acceptable step length α_0 is found by performing a line search, such as that described in Section D.1.1, and the update to the minimiser approximation is calculated from

$$x_1 = x_0 + \alpha_0 p_0 \tag{D.18}$$

and the gradient $g_1 = g(x_1)$ is calculated using this update. The values s_0 and y_0 can now be calculated using Equation D.16 and substituted into the BFGS update to the Hessian approximation

$$B_1 = B_0 - \frac{B_0 s_0 s_0^T B_0}{s_0^T B_0 s_0} + \frac{y_0 y_0^T}{y_0^T s_0}. \tag{D.19}$$

These steps are then repeated until the value of x which minimises the objective function is found, and in doing so the Hessian approximation is continuously improved since it includes information from every previous iteration step. The general BFGS approximation is given by

$$B_{n+1} = B_n - \frac{B_n s_n s_n^T B_n}{s_n^T B_n s_n} + \frac{y_n y_n^T}{y_n^T s_n}. \tag{D.20}$$

The minimiser x_k is then the value of x at an iteration k which causes the objective function $f(x_k)$ to fall below some user-defined tolerance.

Bibliography

[1] Robert A. Kruger, Richard B. Lam, Daniel R. Reinecke, Stephen P. Del Rio, and Ryan P. Doyle. Photoacoustic angiography of the breast. *Medical Physics*, 37(11):6096, 2010. ISSN 00942405. doi: 10.1118/1.3497677. URL http://link.aip.org/link/MPHYA6/v37/i11/p6096/s1&Agg=doi.

[2] Jan Laufer, Peter Johnson, Edward Zhang, Bradley Treeby, Ben Cox, Barbara Pedley, and Paul Beard. In vivo preclinical photoacoustic imaging of tumor vasculature development and therapy. *Journal of Biomedical Optics*, 17(5): 056016, May 2012. ISSN 10833668. doi: 10.1117/1.JBO.17.5.056016. URL http://link.aip.org/link/JBOPFO/v17/i5/p056016/s1&Agg=doihttp://www.ncbi.nlm.nih.gov/pubmed/22612139.

[3] Jan Laufer, Francesca Norris, Jon Cleary, Edward Zhang, Bradley Treeby, Ben Cox, Peter Johnson, Pete Scambler, Mark Lythgoe, and Paul Beard. In vivo photoacoustic imaging of mouse embryos. *Journal of Biomedical Optics*, 17(6): 0612201–0612208, 2012.

[4] Chulhong Kim, Christopher Favazza, and Lihong V Wang. In Vivo Photoacoustic Tomography of Chemicals: High-Resolution Functional and Molecular Optical Imaging at New Depths. *Chemical Reviews*, 110(5):2756–2782, 2010. doi: 10.1021/cr900266s.In.

[5] Alexander Graham Bell. Upon the production and reproduction of sound by light. *Journal of the Society of Telepraph Engineers*, 9(30):404–426, 1880.

[6] John Tyndall. Action of an intermittent beam of radiant heat upon gaseous matter. *Proceedings of the Royal Society of London*, 31:307–317, 1881.

[7] Wilhelm C Röntgen. On tones produced by the intermittent irradiation of a gas. *Philisophical Magazine*, 11(68), 1881.

[8] ML Veingerov. A method of gas analysis based on the optical-acoustic Tyndall-Röntgen effect. In *Dokl. Akad. Nauk SSSR*, volume 19, page 687, 1938.

[9] RA Kruger, P Liu, and CR Appledorn. Photoacoustic ultrasound (PAUS)-reconstruction tomography. *Medical Physics*, 22(10):1605–1609, 1995. URL http://link.aip.org/link/?MPHYA6/22/1605/1.

[10] C G Hoelen, F F de Mul, R Pongers, and a Dekker. Three-dimensional photoacoustic imaging of blood vessels in tissue. *Optics Letters*, 23(8):648–50, April 1998. ISSN 0146-9592. URL http://www.ncbi.nlm.nih.gov/pubmed/18084605.

[11] Alexander a. Oraevsky. Laser optoacoustic imaging of the breast: detection of cancer angiogenesis. *Proceedings of SPIE*, 3597(January):352–363, 1999. ISSN 0277786X. doi: 10.1117/12.356829. URL http://link.aip.org/link/?PSI/3597/352/1&Agg=doi.

[12] R A Kruger, K D Miller, H E Reynolds, W L Kiser, D R Reinecke, and G A Kruger. Breast cancer in vivo: contrast enhancement with thermoacoustic CT at 434 MHz - feasibility study. *Radiology*, 216(1):279–83, July 2000. ISSN 0033-8419. URL http://www.ncbi.nlm.nih.gov/pubmed/10887262.

[13] P. Beard. Biomedical photoacoustic imaging. *Interface Focus*, 1(4):602–631, June 2011. ISSN 2042-8898. doi: 10.1098/rsfs.2011.0028. URL http://rsfs.royalsocietypublishing.org/cgi/doi/10.1098/rsfs.2011.0028.

[14] Lihong V Wang. Prospects of photoacoustic tomography. *Medical Physics*, 35(12):5758–5767, 2008. URL http://link.aip.org/link/?MPH/35/5758/1.

[15] Xin Cai, Li Li, Arie Krumholz, Zijian Guo, Todd N Erpelding, Chi Zhang, Yu Zhang, Younan Xia, and Lihong V Wang. Multi-scale molecular photoacoustic tomography of gene expression. *PloS One*, 7(8):e43999, 2012.

[16] Arie Krumholz, Daria M Shcherbakova, Jun Xia, Lihong V Wang, and Vladislav V Verkhusha. Multicontrast photoacoustic in vivo imaging using near-infrared fluorescent proteins. *Scientific Reports*, 4, 2014.

[17] Song Hu, Konstantin Maslov, and Lihong V Wang. Second-generation optical-resolution photoacoustic microscopy with improved sensitivity and speed. *Optics Letters*, 36(7):1134–1136, 2011.

[18] Lihong Wang. *Photoacoustic Imaging and Spectroscopy*. CRC Press, 1 edition edition, 2009. ISBN 1420059912.

[19] Minghua Xu and Lihong V. Wang. Photoacoustic imaging in biomedicine. *Review of Scientific Instruments*, 77(4):041101, 2006. ISSN 00346748. doi: 10.1063/1.2195024. URL http://link.aip.org/link/RSINAK/v77/i4/p041101/s1&Agg=doi.

[20] Peter Kuchment and Leonid Kunyansky. Mathematics of Photoacoustic and Thermoacousic Tomography. In *Handbook of Mathematical Methods in Imaging*, chapter 19, pages 817–865. Springer, 2011.

[21] Peter Kuchment. *The Radon Transform and Medical Imaging*, volume 85. SIAM, 2014.

[22] B T Cox, S R Arridge, and P C Beard. Estimating chromophore distributions from multiwavelength photoacoustic images. *Journal of the Optical Society of America. A, Optics, image science, and vision*, 26(2):443–55, February 2009. ISSN 1084-7529. URL http://www.ncbi.nlm.nih.gov/pubmed/19183699.

[23] Guillaume Bal and Gunther Uhlmann. Inverse diffusion theory of photoacoustics. *Inverse Problems*, 26(8):085010, August 2010. ISSN 0266-5611. doi: 10.1088/0266-5611/26/8/085010. URL http://stacks.iop.org/0266-5611/26/i=8/a=085010?key=crossref.2e08ec4bcda4c93b6517697febaf5d32.

[24] Hao Gao, Hongkai Zhao, and Stanley Osher. Bregman methods in quantitative photoacoustic tomography. *UCLA CAM report*, 10-42, 2010.

[25] Roger J Zemp. Quantitative photoacoustic tomography with multiple optical sources. *Applied Optics*, 49(18):3566–72, June 2010. ISSN 1539-4522. URL http://www.ncbi.nlm.nih.gov/pubmed/20563210.

[26] Ben Cox, Tanja Tarvainen, and Simon Arridge. Multiple Illumination Quantitative Photoacoustic Tomography using Transport and Diffusion Models. *American Mathematical Society Contemporary Mathematics Series*, 559, 2011.

[27] Peng Shao, Ben Cox, and Roger J. Zemp. Estimating optical absorption, scattering, and Grueneisen distributions with multiple-illumination photoacoustic tomography. *Applied Optics*, 50(19):3145–3154, 2011.

[28] Guillaume Bal and Kui Ren. On multi-spectral quantitative photoacoustic tomography in diffusive regime. *Inverse Problems*, 28(2):025010, February 2012. ISSN 0266-5611. doi: 10.1088/0266-5611/28/2/025010. URL http://stacks.iop.org/0266-5611/28/i=2/a=025010?key=crossref.f8ef1a6e29e46bf4567d82d5a057b6d1.

[29] Hao Gao, Stanley Osher, and Hongkai Zhao. Quantitative photoacoustic tomography. In *Mathematical Modeling in Biomedical Imaging II*, pages 131–158. Springer, 2012.

[30] T Tarvainen, B T Cox, J P Kaipio, and S R Arridge. Reconstructing absorption and scattering distributions in quantitative photoacoustic tomography. *Inverse Problems*, 28(8):084009, 2012. ISSN 0266-5611. doi: 10.1088/0266-5611/28/8/084009. URL http://stacks.iop.org/0266-5611/28/i=8/a=084009?key=crossref.521af4c637d0a261ac00bf77e6e9f2d7.

[31] Kui Ren, Hao Gao, and Hongkai Zhao. A hybrid reconstruction method for quantitative PAT. *SIAM Journal on Imaging Sciences*, 6(1):32–55, 2013.

[32] T Saratoon, T Tarvainen, BT Cox, and SR Arridge. A gradient-based method for quantitative photoacoustic tomography using the radiative transfer equation. *Inverse Problems*, 29(7):075006, 2013.

[33] T Saratoon, T Tarvainen, SR Arridge, and BT Cox. 3D quantitative photoacoustic tomography using the δ-Eddington approximation. In *SPIE BiOS*, pages 85810V–85810V. International Society for Optics and Photonics, 2013.

[34] Guillaume Bal and Kui Ren. Multi-source quantitative photoacoustic tomography in a diffusive regime. *Inverse Problems*, 27(7):5033, July 2011. ISSN 0266-5611. doi: 10.1088/0266-5611/27/7/075003. URL http://stacks.iop.org/0266-5611/27/i=7/a=075003?key=crossref.c8e0bcca40ce59b0652d1e94ebcc035c.

[35] Michael I Mishchenko. Multiple scattering, radiative transfer, and weak localization in discrete random media: unified microphysical approach. *Reviews of Geophysics*, 46(2), 2008.

[36] Akira Ishimaru. *Wave propagation and scattering in random media*, volume 2. Academic press, New York, 1978.

[37] Scott Alan Prahl. *Light transport in tissue*. PhD thesis, University of Texas at Austin, 1988.

[38] Louis G Henyey and Jesse L Greenstein. Diffuse radiation in the galaxy. *The Astrophysical Journal*, 93:70–83, 1941.

[39] W.F. Cheong, S.A. Prahl, and A.J. Welch. A review of the optical properties of biological tissues. *IEEE Journal of Quantum Electronics*, 26(12):2166–2185, 1990. URL http://ieeexplore.ieee.org/xpls/abs_all.jsp?&arnumber=64354.

[40] S J Matcher, M Cope, and D T Delpy. Use of the water absorption spectrum to quantify tissue chromophore concentration changes in near-infrared spectroscopy. *Physics in Medicine and Biology*, 39(1):177–96, January 1994. ISSN 0031-9155. URL http://www.ncbi.nlm.nih.gov/pubmed/7651995.

[41] Scott Prahl. Optical absorption of hemoglobin, December 1999. URL http://omlc.ogi.edu/spectra/hemoglobin/index.html.

[42] Robert LP van Veen, HJCM Sterenborg, A Pifferi, A Torricelli, and R Cubeddu. Determination of VIS-NIR absorption coefficients of mammalian fat, with time-and

spatially resolved diffuse reflectance and transmission spectroscopy. In *Biomedical Topical Meeting*, page SF4. Optical Society of America, 2004.

[43] Steven L Jacques and Lihong Wang. Monte carlo modeling of light transport in tissues. In *Optical-thermal response of laser-irradiated tissue*, pages 73–100. Springer, 1995.

[44] S A Prahl, M Keijzer, S L Jacques, and A J Welch. A Monte Carlo Model of Light Propagation in Tissue. *SPIE Institute Series*, IS 5:102–111, 1989.

[45] Lihong Wang, Steven Jacques, and Liqiong Zheng. Monte Carlo modeling of light transport in multi-layered tissues. *Computer Methods and Programs in Biomedicine*, 47, 1995.

[46] Qianqian Fang and David A Boas. Monte carlo simulation of photon migration in 3d turbid media accelerated by graphics processing units. *Optics Express*, 17(22): 20178–20190, 2009.

[47] S R Arridge. Optical tomography in medical imaging. *Inverse Problems*, 41:40–93, 1999.

[48] T. Tarvainen, M. Vauhkonen, V. Kolehmainen, and J. P. Kaipio. Finite element model for the coupled radiative transfer equation and diffusion approximation. *International Journal for Numerical Methods in Engineering*, 65(3): 383–405, January 2006. ISSN 0029-5981. doi: 10.1002/nme.1451. URL http://doi.wiley.com/10.1002/nme.1451.

[49] M Schweiger, SR Arridge, and M Hiraoka. The finite element method for the propagation of light in scattering media: boundary and source conditions. *Medical Physics*, 22(11):1779–1792, 1995. URL http://www.medphys.ucl.ac.uk/research/borg/pdf/1995Schweiger.pdf.

[50] James J Duderstadt and Louis J Hamilton. *Nuclear reactor analysis*. Wiley, New York, 1976.

[51] Michael S Patterson, Britton Chance, and Brian C Wilson. Time resolved reflectance and transmittance for the non-invasive measurement of tissue optical properties. *Applied Optics*, 28(12):2331–2336, 1989.

[52] Daniele Contini, Fabrizio Martelli, and Giovanni Zaccanti. Photon migration through a turbid slab described by a model based on diffusion approximation. I. theory. *Applied Optics*, 36(19):4587–4599, 1997.

[53] Fabrizio Martelli, Daniele Contini, Adriana Taddeucci, and Giovanni Zaccanti. Photon migration through a turbid slab described by a model based on diffusion approximation. II. comparison with monte carlo results. *Applied Optics*, 36(19): 4600–4612, 1997.

[54] J H_ Joseph, WJ Wiscombe, and JA Weinman. The delta-eddington approximation for radiative flux transfer. *Journal of the Atmospheric Sciences*, 33(12):2452–2459, 1976.

[55] WJ Wiscombe and JH Joseph. The range of validity of the δ-eddington approximation. *Icarus*, 32(3):362–377, 1977.

[56] Xueding Wang, George Stoica, Xueyi Xie, Geng Ku, and Lihong V Wang. Noninvasive imaging of hemoglobin concentration and oxygenation in the rat brain using high-resolution photoacoustic tomography. *Journal of Biomedical Optics*, 11(2): 024015–024015, 2006.

[57] Erich W Stein, Konstantin Maslov, and Lihong V Wang. Noninvasive, in vivo imaging of the mouse brain using photoacoustic microscopy. *Journal of Applied Physics*, 105(10):102027, 2009.

[58] JR Rajian, PL Carson, and XD Wang. Quantitative photoacoustic measurement of tissue optical absorption spectrum aided by an optical contrast agent. *Optics Express*, 17(6):4879–89, March 2009. ISSN 1094-4087. doi: 10.1016/j.bbi.2008.05.010. URL http://www.pubmedcentral.nih.gov/articlerender.fcgi?artid=2689517&tool=pmcentrez&rendertype=abstract.

[59] Adam Q Bauer, Ralph E Nothdurft, Todd N Erpelding, Lihong V Wang, and Joseph P Culver. Quantitative photoacoustic imaging: correcting for heterogeneous light fluence distributions using diffuse optical tomography. *Journal of Biomedical Optics*, 16(9):096016–096016, 2011.

[60] Zijian Guo, Song Hu, and Lihong V Wang. Calibration-free absolute quantification of optical absorption coefficients using acoustic spectra in 3d photoacoustic microscopy of biological tissue. *Optics Letters*, 35(12):2067–2069, 2010.

[61] Alexander A Oraevsky, Steven L Jacques, and Frank K Tittel. Determination of tissue optical properties by piezoelectric detection of laser-induced stress waves. In *OE/LASE'93: Optics, Electro-Optics, & Laser Applications in Science & Engineering*, pages 86–101. International Society for Optics and Photonics, 1993.

[62] Raul Fainchtein, Basil J Stoyanov, John C Murphy, David A Wilson, and Daniel F Hanley. In-situ determination of concentration and degree of oxygenation of hemoglobin in neural tissue by pulsed photoacoustic spectroscopy. In *BiOS'97, Part of Photonics West*, pages 417–428. International Society for Optics and Photonics, 1997.

[63] Jun Xia, Amos Danielli, Yan Liu, Lidai Wang, Konstantin Maslov, and Lihong V Wang. Calibration-free quantification of absolute oxygen saturation based on the dynamics of photoacoustic signals. *Optics Letters*, 38(15):2800–2803, 2013.

[64] Elena V Savateeva, Alexander A Karabutov, Sergey V Solomatin, and Alexander A Oraevsky. Optical properties of blood at various levels of oxygenation studied by time-resolved detection of laser-induced pressure profiles. In *International Symposium on Biomedical Optics*, pages 63–75. International Society for Optics and Photonics, 2002.

[65] Rinat O Esenaliev, Irina V Larina, Kirill V Larin, Donald J Deyo, Massoud Motamedi, and Donald S Prough. Optoacoustic technique for noninvasive monitoring of blood oxygenation: a feasibility study. *Applied Optics*, 41(22):4722–4731, 2002.

[66] Jan Laufer, Clare Elwell, Dave Delpy, and Paul Beard. In vitro measurements of absolute blood oxygen saturation using pulsed near-infrared photoacoustic spectroscopy: accuracy and resolution. *Physics in Medicine and Biology*, 50(18): 4409–28, September 2005. ISSN 0031-9155. doi: 10.1088/0031-9155/50/18/011. URL http://www.ncbi.nlm.nih.gov/pubmed/16148401.

[67] Jan Laufer, Clare Elwell, Dave Delpy, and Paul Beard. Absolute measurements of local chromophore concentrations using pulsed photoacoustic spectroscopy. *Proceedings of SPIE*, 6086:60861J–60861J–8, 2006. ISSN 0277786X. doi: 10.1117/12.657372. URL http://link.aip.org/link/PSISDG/v6086/i1/p60861J/s1&Agg=doi.

[68] Jan Laufer, Dave Delpy, Clare Elwell, and Paul Beard. Quantitative spatially resolved measurement of tissue chromophore concentrations using photoacoustic spectroscopy: application to the measurement of blood oxygenation and haemoglobin concentration. *Physics in Medicine and Biology*, 52(1):141–68, January 2007. ISSN 0031-9155. doi: 10.1088/0031-9155/52/1/010. URL http://www.ncbi.nlm.nih.gov/pubmed/17183133.

[69] Jan Laufer, Ben Cox, Edward Zhang, and Paul Beard. Quantitative determination of chromophore concentrations from 2D photoacoustic images using a nonlinear model-based inversion scheme. *Applied Optics*, 49(8):1219, March 2010. ISSN 0003-6935. doi: 10.1364/AO.49.001219. URL http://ao.osa.org/abstract.cfm?URI=ao-49-8-1219.

[70] Lu Yin, Qiang Wang, Qizhi Zhang, and Huabei Jiang. Tomographic imaging of absolute optical absorption coefficient in turbid media using combined photoacoustic and diffusing light measurements. *Optics Letters*, 32(17):2556, 2007. ISSN 0146-9592. doi: 10.1364/OL.32.002556. URL http://www.opticsinfobase.org/abstract.cfm?URI=ol-32-17-2556.

[71] Zhen Yuan and Huabei Jiang. Simultaneous recovery of tissue physiological and acoustic properties and the criteria for wavelength selection in multispectral photoacoustic tomography. *Optics Letters*, 34(11):1714–6, June 2009. ISSN 0146-9592. URL http://www.ncbi.nlm.nih.gov/pubmed/19488158.

[72] Jorge Ripoll and Vasilis Ntziachristos. Quantitative point source photoacoustic inversion formulas for scattering and absorbing media. *Physical Review E*, 71(3): 1–9, March 2005. ISSN 1539-3755. doi: 10.1103/PhysRevE.71.031912. URL http://link.aps.org/doi/10.1103/PhysRevE.71.031912.

[73] Tanja Tarvainen. *Computational Methods for Light Transport in Optical Tomography*. PhD thesis, University of Kuopio, 2006.

[74] D Razansky, M Distel, C Vinegoni, R Ma, and N. Multispectral opto-acoustic tomography of deep-seated fluorescent proteins in vivo. *Nature Photonics*, 3 (June):412–417, 2009. doi: 10.1038/NPHOTON.2009.98. URL http://www.nature.com/nphoton/journal/v3/n7/abs/nphoton.2009.98.html.

[75] Benjamin T Cox, Jan G Laufer, Komel P Köstli, and Paul C Beard. Quantitative photoacoustic imaging: fitting a model of light transport to the initial pressure distribution. *Proceedings of SPIE*, 5697:49–55, 2005. ISSN 0277786X. doi: 10.1117/12.597190. URL http://link.aip.org/link/?PSI/5697/49/1&Agg=doi.

[76] Benjamin T Cox, Simon R Arridge, Kornel P Köstli, and Paul C Beard. Two-dimensional quantitative photoacoustic image reconstruction of absorption distributions in scattering media by use of a simple iterative method. *Applied Optics*, 45(8):1866–1875, 2006.

[77] B. T. Cox, S. R. Arridge, and P. C. Beard. Quantitative photoacoustic image reconstruction for molecular imaging. *Proceedings of SPIE*, 6086, 2006. ISSN 0277786X. doi: 10.1117/12.644806. URL http://link.aip.org/link/PSISDG/v6086/i1/p60861M/s1&Agg=doi.

[78] Zhen Yuan and Huabei Jiang. Quantitative photoacoustic tomography: Recovery of optical absorption coefficient maps of heterogeneous media. *Applied Physics Letters*, 88(23):231101, 2006. ISSN 00036951. doi: 10.1063/1.2209883. URL http://link.aip.org/link/APPLAB/v88/i23/p231101/s1&Agg=doi.

[79] Lei Yao, Yao Sun, and Huabei Jiang. Quantitative photoacoustic tomography based on the radiative transfer equation. *Optics Letters*, 34(12):1765–7, June 2009. ISSN 0146-9592. URL http://www.ncbi.nlm.nih.gov/pubmed/19529696.

[80] Lei Yao, Yao Sun, and Huabei Jiang. Transport-based quantitative photoacoustic tomography: simulations and experiments. *Physics in Medicine and Biology*, 55 (7):1917–34, April 2010. ISSN 1361-6560. doi: 10.1088/0031-9155/55/7/009. URL http://www.ncbi.nlm.nih.gov/pubmed/20224160.

[81] Thomas Jetzfellner, Daniel Razansky, Amir Rosenthal, Ralf Schulz, K.-H. Englmeier, and Vasilis Ntziachristos. Performance of iterative optoacoustic tomography with experimental data. *Applied Physics Letters*, 95(1):013703, 2009. ISSN 00036951. doi: 10.1063/1.3167280. URL http://link.aip.org/link/APPLAB/v95/i1/p013703/s1&Agg=doi.

[82] Biswanath Banerjee, Srijeeta Bagchi, Ram Mohan Vasu, and Debasish Roy. Quantitative photoacoustic tomography from boundary pressure measurements: noniterative recovery of optical absorption coefficient from the reconstructed absorbed energy map. *Journal of the Optical Society of America. A, Optics, image science, and vision*, 25(9):2347–56, September 2008. ISSN 1084-7529. URL http://www.ncbi.nlm.nih.gov/pubmed/18758563.

[83] B. T. Cox, S. R. Arridge, and P. C. Beard. Gradient-based quantitative photoacoustic image reconstruction for molecular imaging. *Proceedings of SPIE*, 6437: 64371T–1 – 64371T–10, 2007. ISSN 0277786X. doi: 10.1117/12.700031. URL http://link.aip.org/link/PSISDG/v6086/i1/p60861M/s1&Agg=doihttp://link.aip.org/link/PSISDG/v6437/i1/p64371T/s1&Agg=doi.

[84] B. T. Cox, S. R. Arridge, and P. C. Beard. Simultaneous estimation of chromophore concentration and scattering distributions from multiwavelength photoacoustic images. *Proceedings of SPIE*, 6856:68560Y–68560Y–12, 2008. ISSN 0277786X. doi: 10.1117/12.762924. URL http://link.aip.org/link/PSISDG/v6856/i1/p68560Y/s1&Agg=doi.

[85] Guillaume Bal, Alexandre Jollivet, and Vincent Jugnon. Inverse transport theory of photoacoustics. *Inverse Problems*, 26(2):025011, 2010.

[86] Tanja Tarvainen, Aki Pulkkinen, B Cox, J Kaipio, and S Arridge. Bayesian image reconstruction in quantitative photoacoustic tomography. *IEEE Transactions on Medical Imaging*, 32(12), 2013.

[87] A Pulkkinen, BT Cox, SR Arridge, JP Kaipio, and T Tarvainen. A Bayesian approach to spectral quantitative photoacoustic tomography. *Inverse Problems*, 30 (6):065012, 2014.

[88] Ben Cox, Jan G Laufer, Simon R Arridge, and Paul C Beard. Quantitative spectroscopic photoacoustic imaging: a review. *Journal of Biomedical Optics*, 17(6): 061202–1, 2012.

[89] Andrei Nikolaevich Tikhonov and VB Glasko. Use of the regularization method in non-linear problems. *USSR Computational Mathematics and Mathematical Physics*, 5(3):93–107, 1965.

[90] Per Christian Hansen and Dianne Prost O'Leary. The use of the l-curve in the regularization of discrete ill-posed problems. *SIAM Journal on Scientific Computing*, 14(6):1487–1503, 1993.

[91] Per Christian Hansen. Regularization tools: A matlab package for analysis and solution of discrete ill-posed problems. *Numerical Algorithms*, 6(1):1–35, 1994.

[92] Andreï Nikolaevitch Tikhonov. *Numerical methods for the solution of ill-posed problems*, volume 328. Springer, 1995.

[93] Per Christian Hansen. *Rank-deficient and discrete ill-posed problems: numerical aspects of linear inversion*, volume 4. Siam, 1998.

[94] Curtis R Vogel. *Computational methods for inverse problems*, volume 23. Siam, 2002.

[95] Jorge Nocedal and Stephen Wright. *Numerical Optimization*. Springer series in operations research. Springer, New York, NY, 2. ed. edition, 2006.

[96] Alexander D Klose and Andreas H Hielscher. Quasi-newton methods in optical tomographic image reconstruction. *Inverse Problems*, 19(2):387, 2003.

[97] Oliver Dorn. A transport-back transport method for optical tomography. *Inverse Problems*, 14(5), 1998.

[98] Martin Schweiger, Simon R Arridge, and Ilkka Nissilä. Gauss-Newton method for image reconstruction in diffuse optical tomography. *Physics in Medicine and Biology*, 50(10):2365, 2005.

[99] T Tarvainen, M Vauhkonen, and S Arridge. Gauss-Newton reconstruction method for optical tomography using the finite element solution of the radiative transfer equation. *Journal of Quantitative Spectroscopy and Radiative Transfer*, 109(17-18): 2767–2778, November 2008. ISSN 00224073. doi: 10.1016/j.jqsrt.2008.08.006. URL http://linkinghub.elsevier.com/retrieve/pii/S0022407308001854.

[100] Chenggang Chai, Yaqin Chen, Pengcheng Li, and Qingming Luo. Improved steady-state diffusion approximation with an anisotropic point source and the δ–eddington phase function. *Applied Optics*, 46(21):4843–4851, 2007.

[101] SR Arridge, M Schweiger, M Hiraoka, and DT Delpy. A finite element approach for modeling photon transport in tissue. *Medical Physics*, 20(2):299–309, 1993.

[102] Plamen Stefanov and Gunther Uhlmann. Thermoacoustic tomography with variable sound speed. *Inverse Problems*, 25(7):075011, 2009.

[103] Jürgen Frikel and Eric Todd Quinto. Artifacts in incomplete data tomography-with applications to photoacoustic tomography and sonar. *arXiv preprint arXiv:1407.3453*, 2014.

[104] Tanmayi Oruganti, Jan G Laufer, and Bradley E Treeby. Vessel filtering of photoacoustic images. In *SPIE BiOS*, page 85811W. International Society for Optics and Photonics, 2013.